Rigorous Analysis of Reactive Microemulsion Systems for Process Design and Operation

vorgelegt von
M.Sc.
Markus Illner
ORCID: 0000-0003-1500-9588

an der Fakultät III – Prozesswissenschaften
der Technischen Universität Berlin
zur Erlangung des akademischen Grades

Doktor der Ingenieurwissenschaften
- Dr.-Ing. -

genehmigte Dissertation

Promotionsausschuss:

Vorsitzender:	Prof. Dr.-Ing. habil. Harald Kruggel-Emden
Gutachter:	Prof. Dr.-Ing. habil. Jens-Uwe Repke
Gutachter:	Prof. Dr. rer. nat. habil. Reinhard Schomäcker
Gutachter:	Prof. Dr.-Ing. habil. Kai Sundmacher

Tag der wissenschaftlichen Aussprache: 07. Mai 2020

Berlin 2020

To my parents

Acknowledgements

A Ph.D. thesis is seldom the work of a single person. For my research I had the pleasure of working with numerous people, helping me to advance both, professionally and personally.
First of all, I would like to thank Prof. Dr.-Ing. Jens-Uwe Repke for letting me finish my Ph.D. at his department DBTA. I gratefully acknowledge the opportunities and freedom he provided to follow various research directions, as well as the possibility to attend international conferences to broaden my scientific horizon. I am very thankful for his continuous assistance, critical but constructive feedback, and nudging in the right direction. Secondly, I would like to thank Prof. Dr. rer. nat. Reinhard Schomäcker for his co-supervision within the *Collaborative Research Center TR63 InPROMPT* and the close collaboration, marked by very fruitful discussions and hints. I am thankful, that Prof. Dr.-Ing. Kai Sundmacher accepted to review my Ph.D. thesis, completing the scientific committee. At this point, I would also like to express my gratitude towards Prof. Dr.-Ing. Günter Wozny, under whom I initially entered the research project. His useful advice and inspiring ideas were always helpful to develop research-wise and encouraging to look beyond known horizons.

Next, I would like to express my sincere thanks to all the students assisting me throughout the last years and putting up with endless phase separation experiments and abysses of my research ideas. In particular I thank: Joris Weigert for assisting greatly on the state estimation framework; Jan-Paul Ruiken for bringing Raman spectroscopy into microemulsions; Angela Alzate for tackling endless hours of phase separation experiments; Peter Köster, the jack of all trades regarding plant construction who also assisted on the phase separation model. With all their ideas and effort, they have contributed to the great success of the project. My deepest gratitude goes out to the DBTA staff with special thanks to with Marita, Uta, Ewa, Dietmar, Martin, Andreas, Marlos, Philipp, and Tim, making practical science possible. Cheers to all colleagues for fruitful discussions, helping out on numerous mini-plant operations, and making work joyful. Very special thanks go out to my office mate Gregor Tolksdorf and his successor Volodymyr Kozachynskyi for making work a joy and enduring my cursing.

Next in line I thank Dr.-Ing. Tobias Pogrzeba, Dr.-Ing. Marcel Schmidt, and Ariane Weber from the Department of Chemistry at TU Berlin for the very fruitful and close cooperation within

the project. I would like to thank Michael Maiwald, Klas Meyer, and Andrea Paul from the BAM, who have greatly assisted on the analytic side of the project. Very special thanks go out to Dr.-Ing. Erik Esche for his continuous assistance, already since my undergrad studies, and bringing me to process systems engineering. His enthusiasm is always inspiring and his outstanding helpfulness on any issue invaluable.

Finally, this work is dedicated to my family, Doreen, and my friends who never stopped believing in my and helping me to get, where I am today.

Abstract

English Summary

In recent years, significant effort towards more sustainable chemical processes and products is noticeable in both academia and industry. Hence, process development and operation aim for the implementation of new synthesis paths for emerging renewable feedstocks and waste prevention. However, industrial realization of developed process concepts is often enough challenging due to their novelty, unknown fluid properties, and unidentified system phenomena. To overcome this hurdle and nevertheless enable the early stage proof of concept for new innovative process concepts, a systematic procedure is developed within this thesis. It consists of a rigorous system analysis and identification of operation challenges and subsequent development of solution strategies regarding process design and model-based optimal operation strategies.

As a case study, the hydroformylation of 1-dodecene in surfactant containing multiphase media is investigated. These so called microemulsion systems enable atom efficient homogeneously catalyzed reaction paths, as well as efficient product separation and catalyst recycling via exploitation of their thermomorphic phase separation behavior. Aiming for a successful realization of a proof of concept in a mini-plant, the systematic analysis of this innovative solvent system firstly focuses on the reaction itself. With a developed methodology for model adaption, a mechanistic microkinetic model is successfully augmented regarding relevant influences of the microemulsion. Secondly, the dynamic phase separation behavior is systematically studied to identify influencing factors and system inherent challenges, which are hampering process operation. Key therein is the analysis of system controllability regarding available measurements. As a result, a critical immeasurability of relevant surfactant concentrations, an overall very small operation region, and a high sensitivity of reaction and phase separation performance regarding disturbances in concentrations are identified as major obstacles.

Based on this, design upgrades of reactor, settler geometry, and recycle configuration are developed. Moreover, process operation is assisted by the development of optimal control trajectories. As a cornerstone for this, a fully dynamic mini-plant model suitable for optimization is deployed. Key elements therein are the developed adapted kinetic model and a first time implementation of the three-phasic separation of microemulsion systems. From the latter, a model-based soft-sensor for surfactant concentrations is developed, which is based on optical observation of the phase evolution of the microemulsion. The realization of dynamic online optimization then contains a framework for multi-rate moving horizon state estimation. This is used to obtain consistent initial values for optimization from given mini-plant measurements, available on largely varying timescales. This way, the calculation of feasible mini-plant control trajectories via dynamic optimization is possible aiming for product maximization and phase separation stabilization.

Implemented methods and frameworks are tested in mini-plant runs. Here, the kinetic model is successfully validated and a successful transfer of the hydroformylation reaction from the lab into the mini-plant is achieved. The functionality of the phase separation soft-sensor is shown for various operation conditions, gaining vital concentration information from the system. Additionally, a 70 h optimal mini-plant start-up trajectory is successfully generated to assist mini-plant operation during critical transient states. The developed dynamic online optimization framework is then tested using case studies on artificial and plant measurement data. For both data sources, generally feasible trajectories are gained and promising results on convergence behavior and computational time furthermore indicate online applicability.

Finally, these results are combined to obtain the proof of concept for the hydroformylation of 1-dodecene in microemulsions from a long-term continuous mini-plant campaign of 180 h. Control of the critical phase separation step was tested for different operation modes and overall good oil phase purities of up to 99.5 % (amount of oily components in the separated oil phase) were obtained. The reaction performance gained a steady-state product yield of up to 38 % with a chemo selectivity of 92 %, which is in perfect agreement with reference lab-scale investigations.

Keywords: *microemulsions; hydroformylation; mini-plant operation; multi-rate moving horizon state estimation; dynamic real-time optimization*

Deutsche Zusammenfassung

Im Zuge des steigenden gesellschaftlichen Bewusstseins für Nachhaltigkeit sind innerhalb von Industrie und Wissenschaft verstärkte Bestrebungen hin zu nachhaltigen und grünen chemischen Prozessen und Produkten sichtbar. Hierbei zielt die Prozessentwicklung verstärkt auf die Realisierung neuer Synthesewege für die Nutzung von biobasierten Rohstoffen sowie stofflicher Effizienz und Abfallvermeidung ab. Die industrielle Umsetzung solcher neuartigen Prozesskonzepte wird jedoch oftmals durch deren Neuheitsgrad sowie unbekannte Stoff- und Systemeigenschaften erschwert. Um diese Hindernisse zu überwinden und dennoch frühzeitig die Nutzbarkeit neuer innovativer Prozesskonzepte zu realisieren, wird innerhalb der vorliegenden Arbeit ein systematisches Vorgehen entwickelt. Es besteht zum einen aus einer rigorosen Analyse und Identifikation von systemeigenen Herausforderungen im Prozessbetrieb und zum anderen aus der maßgeschneiderten Entwicklung von Lösungsstrategien bezüglich verbessertem Prozessdesign sowie modellbasierter optimaler Prozessführungskonzepte.

Als Beispielprozess wird die Hydroformylierung von 1-Dodecen in einem tensidgestützten schaltbaren Mehrphasensystem untersucht. Diese sogenannten Mikroemulsionssysteme ermöglichen atomeffiziente homogen katalysierte Stoffumwandlungspfade sowie die effiziente Produktabscheidung und Katalysatorrezyklierung mittels Phasentrennung. Mit dem Ziel eines erfolgreichen Machbarkeitsnachweises für die Anwendung in einer Miniplant erfolgt die systematische Analyse des Systems zunächst mit Fokus auf die Reaktion. Unter Nutzung einer entwickelten Methode zur Modelladaptierung wird ein vorhandenes mechanistisches mikrokinetisches Modell erfolgreich um relevante Einflüsse der Mikroemulsion erweitert. Im Weiteren erfolgt die systematische Untersuchung des Phasentrennverhaltens der Mikroemulsion, um relevante Einflussgrößen sowie Herausforderungen für den Prozessbetrieb zu identifizieren. Kernelement ist vor allem die Bewertung der Regelbarkeit des Trennzustands bezüglich real verfügbarer Messgrößen. Als Ergebnis werden die fehlende Messbarkeit relevanter Tensidkonzentrationen, sehr kleine Betriebsfenster zur Phasentrennung sowie hohe Sensitivitäten von Reaktion und Phasentrennung bezüglich Konzentrationsänderungen als kritische Herausforderungen für den erfolgreichen Anlagenbetrieb identifiziert.

Basierend hierauf werden zunächst Designverbesserungen an Reaktor, Abscheidergeometrie sowie der Prozessrezyklierungen entwickelt. Weiterhin wird die Betriebsführung durch die Entwicklung optimaler Betriebstrajektorien unterstützt. Als wichtiges Fundament wird hierzu ein vollständiges dynamisches Miniplant-Modell entwickelt. Kernelemente darin sind das entwickelte adaptierte Kinetikmodell sowie die erstmalige Implementierung einer dreiphasigen Entmischung von Mikroemulsionssystemen. Bezüglich letzterem erfolgt die Entwicklung eines

modellbasierten Soft-Sensors für Tensidkonzentrationen unter Nutzung optischer Auswertungen des Phasentrennzustandes. Die Umsetzung einer dynamischen Echtzeitoptimierung umfasst dann zusätzlich ein Framework zur Zustandsschätzung auf bewegten Horizonten und stark unterschiedlichen Zeitskalen von Messwerten. Hiermit werden gültige Modellinitialisierungen ausgehend von Miniplant-Messdaten ermöglicht. Somit wird die Optimierung künftiger Trajektorien für Reglersollwerte der Miniplant erreicht, wobei seitens des Optimierungsproblems auf Produktmaximierung und Stabilisierung der Phasentrennung abgezielt wird.

Implementierte Methoden und Frameworks werden dann in Versuchen in einer Miniplant getestet. Hier kann eine erfolgreiche Validierung der Reaktionskinetik sowie der erfolgreiche Transfer der Hydroformylierungsreaktion aus dem Labor in die Miniplant aufgezeigt werden. Die Funktionalität des Soft-Sensors zur Phasentrennung wird für diverse Trennzustände in der Anlage bestätigt, wobei sinnvolle Konzentrationsprädiktionen erhalten werden. Zusätzlich erfolgt die Berechnung einer 70 h Anfahrtrajektorie, um den Prozessbetrieb in kritischen transienten Zuständen zu unterstützen. Die dynamische Optimierung wird dann in Fallstudien mittels künstlicher sowie realer Miniplant-Daten getestet. Vielversprechende Ergebnisse bezüglich des Konvergenzverhaltens und Rechenzeit bestätigen dabei eine mögliche Echtzeitanwendung, wobei generell sinnvolle und umsetzbare Trajektorien erhalten werden.

Schlussendlich wurden die entwickelten Strategien im Rahmen eines 180 h Langzeitbetriebes der Miniplant genutzt. Hier konnte sehr erfolgreich die Machbarkeit der Hydroformylierung von 1-Dodecen in Mikroemulsionen bestätigt werden. Das Aufrechterhalten der kritischen Phasentrennung war über den gesamten Zeitraum und diverse Betriebszustände möglich, wobei sehr gute Ölphasenreinheiten von bis zu 99.5 % (Anteil Ölkomponenten in Ölphase) erreicht wurden. Die Reaktion konnte mit einer hohen stationären Produktausbeute von 38 % sowie Produktselektivität von 92 % umgesetzt werden und zeigt zudem eine sehr gute Übereinstimmung mit Labor-Referenzwerten.

Schlüsselwörter: *Mikroemulsionen; Hydroformyleriung; Multiraten-Zustandsschätzung auf bewegten Horizonten; dyn. Echtzeitoptimierung*

Publications

This thesis is partially based on already published contributions. In the following, these are divided into Journal articles, papers within conference proceedings, oral presentations or posters with only abstract, and a list of all supervised theses.

Journal Articles

- D. Müller, E. Esche, T. Pogrzeba, M. Illner, F. Leube, R. Schomäcker, G. Wozny (2015). Systematic Phase Separation Analysis of Surfactant-Containing Systems for Multiphase Settler Design. *Industrial & Engineering Chemistry Research* 54.12, 3205–3217. DOI: 10.1021/ie5049059
- T. Pogrzeba, D. Müller, M. Illner, M. Schmidt, Y. Kasaka, A. Weber, G. Wozny, R. Schomäcker, M. Schwarze (2016a). Superior catalyst recycling in surfactant based multiphase systems – Quo vadis catalyst complex?. *Chemical Engineering and Processing: Process Intensification* 99, 155–166. DOI: 10.1016/j.cep.2015.09.003
- M. Illner, D. Müller, E. Esche, T. Pogrzeba, M. Schmidt, R. Schomäcker, G. Wozny, J.-U. Repke (2016c). Hydroformylation in Microemulsions: Proof of Concept in a Miniplant. *Industrial & Engineering Chemistry Research* 55.31, 8616–8626. DOI: 10.1021/acs.iecr.6b00547
- D. Müller, M. Illner, E. Esche, T. Pogrzeba, M. Schmidt, R. Schomäcker, L. T. Biegler, G. Wozny, J.-U. Repke (2017). Dynamic real-time optimization under uncertainty of a hydroformylation mini-plant. *Computers & Chemical Engineering* 106, 836–848. DOI: 10.1016/j.compchemeng.2017.01.041
- A. Paul, K. Meyer, J.-P. Ruiken, M. Illner, D.-N. Müller, E. Esche, G. Wozny, F. Westad, M. Maiwald (2017). Process spectroscopy in microemulsions—Raman spectroscopy for online monitoring of a homogeneous hydroformylation process. *Measurement Science and Technology* 28.3, 035502. DOI: 10.1088/1361-6501/aa54f0
- K. Meyer, J.-P. Ruiken, M. Illner, A. Paul, D. Müller, E. Esche, G. Wozny, M. Maiwald (2017a). Process spectroscopy in microemulsions—setup and multi-spectral approach for

reaction monitoring of a homogeneous hydroformylation process. *Measurement Science and Technology* 28.3, 035501. DOI: 10.1088/1361-6501/aa54f3

- T. Pogrzeba, M. Schmidt, N. Milojevic, C. Urban, M. Illner, J.-U. Repke, R. Schomäcker (2017b). Understanding the Role of Nonionic Surfactants during Catalysis in Microemulsion Systems on the Example of Rhodium-Catalyzed Hydroformylation. *Industrial & Engineering Chemistry Research* 56.36, 9934–9941. DOI: 10.1021/acs.iecr.7b02242
- E. Esche, C. Hoffmann, M. Illner, D. Müller, S. Fillinger, G. Tolksdorf, H. Bonart, G. Wozny, J.-U. Repke (2017). MOSAIC - Enabling Large-Scale Equation-Based Flow Sheet Optimization. *Chemie Ingenieur Technik* 89.5, 620–635. DOI: 10.1002/cite.201600114
- T. Pogrzeba, M. Illner, M. Schmidt, J.-U. Repke, R. Schomäcker (2017a). Microemulsion Systems as Switchable Reaction Media for the Catalytic Upgrading of Long-Chain Alkenes. *Chemie Ingenieur Technik* 89.4, 459–463. DOI: 10.1002/cite.201600140
- A. Misra, L. de Souza, M. Illner, L. Hohl, M. Kraume, J.-U. Repke, D. Thévenin (2017). Simulating separation of a multiphase liquid-liquid system in a horizontal settler by CFD. *Chemical Engineering Science* 167, 242–250. DOI: 10.1016/j.ces.2017.03.062
- M. Illner, M. Schmidt, T. Pogrzeba, C. Urban, E. Esche, R. Schomäcker, J.-U. Repke (2018c). Palladium-Catalyzed Methoxycarbonylation of 1-Dodecene in a Two-Phase System: The Path toward a Continuous Process. *Industrial & Engineering Chemistry Research* 57.27, 8884–8894. DOI: 10.1021/acs.iecr.8b01537
- T. Pogrzeba, M. Illner, M. Schmidt, N. Milojevic, E. Esche, J.-U. Repke, R. Schomäcker (2019). Kinetics of hydroformylation of 1-dodecene in microemulsion systems using a rhodium sulfoxantphos catalyst. *Industrial & Engineering Chemistry Research*. DOI: 10.1021/acs.iecr.8b06157

Conference Papers

- D. Müller, M. Illner, A. Fleck, E. Esche, T. Barz, R. Schomäcker, G. Wozny (2014). Enabling Online-Optimization for a Multiphase System in a Hydroformylation Mini-Plant. In: *Conference Proceedings of the 20th International Conference of Process Engineering and Chemical Plant Design 2014*. Ed. by M. Kraume, G. D. Wehinger. Copy Print Berlin. ISBN: 978-3-00-047364-7
- M. Illner, T. Pogrzeba, M. Schmidt, D. Müller, E. Esche, R. Schomäcker, J.-U. Repke, Schomäcker, G. Wozny (2016b). Hydroformylation of 1-dodecene in Microemulsions: Operation and Validation of Lab Results in a Miniplant. In: *Technical Transactions - Mechanics Issue 1-M (1) 2016*, 107–120. DOI: 10.4467/2353737XCT.16.011.4975

- D. Müller, E. Esche, M. Illner, T. Pogrzeba, M. Schmidt, R. Schomäcker, L. T. Biegler, G. Wozny (2016). Dynamic Real-time Optimization Under Uncertainty of a Hydroformylation Mini-plant. In: *Computer Aided Chemical Engineering - Proceedings of the 26th European Symposium on Computer Aided Process Engineering*. Vol. 38, 2337–2342
- C. Hoffmann, M. Illner, D. Müller, E. Esche, G. Wozny, L. T. Biegler, J.-U. Repke (2016). Moving-horizon State Estimation with Gross Error Detection for a Hydroformylation Mini-plant. In: *Computer Aided Chemical Engineering - Proceedings of the 26th European Symposium on Computer Aided Process Engineering*. Vol. 38. Elsevier, 1485–1490. DOI: 10.1016/B978-0-444-63428-3.50252-6
- M. Illner, E. Esche, J.-U. Repke (2018a). Optimal Control of Surfactant containing Multiphase Systems - Challenges and Solution Strategies for a stable Mini-Plant Operation. In: *13th International Symposium on Process Systems Engineering (PSE 2018)*. Ed. by M. R. Eden, M. G. Ierapetritou, G. P. Towler. Vol. 44. Computer Aided Chemical Engineering 13. Elsevier, 739–744. DOI: 10.1016/B978-0-444-64241-7.50118-X
- A. Misra, C. Bonamy, L. M. de Souza, L. Hohl, M. Illner, M. Kraume, J.-U. Repke, D. Thévenin (2018). A multi-fluid approach to simulate separation of liquid-liquid systems in a gravity settler. In: *Computer Aided Chemical Engineering - Proceedings of the 28th European Symposium on Computer Aided Process Engineering*. Elsevier, 31–36. DOI: 10.1016/B978-0-444-64235-6.50008-5
- J. Weigert, M. Illner, E. Esche, J.-U. Repke (2018). Development of a State Estimation Environment for the Optimal Control of a Mini-plant for the Hydroformylation in Microemulsions. In: *Chemical Engineering Transactions*. Vol. 70, 973–978

Oral Presentations and Posters with only Abstract

- M. Illner, D. Müller, E. Esche, R. Schomäcker, G. Wozny (2015). Hydroformylation in Microemulsions on a Mini-plant Scale: Operation Challenges and Solution Approaches. In: *ACHEMA 2015, Frankfurt, Germany*
- A. Paul, J.-P. Ruiken, K. Meyer, F. Westad, M. Illner, D. Müller, E. Esche, M. Maiwald (2015). Online Spectroscopy in Microemulsions – A Process Analytical Approach for a Hydroformylation Miniplant II - Calibration and Prediction by Raman Spectra. In: *11. Kolloquium Arbeitskreis Prozessanalytik 2015, Wien, Austria*
- M. Illner, jan-Paul Ruiken, K. Meyer, D. Müller, E. Esche, A. Paul, J.-U. Repke, M. Maiwald (2016f). Systematic Approach for Online Spectroscopy in Technical Systems - Experimental Design for Raman Spectroscopy in Micro Emulsions. In: *Analytica Conference and Fair, Munich, Germany*

- M. Illner, D. Müller, E. Esche, J.-U. Repke (2016d). Hydroformylierung in Mikroemulsionen – Anforderungen und Lösungsansätze im Miniplant-Betrieb. In: *ProcessNet-Jahrestagung und 33. DECHEMA-Jahrestagung der Biotechnologen 2016, Aachen, Germany*
- M. Illner, T. Pogrzeba, M. Schmidt, R. Schomäcker, J.-U. Repke (2016e). Hydroformylation of 1-Dodecene in Microemulsions: Proof of Concept and Long-term Operability on a Mini-Plant Scale. In: *AIChE Annual Meeting, San Francisco, USA*
- T. Pogrzeba, M. Schmidt, M. Illner, R. Schomäcker (2016b). Microemulsion systems as smart solvent systems for homogeneous catalysis: Rhodium-catalyzed hydroformylation of long-chain alkenes in aqueous media. In: *AIChE Annual Meeting, San Francisco, USA*
- M. Illner, D. Müller, E. Esche, R. Schomäcker, J.-U. Repke (2016a). Hydroformylierung in Mikroemulsionen - Anforderungen und Lösungsansätze im Miniplant-Betrieb. In: *Chemie Ingenieur Technik - Special Issue: ProcessNet-Jahrestagung und 32. DECHEMA-Jahrestagung der Biotechnologen 2016, Aachen, Germany*. Vol. 88. 9. Wiley, 1334–1334. DOI: 10.1002/cite.201650346
- M. Illner, K. Meyer, A. Paul, E. Esche, M. Maiwald, J.-U. Repke (2017b). Operation and Optimal Control of Multiphase Systems – Hydroformylation in Microemulsions on the Mini-plant Scale. In: *EUROPACT 2017 - 4th European Conference on Process Analytics and Control Technology, Potsdam, Germany*
- K. Meyer, A. Paul, J.-P. Ruiken, F. Westad, M. Illner, D. Müller, E. Esche, J.-U. Repke, M. Maiwald (2017b). Online Spectroscopy in Microemulsions – A Process Analytical Approach for a Hydroformylation Mini-plant. In: *EUROPACT 2017 - 4th European Conference on Process Analytics and Control Technology, Potsdam, Germany*
- M. Illner, E. Esche, J.-U. Repke (2017a). Miniplant-Betrieb und stabile Prozessführung für Mehrphasenreaktionssysteme – Hydroformylierung langkettiger Alkene in Mikroemulsionen. In: *Jahrestreffen der ProcessNet-Fachgemeinschaft "Prozess-, Apparate- und Anlagentechnik" (PAAT), Würzburg, Germany*
- D. Zedel, M. Illner, M. Kraume, A. Drews (2017). Modelling and prediction of surfactants removal from organic solvents by organic solvent nanofiltration. In: *1th International Congress on Membranes and Membrane Processes (ICOM 2017), San Francisco, USA*
- M. Illner, E. Esche, J.-U. Repke (2018b). Prozessführungskonzepte zur Realisierung neuartiger Prozesse – Hydroformylierung langkettiger Alkene in Mikroemulsionen. In: *Jahrestreffen der ProcessNet-Fachgemeinschaft "Prozess-, Apparate- und Anlagentechnik" (PAAT), Cologne, Germany*
- V. Kozachynskyi, S. Bublitz, M. Illner, J. Weigert, C. Hoffmann, E. Esche, J.-U. Repke (2018). Conceptual data model based on an OPC UA architecture, its benefits and imple-

mentation. In: *Jahrestreffen der ProcessNet-Fachgemeinschaft "Prozess-, Apparate- und Anlagentechnik" (PAAT), Cologne, Germany*

- E. Esche, M. Illner, R. Wilhelm, J.-U. Repke (2018). Auswahl und Implementierung von optimierenden Prozessführungskonzepten. In: *ProcessNet-Jahrestagung und 33. DECHEMA-Jahrestagung der Biotechnologen 2018, Aachen, Germany*. Vol. 90. Chemie Ingenieur Technik 9. Wiley, 1234–1234. DOI: 10.1002/cite.201855226
- A. T. Penteado, T. Karsten, M. Illner, J.-U. Repke (2019). Systematic Approaches for Plant Design and Operation to enable novel Sustainable Processes. In: *5th International Conference on Sustainable Chemical Product and Process Engineering, Tianjin, China*
- M. Illner, V. Kozachynskyi, E. Esche, J.-U. Repke (2019). Systematic System Identification and Analysis of Operability for Surfactant Containing Multiphase Reaction Media. In: *12th European Congress of Chemical Engineering & 5th European Congress of applied Biotechnology, Florence, Italy*. Vol. 01. AIDIC: Italian Association of Chemical Engineering. DOI: 10.3303/BOA1901
- V. Kozachynskyi, S. Bublitz, M. Illner, J. Weigert, C. Hoffmann, E. Esche, J.-U. Repke (2019). OPC UA-based Concept for Online Implementation of Model-based Advanced Process Control Tools. In: *12th European Congress of Chemical Engineering & 5th European Congress of applied Biotechnology, Florence, Italy*. Vol. 01. AIDIC: Italian Association of Chemical Engineering. DOI: 10.3303/BOA1901

Supervised Theses

- J.-P. Ruiken (2015). Entwicklung der Prozessanalytik fur eine Hydroformylierungsanlage: Ramanspektroskopie von mehrphasigen Gemischen. *Master's Thesis*. Technische Universität Berlin
- J. Weigert (2017). Entwicklung einer modellgestützten Plattform zur integrierten Messdatenvalidierung und Zustandsschätzung für eine Anlage zur Hydroformylierung in Mikroemulsionen. *Master's Thesis*. Technische Universität Berlin
- F. Herrmann (2017). Entwicklung eines Extraktionsprozesses zur Gewinnung von Capron- und Caprylsäure aus einer Fermentationsbrühe. *Master's Thesis*. Technische Universität Berlin
- A. Alzate (2018). Design of an Automatic Method for the Soft-sensing of the Surfactant Concentration in a Mini-plant of Hydroformylation of Long-chain Alkenes in Microemulsions. *Master's Thesis*. Politecnico Di Milano

- M. Stockmann (2019). Systematische Entwicklung eines tensidgestützten mehrphasigen Lösemittelsystems für die reduktive Aminierung und Hydroaminomethylierung. *Bachelors Thesis*. Technische Universität Berlin

Contents

List of Figures

List of Tables

List of Symbols

Greek Symbols

Symbol	Description	Unit
α	Oil to water ratio	wt.-%
Δ	Difference	various
ε	Small positive scalar value	–
Γ	Surface excess concentration	$\mathrm{mol\,m^{-2}}$
γ	Activity coefficient	–
γ	Surfactant mass fraction	wt.-%
μ	Chemical potential	$\mathrm{J\,mol^{-1}}$
Φ	Objective function	varable
Φ	Volume fraction	%
ψ	Catalyst pre-equilibia rate constant	$\mathrm{g\,L^{-1}}$
ρ	Density	$\mathrm{g\,L^{-1}}$
σ	Interfacial tension	$\mathrm{N\,m^{-1}}$
σ	Standard deviation	–
σ^2	Parameter or measurement variance	–
τ	Residence time	h
θ	Parameter vector	–

Indices

Symbol	Description
cp	Index collocation points
fe	Index finite elements
i	Index for components
k	Time step index
m	Number of states
n	Parameter index
r	Index of reaction
s	Index for streams
u	Index for units

u	Index iteration steps

Constants

Symbol	Description	Unit
R	Universal gas constant = 8.31446	$\mathrm{J\,mol^{-1}\,K^{-1}}$

Latin Symbols

Symbol	Description	Unit
Λ	Scaling parameter	–
τ	Collocation polynom root	–
Θ	Measurement sensitivity matrix	–
A	Area	$\mathrm{m^2}$
a	Activity	–
c	Concentration	$\mathrm{mol\,L^{-1}}$
E	Activiation energy	$\mathrm{J\,mol^{-1}}$
E	Manipulable variable set	–
F	Stream	$\mathrm{g\,L^{-1}}$
f	Arbitrary function value	–
G	Free enthalpy	J
g	Arbitrary equality constraint	–
g	Molar Gibbs enthalpy	$\mathrm{J\,mol^{-1}}$
h	Arbitrary inequality constraint	–
HU	Hold-up	g
I	Integrator control deviation	–
K	Inhibition coefficient	–
k^{ref}	Enhancement factor	–
KI	Controller parameter	–
KP	Controller gain	–
L	Level	m
l	Collocation polynom	–
M	Molar mass	$\mathrm{g\,mol^{-1}}$
m	Mass	g
n	Amount of substance	mol
P	Parameter	–
P	Probability	–
p	Pressure	bar
Q	Process noise covariance matrix	–
R	Measurement noise covariance matrix	–

r	Reaction rate	$\mathrm{mol\,L^{-1}\,min}$
R^2	Coefficient of determination	–
S	Selectivity	– or %
S	Sensitivity matrix	–
$Slack$	Small scalar value	–
T	Temperature	K
$TRIG$	Sigmoidal function	–
u	Control varaible	–
V	Volume	$\mathrm{m^3}$
v	Measurement noise	–
v	Velocity	$\mathrm{m\,s^{-1}}$
w	Mass fraction	– or wt.-%
w	Process noise	–
X	Conversion	– or %
X	State vector	–
x	Arbitrary variable	–
x	Mole fraction	– or mol.-%
Y	Measurements vector	–
Y	Yield	– or %
y	State variable	–

Dimensionless Numbers

Symbol	Description	Definition
Re	Reynoldszahl	$\frac{wd\rho}{\eta}$

Superscripts

Symbol	Description
cmc	Critical micelle concentration
$Conti$	Continuous operation
em	Emulsion phase
eq	equilibrium
ex	Excess phase
E	Start point or initial
Gas	Gas feed section
II	Phase/State 2
I	Phase/State 1
Lig	Ligand

LM	Ligand to metal ratio
Lvl	Level
L	Liquid
Mix	Emulsion phase
mol	Molar value
Oil	Oil phase
PhS	Phase separation
Reactor	Reactor section
Rh	Rhodium catalyst
SP	Setpoint
Surfactant	Surfactant
tot	Total
V	Vapor
Water	Water phase

Subscripts

Symbol	Description
cat	Catalyst
Feed	Feed section
Hyfo	Hydroformylation
LB	Lower bound
l	Lower limit
Out	Outlet
Rec	Recycle
R	Reaction, Reactor
Settler	Settler section
Sol	Solubility
UB	Upper bound
u	Upper limit

List of Abbreviations

AE	**A**lgebraic **E**quation system
APC	**A**dvanced **P**rocess **C**ontrol
AS	**A**utomation **S**ystem
cmc	**c**ritical **m**icelle **c**oncentration
cp	**c**ritical **p**oint
cst	**c**ritical **s**olution **t**emperature
DAE	**D**ifferential-**A**lgebraic **E**quation (system)
DCS	**D**istributed **C**ontrol **S**ystem
D-RTO	**Dynamic R**eal-**T**ime **O**ptimization
FFKM	Perfluoroelastomer
FKM	Fluoroelastomer
FTIR	**F**ourier-**T**ransform **I**nfra- **R**ed
GC	**G**as **C**hromatography
HSV	**H**ue **S**aturation **V**alue
ICP	**I**nductively **C**oupled **P**lasma
KPI	**K**ey **P**erformance **I**ndicator
LB	**L**ower **B**ound
LLE	**L**iquid-**L**iquid-**E**quilibrium
MB	**M**ass **B**alance
MFC	**M**ass **F**low **C**ontroller
ME	**M**icro**e**mulsion
MES	**M**icro**e**mulsion **S**ystem

MHE	**M**oving **H**orizon **E**stimator
MILP	**M**ixed **I**nteger **L**inear **P**rogramming
MINLP	**M**ixed **I**nteger **N**on**L**inear **P**rogramming
MPC	**M**odel **P**redictive **C**ontrol
NLP	**N**on**L**inear **P**rogramming
NMR	**N**uclear **M**agnetic **R**esonance
ODE	**O**rdinary **D**ifferential **E**quation (system)
OPC	**O**pen **P**latform **C**ommunication
OPC DA	**O**pen **P**latform **C**ommunication **D**irect **A**ccess
PE	**P**arameter **E**stimation
PIT	**P**hase **I**nversion **T**emperature
PLS	**P**artial **L**east **S**quares
PTFE	**P**oly**T**etra**F**luoro**E**thylene
ROI	**R**egion **O**f **I**nterest
RSME	**R**oot **M**ean **S**quared **E**rror
RTO	**R**eal-**T**ime **O**ptimization
STD	**ST**andard **D**eviation
SX	**S**ulfo**X**ant**P**hos
TDC	**T**ri**dec**anal
UB	**U**pper **B**ound
UNIFAC	**UNI**versal **F**unctional Group **A**ctivity **C**oefficients

1 Introduction and Motivation

Since the introduction of the twelve principles of green chemistry by Anastas et al. (2000) in the early 1990s, continuously increasing efforts towards more sustainable chemical processes and products are perceptible in both academia and industry. Following these guidelines, the implementation of new synthesis paths for renewable feedstocks and waste prevention are strived for. Moreover, the environmental impact of applied reactants, solvents, or additives is required to be as low as possible. From a process development perspective, homogeneous catalysis is an exceptionally important basis for sustainable processes, since new synthesis routes utilizing renewable feedstocks can be unlocked. Additionally, desirable system features such as high atom efficiency and target product selectivity, as well as milder reaction conditions are attainable. However, deploying such systems for large-scale industrial applications can be delayed or even widely inhibited due to their complexity and unknown system phenomena or interactions (Ivanković, 2017). Hence, it is necessary to address these challenges in a holistic approach comprising process design and suitable process operation strategies. For this, a systematic system analysis, as well as integrated lab-scale and mini-plant scale investigations are crucial.

1.1 Hydroformylation in Liquid Multiphase Systems

Within the chemical industry, the hydroformylation is one of the most important applications of homogeneous catalysis with large-scale production capacities exceeding 12 million metric tons per year worldwide (2009) (Bahrmann et al., 2013). Predominantly, short-chained alkenes (propene, butene) are converted, yielding essential intermediates. From these, a wide range of higher value products, such as plastifiers, detergents, surfactant alcohols, and flavorings are produced (Cornils et al., 1994; W. A. Herrmann, 2002). The reaction itself was discovered in 1937 by Otto Roelen while studying the Fischer-Tropsch-Synthesis. It constitutes the reaction of olefins with carbon monoxide and hydrogen towards aldehydes in the presence of transition metal catalysts (Roelen, 1938; Gesellschaft Deutscher Chemiker, 2013). Following the general reaction scheme in Fig. 1.1, the hydroformylation of terminal olefins leads to a functionalization by the introduction of a formyl group. A product mixture of linear and branched aldehydes is

obtained of which the terminal products are usually favored. According to Franke et al. (2012), relevant catalysts for industrial applications are based on rhodium or cobalt, considering the former as superior due to higher activity. By applying tailored ligands the reaction performance is then driven towards economically favorable high chemo- and regioselectivities.

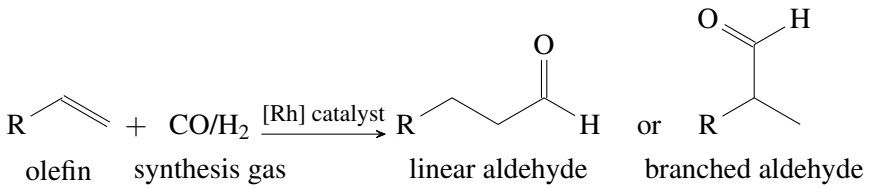

Fig. 1.1: General hydroformylation reaction scheme. R denotes an alkyl group.

Alongside superior reaction performance features homogeneous catalysis however also holds a major drawback: the necessity of efficient catalyst recovery from product streams. Considering the high catalyst costs of 7858 \$/Oz.[1] already catalyst leaching in the order of parts per million causes annual financial loss of several million euros for a 400 kt plant application (Wiese et al., 2006). Significant efforts regarding equipment and energy demand are thus required to avoid catalyst leaching. This led to the development of current state of the art industrial processes, such as the Ruhrchemie / Rhône-Poulenc process (Cornils et al., 1982; Cornils et al., 1995; Auch-Schwelk et al., 2001). Here, two-phase reaction media are applied in which valuable rhodium catalysts are immobilized in an aqueous phase through ligand modification. Hence, efficient catalyst recycling and mild reaction conditions are enabled. However, such a process is limited to short-chained substrates (C<5). Longer-chained olefins (C>5) are thus still converted using more robust but less active and inselective cobalt catalysts in single phase reactions at severe process conditions (300 bar, 200 °C) (Börner et al., 2016).

To overcome this drawback and enable the efficient conversion of also long-chained substrates from renewable feedstocks, new process concepts for homogeneous catalysis in liquid multi-phase systems are strived for. Hereof, the question arises how to merge two contradictory design features of a reaction mixture: perfect miscibility for reaction and perfect separability for separation. Major advancements in this direction stem from academic research and aim for the application of thermomorphic solvent systems (Behr et al., 2005; Zagajewski et al., 2014), ionic liquids (Haumann et al., 2008) and its combination with super critical CO_2 (Webb et al., 2003), or new reactor concepts (Warmeling et al., 2017).

Another very promising approach involves the application of surfactant-based tunable solvent systems and will be investigated within this thesis – hydroformylation in microemulsions. The main idea here is to immobilize the rhodium catalyst in an aqueous phase via ligand modification. Surfactant are then applied to enable necessary large interfacial areas between the long-chained

[1] rhodium price 25th March 2019, source: https://tradingeconomics.com/commodity/rhodium, accessed 2020-01-09

oily substrates and the catalyst solution (Tinucci et al., 1990). Besides promising lab-scale investigations (Vyve et al., 1999; Haumann et al., 2002; Miyagawa et al., 2005), extensive efforts towards a holistic process development have been made within the *Collaborative Research Center TR63 InPROMPT*[2]. Figure 1.2 visualizes the developed general process concept for the production of long-chained aldehydes. Initially, the substrate and aqueous catalyst solution are emulsified in the reactor through application of a surfactant – a macroscopically homogeneous microemulsion system is formed. The hydroformylation reaction is then enabled through the insertion of synthesis gas and carried out at overall mild process conditions. Following the reactor, a separation unit is applied to exploit the thermomorphic separation behavior of microemulsions (M. Müller et al., 2013). Through temperature adjustment, a multiphasic separation in a gravity settler is achieved, which ideally allows for the separation of a highly pure oily phase, as well as the efficient recycling of the valuable rhodium catalyst and surfactants.

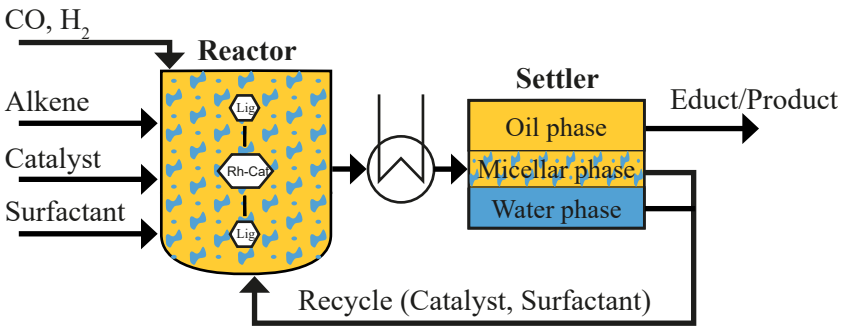

Fig. 1.2: Process Concept for the hydroformylation in microemulsions (Illner et al., 2018a).

Looking at the twelve principles for green chemistry, this process concept offers great potential, since it enables the energy efficient conversion of long-chained renewable substrates via catalysis. Moreover waste prevention and utilization of safe solvents (water) is ensured. However, its viability regarding reaction performance, product separation, and catalyst recycling has yet to be analyzed in detail. Hence, as part of this thesis the operability of such a system is investigated for a technical mini-plant system (Illner et al., 2016c).

1.2 Liquid Multiphase Reaction Media - Challenges for Process Design and Operation

As stated by Illner et al. (2018c) commercial applications of liquid multiphase systems for homogeneous catalysis root back to the 1980s. Prominent examples are the already introduced

[2]https://www.inprompt.tu-berlin.de/

Ruhrchemie / Rhône-Poulenc process or the Shell higher olefin process (SHOP) for the production of alpha-olefins via ethene oligomerization using nickel catalyst homogeneously dissolved in polar solvents such as 1,4-butanediol (Lutz, 1986; Keim, 2013). However, applications are limited to two-phase systems. Actual industrial-scale applications of innovative reaction media, such as microemulsions, are scarce. Thus, the question is raised, what hinders the implementation of new process concepts involving liquid multiphase reaction media and how can their readiness for the chemical industry be improved?
Taking a closer look at homogeneous catalysis and the requirements for economically viable processes using such systems, one major aspect becomes apparent: "the major challenge for most multiphase reaction media lies in quantitative recycling and stability of the expensive catalyst (...) within a viable but low environmental impact multiphase system" (Illner et al., 2018c). Regarding this, Rösler et al. (2018) provide an exemplary review of methods for water-based liquid multiphase systems for homogeneous catalysis and their development towards continuous catalyst recycling. From this, several general challenges arise:

- Homogeneous catalysis is characterized by a high level of complexity with underlying catalytic cycles, as well as several possible catalyst decomposition routes (Leeuwen et al., 2011, p. 1 ff.). Applied to novel multiphase reaction media complexity increases even more, since the chemical matrix of the actual *catalyst solvent* changes dynamically and influences of substances appear (Brunsch et al., 2012; Hamerla et al., 2013b).
- Fluid properties for systems, like microemulsions, as well as substrates from new sustainable feedstocks are often widely unknown and only accessible by extensive studies (Kahlweit et al., 1987).
- The measurability of all necessary process variables for process application might not be given or is only available through the application of advanced process analytical tools, such as spectroscopy.
- Early stage applications of optimizations methods for process design or operability analysis might be difficult, since reliable and predictive models are not available (Mitsos et al., 2018). This is for example true for the desired application of microemulsion systems, for which at the moment no predictive models for multiphasic separation behavior exist.
- The conceptual design of novel multiphase systems initially relies on well-defined lab-scale investigation and often omits characteristics of dynamic operations or disturbances.
- The integration of reaction and separation using internal recycles is crucial since unknown interaction phenomena might occur, such as accumulation of components and subsequently altered reaction behavior (Illner et al., 2016b).

Thereof, two main conclusions can be drawn: Following standard approaches for conceptual process design, which initially rely on well-defined lab-scale experiments, the general viability of such innovative multiphase reaction media cannot be sufficiently analyzed. The early stage integration of mini-plant experiments is thus crucial. Moreover, the overall feasibility of those techniques is then often only attainable by an integrated deployment of (optimal) process design and process operation methods to meet their complexity and dynamic operation characteristics.

1.3 Research Goals

Referring to the afore mentioned challenges for establishing novel process concepts for liquid multiphase reaction media, the overarching research goal for this thesis is given:

The main purpose is to present a holistic guideline for rigorous system analysis to identify system inherent phenomena and arising challenges regarding the operability of larger scale technical realizations. This way, a tailored and efficient development of solution approaches regarding process design and optimal operation is enabled. Hence, not only a faster realization of process applications of liquid multiphase reaction media is aimed for, but also the required efforts towards their operability can be evaluated at an early stage.
Within this thesis, a first approach to this is realized and applied for the hydroformylation of 1-dodecene in microemulsions. For this purpose, several sub-objectives are derived, which represent major developments to achieve the main research goal:

- an approach for the systematic analysis of the phase separation behavior of microemulsions systems regarding their controllability and suitability for continuous processes
- a thermodynamically founded model for the three-phase separation of microemulsions,
- adequate separation unit design applicable for microemulsion systems,
- the development of a soft-sensor to enable inference of immeasurable concentrations,
- a systematic approach to formulate adapted macrokinetic models,
- and a framework for online state estimation and calculation of optimal trajectories considering measurement data from a mini-plant system available on different time scales.

1.4 Outline of Thesis

To achieve these objectives **Chapter 2** initially provides relevant theoretical fundamentals and background information. Therefore, a brief review of the status quo for process design and operation strategies for surfactant based liquid multiphase systems is provided. Thermodynamic fundamentals and coalescence behavior of microemulsions are mandatory and thus reviewed. Likewise, the kinetics and the catalytic cycle for the hydroformylation reaction are presented. Subsequently, guidelines for the systematic analysis of microemulsion systems are given, including microemulsion separation behavior, as well as a kinetic model adaption methodology. Process model formulation and reformulation strategies for process optimization are outlined. Finally, principles for chemical plant automation and the implementation of dynamic real-time optimization and state estimation are given.
In **Chapter 3** the rigorous system analysis for the hydroformylation of 1-dodecene in microemulsion is carried out, focusing mainly on the hydroformylation reaction and the phase separation characteristics of the microemulsion. Both aspects are analyzed in close regard of the application in a technical mini-plant system and its operability.
Chapter 4 then highlights the development of tailored process design and operation strategies. Firstly, the setup of a mini-plant system and improvements of units are given. In addition, the implementation of process analytics, automation, and communication structures are shown. A dynamic mini-plant model is derived based on first principles and empiric correlations. Therein, a first-time modeling approach for the three-phasic separation of microemulsions including compound distribution is shown. Additionally, an adapted kinetic model for the hydroformylation of 1-dodecene based on a mechanistic model is developed. Finally, methods for optimal process operation are presented: an online soft-sensor implementation for immeasurable concentrations, a moving horizon state-estimator handling multi-rate measurements, and a framework for dynamic real-time optimization for mini-plant trajectory development.
Chapter 5 is then dedicated to a *proof of concept* for the developed unit design improvements and operation strategies. Hence, a series of mini-plant operations is presented with results on the crucial performance criteria: reaction performance, phase separation efficiency and controllability. Hereof, model validity, soft-sensing, as well as state-estimation and developed optimal mini-plant trajectories are tested. This also focuses on the feasibility of controlling the mini-plant system throughout different operation modes. Concluding, a successful realization of a long-term continuous operation of the mini-plant is presented.
Finally, **Chapter 6** concludes with a summary of the relevant aspects and results of this thesis before giving an outlook on future developments and research directions.

2 Theoretical Fundamentals and Background Information

To further organize this thesis in accordance with the stated objectives, Fig. 2.1 provides the structure for a systematic procedure to realize novel and severely challenging process concepts, which is subsequently applied on the system at hand. Based on that, this chapter initially introduces the relevant theoretical background for carrying out the crucial steps therein.

Entering this workflow, a problem formulation and specification of goals is given – the hydroformylation of 1-dodecene in microemulsions applied on a continuous mini-plant system. Thus, a profound understanding of the reaction mechanism and the solvent system is essential. Hence, the physical and thermodynamic properties of **M**icro**e**mulsions (MEs) are presented in Sec. 2.1. In the following, details on the reaction mechanism and kinetics of the rhodium catalyzed hydroformylation are given in Sec. 2.2. These theoretical fundamentals are key to a subsequent systematic analysis of the system outlined in Sec. 2.3. This analysis should explicitly contain the combination of crucial reaction and separation steps to reveal relevant interactions. Moreover, testing in already larger-scale systems, such as a mini-plant is vital to identify operational challenges arising from unavoidable disturbances or impurities.

This way, key operational challenges are systematically identified and subsequently resolved by the development of tailored process design upgrades or advances strategies for process operation. Hence, this chapter provides further theoretical background, starting with a short excerpt on separation unit designs in Sec. 2.3.3. Section 2.4 then addresses strategies for a systematic process model development, model reformulation strategies, and parameter estimation. Concluding, deliberations on the implementation of dynamic real-time optimization, involving state estimation and dynamic optimization are given in Sec. 2.5.

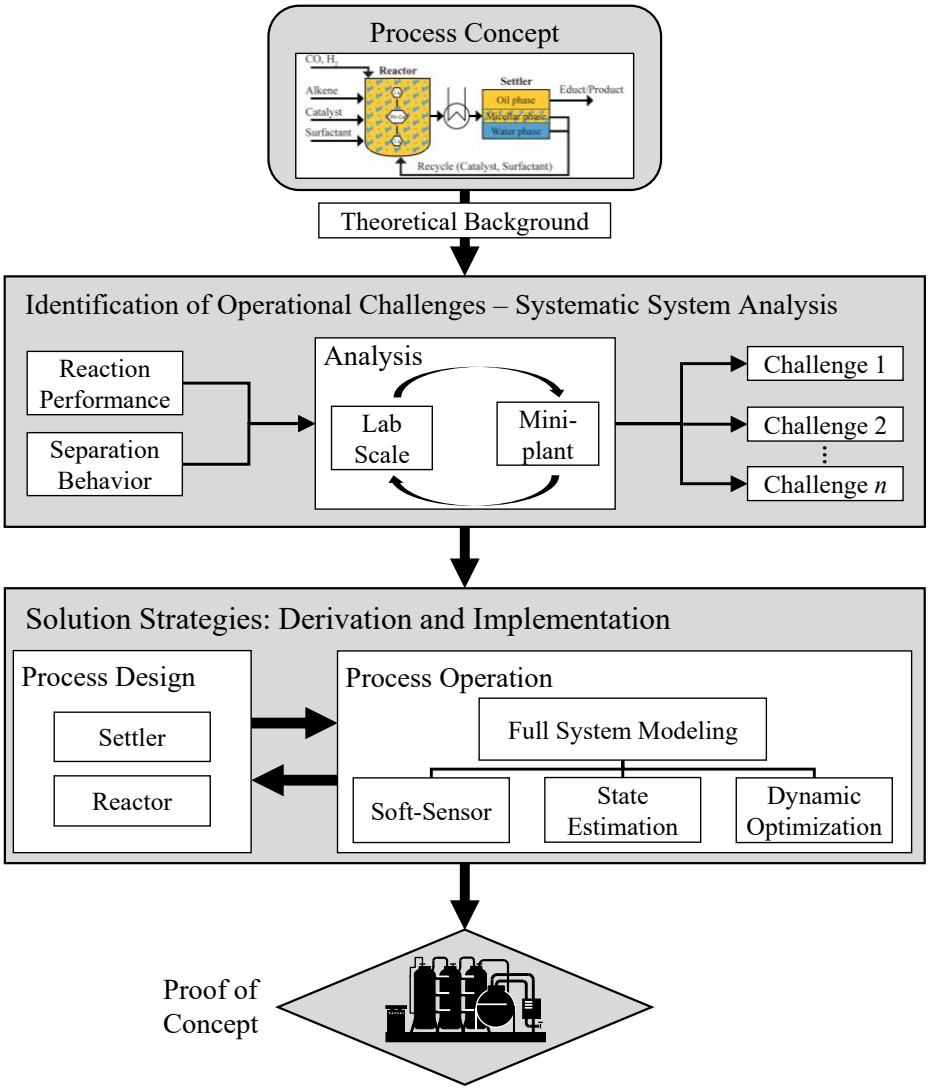

Fig. 2.1: Workflow for the rigorous analysis of surfactant-based multiphase systems and derivation of process design and operation strategies.

2.1 Thermodynamics & Characteristics of Microemulsions

Microemulsion systems form the cornerstone of the process concept regarded in this thesis. Hence, this section provides a detailed description of these system. Of special interest are the key features of providing intensified mixing of oil and water for reactive systems, the specific phase separation behavior as well as relevant influences and control parameters.

In general emulsions can be considered as disperse systems of two immiscible liquids, such as water and nonpolar oily compounds. Formed water in oil (w/o) or oil in water (o/w) emulsions are thermodynamically instable and tend to separate quickly. However, the stability of these emulsions can be increased by applying an amphiphilic compound, which is soluble in oil and water. Given a sufficient amount of amphiphile, its molecules aggregate at the water/oil interface and enable a successive solubilization. Thus, an optically homogeneous and stable emulsion is obtained. First descriptions of such a system were provided by J. H. Schulman et al. (1943) and Winsor (1956), followed by extensive studies in the following years (J. H. Schulman et al., 1946; J. Schulman et al., 1948; J. Schulman et al., 1949; Bowcott et al., 1955). In 1959 J. H. Schulman et al. (1959, p. 1677) characterized these systems as "optically isotropic transparent oil and water dispersions" and derived the name 'micro-emulsion' based on estimated emulsion droplet diameters around 100 to 500 Å. Indeed, microemulsions were later found to be nano-structured with average droplet diameters around 10 to 200 nm (Tadros, 2013).
Following the question of Kahlweit (1988, p. 617) "what are microemulsions good for?", a variety of applications can be found. These range from enhanced oil recovery (see reviews by Abe (1996) and Bera et al. (2014)) over cosmetics and pharmaceutics (Boonme, 2007; Hong et al., 2001; Hloucha et al., 2014) to chemical reaction media (Schwuger et al., 1995; Klier et al., 2000; Schomäcker et al., 2009). All of these applications trace back to the special characteristics of microemulsions to efficiently reduce the interfacial tension between hydrophobic and hydrophilic phases. Thus, MEs allow for efficient emulsification, as well as a specific phase separation behavior. These features are also exploited for the process concept at hand (Fig. 1.2).

Remark: For this thesis, only nonionic surfactants are considered as emulsifiers and the following discussion is confined accordingly.

2.1.1 Surfactant Adsorption on Surfaces and Micelle Formation

In general, surfactants are components, which are active at the interface between e.g. hydrophilic and hydrophobic substances. Several system features, such as interfacial tension, conductivity, and turbidity are thus altered (Myers, 2005a). If for two contacting phases I and II all components in each phase would be uniformly distributed, the total free enthalpy G would be the sum of the free enthalpy of the phases. With surfactant molecules accumulating at the interface this assumption does not hold. This deviation is expressed as Gibbs surface energy $G(\sigma)$ (Eq. (2.1a)), from which the surface excess concentration Γ, denoting the adsorption or desorption of a component i at interface A, can be derived (Atkins et al., 2010):

$$G(\sigma) = G - (G(I) + G(II)) \tag{2.1a}$$

$$\Gamma_i = -\frac{1}{RT} \cdot \frac{\mathrm{d}\sigma}{\mathrm{d}\ln c_i} \tag{2.1b}$$

If now i adsorbs at the interface, Γ is to be positive and thus the change in interfacial tension will be negative. This can also be seen in Fig. 2.2. Note, that in this case Γ is expressed as the ratio of $\Gamma(c_i)$ and the saturation concentration at the interface. Starting at $c_0 = 0\,\mathrm{mol\,L^{-1}}$, the

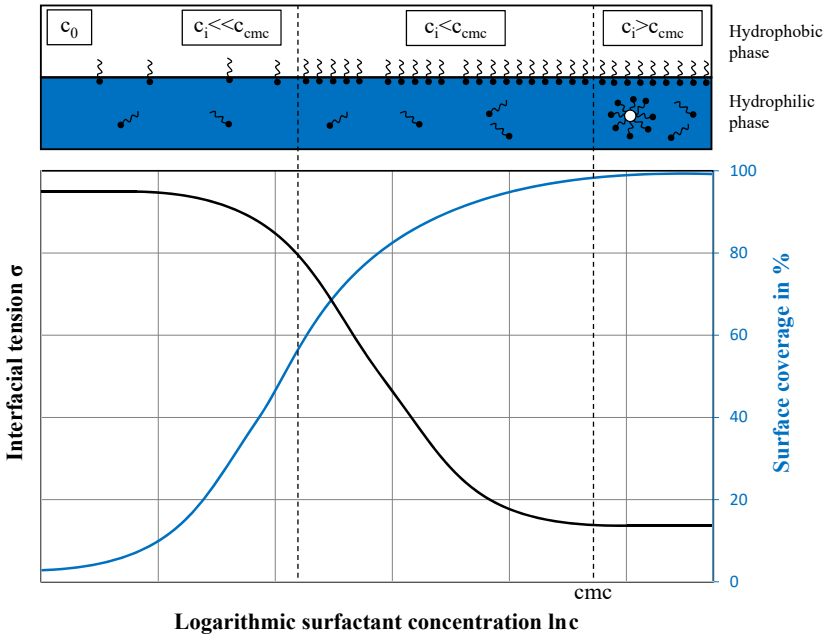

Fig. 2.2: Qualitative representation of the interfacial tension and the surface coverage depending on the logarithmic surfactant concentration. Above the diagram, the coordination of the surfactant molecules at the interface of a two-phase system is schematically shown.

interfacial tension of the two-phase system applies. With increasing surfactant concentration the surface coverage rises accordingly, till at roughly 60 % coverage a significant decrease of the interfacial tension occurs (Menger et al., 2011). Surfactant molecules increasingly aggregate at the interface and start to align their head with the hydrophilic phase. Thus, a new interface is formed, for which the interfacial tension is reduced, due to the higher interactions between e.g. water and the hydrophilic head of surfactant molecules. Once the interface is fully covered with surfactant molecules, the interfacial tension remains constant. The corresponding concentration is introduced as the **c**ritical **mi**celle **c**oncentration (cmc). This phenomenon can also be exploited to easily access the cmc of surfactants in liquid solvents by interfacial tension measurements (Oetter et al., 1988). First predictive thermodynamic models for the cmc based on **UNI**versal **F**unctional Group **A**ctivity **C**oefficients (UNIFAC) have already been shown by Flores et al.

(2001) and Cheng et al. (2002). However, especially for aliphatic ethoxylate style surfactants predictions are rather poor and the introduction of new group contributions and subsequent experimental quantification is still necessary. For water-oil systems the cmc is of great importance, as it marks the beginning phase transfer activity of the surfactant. Above the cmc, surfactant molecules form energetically favorable spherical aggregates in the bulk phase, which are able to e.g. *trap* oil in the water (see Fig. 2.2). The structure of these so called micelles and aggregate numbers are dependent on various influences (Myers, 2005b; Lindman et al., 2018).

2.1.2 Properties and Phase Behavior of Microemulsion Systems

Investigating microemulsions, "the primary aim (...) is to find the conditions under which the surfactant solubilises the maximum amounts of water and oil" (Sottmann et al., 2009, p. 2). This is closely related to the phase separation behavior and finding relevant advantageous characteristics for e.g. mixing and separation unit operations.
Considering a ternary system of water (A), oil (B), and an amphiphile (C), the composition variables are typically chosen as the oil to water ratio α and the amphiphile mass fraction γ:

$$\alpha = \frac{m_B}{m_A + m_B} \tag{2.2}$$

$$\gamma = \frac{m_C}{m_A + m_B + m_C} \tag{2.3}$$

With the influence of temperature T being dominant and weak influence of pressure p on the phase equilibria, the phase behavior of ternary systems can be represented by the Gibb's phase prism in Fig. 2.5 with components A, B, C as base and T as ordinate (Kahlweit et al., 1990).
Since the phase behavior of the ternary system is a direct consequence of the features of the related binary systems, these are firstly analyzed using the unfolded phase prism in Fig. 2.3. It is evident, that for the **A** - **C** system a mutual solubility of water and the nonionic surfactant is given at lower temperatures. At elevated temperatures, an upper miscibility gap with lower **c**ritical **s**olution **t**emperature (cst) is formed (cp_β). The inverted case is present for the **B** - **C** system. Here, a miscibility gap with upper cst is present at low temperatures but the nonionic surfactant gets increasingly soluble in oil with increasing temperature. Additionally, an extended miscibility gap exists for the system water and oil with an upper critical solution temperature well above to boiling point of the mixture. It is obvious, that the position of the critical points in the systems **A** - **C** and **B** - **C** depend on the choice of the surfactant. Discussing the phase behavior of the ternary mixture, it can be anticipated, that it mainly results from the interplay of the binary miscibility gaps and respective critical points cp_{alpha} and cp_{beta}. Thus, Fig. 2.4 outlines Gibbs diagrams at increasing temperatures for the ternary system:

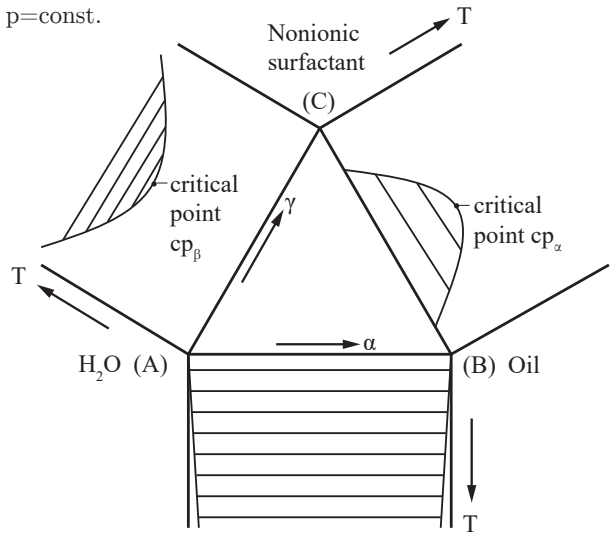

Fig. 2.3: Schematic illustration of unfolded phase prism showing binary phase diagrams for systems of water (A), oil (B), and a nonionic surfactant (C). Figure adapted from (Kahlweit et al., 1985).

- At low temperatures (T_1) the nonionic surfactant **C** is well soluble in water **A**, whereas the miscibility gap between oil and water is still dominant. Thus, a large miscibility gap is formed. Here, "the negative slope of the tie lines indicates that a nonionic surfactant-rich water phase (A^{em}) coexists with an oil-excess phase (B^{ex})" (Sottmann et al., 2009, p. 4). This separation state is denoted as the two lower region 2 following Knickerbocker et al. (1979) or Winsor **I** system (Winsor, 1956).

- With increasing temperature the plait point cp_β of system **A**-**C** is approached and the binary miscibility gap is influencing the central miscibility gap. Thus, a second plait point appears on the water rich side, forming another two-phase region at T_2. For thermodynamic reasons, the water-rich phase (A^{em}) separates into a surfactant rich phase (ME, the actual microemulsion) and an aqueous excess phase (A^{ex}). Therefore, a central three-phase region (**3** or Winsor **III**) is formed, surrounded by three adjacent two-phase regions.

- Further temperature increase raises the mutual solubility of oil and surfactant. Accordingly, phase ME moves along the binodal of the central miscibility gap, closing the three-phase body and finally merges with the oil rich phase (B^{ex}). Thus, another extended miscibility gap exists. The positive slope of the tie lines indicates the formation of a surfactant rich oil phase (B^{em}) and an aqueous excess phase (A^{ex}). This situation is denoted as $\overline{2}$ or Winsor **II** system.

- A homogeneous and stable emulsion phase (**1** or Winsor **IV**) is formed, if the surfactant concentrations exceeding the plait point (see Fig. 2.5).

- At high surfactant concentrations in the Winsor **IV** system, lyotropic mesophases or liquid crystal phases can occur. These are partly of high viscosity, hindering e.g. pumpability of liquids. For additional information see (Langevin, 1986; Kahlweit et al., 1985).

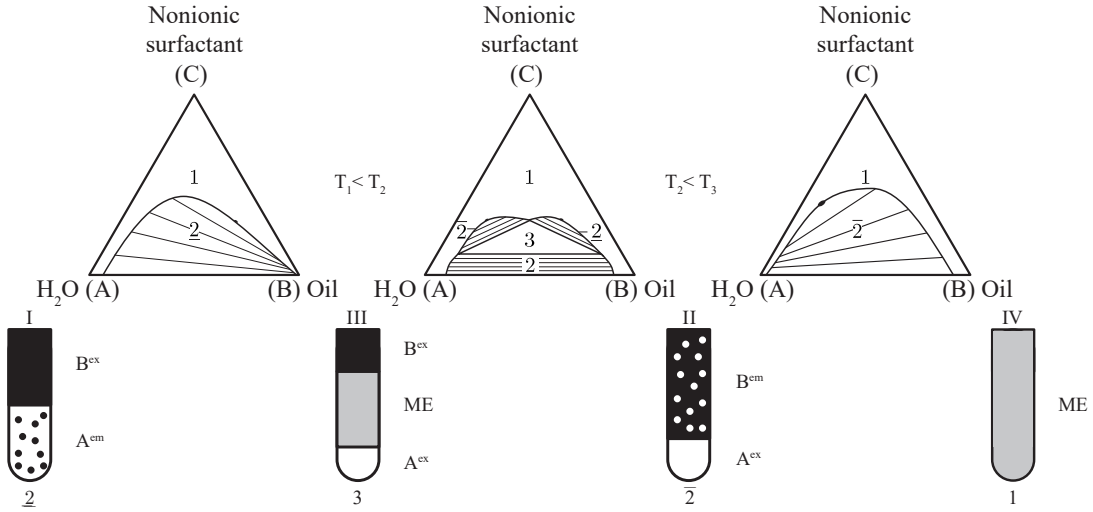

Fig. 2.4: Schematic isothermal Gibbs triangles for mixtures of oil (**B**), water(**A**), and a nonionic surfactant (**C**) at rising temperatures. Phase equilibria are either denoted with $\underline{\mathbf{2}}, \mathbf{3}, \overline{\mathbf{2}}, \mathbf{1}$ or **I - IV** according to Winsor (1956). The developed phases are labeled according to the continuous liquid: **B** (oil), **A** (water), and **ME** (bi-continuous microemulsion phase); with superscripts $^{\mathbf{ex}}$ (excess phase) and $^{\mathbf{em}}$ (emulsion phase). The figure is adapted from (Sottmann et al., 2009).

The knowledge of the phase behavior, component distribution, and volume fractions of existing phases is of high relevance for potential industrial applications. Here, the so called "Kahlweit's Fish Diagram" on the left in Fig. 2.5 provides a qualitative representation. It represents a slice through the Gibbs phase prism at a constant oil to water ratio of $\alpha = 50, wt.-\%$ and allows for the following statements:

- A minimum amount of nonionic surfactant γ_0 is needed to allow for the formation of emulsion phases. This is closely related to the cmc described in Sec. 2.1.1. Below the cmc, the phase behavior of the water-oil-system is dominant.
- At low temperatures and above the cmc the $\underline{2}$ region is established with an oily excess phase and an surfactant-rich aqueous phase in which micelle structures are formed.
- At high temperatures and above the cmc the $\overline{2}$ region is established with an aqueous excess phase and an surfactant-rich oil phase in which inverse micelle structures are formed.
- Within a defined temperature window $[T_l, T_u]$ the three-phase body is established, in which a surfactant-rich bi-continuous emulsion phase is formed, holding also water and oil. Additionally, oily and aqueous excess phases are formed.

- The ideal state of the ME is located at $\tilde{X}$. "It defines both the minimum mass fraction $\tilde{\gamma}$ of surfactant needed to solubilise water and oil (...), as well as the corresponding temperature $\tilde{T}$, which is a measure of the phase inversion temperature" (Sottmann et al., 2009).

Keeping this in mind, **M**icro**e**mulsion **S**ystems (MESs) can basically be tailored towards a potential application: either a high solubilization is strived for, or the *immobilization* of components in either hydrophobic or hydrophilic phases is desired. For the process concept at hand, this will be discussed in Chap. 3.

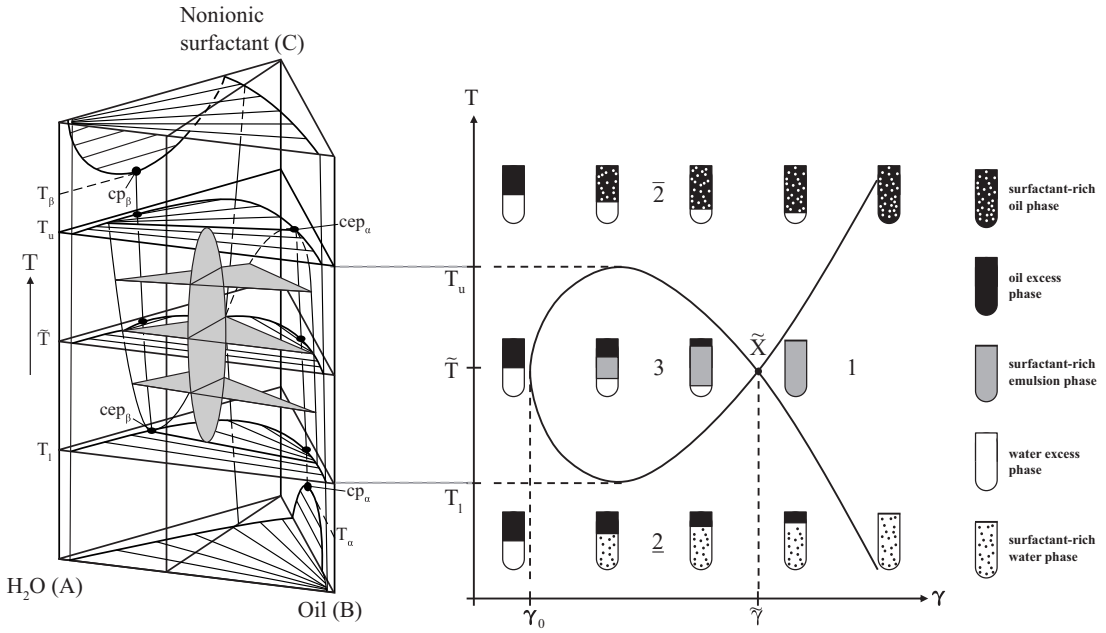

Fig. 2.5: Left: Schematic phase prism of the ternary system water, oil, and nonionic surfactant showing the general temperature dependent phase behavior. Right: Phase behavior and qualitative evolution of phase volume fractions depicted in a T,γ-diagram at constant oil to water ratio $\alpha = 50\,wt.-\%$. The diagrams are based on figures shown in (Sottmann et al., 2009).

2.1.3 Features and Description of the Three-Phase Body

It has been outlined by Illner et al. (2016c) and Illner et al. (2018a) that component distributions and separation dynamics of the three-phase system are advantageous for the process concept at hand. Thus special attention is given to its characteristic features and description. To guide the discussion Fig. 2.6 depicts an isothermal Gibbs triangle and possible separation states. If a three-phase separation is established starting from a prepared mixture at setpoint $SP1$, a central microemulsion phase is formed with adjacent excess phases of oil and water. From a thermodynamic point of view, the following features of such a system can be stated:

- The volume fraction Φ of each phase depends on $SP1$ and the corresponding corners of the three-phase body at the current temperature (levers).
- The component concentrations in these individual phases however are the same for any $SP1$ in the three-phase body, as long as T and other external influences remain constant.
- As phase ME moves clockwise towards the B-side of the triangle with rising temperature, one will encounter shifting volume fractions. The aqueous excess phase will grow with temperature, while the oil phase will shrink (see right illustration in Fig. 2.6.)
- The surfactant concentrations of the excess phases water A^{ex} and oil B^{ex} are approximately at the level of the cmc for corresponding binary systems. For temperatures varying from 0-40 °C, cmcs of 10^{-5}-10^{-4} mol L^{-1} are found for water ((Rosen et al., 1982)).
- The composition of the excess phases A^{ex} and B^{ex} is then mainly determined by the two-phasic oil-water miscibility gap below the three-phase body.
- The cmc of a nonionic surfactant in the aqueous and oily excess phase is temperature dependent. With increasing temperature, $cmc(A)$ will decrease, while $cmc(B)$ will increase (Kahlweit et al., 1990).

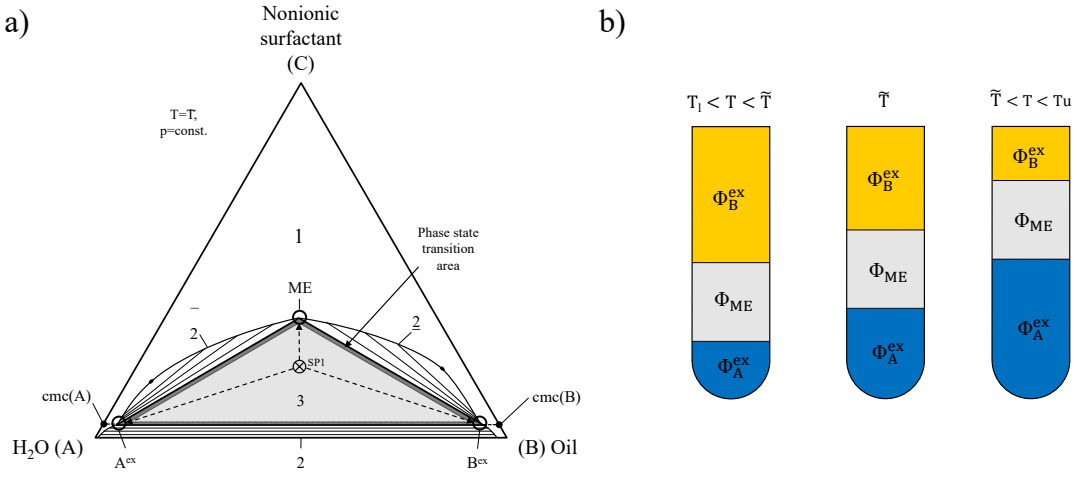

Fig. 2.6: Left: Schematic isothermal triangle of the ternary system at $\tilde{T}$ with miscibility gaps. Right: Schematic evolution of the volume fractions of the developed phases over temperature within the three-phase body.

Influence of Surface Active or Polar Substances on the Three-Phase Body

For the application of microemulsions as reaction media, several surface active or polar components are added to the MES, such as catalyst precursors or ligands. This will alter the phase separation behavior and especially the expanse and position of the three-phase body.

Since polar compounds, such as salts, are mainly soluble in water also the solubility of the surfactant in water is altered. In general, lyotropic salts, like NaCl, or Na_2SO_4 reduce surfactant solubility and thus lead to a widening of the three-phase body, although its position on the T ordinate is lowered (Kahlweit et al., 1988; Ritter et al., 2016). For hydrotropic salts, the opposite behavior is found.
The influence of catalyst precursors, preformed catalysts, or ligands on the system can be various, depending on the structure of the added molecules. Besides extended experimental investigations, quantum chemistry based methods can be deployed to predict chemical potentials of components and acquire distribution coefficients, as well as phase behavior characteristics. A comprehensive analysis hereof is provided by Wille (2013).

2.1.4 Coalescence Behavior and Separation Dynamics

A key feature for understanding the separation dynamics in a microemulsion system is the preferential contact between the phases involved. Here, an "important property of the three-phase body (...) is the minimum of the interfacial tension $\sigma_{A^{ex}-B^{ex}}$ between the aqueous and the oil-rich phase at $\tilde{T}$" (Kahlweit et al., 1988, p. 507). With the starting evolution of the three-phase body the surfactant rich water phase separates into phase A^{ex} and ME. The interfacial tension between these phases will start from zero and increases with temperature. Concurrently, the interfacial tension between microemulsion phase and oily excess phase will decrease, till reaching zero at T_u (see Fig. 2.7 and the discussion in (Kahlweit et al., 1988)). This effect is mainly due to the "movement" of the surfactant from the water-rich to the oil-rich phase.

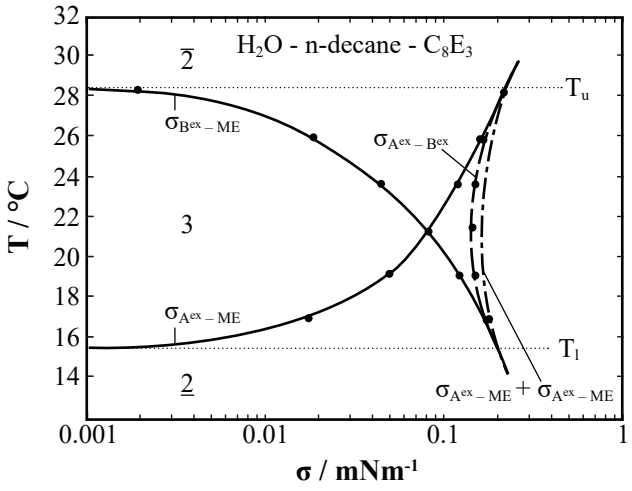

Fig. 2.7: Temperature dependent evolution of the interfacial tension of the coexisting phases in the three-phase body. Image based on figure and data shown in (Kahlweit et al., 1988).

It is apparent, that the near-critical phases in the "border" region of the three-phase body (excess phases and microemulsion phase) show increased mutual wetting. Here, the interfacial tensions $\sigma_{A^{ex}-ME}$ and $\sigma_{B^{ex}-ME}$ drop to zero. However, within the body of Kahlweit's Fish the $\sigma_{A^{ex}-ME}$ and $\sigma_{B^{ex}-ME}$ are well above zero. This leads to a specific phase separation behavior: the time to reach thermodynamic equilibrium for a separating emulsion is significantly larger at the boundaries of the three-phase body (Kahlweit et al., 1987).

Fig. 2.8 displays the phase separation dynamics for an exemplary ternary mixture water–n-tetradecane–$C_{12}E_4$. A zone of fast separation at the center of the three-phase body is surrounded by rather extended areas of reduced coalescence and slow separation. A similar situation is observed for the kinematic viscosity of the stirred mixture. According to Kahlweit et al. (1987, p. 441) "the curve shows two weak maxima close to T_l and T_u, and a distinct minimum close to the mean temperature of the three-phase interval. The width of this minimum corresponds well with that of the region of rapid phase separation (...)". These findings are major aspects to be considered for technical applications of microemulsions, especially in separation units. Even small changes in process variables, such as temperature or concentrations are prone to significantly alter the mixture properties.

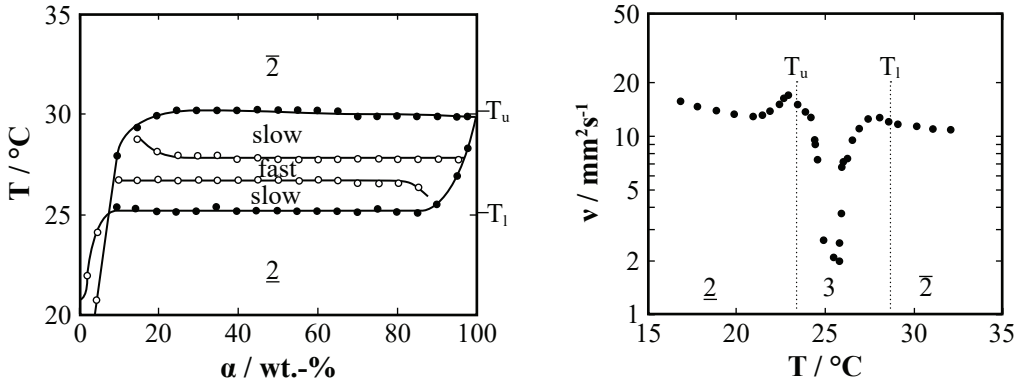

Fig. 2.8: Left: Dynamics of the phase separation in a ternary system of H_2O–n-tetradecane–$C_{12}E_4$ with $\gamma = 2$ wt.-%. *fast* indicates a separation within less than 30 min. Right: Temperature dependent viscosity of the system. Image based on figure and data shown in (Kahlweit et al., 1987).

Coalescence Behavior

Furthermore, the understanding of the coalescence behavior of microemulsions is inevitable for process applications. The coalescence of droplets or droplets on interfaces has been in the focus of research for many years with a major application field in liquid-liquid extraction (A. R. Smith et al., 1963; Bohnet, 1976; Deibele et al., 2000). Up to date, numerous modeling approaches for two-phase systems have been developed, subsequently increasing the level of detail (see reviews

by Vijayan et al. (1975), Liao et al. (2010)). However, droplet coalescence underlies several influences, which also include surface active substances. Thus, a profound analysis of the influence of surfactant and other substances on the coalescence of a multiphase mixture is inevitable. Exemplarily, it is referred to the work of Danov et al. (1999) and Alexandrova et al. (2018), who investigated the effect of soluble and insoluble surfactants on film drainage and coalescence. Due to the afore outlined complexity of MESs, a rigorous description of their multiphase (and dynamic) separation is highly challenging and yet demands a deep understanding of the system and extended experimental investigations. Hence, the coalescence behavior of MESs will be discussed from a more general perspective on the basis of Fig. 2.9. The aim is to set up heuristics to aid equipment design and process operation. Further information on theoretical background and experimental methods is provided by Kahlweit et al. (1988).

- With the beginning three-phase body ($\underline{2}/3$ transition) droplets of oily excess phase (oil) and surfactant rich phase (ME) exist as singlets in a continuous (surfactant rich) water phase (aq). The interfacial tension between water and emulsion phase is almost zero and the separation is slow (see Fig. 2.7). Hence, one observes rising oil droplets dragging surfactant, while the evolution of water and microemulsion phase is slow. Moreover surfactant may accumulate at the interface of oil and microemulsion phase.
- Increasing the temperature leads to an accelerated separation within the three-phase body. With the changing interfacial tensions the formation of different emulsion states is enforced. These may have the character of a droplet in droplet emulsion, as has been shown by Hohl et al. (2016). These dual droplets again will rise up in an aqueous phase and disrupt at the *aq-ME* interface. With sufficiently large interfacial tensions, the *ME* droplet quickly coalesces with the *ME* phase. The oil droplet continues to rise due to density differences and finally merges with the oil phase.
- The inverted case is present, if the top of the three-phase body is approached ($T > \tilde{T}$). Here dual droplets of water and microemulsion phase are found in an oily continuous phase. If such a system is stirred and then set to separate, one observes descending dual-droplets. Again, these break at contact with the *ME* phase. As the *ME* droplet merges, the *aq* droplet descends towards the water phase.
- In the transition zone towards the $\overline{2}$-phase region, the interfacial tension between microemulsion phase and oil drops to zero. Again, only single droplets are present as disperse phase in an oily continuous phase. On separation, falling water droplets dragging surfactant are observed. The separation of oil and emulsions phase is very slow and again surfactant accumulation can occur at the interface *water-ME*.
- At $\tilde{T}$ also bi-continuous microemulsion phases can be present, which separate rather fast, as the disperse oil and water droplets move towards their corresponding phases.

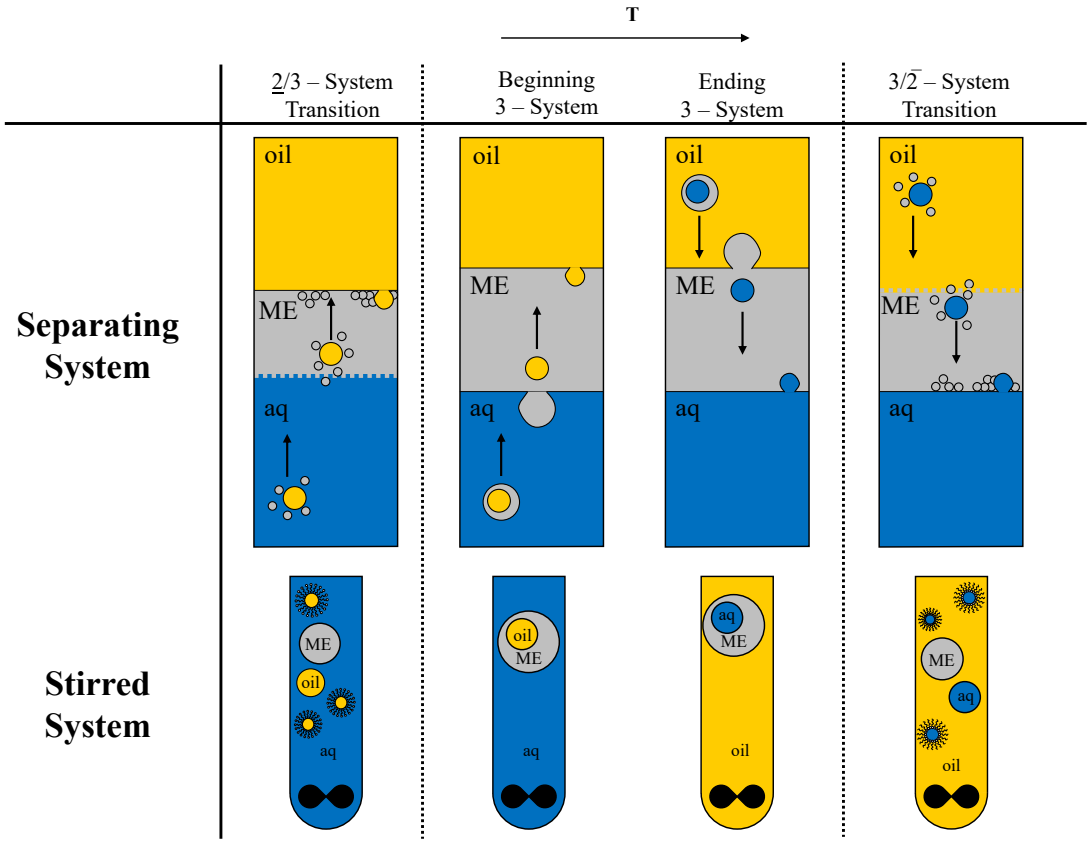

Fig. 2.9: Schematic illustration of the coalescence behavior along the three-phase body. The upper section shows separating systems with droplet configurations and coalescence. The lower part sketches the situation of continuous and disperse phases in the stirred system. *oil*: oil rich phase, *aq*: aqueous phase, *ME*: microemulsion phase.

2.2 Kinetics of Rhodium-Catalyzed Hydroformylation Reactions

From a process design and control perspective, the knowledge of reaction kinetics is vital to optimize reaction yield and selectivity, which thus will be shortly outlined.

In 1961 Heck et al. (1961) proposed a first mechanism for the cobalt-catalyzed hydroformylation based on theoretical assumptions, which was later expanded and validated through experiments and further theoretical investigations (Heck et al., 1963). This formed the basis for the formulation of a reaction mechanism of the hydroformylation based on ligand modified rhodium catalysts (Evans et al., 1968; Wilkinson et al., 1968; Brown et al., 1970). Despite the *Wilkinson* mechanism being well accepted and hydroformylation processes being successfully applied in

chemical industry for more than sixty years, current research still aims for a detailed understanding of reaction mechanisms and formulation of suitable ligand-Rh-catalyst systems (Shylesh et al., 2013; Jörke et al., 2017; Wodrich et al., 2018).

Important advances in ligand development were achieved with the synthesis of bidendate diphosphine ligands. This led to significant improvement in regioselectivity of the reaction due to steric effects resulting from the ligand's "bite-angle" (Tolman, 1977). In 1995 Kranenburg et al. (1995) found optimal selectivities for the Rh-catalyzed hydroformylation of 1-octene, if Xantphos (4,5-bis(diphenylphosphino)-9,9-dimethylxanthene) was used as a ligand. Later, Goedheijt et al. (1998) described the synthesis of a sulfonated form of Xantphos – SulfoXantPhos (4,5-Bis(diphenylphosphino)-9,9-dimethyl-2,7-disulfoxanthene disodium). This highly hydrophilic ligand enables the formation of water-soluble catalyst complexes besides high regioselectivities around 97 %. With water-soluble catalysts being of interest for this thesis, a catalyst complex can be formed using the catalyst precursor $Rh(CO)_2(acac)$ and SulfoXantPhos (see Fig. 2.10).

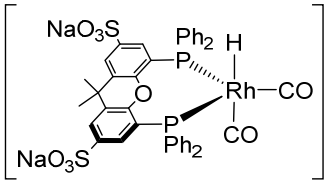

Fig. 2.10: Structure of the hydrophilic Rh-SulfoXantPhos catalyst complex. Figure taken from (Pogrzeba et al., 2017b).

To understand reaction performance and influences on the reaction in lab and mini-plant, the mechanism of the Rh-catalyzed hydroformylation, reduced to the formation of linear aldehydes, is presented in Fig. 2.11 (Pogrzeba, 2018). Initially, the catalytically active species (**1a**) is formed from $Rh(CO)_2(acac)$ and SulfoXantPhos in the presence of synthesis gas. This species is in equilibrium with an inactive rhodium dimer (**1c**) and the non-selective unmodified rhodium-tetracarbonyl species (**1b**), depending on the partial pressures of CO and H_2 (Sandee et al., 1999; Li et al., 2002; Silva et al., 2003). The catalytic cycle starts with the dissociation of CO from rhodium species (**1a**) and subsequent coordination of the alkene (**3**). In the next step, the alkene is inserted into the catalyst complex (**4**), whereas the orientation of the ligand at the metal center influences the regioselectivity of the reaction, as either the terminal or inner carbon atom is linked to the complex. Afterwards CO is added (**5**) and inserted into the rhodium-alkyl bond to form species (**6a**). At this stage high CO concentrations promote the formation of a catalytically inactive acyl species (**6b**), which is in equilibrium with (**6a**). The cycle is closed with the addition of H_2 to form species (**7**) and the following reductive elimination of the aldehyde.

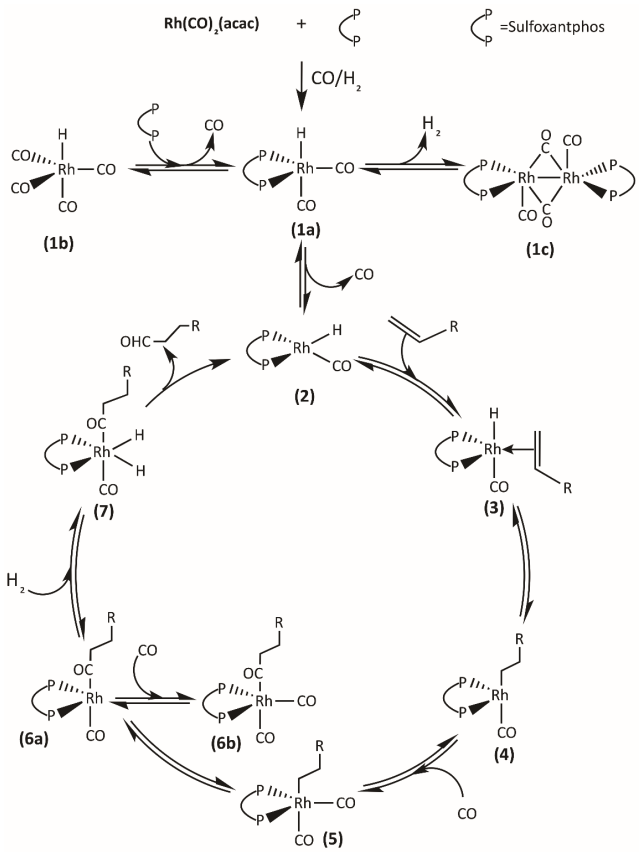

Fig. 2.11: Mechanism of rhodium-catalyzed hydroformylation of alkenes using a bidentate diphosphine ligand. Based on the mechanism by Wilkinson et al. (1968) and further developed by Deshpande et al. (2011). Figure taken from (Pogrzeba et al., 2019).

2.3 Systematic Investigation of Reactive Microemulsion Systems for Process Design and Operation

The realization of novel process concepts involving liquid multiphase systems requires sufficient understanding of system inherent phenomena and challenges. Hence, knowledge on the desired reaction with underlying catalytic system, the multiphase reaction media with physical and thermodynamic features, as well as the interaction of both is to be build up. Systematic and efficient methodologies for this are key to an enhanced process development, earlier readiness of novel process concepts, and increased relevance for industrial applications. Focusing on microemulsion systems, this section thus discusses methodologies for investigating such systems and the aligned derivation of strategies to enable application.

2.3.1 Status Quo: Process Design and Operation for Homogeneous Catalysis in Microemulsion Systems

Microemulsions as reaction media were already reported more than 50 years ago by Cordes et al. (1969) or Wallace et al. (1973). Recently, further activity for specifically conveying organic reactions using long-chained substrates is noticeable (Haumann et al., 2002; Dwars et al., 2005; Hamerla, 2014). Most of these contributions stem from academia and comprise batch experiments evaluating reaction performances using varying microemulsion formulations. Thus, at least selection guidelines for the formulation of MES can be derived. However, industrial applications of developed MES for organic reactions are still very limited (Schomäcker et al., 2009). Moreover, modeling approaches for MES are scarce and mainly focus on equilibrium state calculations with reduced applicability in ternary systems (García-Sánchez et al., 2001) or are still subject to extended experimental investigations (Torrealba et al., 2018). A significant deficiency of methodologies on how to design and operate actual processes involving such novel solvent systems can thus be stated.
To close this gap, increasing efforts in understanding microemulsion systems have been made within the *Collaborative Research Center TR63 InPROMPT* with the aim to unlock a holistic process development for such systems but yet also deepen the understanding of its inherent features. Essential deliberations, aiding the analysis of MES encompass the investigation of mass transfer phenomena regarding the application of homogeneously catalyzed reactions (Hamerla et al., 2013a) and the coalescence behavior of microemulsions (Hohl et al., 2018). Additionally, Pogrzeba et al. (2016a) and Pogrzeba et al. (2017b) provide insights on the influence of surfactant type and microemulsion system on the reaction performance for the hydroformylation of 1-dodecene, as well as the catalyst recycling. Moreover, M. Müller et al. (2013) and D. Müller et al. (2015) provide heuristics on process design, analysis of MESs regarding separation unit design, and modeling approaches.

Despite these advances, early stage implementations of reactive MEs in mini-plant systems still reveal significant challenges regarding stable continuous operations and reaction performance (Illner et al., 2016a; Illner et al., 2016b). Within long-term operations, significant byproduct formation and the frequent loss of feasible product and catalyst separation was observed. Moreover, the causality between operation, intervention, or disturbances and the observed phenomena were not fully understood. Regarding industrial-scale applications, this situation is not acceptable and significant improvement on available methodologies for the realization of MESs as reaction media is necessary.

2.3.2 Systematic Analysis of Microemulsion Systems for Process Application

As part of the workflow for a rigorous analysis of surfactant-based multiphase system in Fig. 2.1, a profound identification of relevant operational challenges is crucial. Hence, a systematic workflow for the analysis of such systems for technical applications is developed in the following. Considering the complex nature of microemulsions and the catalytic system of the hydroformylation reaction several general requirements for such an analysis must be met:

- Reaction performance and phase separation behavior must be investigated considering all compounds existing in the final application due to significant influences.
- This also means to consider interactions between the reaction and separation performance.
- Challenges arising from the dynamic operation in a continuously operated plant need to be analyzed – operation with internal recycles must be considered regarding possible disturbances like concentration shifts, mixing behavior, or accumulations.
- Special attention should be given to the measurability and controllability. Thus, whether all system variables having significant influence on the reaction performance and phase behavior are trackable and controllable with available instruments and actuators.
- If the latter is not the case, the application of advanced analytics or deployment of model-based methods (e.g. state estimation) is to be checked.

To acquire sufficient and relevant data for this, a workflow for the analysis of surfactant containing multiphase systems for technical applications is introduced. The main idea is to use preliminary screening experiments, to quickly characterize the (dynamic) separation behavior and develop first equipment designs as well as process models. Starting from deliberations in our own contribution (D. Müller et al., 2015) this workflow is substantially extend to meet the above mentioned requirements. This way, the acquisition of suitable data models of the phase separation behavior for process control purposes and vital information on the controllability of the system, as well as reduction of the experimental effort is ensured. The general structure of this systematic guideline consists of six successive steps:

Step 1 defines constraints and requirements for process application. Firstly, desired features of the multiphase system are defined. For a mixer-settler system this could be sufficient solubilization of reactants and a favorable component distribution in the separated system. Secondly, already predominant limitations of the technical system are to be collected. These could entail constraints on applicable temperatures, pressure, or the availability of sensors and actuators to measure and influence state variables of the multiphase system. Finally, the component system is specified. This includes microemulsion formulation, the catalyst system, reaction educts and

products, applied gases, and potential additives. These specifications are most relevant, because changes in the component system alter phase equilibria and systems dynamics significantly.

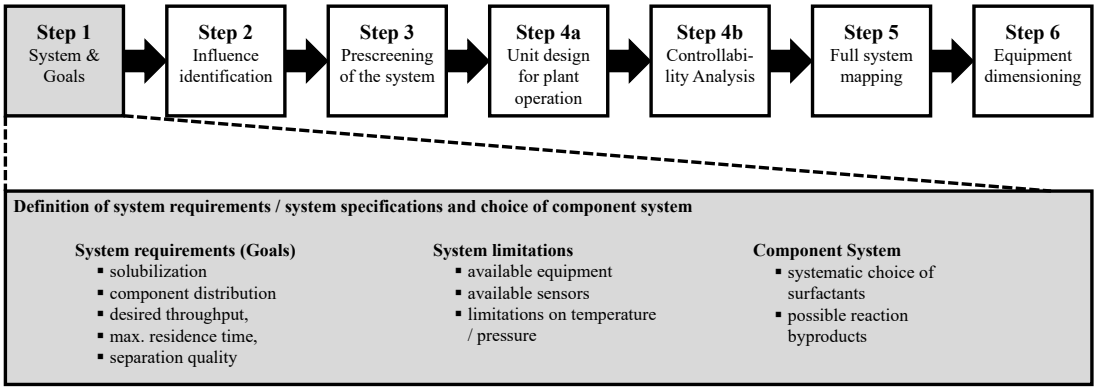

Fig. 2.12: Systematic analysis of surfactant containing multiphase systems, Step 1: system specification and goals for process operation. Figure adapted and extend from (D. Müller et al., 2015).

Step 2 then handles the identification of relevant influencing factors on the behavior of multiphase systems and possible ranges of interest. This prescreening is performed theoretically, including a thorough literature survey. For multiphase systems holding nonionic surfactants, deliberations of Kahlweit et al. (1985), Kahlweit et al. (1987), and Sottmann et al. (2009) were essential to set up the guiding scheme in Fig. 2.13.

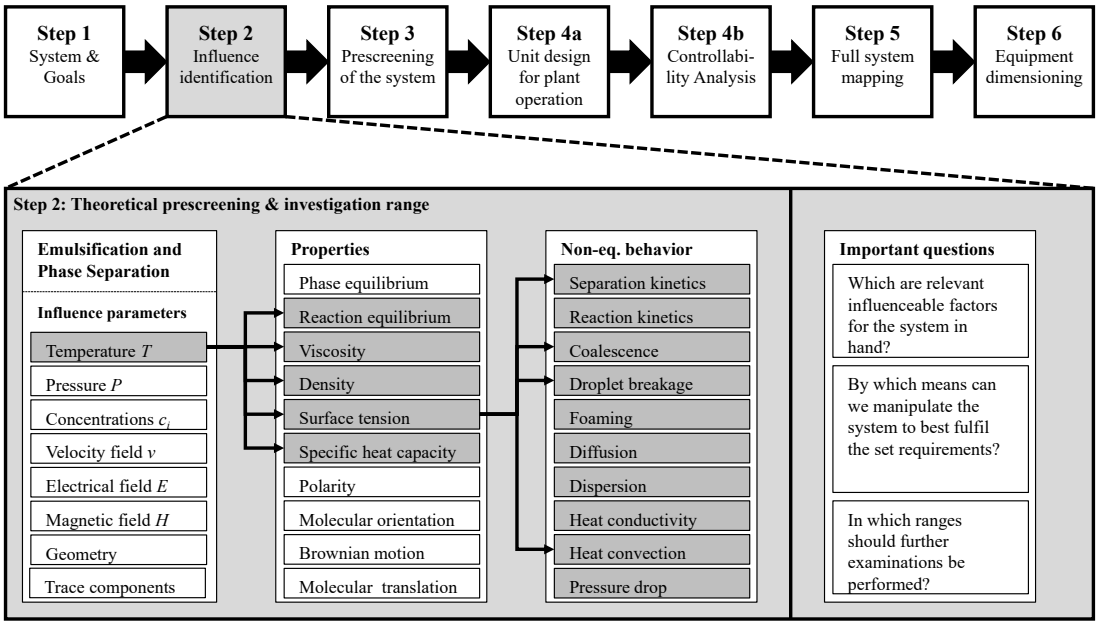

Fig. 2.13: Systematic analysis of surfactant containing multiphase systems, Step 2: influence identification. Figure adapted and extend from (D. Müller et al., 2015).

Note, that limitations defined in **Step 1** are to be considered. Hence, if devices providing electric or magnetic fields (application on MES shown in (Tekle et al., 1989; Palyska et al., 1993)) cannot be used in the final process application, the corresponding influence is omitted.

Step 3 aims for an evaluation of defined influences. Therefore, simplified prescreening experiments (*Shake & Wait*) are suggested. Multiple test tubes with varying compositions are prepared and heated in thermostatic baths. Once the desired temperature is reached, the test tubes are removed from the bath, vigorously shaken, and returned into the bath. Phase separation for all compositions is then observed for a fixed time (Investigation Stage 1). Thus, the general separation kinetics and forming phase equilibria are observed (Observation Stage 1). A feasibility analysis is connected to this step. Here, the system observations are to be scanned for suitable separation dynamics and phase equilibrium states in accordance with defined goals in **Step 1**.

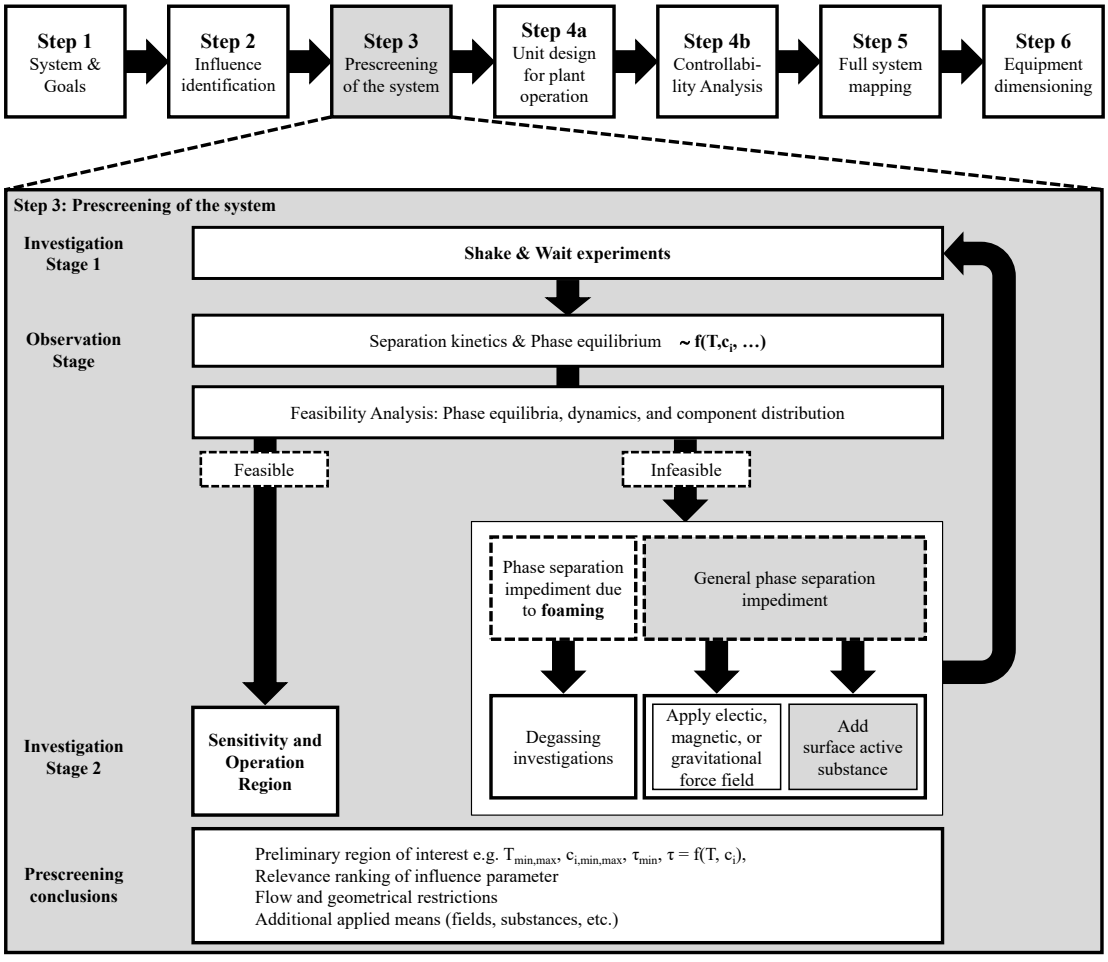

Fig. 2.14: Systematic analysis of surfactant containing multiphase systems, Step 3: Preliminary screening and sensitivity analysis. Figure adapted and extend from (D. Müller et al., 2015).

Several reasons for impeded applicability of the current system can exist such as foaming or changing of interfacial tensions due to ongoing chemical reactions. The application of counter measures is then tested on Investigation Stage 2. If the feasibility test is successful, an additional assessment on the sensitivity of the influence factors on separation quality and dynamics is done. Mostly insensitive influence factors are to be discarded for further investigations. From the feasibility step, also possible operation regions for phase separation, as well as lower and upper bounds on the influence parameters can be estimated. On infeasibility, further investigations (return to Investigation Stage 1) are considered.

Step 4 is designed twofold. Firstly a preliminary unit design is to be performed based on the

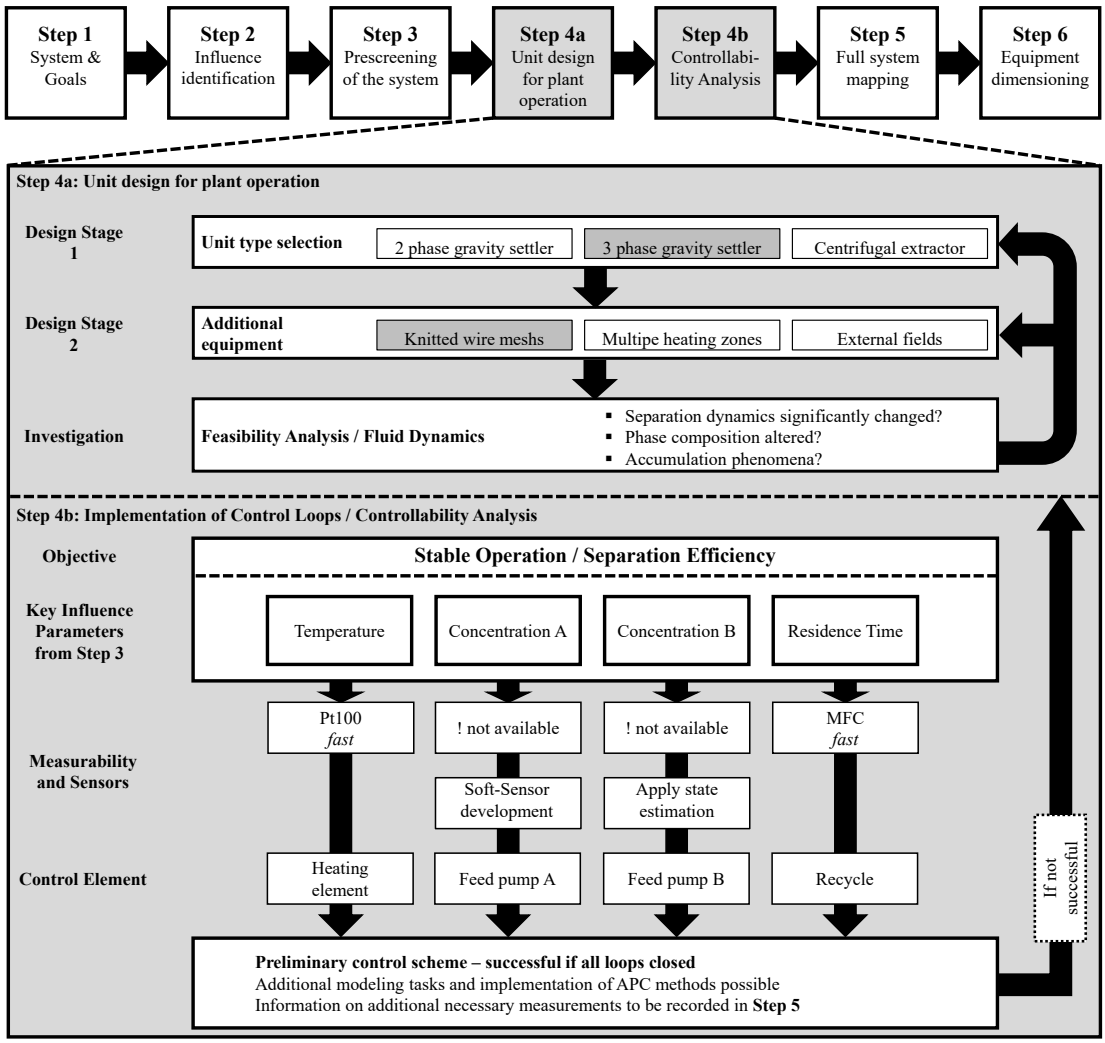

Fig. 2.15: Systematic analysis of surfactant containing multiphase systems, Step 4: Unit design and operability analysis for continuous processes. Figure extend from (D. Müller et al., 2015).

gained information on the multiphase system. Decisions are to be made on type of unit, applied force field, and the number of handled separated phases. Additionally, internals can be chosen. Following the discussion in Sec. 2.3.3, the technical realization of a separation process can alter the separation dynamics. This has to be checked regarding hampering effects. Exemplarily, the implementation of knitted wire meshs can lead to significant accumulations of certain components in a settler unit and inhibit its operation.
The second part of **Step 4** involves the operability and controllability of the system. To this extend of the guideline, a certain relevant set of parameters influencing the phase separation of a multiphase system has been identified (Key Influence Parameters). It now has to be considered, if these actually can be technically controlled in the real application. For this purpose, the measurability of these influences and available sensors is checked. Of interest might also be the available sampling rate of the corresponding sensor, which should match with the observed sensitivity of the corresponding influence parameter. If no apparent technical measuring method is available one also could proceed with **A**dvanced **P**rocess **C**ontrol (APC) methods. Exemplarily, soft-sensor development is named at this point. If measurability is ensured for all relevant influence parameters, their controllability is checked. This means the availability of corresponding control elements. If this is not true, the unit concept needs to be changed in an iterative process. The major outcome of **Step 4** is thus a preliminary unit design and most important, information on additional necessary measurements to quantify certain influence parameters.

Step 5 then continues with the main experimental section of this guideline. Up to now, a reduced set of influence parameters and relevant operation regions for the separation of the multiphase system has been identified. A feasible set of measurements has been listed, which ensures a reliable tracking of key influence parameters and states. Hence, an appropriate experimental testing system can be designed, alongside an efficient experimental plan. Based on this, mapping experiments are performed to determine separation dynamics and states.

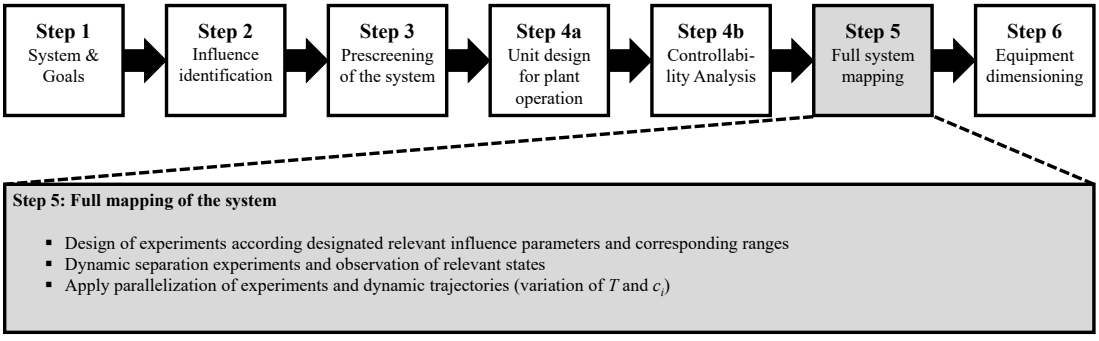

Fig. 2.16: Systematic analysis of surfactant containing multiphase systems, Step 5: Full system mapping. Figure adapted and extend from (D. Müller et al., 2015).

This information is then used to generate empiric input/output models for the phase separation dynamics and component distribution in the system. With the guideline at hand, their usage in real technical applications is ensured, as the consideration of measurability or observability of relevant states is enforced. Additionally, this information is used to proceed with a detailed design and construction of the chosen separation unit (**Step 6**).

2.3.3 Equipment for Multiphasic Separation

For the scope of this thesis, the separation of MES is to be continuously operated in a mini-plant. Hence, a short outline on technical realizations of separation units is given.
Depending on the thermodynamic and physical properties of the mixture to be separated, a variety of technical realizations exist. Applying a systematic guideline shown by Seader et al. (2011, p. 309) on the component system discussed (Sec. 3.1), a single stage mixer-settler process is favorable. With sufficiently large density differences of the substances the separation can be performed in a gravity settler. The apparatus itself is designed as a horizontal or slightly inclined separation chamber with an inlet, separation area, possible internals, and phase drains (see Fig. 2.17). The inlet is positioned at the level of the expected interface to avoid back-mixing of already separated phases (Padilla et al., 1996).

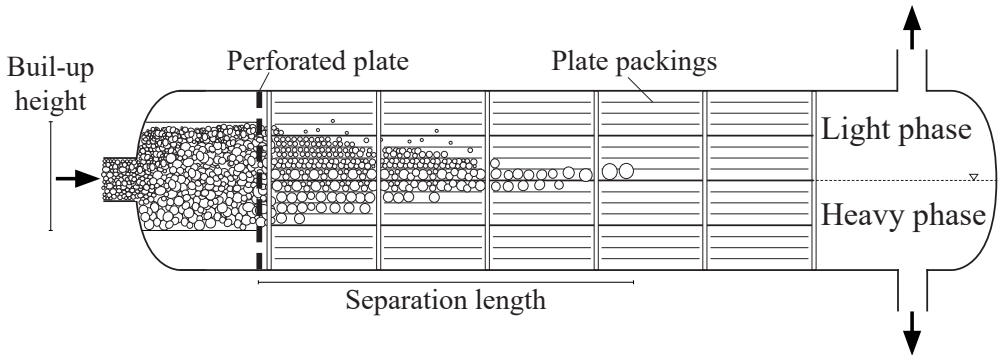

Fig. 2.17: Schematic representation of a gravity settler with several internals for the separation of a heavy dispersed phase. Illustration based on (Schlieper et al., 2004).

The phase evolution over the length of the settler first of all depends on the coalescence behavior of the mixture. In addition, also the flow regime is relevant for a continuous process. Investigations by Jeffreys et al. (1970) showed, that mixing processes at the settler inlet lead to a stabilization of the emulsion. Moreover, a radial velocity gradient might occur. Thus circulation flows or reflux are observed, hampering separation efficiency (Drown et al., 1977).
Apparently, the separation efficiency can be increased by the use of internals, such as plates, baffles, perforated plates, or knitted wire meshs. Coalescence enhancement mostly results from

the contact of the emulsion with metals, for which the disperse phase shows a high wetability. The disperse phase forms a liquid film on the surface, from which then larger droplets detach (Berger, 1986). Additionally, a simple filtration effect is exploited for knitted wire meshs. With emulsion droplets larger than the mesh free diameter, droplets are impounded and coalescence is enhanced because of the increased velocity at droplet collisions (Bohnet, 1976).

2.3.4 Systematic Workflow for the Influence Identification and Derivation of Adapted Kinetic Models

The formulation of kinetic models to predict reaction performance is to date challenging. Usually, expensive and time consuming experimental studies have to be performed if these models are to be developed for process simulations or process optimization (Mitsos et al., 2018). According to Besora et al. (2018, p. 3), especially homogeneously catalyzed reactions include a multitude of steps, like "off-cycle formation of the catalyst from a pre-catalyst, formation of adducts between the reactants, catalyst deactivation processes, (...) isomerizations", which have to be initially identified. Spectroscopic methods can be applied to identify active catalytic compounds, states, and detailed reaction routes (Bhaduri et al., 2014; Grabow et al., 2014). From that, complete mechanistic or microkinetic models can be formulated, aided by quantum chemistry computational tools (Murzin et al., 2016; Besora et al., 2018). Using kinetic experiments, actual reaction rates and kinetic parameters can be estimated. However, this is mostly done for idealized systems, yielding microkinetic descriptions. Often enough, additional influences on the kinetics are present for practical applications. These are induced by trace components, interaction with mass transfer or changes of the actual reaction media. Thus, an adaption of the kinetic model towards the application is necessary. For this, a systematic workflow is presented in our contribution (Pogrzeba et al., 2019) and shown in Fig. 2.18.

Step 0 therein is used to collect available data on the regarded component system and reaction. First of all, the literature is reviewed for available kinetic models (microkinetic, mechanistic, or even empiric) $Model_0$ and kinetic parameters. For a variety of reactions, this is successful and yields in a profound basis for kinetic model formulations. Additionally, necessary physical properties for the system at hand are collected.

In **Step 1** the initial $Model_0$ is tested for its general suitability for the application case, the system S_{real}. Kinetic experiments are conducted under idealized conditions, for which only the inputs I_0 and controls u_0 included in $Model_0$ are varied. With the experimental results, a parameter estimation is performed on the kinetic parameters of $Model_0$ and it is checked, whether $Model_0$ sufficiently describes the kinetics in S_{real} for variations of I_0 and controls u_0.

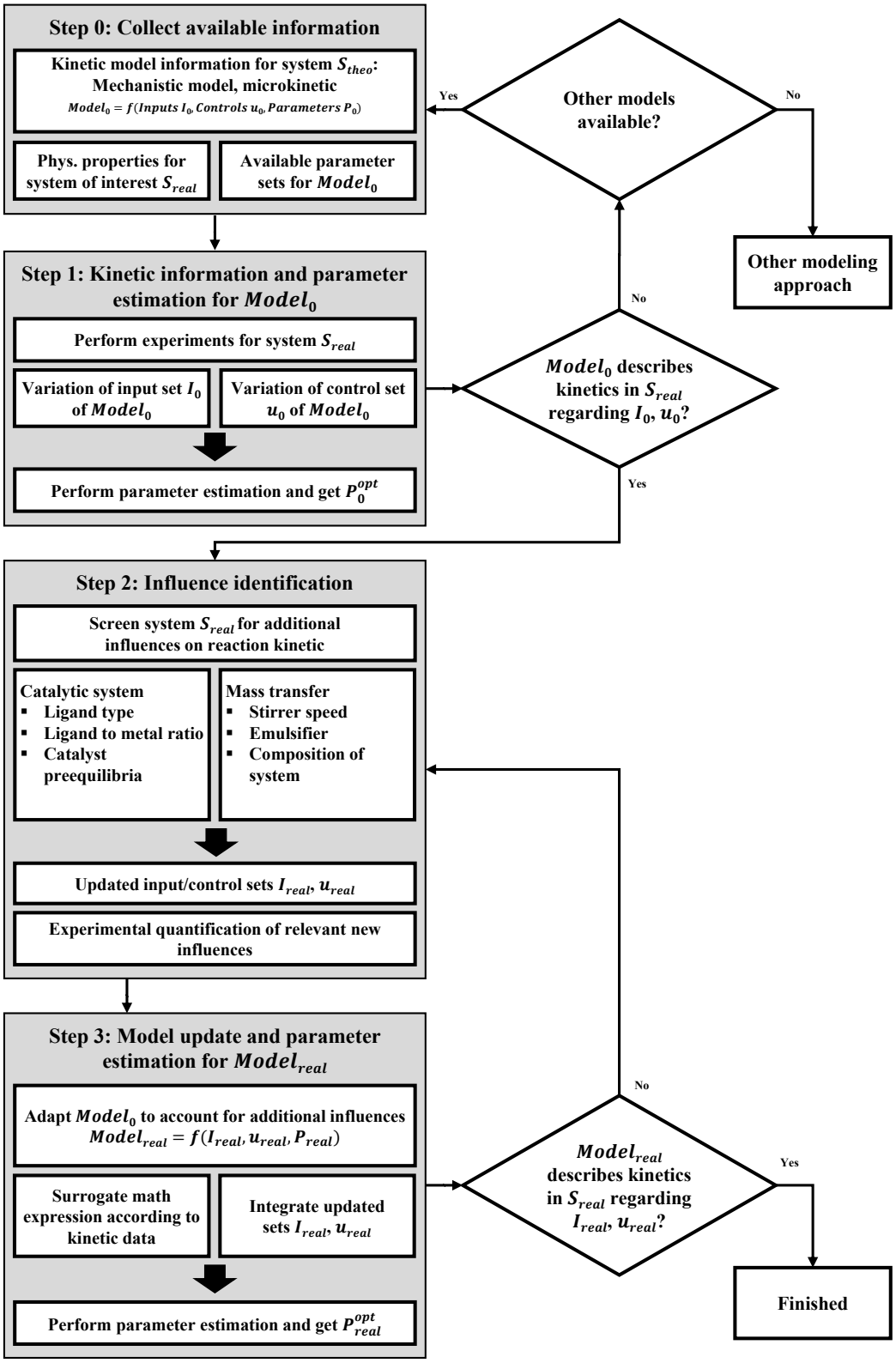

Fig. 2.18: Workflow for the adaption of microkinetic or mechanistic models to describe the reaction performance for systems with inherent additional influences. Figure adapted from (Pogrzeba et al., 2019).

If this is true, **Step 2** then deals with the identification of relevant influences of S_{real} on the reaction performance. This includes systematic screening experiments on additionally applied components (co-solvents, emulsifiers), the catalytic system (applied ligand), and the technical realization (stirrer speed, pressure drop, recycling of the reaction mixture). Influences, which show a significant sensitivity on the reaction performance, are included in updated sets of inputs I_{real} and controls u_{real}. Additional kinetic experiments are then used to quantify these influences. **Step 3** then handles the model update. The additional relevant influences of S_{real} are implemented into the kinetic model by augmentation of the rate equations to obtain the adapted kinetic model $Model_{real}$. With the collected experimental data sets for I_{real} and u_{real}, a parameter estimation is performed. Finally it is checked, whether $Model_{real}$ sufficiently describes the kinetics in S_{real} for variations of I_{real} and controls u_{real}. If this is not the case, possible hidden effects are present and the influences identification in Step 2 is repeated. Otherwise, an adapted kinetic model is obtained, describing the reaction performance for the desired application case.

2.4 Modeling for Dynamic Process Operations and Control

The derivation of a dynamic mini-plant model including relevant phenomena related to the hydroformylation reaction and the microemulsions system is a key element for the subsequent development of desired optimal process operation strategies. However, finding a suitable model formulation for this is challenging, since contradictory objectives apply: sufficient accuracy regarding system-level phenomena and low computational effort for optimization calculations. Connected to this, several reviews display recent advances in model derivation and today's possibilities in conceptual process design (Mitsos et al., 2019) and nonlinear process optimization (L. T. Biegler, 2018). Consequently, an overview on methods for the derivation of models for process optimization, model simplification, and improvement of convergence behavior relevant for this work is given in the following.

2.4.1 Modeling Strategies and Implementation for Optimization Purpose

According to Hangos et al. (2001, p. 14) "Process modelling is one of the key activities in process systems engineering (...) driven by such application areas as process optimization, design and control". Thus, also a multitude of approaches is available for the derivation of models, which can be categorized from so called "white box" models based on physical or chemical laws to data-driven "black box" models (Edgar et al., 2001, p. 41) or any combination of both, called "grey box" modeling.

Mechanistic or First Principles Models

Regarding the evaluation and optimization of process operations, rigorous models based on physical or chemical fundamentals are important, since they inherently offer high accuracy and superior inter- and extrapolation features. Moreover, these models are "conceptually attractive because a general model for any system size can be developed even before the system is constructed" (Edgar et al., 2001, p. 41).
Following (Wozny et al., 2006, p. 95ff.), the systematic model derivation starts with the subdivision of a considered process into sub spaces according to the desired modeling depth. For each sub space a complete set of linearly independent balance equations is formulated adhering to the MESH-I-systematics (**M**aterial balances, **E**quilibrium relations, **S**ummation equations, and **H**eat balances, and **I**: momentum balances). These could be further expanded considering non-equilibrium modeling and rate equations for heat and mass transfer. Additionally, mechanistic kinetic models are included to describe reaction rates. Regarding process optimization, this set of equations is then expanded by an objective function (e.g. economic criteria) and inequality constrains (physical limitations or quality goals). However, obtained equations can hold any degree of complexity and thus fast convergence is not ensured. Subsequent handling of equation system scaling, reformulations, or model simplifications are mandatory to enable model application for optimization purpose.

Surrogate Models

One approach to tackle the complexity of first principles models is to replace complex elements therein by surrogate models. Thereby, the input-output relation of the original model is well approximated by a different and ideally far less complex model structure. This feature, beneficial for computational speed, has also led to an increasing application of surrogate models in the domain of chemical engineering (Bhosekar et al., 2018; McBride et al., 2019).
Several workflows for modeling surrogates exist, for which Forrester et al. (2008, p. xvii) depict an exemplary scheme. Initially, samples or snapshots from the original model are generated. Afterwards the actual model structure is designed, adapted to the available sample data and finally validated. One generalistic MatLab framework is presented by Gorissen et al. (2010), providing a variety of applicable surrogate types, active learning (sampling data choice), and automated model selection.

2.4.2 Implementation of Dynamics and Reformulation of Equations

Chemical engineering applications are widely characterized by a nonlinear process behavior. Thus, sophisticated dynamic models must also sufficiently cover dynamics, such as step-wise

transitions caused by switching of phase equilibria or stream de-/activation. This is especially important for the microemulsion system at hand with multiple possible phase configurations. Hence, continuous switching functions, as well as continuous formulations of conditional statements are outlined in the following. In addition, model simplifications, involving structural reformulation of equations are shown in Sec. C.1 and consequently applied throughout the modeling work for this thesis. These reformulations are used to counter the usually large structural complexity of dynamic process models, which causes slow convergence for simulation and optimization applications.

Min/Max-operators:

Adhering to physicality, state variables such as flows, concentrations, or pressures solely show values greater than zero. This then also needs to be represented in respective models and thus a formulation for the smooth max-operator max(0,x) is introduced:

$$max(0,x) \approx \frac{0+x+((x-0)^2+\varepsilon)^{0.5}}{2} \qquad \varepsilon > 0 \tag{2.4}$$

This function enables the left hand side value cut-off at the value of zero, if x gets negative. A small positive value ε is deployed to render this equation twice continuously differentiable and avoid singularities. As a default value $\varepsilon = 10^{-5}$ is used throughout this thesis.
If an upper limitation of model variables is desired, the respective min(x,a) operator is applied:

$$min(a,x) \approx \frac{a+x-((x-a)^2+\varepsilon)^{0.5}}{2} \qquad \varepsilon > 0 \tag{2.5}$$

Switching Functions for Dynamic Model Switching

In the following, a mathematical expression for the conditional activation of model elements is introduced. This is of utmost importance for the modeling work in this thesis, where dynamic switching of, e.g., phase separation behavior is to be represented. To maintain twice continuous differentiability, sigmoidal functions are applied using two implementations within this work:

$$\text{Exponential sigmoidal function}: \quad Trig^{Exp}(x) = \frac{c}{1+\exp(-a\cdot(x+b))} \tag{2.6}$$

$$\text{Smooth square root approximation}: \quad Trig^{SSQRT} = \frac{c}{2} + \frac{\frac{c}{2}\cdot(x+b)}{\sqrt{(x+b)^2+a}} \tag{2.7}$$

In both cased x is the argument of the function and a continuous switching from zero to a specified parameter value c is performed, when $(x+b)$ changes from negative to positive values. Parameter a is used to adjust the *steepness* of the switching functions. Two general goals apply

for adjusting a. On the one hand a smooth gradient while switching is desired to avoid large Jacobian or Hessian entries and possible singularities. On the other hand, the switch should quickly approach the desired value c. Additionally, arguments of the exponential function larger than ≈ 300 must be avoided in Eq. (2.6). Figure 2.19 depicts the respective function behavior of the sigmoidals for varied parameters a, b, and c. Comparing the function behavior of both sigmoid types, it is obvious, that the exponential formulation is advantageous regarding its switching behavior. The smooth square root approximation however is generally considered as numerically favorable in avoiding the exponential function.

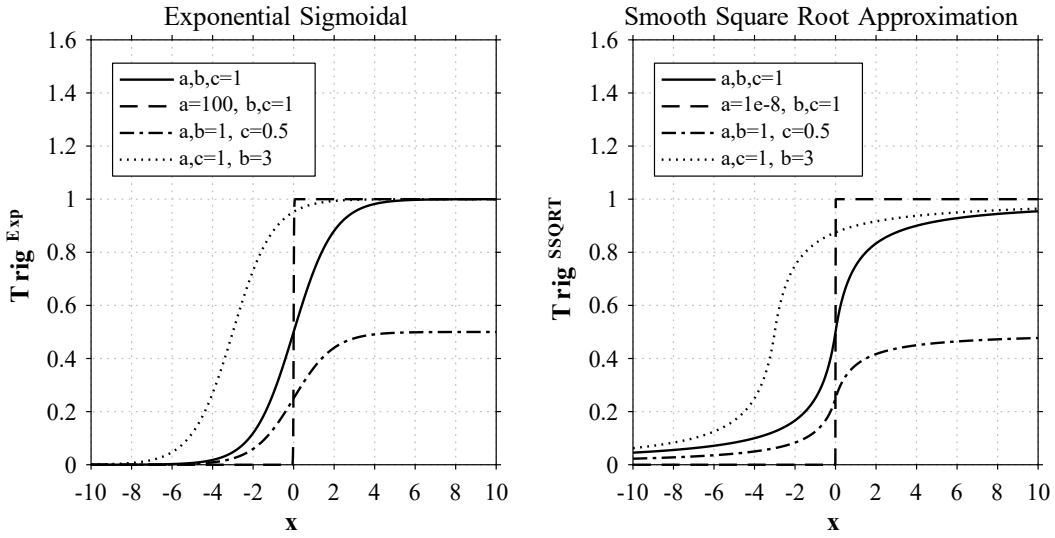

Fig. 2.19: Curvature sigmoidal function implementations, depending on parameters a, b, and c.

2.4.3 Parameter Estimation and Identifiability Analysis

Closely related to the formulation of process models is the task to identify parameters used therein. Several strategies can be found in literature to perform **P**arameter **E**stimation (PE), for which a detailed discussion of estimation methods, statistical background, and evaluation can be found in (Bard, 1973). The corresponding parameter estimation is then defined as an optimization problem of the form

$$\theta := \min_{\theta} \Phi^{WLSQ}(u,\theta) \tag{2.8}$$

$$\Phi^{WLSQ}(u,\theta) := \frac{1}{2}(y(u,\theta)-\bar{y})^T W_y^{-1}(y(u,\theta)-\bar{y}). \tag{2.9}$$

with Φ^{WLSQ} denoting the objective function in a weighted nonlinear least square formulation, experimental data $\bar{y}$, y being the model response, and a weighting matrix W_y^{-1} being the inverse of the measurement error covariance matrix. The solution of the problem are the estimated model parameters θ. Assuming measurement errors being independent, of normal distribution, unbiased, and with zero mean the measurement covariance matrix can be derived from known measurement standard deviations and Eq. (2.9) yields the maximum likelihood estimation problem (Bard, 1973). According to López et al. (2015) the solutions of PE problems is usually done iteratively using gradient-based methods, such as Levenberg-Marquardt (Marquardt, 1963) or trust-region methods (Sorensen, 1982). Therein, Jacobian and Hessian information is used to calculate step size and search direction regarding the parameter values to iteratively approach the (local) optimum of Eq. (2.8) (L. Biegler et al., 1986).

Parameter Estimation for Empirical Models

Next, a short outline for model preparation and parameter estimation for empirical models is given. For this, Forrester et al. (2008) provides a comprehensive guideline, which forms a basis for subsequent derivations in this work:

Step 1 Modeling: From system analysis and experimental observations, an empirical model structure is firstly designed. The choice of the model structure is *a priori* not clear and one is prone to choose too complex models causing overfitting of data (and noise). With overfitting, interpolation between actual measurement data points might heavily deteriorate. Hence, revision of available data under consideration of physical phenomena should be done to identify major correlations (e.g. quadratic temperature dependence).

Step 2 Estimation: Given model structure and data, a parameter estimation is performed, solving the optimization problem from Eq. (2.8).

Step 3 Testing: Afterwards, the model is tested or cross validated using a test data set, which has been randomly separated from the initial measurement data set (validation data) (James et al., 2017). The accuracy of the validation and test data set is then compared using the **R**oot **M**ean **S**quared **E**rror (RSME) as an accuracy measure over n samples:

$$RSME = \sqrt{\frac{\sum_{i=1}^{n} y_i - \bar{y}_i^2}{n}} \tag{2.10}$$

Parameter Subset Selection and Identifiability Analysis

For chemical engineering, PE problems are usually carried out on highly nonlinear and complex systems, such as reactions kinetics. Often enough, these problems pose a poor identifiability of

model parameters due to limited experimental data, inadequate model structures, or correlated parameters (Cobelli et al., 1980; Jacquez et al., 1985). According to López et al. (2015, p. 95) "this generates problems in parameter estimation (PE), e.g. multiple, meaningless, inaccurate or unstable solutions, and/or convergence and numerical problems in the solver". To overcome this hurdle, regularization techniques are applied, such as parameter subset selection (Burth et al., 1999), truncated singular value decomposition (Hansen, 1987), or Tikhonov (Tikhonov, 1963). D. Müller et al. (2014) provide an algorithm, which expands the general idea of subset selection and identifiability analysis towards uncertainty quantification of model parameters. The idea is to estimate variances of those parameters more precisely, which are actually identifiable. This algorithm is used for parameter estimation tasks within this thesis. Detailed deliberations are waived at this point and it is referred to D. Müller et al. (2014) and Cárdenas (2016).

2.5 Optimal Process Operation Strategies: State Estimation & Dynamic Optimization

The inherent complexity and operational challenges of processes involving surfactant-based multiphase reaction media require the consideration of model-based dynamic optimization strategies at an early stage and systematic (online) integration into process automation. Hence, fundamentals of (dynamic) real-time optimization, as well as its integration into the general plant automation hierarchy are briefly revised. Since also the efficient determination of the current plant's state is mandatory therein, state estimation procedures are subsequently looked at.

2.5.1 Dynamic Real-Time Optimization and Automation Hierarchy

Driven by the steady increase of computational power and improvements on solvers for optimization problems, **R**eal-**T**ime **O**ptimization (RTO) emerged as an essential technique for optimal process operation and is nowadays widely applied online in chemical and petrochemical industry (L. Biegler et al., 2015). Here, optimization problems are directly connected to the process and consider online data. Usually, steady-state models are deployed, which are solved in *real-time* with respect to the time constants of the processes (Darby et al., 2011). A typical scheme of a company's plant automation hierarchy with integrated RTO is given on the left in Fig. 2.20, for which the decision frequency rises from top to bottom. It is divided into a top part, comprising offline long-term economically driven decision making on corporate planning and scheduling. Infrequently, the *Scheduling and Time Planning* layer provides updated target production specifications and quality constraints stemming from MILP or MINLP optimizations (L. Biegler et al.,

2009). These are then used in the online, bottom part of the automation hierarchy.
Using online plant data, the *Supervisory Online Optimization* layer approximates the steady-state of the plant (plant-model mismatch reduction) and calculates new optimal steady-state conditions or operation trajectories. The transition towards this new optimal operation point can be handled on a time-discrete optimal trajectory using **M**odel **P**redictive **C**ontrol (MPC) (Darby et al., 2011). The **D**istributed **C**ontrol **S**ystem (DCS) encompasses the regulatory control, usually applying PID controllers and performing control actions every second.
However, this control structure poses several drawbacks, such as infeasible trajectories since the steady-state nonlinear RTO neglects the transition of steady states or instabilities due to the mismatch of RTO and MPC models. This is especially severe for highly dynamic nonlinear processes, which are never at a steady-state (Toumi et al., 2005; Zavala, 2008). Consequently, the dynamic model is to be implemented into the optimization process itself. Thus RTO and MPC are merged into one **D**ynamic-RTO layer. A variety of developments on that can be found, whose feasibility is further enhanced through recent developments on algorithms for the efficient solution of large-scale NLP problems (L. T. Biegler, 2018). Recent applications include nonlinear model predictive control for a two-stage distillation sequence (L. Biegler et al., 2015) or adsorption chillers (Bau et al., 2019), economic NMPC's evaluated in a review by Wolf et al. (2016) or applied on air separation units (Caspari et al., 2018), and dynamic real-time optimization applied on polymerization reactions (Pontes et al., 2015).

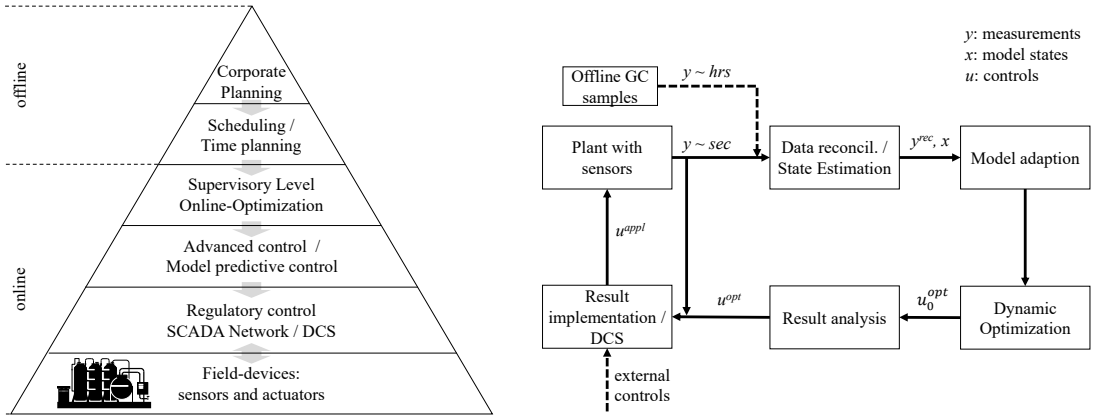

Fig. 2.20: Left: Real-time decision making and process automation hierarchy. Figure redrawn and extended from (L. Biegler et al., 2009). Right: Control loop for dynamic real-time optimization.

A typical control loop for D-RTO is depicted on the right in Fig. 2.20. Core elements are the process itself, including sensors and actuators, as well as a connected DCS handling the regulatory control of this plant relying on measurement data y. This data is subdivided into available online sensor data and slow measurements, such as quality sampling from offline analytical methods. The measurements are then validated to avoid the implementation of faulty data, like gross error

or noise. This is usually included into a state estimation step, which aims for the calculation of a valid model state for a given future time according to the given measurements. This step is of utmost importance, since these calculated model states x serve as the initial conditions for subsequent optimization tasks and naturally not all model states x are measured. Based on this, a model adaption through parameter refitting is often placed prior to the optimization to handle plant-model mismatch (C. Y. Chen et al., 1987; Faber et al., 2007). More sophisticated approaches, such as the *modifier adaption with quadratic approximation* assume also structurally imperfect plant models. The plant-model mismatch is then handled by iteratively adding bias and gradient corrections to the objective function and constraints of the model to match it to the plant state (Ahmad et al., 2019).
The standard approach, however, considers the calculation of an optimal trajectory i.e. controller setpoints u_0^{opt} for a given plant model and adhering to an economic cost function as well as constraints. The optimization problem therein is usually formulated as an **N**on**L**inear **P**rogramming (NLP) problem deploying a time-discretized plant model:

Definition 2.1 (Optimization problem formulation for NLP's):

$$\arg\min_{u} \quad f(x,u,P) \tag{2.11}$$
$$s.t. \quad g(x,u,P) = 0 \tag{2.12}$$
$$h(x,u,P) \leq 0 \tag{2.13}$$
$$x_{LB} \leq x \leq x_{UB} \tag{2.14}$$
$$u_{LB} \leq u \leq u_{UB} \tag{2.15}$$

Here, $x \in \mathbb{R}^{n_x}$ is the vector of model states, $u \in \mathbb{R}^{n_u}$ the vector of decisions or controls, and $P \in \mathbb{R}^{n_P}$ (fixed) model parameters. $f : \mathbb{R}^{n_x+n_u+n_P} \to \mathbb{R}$ the objective function, $g : \mathbb{R}^{n_x+n_u+n_P} \to \mathbb{R}^{n_{eq}}$ the n_{eq} vectorial function containing equality constraints, and $h : \mathbb{R}^{n_x+n_u+n_P} \to \mathbb{R}^{n_{ineq}}$ the inequality constraints. Additionally, x and u adhere to specified lower and upper bounds.

Obtained results $u(t_k)$ from this optimization problem are checked regarding consistency and applicability, yielding $u^{opt}(t_k)$. The latter are then handed forward to the DCS, which implements these optimal trajectories into the process. It has to be remarked, that for online applicability the availability of optimal trajectories must be ensured at any time. Therefore, parallel time-wise shifted instances of the **D-RTO** loop are usually employed, or a backup offline optimal trajectory (*external controls*) is provided.

2.5.2 State Estimation

In the previous section, the necessity of estimating unmeasured or correcting measured states of a plant model from actual plant measurement data was outlined. To tackle this, several strategies for state estimation, also called observers have been developed to efficiently track these missing states and overcome technical measurability limitations or reduce costs for sensor installation (Dochain et al., 2009). For the sake of completeness, the reader is referred to Ali et al. (2015), who provide an extensive review and classification scheme of recent observer implementations. Following this classification and based on our own work regarding the application of state estimation methods on novel surfactant-based multiphase reaction media (Weigert et al., 2018), the focus is laid on *Bayesian Estimators*. This is mainly due to their applicability on nonlinear dynamic systems and handling of constraints (Ji et al., 2015).

Bayesian State Estimation

These methods are mainly based on the estimation of the probability density function of model states based on available measurement data and are naturally derived from stochastic considerations. The general state estimation problem is described by the time-discrete dynamic system

$$x_{k+1} = F(x_k,u_k) + w_k \qquad \text{with } w \sim \mathcal{N}(0,Q) \tag{2.16}$$

$$y_k = h(x_k + v_k) \qquad \text{with } v \sim \mathcal{N}(0,R) \tag{2.17}$$

for which x are the model states at time point t_k, u system controls, and y the measured variables. F then is the discretized model and h the time-invariant part of the model, holding correlations of y with model states. w and v then represent the independent random process and measurement noise with respective covariance matrices Q and R (López-Negrete et al., 2012).
Bayesian estimators now aim at determining the estimate of the state trajectory X_{k-N}^k on the time horizon from current time point k till N past steps under the condition that for $t_0 \dots t_k$ measurements Y_0^k occurred. Thus, an optimization problem is set up, maximizing the conditional probability $P(X_{k-N}^k|Y_0^k)$ through manipulating states x_k:

$$\max_{x_{k-N},\dots,x_k} P(X_{k-N}^k|Y_0^k) \tag{2.18}$$

$$X_{k-N}^k = \{x_{k-N},\dots,x_k\} \tag{2.19}$$

$$Y_0^k = \{y_0,\dots,y_k\} \tag{2.20}$$

Including the entire available measurement data time horizon into the optimization problem would result in extremely large equation systems and is thus infeasible. To overcome this hurdle,

generally two approaches are considered (Rawlings et al., 2006): firstly recursive predictor-corrector methods, such as *extended Kalman Filter*, *unscented Kalman Filter*, or *sequential Monte Carlo Filters* and secondly NLP formulations on larger but finite time horizons considering the last N measurements, the so called **M**oving **H**orizon **E**stimators (MHEs).

Unlike the filtering methods, the MHE provides a more generic approach towards state estimation and does not rely on simplifications. It is thus applicable for any nonlinear process (Küpper et al., 2009). It provides robust convergence features, also under erroneous a-priori distributions of measurements or states and additionally allows for the handling of constraints on state variables (Nicholson et al., 2014). Moreover, it enables the handling of different sampling rates and/or delays of measurements, which is a very common case for chemical processes (Krämer et al., 2005; Ji et al., 2015). In contrast, mentioned filtering methods severely rely on accurate estimates of the process noise and the respective covariance matrix Q (Weigert et al., 2018). Gathering Q for a technical plant system, a non-exact model, and limited prior measurement data is considered challenging. Following the discussion in our own contribution (Weigert et al., 2018), MHE is hence regarded as superior concerning the desired application on the hydroformylation in microemulsion and further looked at in detail.

Moving Horizon Estimator Formulation

As already stated above, the moving horizon state estimator only considers model states and measurements in a predefined past time interval. The actual formulation of the estimator is performed based on the following statistical assumptions (Z. Chen, 2003; W. Chen et al., 2004):

- All states x adhere to a first order Markov process. Thus the next state x_k can be predicted by only knowing the last state x_{k-1}.
- Noise of measurements are independent from those of the states.
- Measurements are mutually independent. In practice this might be violated because of e,.g., hysteresis effects.
- All noise variables have zero mean and are assumed Gaussian, as defined in Eq. (2.16)-2.17. This is practically not always ensured, since baseline-offsets of sensors might appear as well as hanging sensors or measurement range violations.

Considering the problem statement from Eq. (2.18), the conditional probability density function $P(X_{k-N}^k|Y_0^k)$ can be rewritten applying Bayes theorem:

$$P(X_{k-N}^k|Y_0^k) = \frac{P(Y_0^k|X_{k-N}^k) \cdot P(X_{k-N}^k)}{P(Y_0^k)} \tag{2.21}$$

Based on this, the optimization problem in Eq. (2.18) can be further developed towards the *smoothed arrival cost* objective function formulation of the MHE (Rao et al., 2000):

Definition 2.2 (NLP Moving Horizon Estimation):

$$\{\hat{x}_{k-N},\ldots,\hat{x}_k\} = \arg\min_{\{x_{k-N},\ldots,x_k\}} \left(\phi(k-N) + \frac{1}{2}\sum_{i=k-N}^{i=k} v_i^T R_i^{-1} v_i + \frac{1}{2}\sum_{i=k-N}^{i=k} w_i^T Q_i^{-1} w_i \right) \quad (2.22)$$

$$s.t. \quad x_{i+1} = F(x_i,u_i) + w_i \quad (2.23)$$

$$y_i = h(x_i) + v_i \quad (2.24)$$

$$x^{LB} \leq x \leq x^{UB} \quad (2.25)$$

Therein, $\hat{x}$ is the optimal state vector at a specific discretization point, for which inequality constraints regarding x^{LB} and x^{UB} apply. v and w are the Gaussian measurement and process noises with their respective covariance matrices R and Q. f_{est} described a correlation or estimator function, evaluating and weighting the deviation of model and measurement variables y. Finally, F is the respective process model and h the measurement model.

In Def. 2.2, $\phi(k-N)$ describes the *arrival cost*, which represent a corrector based on the influence of past measurements prior to the current horizon. This becomes important for state estimations on short horizons for which the information content of measurement is insufficient to obtain adequate results. In contrast, the influence of $\phi(k-N)$ becomes negligible with growing estimation time horizon (López-Negrete et al., 2011). Statistically it represents the conditional probability of gaining x at time step $k-N$ under the condition, that all prior measurement data Y_0^{k-N-1} occurred. This probability is not accessible from scratch and thus several techniques have been developed to approximate the arrival cost. Often enough filtering techniques based on the extended Kalman filter or sequential Monte Carlo filter are deployed, which are again disadvantageous regarding unconstrained states and necessarily accurate estimates of Q (Rawlings et al., 2006; López-Negrete et al., 2011). Further developments thus approximate the arrival costs using the inverse of the reduced Hessian of the NLP Lagrange from prior estimations (López-Negrete et al., 2012).

Data Reconciliation and Handling of Gross Errors

Measurement data in chemical plants are often erroneous and inconsistent with respect to the plant model and conservation equations therein. In contrast to the assumptions made for deriving the MHE, these deviations or noises can also be non-Gaussian. This is true, if systematic errors or offsets, sensor failure, and introduced gross error due to wrongly prepared offline quality

samples are considered (Zhang et al., 2015). Handling of these is crucial, since otherwise the state estimation result deviates significantly from the true state and the subsequent D-RTO might yield infeasible results, leading to violated safety restrictions or infeasible process operation.
To overcome this hurdle, data reconciliation strategies have been proposed and developed towards application on dynamic nonlinear systems (Özyurt et al., 2004). Therein, estimators f_{est} are used for weighting the measurement deviation v between real data and the model $v = y - \hat{y}$, deployed in a minimizing optimization problem. A widely applied class are Maximum-Likelihood-Estimators. For those, M-estimators, such as Fair-Function and Redescending-Estimator provide a large robustness regarding gross errors (Nicholson et al., 2014). At this point, it is proposed to directly implement these estimators into the Bayesian MHE to enable the direct reconciliation of data within the state estimation step, without further handling in an external data reconciliation loop. Related to Def. 2.2 this implies the following substitution:

$$\sum_{i=k-N}^{i=k} v_i^T R_i^{-1} v_i = \sum_{i=k-N}^{i=k} f_{est}(v_i) \tag{2.26}$$

This approach has been largely tested in our own prior work, using artificial data from an early model implementation of the hydroformylation of 1-dodecene in microemulsions (Hoffmann et al., 2016). Concluding, a comparison of estimators relevant for this work, their definitions, and remarks regarding their implementation is given:

Definition 2.3 (Fair-Function): The Fair-Function as defined by (Özyurt et al., 2004) is a convex Hubert-estimator and thus provides continuous first and second order derivatives. The parameter C is used for tuning and is set to 6 in accordance with (Nicholson et al., 2014).

$$f_{FF} = C_{FF}^2 \left[\frac{|\frac{v}{\sigma}|}{C_{FF}} - \ln\left(1 + \frac{|\frac{v}{\sigma}|}{C_{FF}}\right) \right] \tag{2.27}$$

Definition 2.4 (Redescending-Estimator): The redescending-estimator was proposed by Hampel (1974) and enables an efficient cut-off of the estimator function value on rising measurement deviations v. However, its standard implementation is non-convex and thus a smoothed formulation is given below. Parameters a_{RE}, b_{RE}, and c_{RE} are deployed to adjust intervals of quadratic, linear or constant behavior of the estimator.

$$f_{RE} = \begin{cases} \frac{1}{2}\left(\frac{v}{\sigma}\right)^2, & 0 \leq |\frac{v}{\sigma}| \leq a_{RE} \\ a_{RE} \cdot |\frac{v}{\sigma}| - \frac{a_{RE}^2}{2}, & a_{RE} < |\frac{v}{\sigma}| \leq b_{RE} \\ a_{RE} \cdot b_{RE} - \frac{a_{RE}^2}{2} + \frac{a_{RE} \cdot (c_{RE} - b_{RE})}{2}\left[1 - \left(\frac{c_{RE} - |\frac{v}{\sigma}|}{c_{RE} - b_{RE}}\right)^2\right], & b_{RE} < |\frac{v}{\sigma}| \leq b_{RE} \\ a_{RE} \cdot b_{RE} - \frac{a_{RE}^2}{2} + a_{RE} \cdot \frac{(c_{RE} - b_{RE})}{2}, & |\frac{v}{\sigma}| > c_{RE} \end{cases} \tag{2.28}$$

Smoothed resdescending-estimator:

$$f_{RE,g} = -c_1\left(1 - \frac{2}{1 + exp\left(-2 \cdot \kappa_1\left(\frac{v}{\sigma}\right)^2\right)}\right) - c_2\left(1 - \frac{2}{1 + exp\left(-2 \cdot \kappa_2\left(\frac{v}{\sigma}\right)^2\right)}\right) \tag{2.29}$$

Approximation parameters c_1,c_2, κ_1, and κ_2 are to be adjusted in parameter estimation according to Eq. (2.28) and using tuning parameters a_{RE}, b_{RE}, and c_{RE} therein.

In Fig. 2.21 a comparison of these robust estimators to the well known weighted least-squares estimator is given. It is apparent, that both, Fair-Function and Redescending-Estimator are superior, since the occurrence of gross errors (large values of v) only has reduced influence

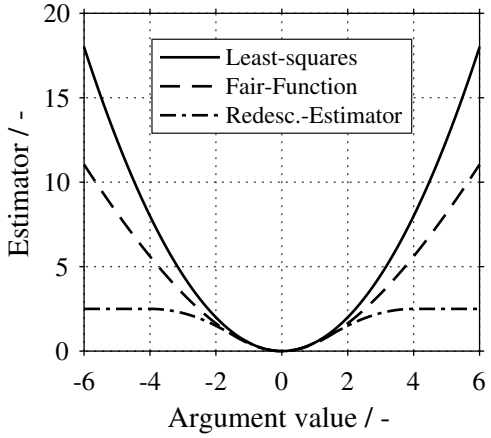

Fig. 2.21: Comparison of least-squares, Fair-Function, and Redescending-Estimator. Used parameters: $C_{FF} = 6$, $a_{RE} = 1$,$b_{RE} = 2$, $c_{RE} = 4$.

on the estimators. However, due to the non-convexity of the Redescending-Estimator and thus also of deployed objective functions, convergence into local minima is possible. Hence, for this thesis the Redescending-Estimator is used together with an initialization run based on the Fair-Function as convex estimator.

State Estimation on Multiple Sampling Frequencies

To this end, presented state estimators depend on the availability of all necessary measurements to calculate respective probability density functions. For online application of state estimation, this is true for measurements, such as temperature or pressure, which are available every, e.g., second. In contrast, concentration data is usually only infrequently available. Moreover these measurements are delayed due to sampling and analysis time. Ideally, the fast measurements are still sufficient to observe or estimate the state vector and the moving horizon estimator might be applied as is. In case of a high relevance of slow and delayed measurements, state estimation is to be adapted towards the handling of multi-rate measurements (López-Negrete et al., 2012).

Connected to this, the measurability of a system, also named observability, is of interest:

Definition 2.5 (Measurability): The system defined by Eq. (2.16)-2.17 is measurable if it is possible for all $t \in [0,t_{end}]$ to derive the initial conditions of the system x_0 for any initial point solely from the available measurements $y(t)$ and control variables $u(t)$ (Salau et al., 2014).

Focusing on MHEs, successful implementations for state estimation using multi-rate measurements can be separated into two major approaches: fixed structure and variable structure estimators. The former use slow measurements only on availability and otherwise perform mostly linear or polynomial extrapolation of the measurement noise for the slow measurements (Tatiraju et al., 1999; Kramer et al., 2005). However, this is disadvantageous regarding high nonlinear and dynamic systems or significant measurability improvement of the model states through the slow measurements. For the latter, López-Negrete et al. (2012) provide an implementation with a variable structure of the measurement model, depending on the availability of slow measurements and subsequent (also variable) arrival cost formulations.

However, all implementations and case studies still assume a moderate ratio of sampling rates between 1:10 and 1:100. Practical applications on real plant systems, as presented also in this work nevertheless hold ratios of sampling rates of more than 1:10000. To cope with this, weighting of the objective function elements or even sequential two-step estimation approaches are to be considered.

3 Systematic Analysis of Reactive Multiphase Systems – Hydroformylation of 1-dodecene in Microemulsions

Due to the complexity of reactive microemulsion systems,like introduced in Sec. 1.1, the derivation of a suitable process or unit design, as well as strategies for process operation is still challenging. Usually, a multitude of investigations and iterations in development stages between lab-scale and a mini-plant test system are required. Within the scope of this work, the obstacles for the realization of such processes are faced with a systematic analysis of the system and its operability (Fig. 2.1). This encompasses not only the liquid multiphase system and the hydroformylation reaction, but also interactions of both and the application in a continuously operated mini-plant. Aiming for such a technical application, Fig. 1.2 already showed the desired scheme of the process design. It combines the realization of the reaction in a reactor unit, as well as a subsequent multiphasic separation in a settler. Both unit operations are characterized by high operational complexity. This is further increased by multiple internal recycles, which are mandatory for the efficient reuse of catalysts and additives.

To cope with this, a systematic influence identification for the catalytic system and the reaction kinetics is performed based on Fig. 2.18 and under consideration of the technical realization and resulting obstacles. In the following, the guideline for the systematic analysis of multiphase media for process operation, presented in Sec. 2.3.2 is applied on the system at hand. The obtained results form the cornerstone for subsequent modifications on the process design and the derivation of strategies for process operation .

3.1 Applied Substances

Chemical substances used within this work are listed in Tab. 3.1 together with information on purity and vendors. The microemulsion system hereby is formed with 1-dodecene as long-chained oily substrate, the nonionic surfactant Marlipal® 24/70, and an aqueous catalyst solution consisting of water, rhodium precursor, and SulfoXantPhos as a ligand.

Tab. 3.1: Applied substances for plant operation, lab experiments, and analytics.

Substance	Purity	CAS-Number	Supplier
1-dodecene	$\geq 94\,\%$	112-41-4	Merck KGaA
2-propanol	$\geq 99.9\,\%$	67-63-0	Carl Roth
Dodecane	$\geq 99\,\%$	112-40-3	Merck KGaA
Marlipal® 24/70	-	68439-50-9	Sasol[1]
Nitrogen	$\geq 99.8\,\%$	7727-37-9	Linde
$[Rh(acac)(CO)_2]$[2]	$\geq 98\,\%$	14874-82-9	Umicore
Sodium sulfate	$\geq 99\,\%$	7757-82-6	Carl Roth
SulfoXantPhos	-[3]	215792-51-1	Molisa GmbH
Synthesis gas	CO 3.7	630-08-0	Linde
($CO:H_2$ 1 : 1 mol %)	H_2 5.0	1333-74-0	Linde
Tridecanal	$\geq 96\,\%$[4]	10486-19-8	Alfa Aesar
Tridecanoic acid	$\geq 99\,\%$	638-53-9	Sigma Aldrich
Water	deionized, degassed	7732-18-5	-

[1] nonionic aliphatic surfactant provided as a donation from Sasol without further information on purity (technical grade)

[2] Rhodium precursor (Acetylacetonato)dicarbonylrhodium(I) donated by Umicore

[3] purchased from Molisa GmbH without further information on batch quality

[4] contains stabilizer α-tocopherol

3.2 Hydroformylation Reaction Network

Within this work, the C12-alkene 1-dodecene is used as a model substance to investigate the hydroformylation of long-chained unsaturated substrates in MESs. The conversion of 1-dodecene in the presence of synthesis gas and a transition metal catalyst yields the target tridecanal as the target product and several byproducts, such as isomers, aldols, alcohols, and hydrogenation

products (Pruett, 1979). Thus, the knowledge of the underlying reaction network, reaction kinetics, and especially relevant parameters influencing the overall reaction performance is vital. Extensive studies on the reaction network have been performed for the system at hand. Markert et al. (2013) identified the reaction network shown in Fig. 3.1 consisting of six main reactions:

Target Reaction

r_{HyfoB} Hydroformylation of 1-dodecene towards target product tridecanal

Side Reactions

r_{iso} Isomerization of 1-dodecene (equilibrium reaction)
r_{HydA} Hydrogenation of iso-dodecene and formation of dodecane
r_{HydB} Hydrogenation of 1-dodecene and formation of dodecane
r_{HyfoA} Hydroformylation of 1-dodecene towards byproduct iso-tridecanal
r_{HyfoC} Hydroformylation of iso-dodecene towards byproduct iso-tridecanal

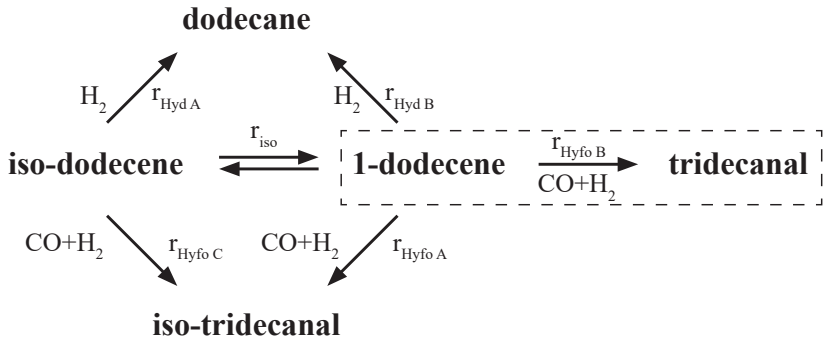

Fig. 3.1: Hydroformylation reaction network with isomerization, hydrogenation, and hydroformylation reaction paths postulated by (Markert et al., 2013). Figure taken from (Pogrzeba et al., 2019).

Caused by the side reactions, a variety of internal alkenes and branched aldehydes can theoretically be formed. However, for long-chained alkenes, hydroformylation reaction rates significantly drop for internal alkenes (Wender et al., 1956). In this case, iso-tridecanal is considered as a pseudo-component mainly represented by 2-methyldodecanal for the remainder of this thesis. Accordingly, iso-dodecene is introduced as a pseudo component for all internal C12-alkenes.

Optimal Reaction System and Reference Kinetic Trajectory from Lab-Scale

Several prescreening experiments regarding the formulation of the microemulsion and optimal conditions for the hydroformylation of 1-dodecene have been carried out (Rost et al., 2013; Hamerla, 2014; Pogrzeba et al., 2015). Here, the nonionic aliphatic surfactant Marlipal® 24/70 was found to be a suitable emulsifier for 1-dodecene in an aqueous catalyst system. The water

solubility of the rhodium catalyst [[Rh(acac)$(CO)_2$]] is achieved by using the sulfonated diphosphine ligand SulfoXantPhos (see Fig. 2.10). For such a system, the typical reaction trajectory for experimentally optimized conditions is given in Fig. 3.2. The reaction performance is characterized by a very high chemo-selectivity of up to 94 % towards tridecanal and linear to branched (n/iso) selectivities above 98 %. Within 48 h of reaction, only small amounts of byproducts are formed with the isomerization being dominant among them.

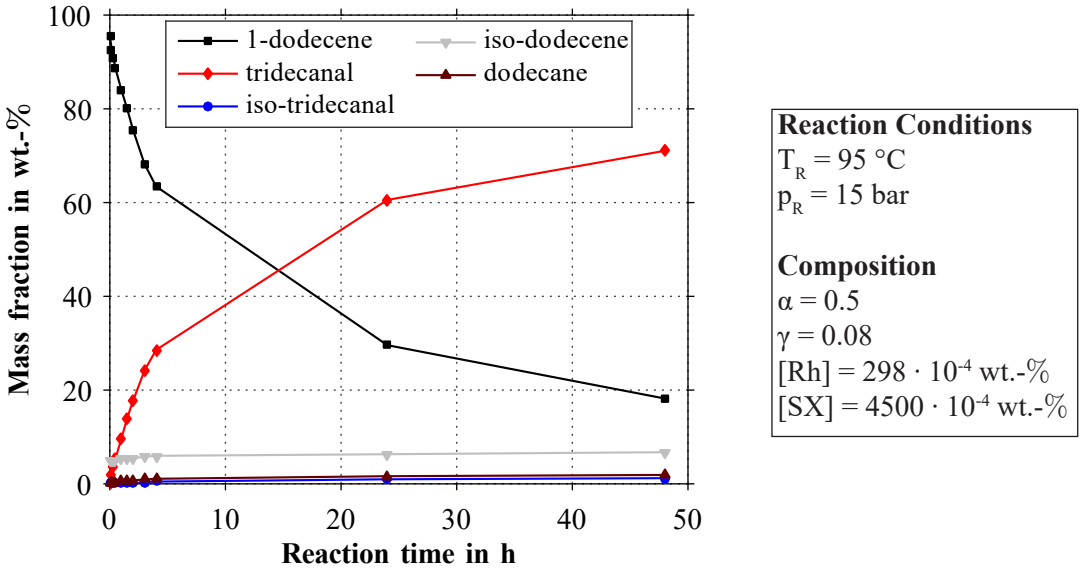

Fig. 3.2: Reference kinetic trajectory from the lab-scale for the hydroformylation of 1-dodecene. Experimental conditions: SX:Rh ratio = 4:1 with [Rh(acac)$(CO)_2$] $= 1 \cdot 10^{-3}$ mol L^{-1}, 2.4 mol L^{-1} 1-dodecene, 20 g water, 3.5 g Marlipal® 24/70, 1 wt.-% Na_2SO_4, reaction volume = 50 mL, stirrer speed = 1200 rpm. Maximum measurement error: ±3 %. Data generated by Tobias Pogrzeba, Technische Universität Berlin, Department of Chemistry.

3.3 Analysis of Influencing Factors on Reaction Performance in the Mini-Plant

For the transfer of the hydroformylation reaction from the lab-scale into the mini-plant (introduced in Sec. 4.1), several influences on the reaction performance are of interest. Exemplarily, the concentration of the surfactant is prone to vary in the reactor of a mini-plant with internal recycles. Hence, additional variations of concentrations or completely new influences have to be considered and evaluated. This way, tailored improvements of unit design and additional development of kinetic models focusing on the reaction performance in the mini-plant are enabled.

Such an analysis has been carried out on the system at hand using a close feedback of lab-scale investigations and pretesting in a mini-plant system. Initially, influencing factors with their direct impact on the reaction or catalytic system have been identified via a comparison of the reaction conditions in the used laboratory scale setup (see (Pogrzeba et al., 2017b)) and the mini-plant system, as well as several mini-plant test runs. The subsequent quantification was then performed on the lab-scale to ensure reproducibility.
To guide the following discussion of results, Tab. 3.3 is introduced. Note, that the presented experimental data in the remainder of this section were obtained in cooperation with Tobias Pogrzeba, Technische Universität Berlin, Department of Chemistry and are partly already published in our own contributions (Pogrzeba et al., 2017b; Pogrzeba et al., 2019).

Tab. 3.3: Additional identified influencing factors on reaction performance for the mini-plant system.

Influencing factor	**Influenced by**	**Effect reaction performance**	**Reference**
Rhodium concentration	feed, separation and recycle operation	available active catalyst and equilibria; reaction rates and selectivity	Figure 2.11 Figure A.1
Ligand concentration	feed, separation and recycle operation, decomposition	cat. species equilibria; reaction activity and selectivity	Figure 2.11 Figure 3.3
Dissolved gasses	system pressure, phase composition in reactor and settler	cat. species equilibria; reaction activity and selectivity	Figure 2.11 Figure 3.4
Micelle structure, phase behavior	mixture composition, temperature	none observed	Figure 3.5
Emulsification, interfacial area	stirrer speed	none in operation region	Figure A.2
Surfactant concentration	feed, separation and recycle operation, loss product stream	reaction rates	Figure 3.6

Catalyst and Ligand Concentration

First of all, the effect of the catalyst concentration is discussed. Interestingly, the catalyst activity is highest for low catalyst concentrations (diagram in Fig. A.1). However, the selectivity towards the main product tridecanal is also low and only stabilizes at higher catalyst concentrations above $2.5 \cdot 10^{-4}\,\mathrm{mol\,L^{-1}}$. A similar behavior is found in Fig. 3.3 regarding reaction conversion and selectivity for different ligand concentrations. As stated by Pogrzeba et al. (2019), "this reaction behavior is due to the two preequilibria of the active Rh-sulfoxantphos complex (Fig. 2.11, species 1a) with the corresponding dimeric Rh species (1c) and the unmodified Rh species (1b)". Especially low ligand concentrations in the presence of CO are prone to promote the formation of the inselective species (1b), featuring higher conversion but also increased formation of byproducts (Börner et al., 2016, p. 18). This is to be considered for mini-plant operations, as concentration shifts can severely alter the reaction performance.

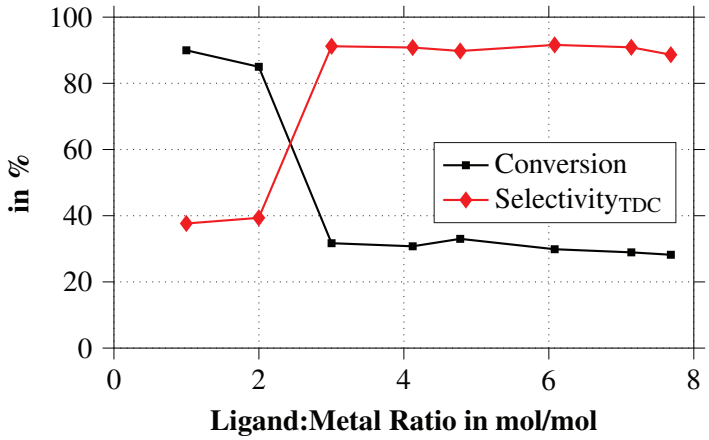

Fig. 3.3: Influence of ligand concentration on conversion and chemo selectivity towards the target product tridecanal for the hydroformylation of 1-dodecene. Experimental conditions: $[Rh(acac)(CO)_2] = 1 \cdot 10^{-3}\,\mathrm{mol\,L^{-1}}$, $2.4\,\mathrm{mol\,L^{-1}}$ 1-dodecene, 20 g water, 3.5 g Marlipal® 24/70, ($\alpha = 0.50$, $\gamma = 0.08$), 1 wt.-% Na_2SO_4, reaction volume = 50 mL. $p_R = 15$ bar syngas, $T_R = 95\,^{\circ}\mathrm{C}$, stirrer speed = 1200 rpm, duration: 4 h. Maximum measurement error: $\pm 3\,\%$.

Also, ligand degradation can occur during long-term operation. This was recently investigated by Gerlach et al. (2017) for the diphosphite ligand BiPhePhos in thermomorphic solvent systems. In their case, hydroperoxides were present in the substrate feed causing oxidation of the ligand. Despite the fact that high hydroperoxide amounts were found in 1-dodecene provided by Merck KGaA, this decomposition path was not observed in lab-scale experiments and is considered not to be relevant. Possibly, a stabilization of the ligand in the aqueous phase takes place in the case of the MES.

Concentration of Dissolved Gasses

Carbon monoxide plays an important role in catalytic equilibria and the formation of inselective unmodified Rh species, as described in Sec. 2.2. For a continuously operated mini-plant, concentrations of dissolved gasses are assumed to be constant for the reactor. However, when the mixture enters the settler, multiple phases are developed. Due to the creeping flow of phases, gas replenishing is limited to diffusion from the bulk gas phase through all liquid phases. Related to this, Fig. 3.4 depicts the comparison of kinetic experiments. For these, the stirrer was stopped for a specific time to mimic the situation of mixture separation in a settler and subsequent reentering into the reaction zone of the mini-plant (stirrer restart). It is obvious that for long resting times (2 h) chemo-selectivity significantly drops and large amounts of iso-dodecene are formed. Interestingly, conversion increases by 22 percentage points, even for the separated system.

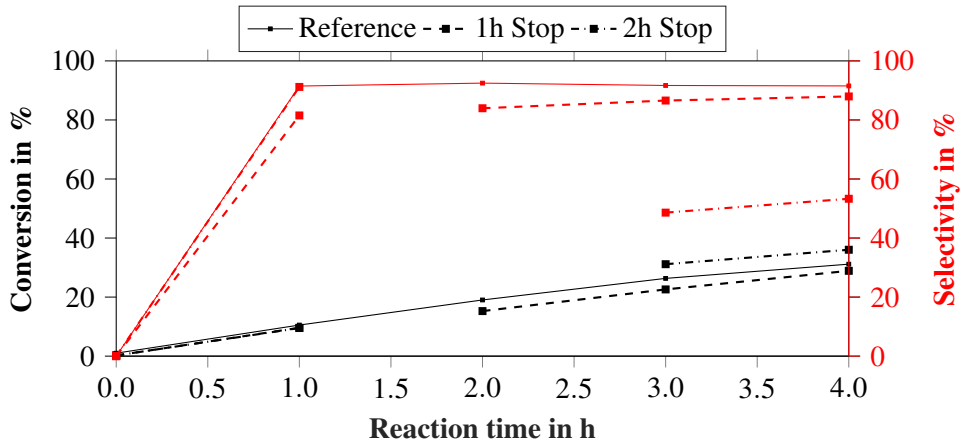

Fig. 3.4: Influence of stopped stirrer operation on conversion and chemo-selectivity towards the target product tridecanal for the hydroformylation of 1-dodecene. Experimental conditions: $[Rh(acac)(CO)_2] = 1 \cdot 10^{-3}\,mol\,L^{-1}$, molar ratio SX:Rh 4:1, $2.4\,mol\,L^{-1}$ 1-dodecene, 20 g water, 3.5 g Marlipal® 24/70, ($\alpha = 0.50$, $\gamma = 0.08$), 1 wt.-% Na_2SO_4, volume = 50 mL. $p_R = 15$ bar syngas, $T_R = 95\,^{\circ}C$, stirrer speed = 1200 rpm. Maximum measurement error: $\pm 3\,\%$.

With an immobile stirrer, phase separation takes place forming the $\overline{2}$-system at high temperatures (Sec. 2.1). Hence, larger amounts of catalyst are carried into the oil phase due to the surfactant being located there. With carbon monoxide solubility being rather high in the oil phase (see gas solubility data in Sec. 4.3.5) and the ligand being water soluble, the local concentrations thus promote the presence of the unmodified Rh species (species 1b in Fig. 2.11). This results in increased non-selective alkene conversion despite possible limitations of mass transfer. However this effect does not set in immediately and is due to ongoing reaction in the oil phase or at the interface. For a one hour-long stirrer stop only negligible changes in selectivity and conversion were observed. Accordingly, the residence time in the separation and recycle section of a continuously operated mini-plant should be kept as low as possible.

Micelle Structure, Phase Behavior, and Emulsification

For MESs a variety of phase states are possible (Fig. 2.4). Apart from that, structure and size of micelles as well as the types of continuous and disperse phases change dramatically. Nevertheless, the reaction performance is not affected by this for the system at hand. Figure 3.5 confirms that with a comparison of reaction kinetics at equal conditions, but modified emulsion type. According to Pogrzeba et al. (2017b), "the hydroformylation in the water-in-oil (w/o) emulsion is slightly slower due to the higher amount of salt in the mixture". In addition to that, Fig. A.2 depicts the effect of the stirrer speed on the reaction trajectory. Again no significant influence is observable. In both cases the feature of MES to form nano-scaled droplets due to the low interfacial tensions is beneficial. Sufficiently high interfacial area even at low energy input into the system is thus provided. In consequence, it can be stated, that the hydroformylation in MES is not limited by mass transfer.

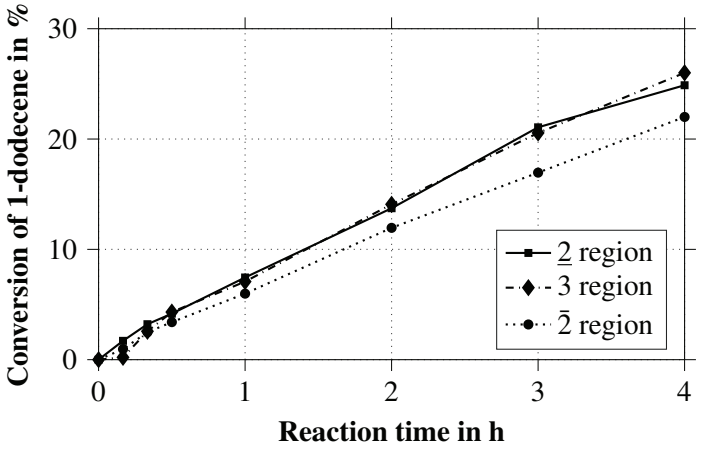

Fig. 3.5: Influence of phase behavior on conversion of 1-dodecene. Experimental conditions: $[Rh(acac)(CO)_2] = 1 \cdot 10^{-3}\,mol\,L^{-1}$, molar ratio SX:Rh 4:1, $2.4\,mol\,L^{-1}$ 1-dodecene, 20 g water, 3.5 g Marlipal® 24/70, ($\alpha = 0.50$, $\gamma = 0.08$), 1 wt.-% Na_2SO_4, reaction volume = 50 mL. $p_R = 15\,bar$ syngas, $T_R = 95\,°C$, stirrer speed = 1200 rpm, duration: 4 h. Na_2SO_4 added to adjust phase behavior: $\underline{2}$: 0.1 wt.-%, 3: 1 wt.-%, $\overline{2}$: 3 wt.-%. Max. measurement error: $\pm 3\,\%$.

Surfactant Concentration

The last finding only holds, in case sufficient emulsifier is present to enable ME formation. Naturally, the amount of surfactant has a crucial effect on the reaction, as can be seen in Fig. 3.6. The amount of surfactant determines the amount of aqueous and oily phase, emulsified by the microemulsion (lowering their mutual interfacial tension). Thus, the conversion increases rapidly with rising γ. In contrast, the selectivity is constantly above 90 %. For tracking and predicting the reaction performance in a mini-plant system, sensing and control of the surfactant concentration

is therefore mandatory. Additionally, a distinct upper limit for γ exists, since the formation of one homogeneous phase (Winsor I system, Fig. 2.5) at high surfactant concentrations prevents a successful phase separation and thus settler operation.

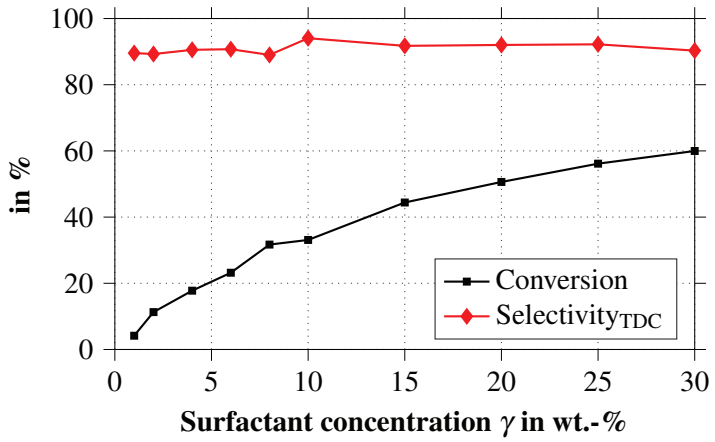

Fig. 3.6: Influence of surfactant concentration on conversion and chemo selectivity towards the target product tridecanal for the hydroformylation of 1-dodecene. Experimental conditions: $[Rh(acac)(CO)_2] = 1 \cdot 10^{-3}\,mol\,L^{-1}$, molar ratio SX:Rh 4:1, $2.4\,mol\,L^{-1}$ 1-dodecene, 20 g water, ($\alpha = 0.50$), 1 wt.-% Na_2SO_4, reaction volume = 50 mL. $p_R = 15\,bar$ syngas, $T_R = 95\,°C$, stirrer speed = 1200 rpm, duration: 4 h. Maximum measurement error: $\pm 3\,\%$.

3.4 Systematic Analysis of Microemulsion Systems for Process Design and Operation

The systematic guideline presented in Sec. 2.3.2 is now applied. Again, the focus lies on the actual application in the available mini-plant. Hence, relevant information on system phenomena and challenges is desired.

3.4.1 Step 1: Definition of System Requirements & Component System

Process Requirements for a Continuously Operated Mini-Plant

Initially, goals and requirements for the desired process operation are specified. Then, available information on technical equipment and dimensioning, as well as the applied substances is gathered.

- **Fast separation:** The residence time in a settler unit for phase separation must be below 60 min to avoid byproduct formation (see Fig. 3.4). It is set to 30 min.
- **Reaction performance and efficient separation of oil:** The MES formulation should enable efficient emulsification of 1-dodecene and the aqueous catalyst solution and thus high reaction rates (see Fig. 3.6). Reaction products need to be efficiently separated from the reaction mixture at low energy costs via phase separation (oil phase purity $\geq 95\,\%$).
- **Catalyst recovery:** The valuable Rh catalyst and ligand are to be efficiently recycled within the plant after phase separation (catalyst leaching into oil phase ≤ 1 ppm).
- **Throughput:** Settler design and residence time are to be specified to enable the processing of 1-dodecene feedrates of up to 760 g/h
- **Operability:** Stable phase separation is to be achieved also in the presence of disturbances. Concentration shifts and accumulations should be avoided (influence on reaction)

Limitations of Mini-Plant System

Phase separation enhancement by applying external magnetic or electric fields is not possible due to technical restrictions in the mini-plant. Online sensors of the plant encompass measurements of temperature, flow, pressure, and level in their respective ranges (Sec. 4.2). Offline analytics for liquid phase sampling is available via **G**as **C**hromatography (GC), but limited to oily reactants.

Component System

The regarded substances are mainly dictated by the reaction system and the given optimal formulation (Sec. 3.2). For the analysis of the phase separation behavior of the MES, also the formation of tridecanal and relevant byproducts has to be considered. For the latter, iso-dodecene is found to be dominant. Since its chemical structure is comparable to the terminal olefin, it is waived for the further discussion. The reaction network also comprises several catalytic species. These are considered as surface active molecules (nonpolar catalyst precursor linked to polar ligand or CO). Hence, catalyst activation and possible alterations are considered as factors influencing the behavior of the phase separation.

To simplify the discussion, quantitative statements on the mixture composition are given in the common indicators for MES from now on. According to Eq. (2.2) α hence denotes the oil to water ratio. Therein, oil comprises all organic reaction educts and products. Water is represented by the aqueous catalyst solution with a fixed composition according to the optimal reaction setpoint (98.96 wt.-% water, $6.48 \cdot 10^{-2}$ wt.-% [[Rh(acac)$(CO)_2$]], 0.98 wt.-% **S**ulfo**X**ant**P**hos

(SX)). The surfactant mass fraction is given by γ (Eq. (2.3)). Additionally, the reaction yield Y is used to denote the current content of tridecanal:

$$Y = \frac{m_{Tridecanal}}{m_{1-dodecene} + m_{Tridecanal} + m_{Byproducts}} = \frac{m_{Tridecanal}}{m_{Oil}} \tag{3.1}$$

3.4.2 Step 2: Influence Identification

Relevant influences on the separation behavior of the MES are now identified. This is based on theoretical considerations and literature review, outlined in Sec. 2.1:

1) Looking at Fig. 2.11, different surface active catalyst species act as **trace components** and are prone to affect the phase separation (dynamics) due to varying interfacial tensions or surfactant solubility (Sec. 2.1.3). Thus, the catalyst activation in the presence of synthesis gas should be investigated first.

2) In general, the influence of **pressure** on LLEs is found to be negligible. However, for a dynamic process application its influence on the separation dynamics is to be checked.

3) The separation dynamics depend on the distribution of droplet size of the stirred mixture. Thus the effect of **stirrer type and speed** are to be analyzed.

4) Following Sec. 2.1, **Concentrations** of water, catalyst, reactants, and surfactant directly affect phase equilibria and separation dynamics and should be investigated respectively.

5) **Temperature** is one of the most important state variables for multiphase systems. Also several physical properties hold a high dependency on temperature.

Ranges of interest for screening these influences are then listed in Tab. 3.4. They mostly depend on the expected operation conditions inside the mini-plant. A **Plant setpoint** is hence derived from the optimal reaction system in Fig. 3.2. Variations thereof are considered regarding mini-plant tests and preliminary experiments (Tab. 3.3, (Pogrzeba et al., 2016a)).

Tab. 3.4: Ranges of interest for influencing factors on phase separation behavior.

Influencing factor	Plant setpoint	Range of interest
Catalyst activation	activated	inactive / activated
Pressure	15 bar	[1,18] bar
Stirrer speed	1200 rpm	[800,1400] rpm
α	50 %	[40,60] %
γ	8 %	[6,10] %
Y	40 %	[0,40] %
T	-	[25,95] °C

3.4.3 Step 3: Prescreening of the System

The prescreening is performed with particular attention on the feasibility of the observed separation behavior regarding the process requirements. Information on used experimental setups and conditions can be found in Sec. A.2.

Prescreening Results

First of all, the catalyst activation is tested. Here, Fig. 3.7 reveals a complete impedance of the phase separation, in case syngas is applied. No separation is achieved in reasonable time for the given temperature range and a process application is not possible. The main reason for this phenomenon is the aforementioned surface activity of the activated catalyst. To cope with this, a lyotropic salt – sodium sulfate – is added to the system, whose ionic strength efficiently counteracts the emulsion stabilization due to the catalyst. This can be seen from experiments shown in red plots, for which sufficiently high oil levels are reached after short settling times.

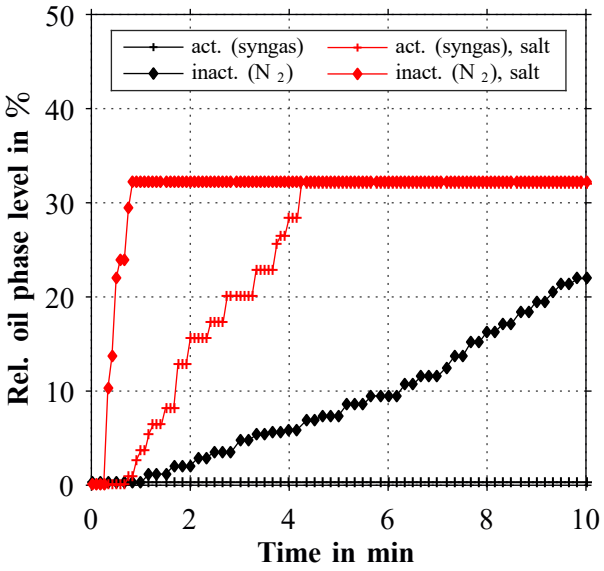

Fig. 3.7: Relative level of oil phase over time for different catalyst activation states in the unmodified system (black lines) and after addition of 1 wt.-% Na_2SO_4 (red lines). Test conditions for reference mixture ($\alpha = 0.50$, $\gamma = 0.08$): 85 °C, 3 bar for unmodified system. With Na_2SO_4 addition: 78 °C and 3 bar (N_2) and 8 bar (syngas).

Moreover, the overall separation dynamics are significantly increased due to salt addition and a steady state is reached in less than 4 minutes. For both catalyst states, the final level of the oil phase is equal (see also Fig. A.6 for an extended screening) and hence no significant influence of the catalyst activation state on the phase equilibrium is visible.

The influence of pressure is then also discussed regarding the experimental data in Fig. 3.7. Comparing the experiments with salt addition (red plots), a slightly slower separation is noticeable, while the equilibrium state remains unchanged. These impeded dynamics are mainly caused by the pressure increase of 5 bar for the activated case and cannot be not fully related to the influence of catalyst activation. Regarding a process application with a projected system pressure of 15 bar, this effect however is negligible and can easily be handled with an adequate residence time in a respective settler unit.
Finally, the influence of varying stirrer speeds on the phase separation dynamics and phase equilibria has been found to be minimal (Fig. 7 left in (D. Müller et al., 2015).

At this point, a salt concentration of 2.17 wt.-% in the aqueous phase (1 wt.-% in the total mixture with respect to $\alpha = 0.5$ and $\gamma = 0.08$) is defined and used for future investigations. Additionally, the effect of syngas, system pressure, and stirrer speed are neglected hereafter to simplify experimental setups.

Feasibility analysis

Starting from the optimal formulation of the reaction mixture and the defined process requirements, a feasible phase state after separation is to be identified – the operation region for phase separation. For this, Fig. 3.8 depicts observed separation states after 20 min of settling time and selected analytical data on oil phase purity via GC and catalyst distribution measured via **I**nductively **C**oupled **P**lasma (ICP). Furthermore, settling times depending on temperature are depicted in Fig. 3.9. With the supporting information on possible phase states of MES from Sec. 2.1 the observed phase equilibria and emulsion types are identified, leading to the following conclusions:

- Feasible oil phase volume fractions > 15 % are only present for the 3-phase region.
- In agreement with Fig. 2.8, applicable settling times are solely found for the three-phase region.
- For the transition between two-phase and three-phase regions, the formation of dense and highly viscous surfactant layers is observed alongside generally decelerated dynamics.
- Oil phase purity (amount of oily components in oil phase) is close to 100 % in the three-phase region, but slowly decreases with temperature due to increased surfactant solubility in the oil phase. Main impurity is the surfactant itself, while catalyst leaching into the oil phase is minimal (see also (Pogrzeba et al., 2015)).

Hence, the three-phase region, avoiding meta-stable peripheral zones, is identified as feasible operation region for the process at hand, dictating also the according separation unit design.

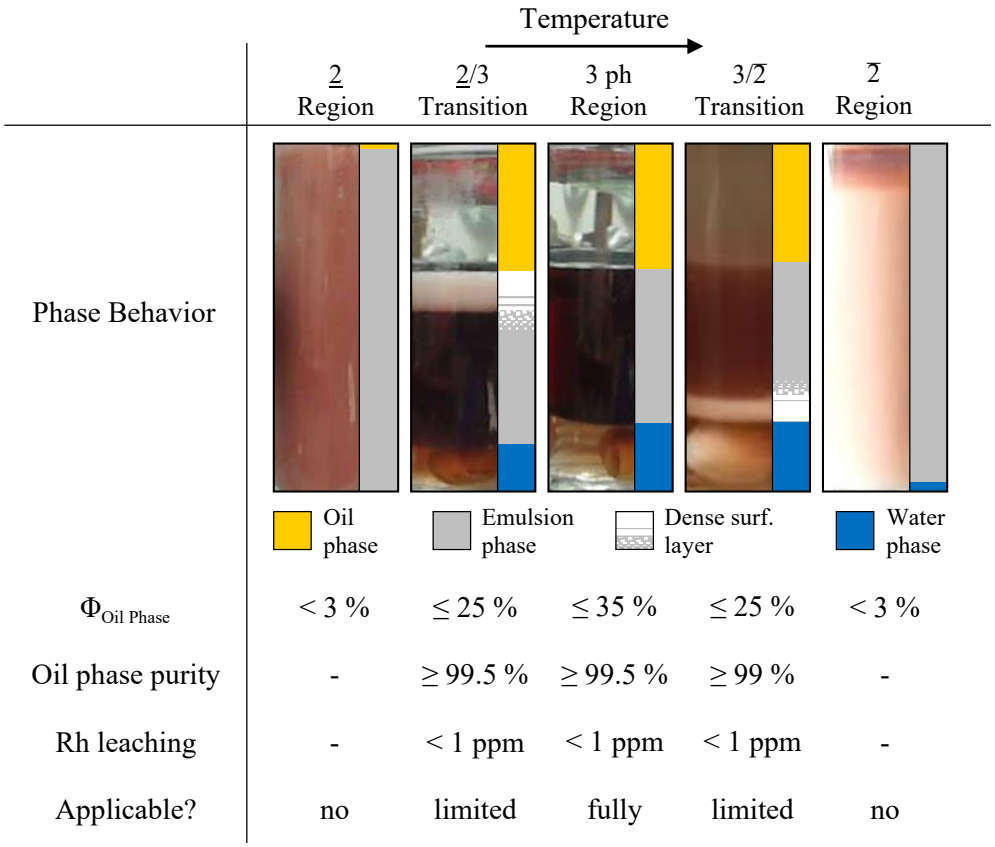

	2 Region	2/3 Transition	3 ph Region	3/2 Transition	2 Region
$\Phi_{\text{Oil Phase}}$	< 3 %	≤ 25 %	≤ 35 %	≤ 25 %	< 3 %
Oil phase purity	-	≥ 99.5 %	≥ 99.5 %	≥ 99 %	-
Rh leaching	-	< 1 ppm	< 1 ppm	< 1 ppm	-
Applicable?	no	limited	fully	limited	no

Fig. 3.8: Observed phase behavior of the MES and feasibility analysis towards process application. Mixture set to $\alpha = 50\,\%$, $\gamma = 8\,\%$, and Y=0 %, photos taken after 20 min of settling time.

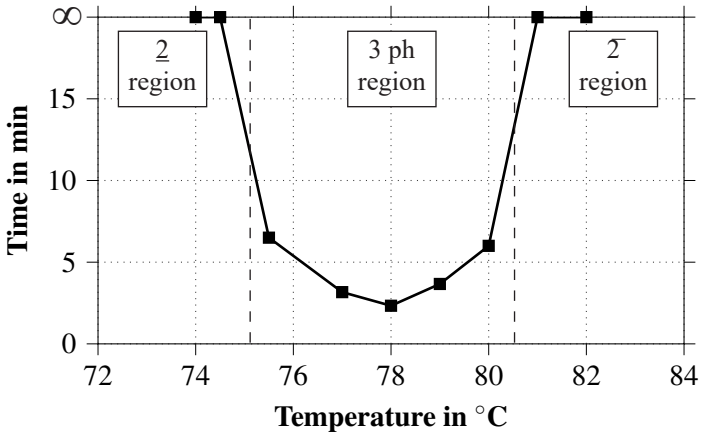

Fig. 3.9: Phase separation time over temperature for the mixture $\alpha = 50\,\%$ - $\gamma = 8\,\%$ - $Y = 0\,\%$. ∞ denotes very long settling times of several days.

In addition, Fig. 3.10 depicts the evolution of the relative oil and water phase volumes depending on temperature and settling time for the reference mixture $\alpha = 50\,\%$, $\gamma = 8\,\%$, $Y = 0\,\%$. Again, large volume fractions of more than 35 % and 20 %, for oil and water phase respectively are only found for an enclosed operation region. With increasing temperatures, a continuous shift towards lower oil phase levels is observed, while the water phase level increases. Moreover, the oil phase forms faster than the water phase at lower temperatures, while inverse behavior is found at high temperatures. Looking at Sec. 2.1.3, this behavior is expected since surfactant solubility changes towards higher oil affinity, affecting interfacial tensions and thus separation dynamics. Hence, the operation strategy for the settler should aim for three-phase separation ideally below the **P**hase **I**nversion **T**emperature (PIT) to obtain fast developing oily excess phases.

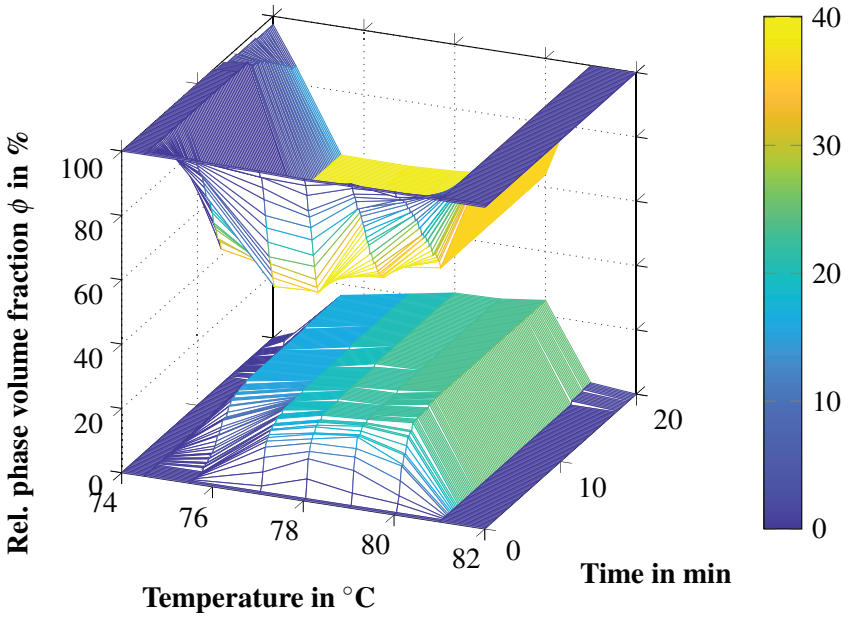

Fig. 3.10: Experimental results on the relative phase volume fraction evolution over temperature and time for the mixture $\alpha = 50\,\%$ - $\gamma = 8\,\%$ - $Y = 0\,\%$. Top: oil phase, bottom: water phase.

Finally, Fig. 3.11 shows – Kahlweit's Fish diagram – for the MES to analyze the influence of surfactant content, reaction yield, and temperature on the desired three-phase operation region. Apparently, the surfactant concentration has a major influence, as the respective temperature interval decreases drastically with increasing γ. Moreover, the surfactant concentration should not exceed 12 wt.-% to avoid the homogeneous ME phase state. The temperature-wise expanse of the three-phase region is severely limited and decreases from $\approx 9\,°C$ at $\gamma = 6$ wt.-% to $\approx 5\,°C$ at $\gamma = 10$ wt.-%. If tridecanal is present, a shift of the *fish* towards lower temperatures and a widening temperature interval for three-phasic separation is observed. In addition, an increasing oil to water ratio shifts the three-phase region towards higher temperatures (see Tab. 3.5).

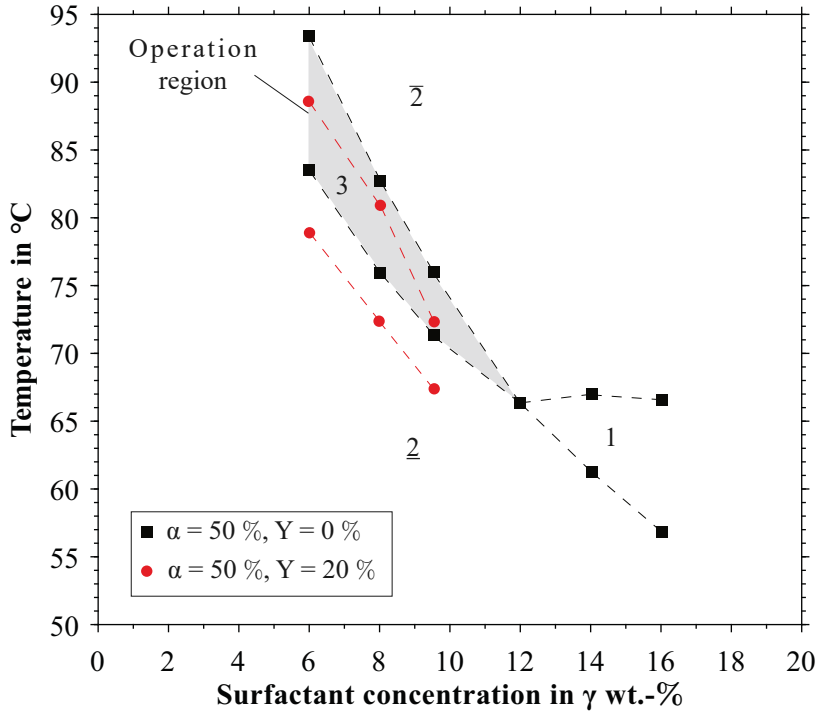

Fig. 3.11: Phase diagram for the mixture 1-dodecene-water-Marlipal® 24/70. Black squares mark the feasible operation region (3: three-phase region). Red dots show the shift of the operation region at increased reaction yield. Data for $\gamma \geq = 12$ wt.-% generated by Tobias Pogrzeba, Department of Chemistry, Technische Universität Berlin.

Sensitivity analysis

By now, the initial set of influencing factors on the phase behavior of the MES has been significantly reduced. To allow for a reduction of the experimental effort for the full system screening in **Step 5**, a sensitivity analysis of the remaining relevant influences is given in Tab. 3.5. Therein, respective sensitivities are given regarding the three-phase region, which is characterized by its temperature-wise location T_{opt} (mean upper and lower three-phase region boundaries) and its extent $(T_u - T_l)$. Based on this, respective increments are proposed for further detailed investigations. Note, that Y is sampled at a larger increment due to the high cost of tridecanal.

Tab. 3.5: Sensitivity of position of three-phase region (T_{opt}) and expanse ($T_u - T_l$) at local composition $\alpha = 50\%$, $\gamma = 8\%$, $Y = 0\,\%$ regarding influencing factors.

Influencing factor	Sensitivity on T_{opt}	Sensitivity on $T_u - T_l$	Suggested increment
α	$0.1\,°C\,\%^{-1}$	$-0.2\,°C\,\%^{-1}$	10 %
γ	$-4.4\,°C\,\%^{-1}$	$-1.8\,°C\,\%^{-1}$	0.5 %
Y	$-0.2\,°C\,\%^{-1}$	$0.1\,°C\,\%^{-1}$	20 %

3.4.4 Step 4a: Unit Design

At this point, a study on the design of the phase separation unit is given. For the MES, the feasible three-phasic separation can be carried out in a standard gravity settler with three drains, since necessary settling times are found to be low. For this work, a modular settler concept, introduced by D. Müller et al. (2015) is adapted and further extended. However, a critical revision on the proposed application of coalescence enhancers is conducted regarding Fig. 3.12.

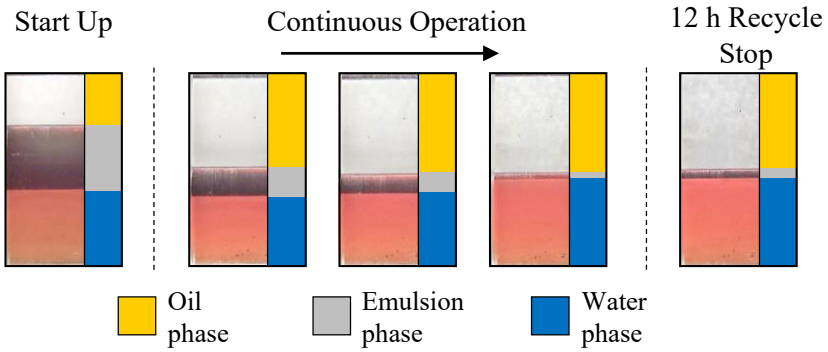

Fig. 3.12: Test of the settler operation using knitted wire meshs as internals. The phase separation state is observed through a settler gauge glass. Test conditions: $\alpha = 50\,\%$ - $\gamma = 8\,\%$ - $Y = 0\,\%$, $T_{Settler} = 85\,°\mathrm{C}$, $p_{Settler} = 15\,\mathrm{bar}$, 1 h residence time.

In preliminary mini-plant test runs, the continuous phase separation was investigated in a settler module equipped with a knitted wire mesh and displacer. The experiment entailed reactor, settler, and recycling of the separated mixture back into the reactor. After initial filling of the system, phase separation was established in the settler during *Start Up*. Afterwards, the recycle pumps were activated to establish a *Continuous Operation*. Here, a continuous shrinking of the emulsion phase was encountered. In this case, the knitted mesh induced accumulation of the surfactant rich microemulsion phase in the inlet section of the settler. To verify this, the recycle was stopped to obtain a re-equilibration. After 12 h, the volume fraction of the microemulsion phase doubled. This indicates that accumulated surfactant was at least partially redistributed in the settler. Regarding the process operation, these critical accumulations of surfactant are prone to alter the separation state, dynamics, and impede process control. Hence, coalescers are not considered for settler design.

Another operational challenge was identified in the build-up of surfactant rich dense layers. Regarding this, Fig. 3.13 shows the result from a mini-plant test run with continuous phase separation. In this case, the emulsion starts to separate immediately after exiting the reactor. This is due to the system's limitations of a maximum stream velocity of only $v_{R,Out} = 0.02\,\mathrm{m\,s^{-1}}$. The separation then occurs at an unknown temperature well below reactor temperature due to

heat loss at the pipe connecting reactor and settler. Considering phase configurations of the microemulsion and coalescence behavior from Fig. 2.9, the build-up of dense surfactant layers becomes plausible, when this prior separation occurs at a temperature related to the $\overline{2}$ or $3/\overline{2}$ transition state. In both cases, larger quantities of surfactant or emulsion droplets are present in the oil phase. If this pre-settled mixture enters the settler, it will distribute according phase densities and larger quantities of surfactant are carried to the settler oil phase. Since the settler operates at lower temperatures, the surfactant is then driven towards the middle phase and starts to drain out of the oil phase. In this process, accumulation of surfactant is prone to occur at the interface oil/emulsion due to small interfacial tensions.

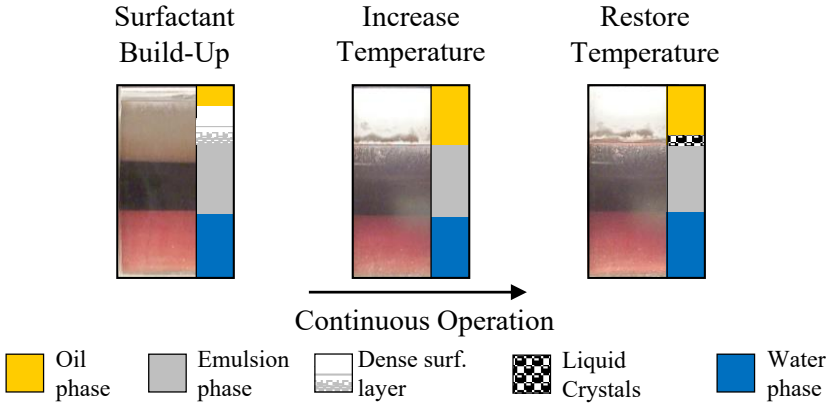

Fig. 3.13: Dense surfactant layer build-up (left) and subsequent formation of liquid crystals (right) after settler heat up (middle). Settler gauge glass photos, taken at test conditions: $\alpha = 50\,\%$ - $\gamma = 8\,\%$ - $Y = 0\,\%$, initial $T_{Settler} = 80\,^{\circ}\mathrm{C}$, $p_{Settler} = 15\,\mathrm{bar}$, 0.5 h residence time.

For the plant operation, this state is critical, since the backmixing of accumulated surfactant is very hard to achieve. One solution is to increase the settler temperature and *dissolve* the surfactant back into the oil phase. However, following Fig. 3.13 this is prone to trigger the formation of liquid crystal like structures of the surfactant. These show very disadvantageous fluid properties and are critical regarding pump operation and possible pipe blocking in the plant's recycle. Hence, an updated design of the settler united is proposed in Sec. 4.1.3, including additional mixing zones at the inlet of the settler and uniform heating for separation.

3.4.5 Step 4b: Analysis of Controllability of Influencing Factors

The systematic phase separation system analysis was used to identify relevant influencing factors for the phase separation behavior. Next, the adjustability of these variables with respect to process application is discussed using Tab. 3.6.

Tab. 3.6: Analysis of relevant influencing factors of the phase separation behavior, their sensitivity on the position of the separation operation region, measurability, and controllability.

Influencing factor	Sensitivity	Measurement	Sample rate	Control element
α	moderate	not possible[1]	-	feed rate, recycle ratio
γ	very high	not possible[1]	-	feed rate, recycle ratio
Y	moderate	GC[1]	1 h	feed rate, recycle ratio, reaction conditions
T	high	Pt100	0.5 s	heater unit of settler

[1] sufficient accuracy of concentration measurement via offline analytics is only possible for 1-dodecene, iso-dodecene, dodecane, iso-tridecanal, and tridecanal (see Sec. 4.2.3)

To directly control the phase separation state, the composition of the mixture entering the settler needs to be known. The temperature can then be adjusted accordingly. Regarding this, Illner et al. (2018a, p. 3) state, that "besides the separation temperature, which is easily accessible and measured in sufficient accuracy, relevant influence parameters are only available with a large delay (oil phase concentration measurements) or are not accessible at all (surfactant concentration). Especially the latter hinders the controllability of the system dramatically, since also the influence on the phase separation is the largest. Thus, frequent failures of operation are to be expected, even with only small perturbations of a steady state operation point." The applicability of MES as reaction media in a continuously operated mini-plant is hence hindered by the immeasurability of relevant states and lack in predictive thermodynamic models.

To overcome this hurdle, the development of a model based soft-sensor is proposed. The main idea is to exploit the features of the three-phase body of MES described in Sec. 2.1.3. With constant temperature T and pressure p, the microemulsion separates into three liquid phases (corners of the inner triangular miscibility gap in Fig. 2.6) with respective concentrations c_i^{Phase}. Depending on the initial composition of the mixture, volume fractions of phases Φ^{Phase} are observed. If the initial mixture is varied within the range of the three-phase miscibility gap, the respective compositions of the observed phases c_i^{Phase} remain the same, but volume fractions change. Hence, the initial composition of the mixture c_i^{Feed} can be correlated with the observation of the volume fractions of developed phases and their respective concentrations c_i^{Phase}:

$$c_i^{Feed}(T,p) = f\left(c_i^{Phase}(T,p), \Phi^{Phase}(T,p)\right) \tag{3.2}$$

Hence, Φ^{Phase} serve as new measurements, which must be considered for mini-plant automation (e.g. camera system) and the following full system mapping. From this, an empirical model based on experimental data is derived, for which a detailed discussion is given in Sec. 4.3.6.

3.4.6 Step 5: Full System Mapping

Finally, the full system mapping includes the actual empirical investigation of the phase separation behavior and collection of data, which is used for model formulation later on. With the performed influence and sensitivity analysis, the relevant factors and necessary levels for a full factorial design have been decided to a $3^1 9^1 3^1$ design for the respective experimental parameters oil:water ratio α, surfactant concentration γ, and tridecanal content Y. Table 3.7 additionally shows the applied experimental ranges and increments, as well as desired experimental observations. A detailed description of the experimental setup and procedure can found in Sec. A.2. Additionally, Tab. A.1 provides a list of conducted experiments, actual concentration information and observed upper and lower temperature limits for the three-phase body.

Tab. 3.7: Experimental ranges of parameters for the full system mapping and gathered observations.

Parameter	**Range**	**Increment**	**Measurement**
α	[40,60] %	10 %	gravimetric
γ	[6,10] %	0.5 %	gravimetric
Y	[0,40] %	20 %	gravimetric
T	variable	1-2 K	temperature sensor

Observation	**Measurement**
Phase State	Qualitative optical evaluation
Φ^{Phases}	Video capture and level detection

3.5 Summary on System Analysis – Identified Challenges

The systematic analysis for the hydroformylation of 1-dodecene in microemulsions revealed several obstacles regarding applicability and operability towards a desired continuously operated process. This is due to the system inherent properties and dependencies regarding reaction and separability of the ME. Hence, the following design and operational challenges are stated:

- Reaction performance depending on mixing state and sensitive catalyst equilibria
- Byproduct formation due to long residence times in separation and recycling steps
- Small feasible operation region regarding phase separation
- High sensitivity of operation region position regarding virtually all system concentrations
- Critical immeasurability of relevant component concentrations
- Severely changing fluid properties due to concentration or state variable changes

4 Derivation of Strategies for Process Design & Operation

Following the systematic system analysis in Chap. 3 it is obvious, that the transfer of the process concept presented in Fig. 1.2 towards a continuously operated process is severely hindered by system inherent challenges. Hence, also common procedures for realizing reactor-separator systems with internal recycles, as presented by L. T. Biegler et al. (1997) or R. Smith (2005, p. 18ff) are not applicable. To nevertheless exploit the highly advantageous features of MES applied on the hydroformylation of 1-dodecene, the development of tailored strategies for specific process design and advanced model-based methods for process operation and control is necessary. As an introduction to that, Fig. 4.1 provides a schematic overview.

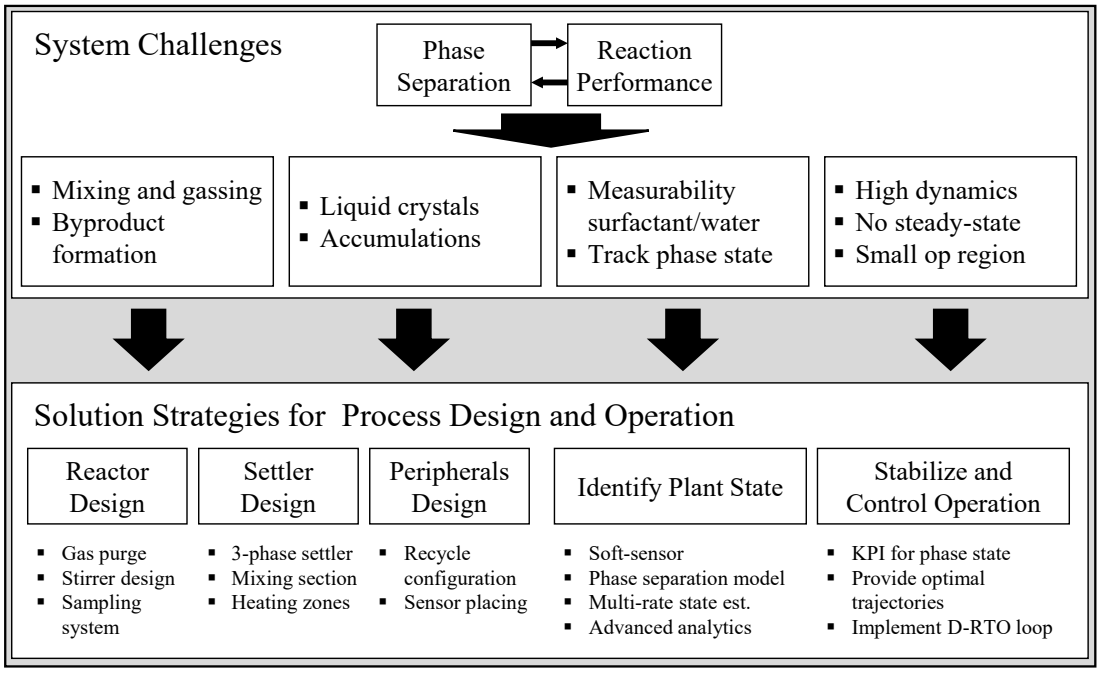

Fig. 4.1: Overview of applied strategies to cope with system inherent challenges.

Outlines on developed solution approaches are then presented in this chapter. First of all, the technical realization of the mini-plant system, its subsequent redesign and equipment modification with special focus on reactor and settler unit is shown. The connection of process design and operation is then given by deliberations on process automation, additionally implemented analytics, and relevant communication structures.

One of the key features of this thesis is then presented with the developed dynamic mini-plant model. Highlights therein are an adapted kinetic model formulation for the hydroformylation in microemulsions and a profound empiric model formulation for the three-phase separation of the microemulsions system. Both of these model features are crucial to tackle the aforementioned challenges in a quantitative manner and enable a profound first time description of the dynamic process behavior. This then forms the cornerstone for subsequent development of key (optimal) process operation strategies to cope with the very high dynamics and non-steady state behavior of the system.

4.1 Mini-Plant Setup and Redesign

The initial mini-plant system design was set up and realized by M. Müller et al. (2013). However, first tests on the hydroformylation of 1-dodecene in MES confirmed a variety of already identified challenges like massive byproduct formation, impeded phase separation and surfactant accumulations (Sec. 5.1, (Illner et al., 2016b)). To tackle these, several modifications have been implemented during the course of this thesis regarding the reaction section, recycle, and settler design. To allow for an insight into the technical realization of mini-plant system, firstly the general design is introduced.

4.1.1 General Remarks on Design Specifications

The mini-plant itself is installed in a three storeys high housing and set up in a modular way to allow for easy reconfiguration and integration of new equipment. According the chemical matrix, tanks and pipes are made of stainless steel of type EN 1.4404 or EN 1.4571. PTFE, FFKM, or FKM are used as sealing compounds. The total plant volume of the main reactor, settler, and recycle section is given with 2.35 L, while the total liquid volume is 1.45 L. A detailed list of container dimensions and the determined volume of the piping system is given in the appendix in Tab. B.2. A simplified process flow diagram of the mini-plant is depicted in Fig. 4.2 for which the subsequent naming of units and sensors applies.

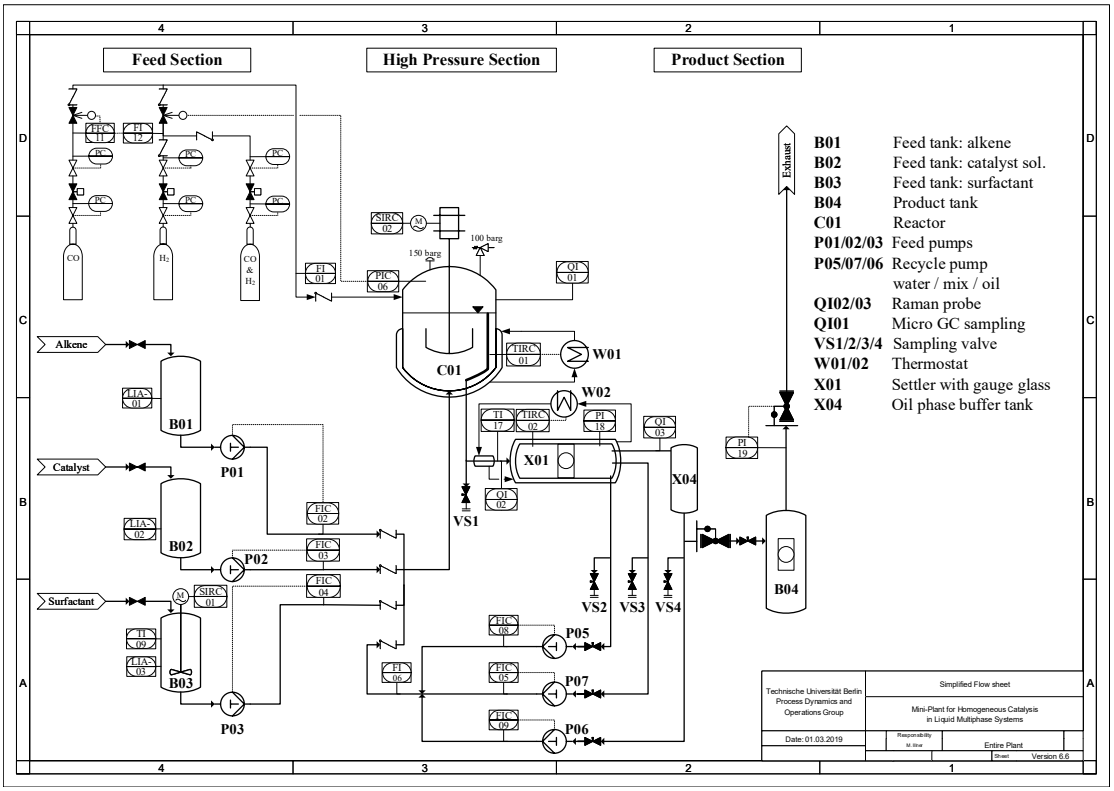

Fig. 4.2: Simplified process flow diagram of the mini-plant.

The setup is divided into three main sections, the **feed section**, a **high pressure section** holding reactor, settler, and the recycle section, as well as the **product section**. Due to the presence of synthesis gas and flammable substances, the mini-plant fully complies to ATEX zone 2 specifications. Hence, all equipment used inside the plant complies with respective specifications and temperature classes for 1-dodecene and synthesis gas. The mini-plant's housing is equipped with a ventilation system to avoid accumulation of synthesis gas in the room. The entire internal plant volume can be fully inertized with nitrogen. This is necessary since the catalyst decomposes under contact with oxygen and the formation of explosive mixtures of gas is to be avoided. Additionally, a vacuum pump is installed for purging gas from the system.

Feed Section

The basement area of the plant holds the feed section with containers for 1-dodecene (**B01**), catalyst solution (**B02**), and surfactant (**B03**). **B03** is stirred and heated to ensure homogenization and reduced viscosity of the technical grade surfactant. The respective pumps **P01** to **P03** feed the substances into the reactor. Additionally, gas containers for either syngas or pure gasses CO and H_2 are supplied and fed to the reactor via pressure regulation and ratio control.

High Pressure Section

The high pressure section of the plant is sketched and depicted in Fig. 4.3. The hydroformylation reaction is carried out in reactor **C01**, which is equipped with a heating jacket and a gassing stirrer with a maximum speed of 2000 rpm. A liquid drain is installed at approx. 40 % of the reactor height. The downstream settler **X01** is designed as a horizontal cylinder and equipped with a heating jacket to allow for temperature adjustment. For recycling of respective microemulsion phases, three individual recycle streams are installed and operated by pump **P05** for the aqueous phase, **P06** for the oil phase, and **P07** for the emulsion phase. Additionally, a buffer tank **X04** for the recycle of the oil phase is installed. Both, reactor and settler are equipped with thermostats **W01, W02** for temperature control. In general, the high pressure section is designed for pressures of up to 32 bar gauge and temperatures up to 120 °C, while for the reactor pressures of 150 bar and temperatures of 250 °C are permissible.

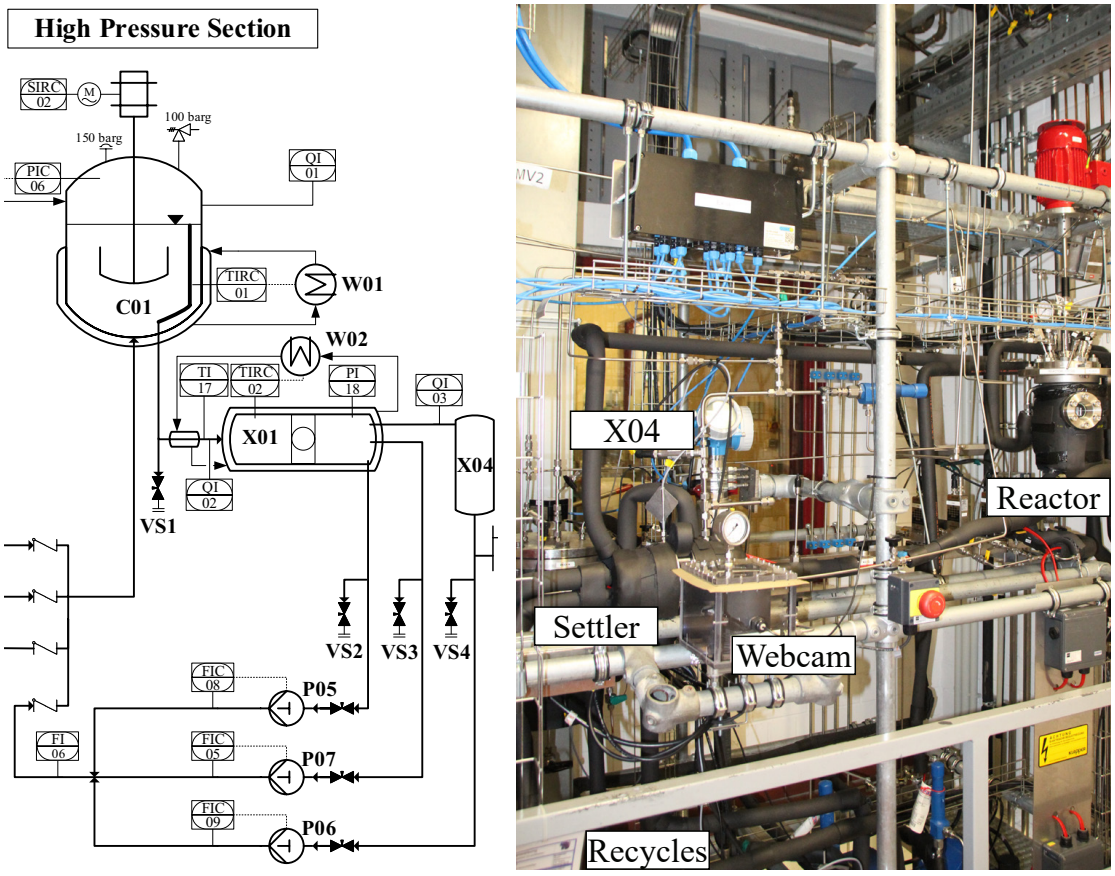

Fig. 4.3: Simplified process flow diagram and picture of the mini-plant's high pressure section.

Product Section

The product drain is realized with a control valve connected with the level regulation of buffer tank **X04**. Thus, a continuous operation of the plant can be established with a certain feed rate of alkene and respective drain towards product tank **B04**. Therein, also the degassing of syngas is conducted at a reduced internal pressure of 2 bar. All vented gasses from the plant are led into a collection tank **B06** for separation of condensables and then vented to the atmosphere.

4.1.2 Redesign of Reaction Section

In Section 3.3 several influences on the reaction performance were identified. These are mainly related to the catalytic system and formed equilibria of catalytically active species, which partly depend on the concentrations of CO and H_2 in the liquid phase. Regarding this, the designated reaction performance can be ensured firstly by proper gassing and thus dissolution of syngas. Secondly, shifts of the gas phase concentrations are to be avoided to maintain the operational setpoint of an equimolar mixture of CO and H_2. Despite the excellent emulsification properties of MES and identified minor influence of stirrer speed on the reaction performance, the stirrer configuration is revised. Due to a variety of sensors and internal piping the stirrer operation in the used 1.5 L autoclave is severely impeded and the formation of dead zones, especially of separated oil, were identified in preliminary plant experiments.

Reactor modifications thus include the insertion of two Rushton turbines, one located at the lower end of the shaft and a second roughly 5 mm below the total liquid level of the reactor. Additionally, baffles are positioned close to the stirrers to avoid vortices. This way sufficient mixing of the ME can be ensured. Additionally, the gassing with syngas and distribution of gas bubbles in the mixture is improved. To ensure a specified syngas composition in the reactor, an additional continuous gas purge has been implemented. This is augmented with a micro-GC to constantly monitor the composition of the gas phase and adjust the gas purge. A respective P&ID is found in Fig. B.8. Moreover, the reactor is equipped with a semi-automated sampling system. The sampling from the reactor is crucial to determine the plant's operational state. Using a pipe connection for sampling, dead volume needs to be purged for sampling of liquids. However, since phase separation also occurs in the sampling pipe, it is virtually impossible to purge dead volume and afterwards draw a homogeneous sample from the reactor manually. In contrast, the designed sampling system enables the simultaneous purge of dead volume from the sampling pipe connection and loading of a homogeneous sample into a sample loop using a tailored flow pattern and 6-way cross flow valve. Pipe dimension are optimized to withdraw minimum liquid content per sample. A dead volume of 9 mL and a 0.2 mL sample loop can thus be realized. The designed implementation and remarks on its usage are given in Sec. B.1.

4.1.3 Redesign of Settler and Recycle

First deliberations for designing a settler unit for the application in multiphase media were initially proposed by D. Müller et al. (2015). A key feature is the modular design, which enables the fast adaption of the internal volume, application of internals, or additional sensors. However, concerning the unit requirements gained from the system and operability analysis of the reaction and microemulsion system an adequate design is proposed:

Especially the large unit volume and corresponding residence times of the ME in the settler is prone to trigger byproduct formation due to an altered catalyst state, as described in Sec. 3.3. Thus, the settler design is initially set to the configuration shown in Fig. 4.4. Minimizing the internal volume, 0.45 L total liquid volume and an inner diameter of 55 mm are chosen. Three phase drains are applied to allow for the recycling of respective microemulsion phases and a central gauge glass is installed to enable observation of the phase separation. Temperature control is guaranteed by a Pt100 sensor and an implemented heating jacket, fed by a thermostat.

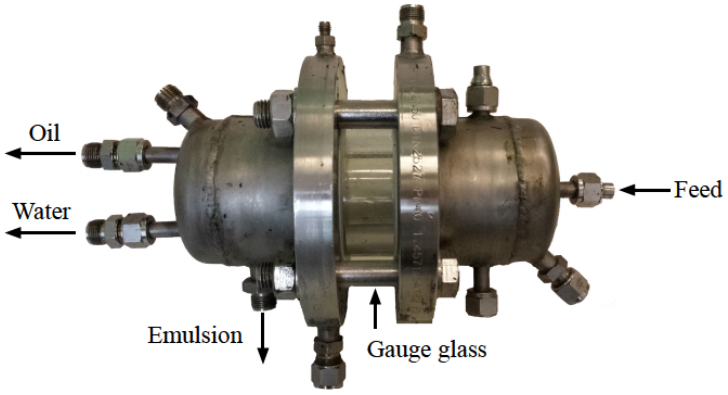

Fig. 4.4: Modular settler configuration with two end caps and a central gauge glass.

In Fig. 3.4.4 it is also discussed, that internals like knitted wire meshs are prone to trigger surfactant accumulation during continuous operation. Consequently these are excluded from the settler design. Additionally, it is shown, that initial phase separation of the microemulsion before entering the settler severely hinders operation stability due to *undefined* separation states and possible formation of dense surfactant layers or liquid crystals. The connecting pipe between reactor and settler is thus equipped with a heating jacket, positioned closely to the settler inlet. This setup is also depicted in Fig. 4.2 and includes an additional temperature sensor at the settler inlet to enable observation or control. The heating jacket is supplied with thermo-oil from the settler's thermostat in an interconnected loop. Initially, co-current flow of the thermo-oil is preferred to ensure sufficient pre-heater operation and avoid increased surfactant concentrations in the oil phase at the settler outlet.

Realization of a Mixer-Settler Unit

Maintaining a stable separation operation also involves adjusting the separation conditions for the MES according a small operation region, which is also sensitive to concentration shifts. The description of the separation behavior and the empirical model formulation in Sec. 4.3.6 is performed and virtually only possible for the separation process starting from the fully emulsified system. The ideal design of the separation unit then must allow for the immediate separation of the mixed emulsion at the optimal separation temperature.

To realize this, the integration of a mixing zone and an optimized heating zone into the settler is proposed. Here, Fig. 4.5 depicts a second developed mixer-settler design. A stirrer module is installed to re-emulsify and preheat the entering mixture to the optimal separation temperature. Again a Rushton turbine is implemented as a stirrer. Baffles are omitted due to the overall small volume of the mixing compartment. Via an overflow weir, the mixture then enters the heating module, which is equipped with a heating jacket and an internal heating coil to avoid radial temperature gradients. In this module, the separation of the emulsion takes place, whose current state is then observed in a subsequent gauge glass. Three phase drains allow for recycling of the individual phases. The overall volume of the separation zone is approx. 650 mL with additional 400 mL mixed zone. Thus, a residence time well below 1 h for the separated system can be ensured to avoid the formation of inselective catalyst species, as discussed earlier. Additionally, both mixing and separation compartment are individually equipped with a gas inlet connected to the reactor gas phase, enabling pressure equilibration and gas re-feed.

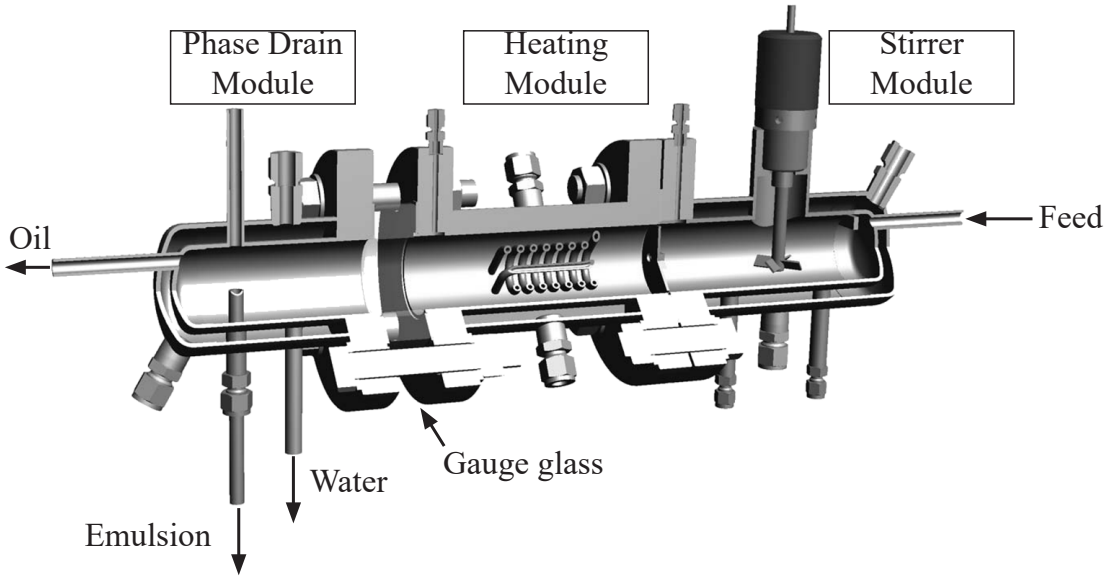

Fig. 4.5: New settler design with mixing section, separation section with internal heating coil and updated phase drains. A gauge glass is installed for phase separation observation.

Recycle Redesign

All three phases of the microemulsion must be recycled individually to be able to adjust their ratio of recycling to the current phase separation state. Hence, concentration shifts in reactor and settler can be avoided. The dimensioning of respective pumps is done according to the expected fractions of phase volumes from the systematic analysis of the phase behavior. The piping is then equipped with additional heating elements to avoid blockage and to reduce the viscosity of the emulsion phase. Since the recycled phases show different fluid properties, such as densities (754.67 g/L for 1-dodecene and 993.79 g/L for water at 25 °C (AspenProperties V10, 2019)) and viscosities (0.8 mPas for 1-dodecene, 13.7 mPas for emulsion phase, both at 60 °C) check valves are supplied for each recycle line close to the recycle mixer to avoid backflows and backlog.

4.2 Process Automation and Analytics

For the development of model-based strategies for process operation and control, information on available sensors, actuators, and analytically accessible information from the plant is vital. Hence, this section presents the supplied process automation system, positioning and properties of implemented sensors and actuators, and the variety of tested and applied analytics to improve the availability of vital concentration information. Furthermore, special attention is given to the communication structure of the plant and bi-directional data handling between the automation system and external software frameworks for state estimation and dynamic optimization.

For later presentation of results and plant measurements, information on sensor accuracy or measurement variances from this chapter are used to calculate measurement errors. These are generally presented as standard deviation σ. Further information on handling and calculation of measurement errors can be found in Sec. B.3.

4.2.1 Process Monitoring and Control

For reliable and safe process operation, the mini-plant is fully automated with the industrial-grade process automation controller system **Siemens SIMATIC S7-400** and respective process control software **Siemens SIMATIC PCS 7 V7.1**. Used measurements and actuators for process monitoring and control actions therein are listed in Tab. 4.1 and Tab. 4.2 together with information of applicable value ranges, control action, and measurement errors. The following discussion focuses on devices relevant for the mini-plant model functionality and related state estimation.

Tab. 4.1: Installed sensor devices in the mini-plant. Information is given on measurement range, intended use, and measurement error.

Tag	Measurement	Range	Application	Error
FI01	Mass flow	8 ... 400 $g\,h^{-1}$	Syngas feed	4.5 %[1,3]
FICA02	Mass flow	80 ... 4000 $g\,h^{-1}$	Alkene feed	4.7 %[1,3]
FICA03	Mass flow	10 ... 1000 $g\,h^{-1}$	Catalyst feed	4.7 %[1,3]
FICA04	Mass flow	20 ... 200 $g\,h^{-1}$	Surfactant feed	4.7 %[1,3]
FICA05	Mass flow	80 ... 4000 $g\,h^{-1}$	Emulsion recycle	4.7 %[1,3]
FI06	Mass flow	60 ... 6000 $g\,h^{-1}$	Total recycle	4.7 %[1,3]
FI07	Mass flow	40 ... 4000 $g\,h^{-1}$	Product stream	4.7 %[1,3]
FICA08	Mass flow	10 ... 1000 $g\,h^{-1}$	Water recycle	4.7 %[1,3]
FICA09	Mass flow	40 ... 4000 $g\,h^{-1}$	Oil recycle	4.7 %[1,3]
LIA01	Level	0 ... 100 %	Alkene feed tank	0.5 - 13.4 %[2,4,5]
LIA02	Level	0 ... 100 %	Catalyst feed tank	0.5 - 8.9 %[2,4,5]
LIA02	Level	0 ... 100 %	Surfactant feed tank	0.5 - 13.4 %[2,4,5]
LICA06	Level	0 ... 100 %	Oil phase buffer tank	0.7 - 20.0 %[2,4,5]
LIA+09	Level	0 ... 100 %	Product tank	4.5 %[2,5]
PICA06/18	Pressure	0 ... 25 bar	Reactor - Settler	0.5 %[2,6]
TIRC01	Temperature	-50... 250 °C	Reactor	0.5 %[7,8]
TIRC02	Temperature	-50... 250 °C	Settler	0.5 %[7,8]
TIRC03	Temperature	-50... 250 °C	Settler inlet	0.5 %[7,8]
TI04	Temperature	-50... 250 °C	Water recycle	0.5 %[7,8]
TI05	Temperature	-50... 250 °C	Product stream	0.5 %[7,8]
TI06	Temperature	-50... 250 °C	Catalyst feed	0.5 %[7,8]
TI07	Temperature	-50... 250 °C	Alkene feed	0.5 %[7,8]
TI08	Temperature	-50... 250 °C	Surfactant feed	0.5 %[7,8]
TI13	Temperature	-50... 250 °C	Oil recycle	0.5 %[7,8]
TI14	Temperature	-50... 250 °C	Emulsion recycle	0.5 %[7,8]

[1] Of actual value plus zero-point stability of 6 $g\,h^{-1}$, expect for FI01 and FICA02 (0.2 $g\,h^{-1}$)

[2] Error related to total range

[3] Source: Calibration data and information from contacted manufacturer (Bronkhorst)

[4] Error increases gradually at the end points of the measurement range

[5] Source: (Endress+Hauser, 2011a; Endress+Hauser, 2011b; E.L.B., 2011)

[6] Source: (WIKA, 2009)

[7] Measurement error with respect to actual value. Additional offset of 0.3 °C applies

[8] Source: Information from contacted manufacturer (TC GmbH)

Several coriolis flow sensors are installed in the plant to monitor and operate feed and recycle streams. Their usage for direct control of the pump speeds however is disregarded for plant operations, since the application of coriolis flow sensors for MES was found to be unreliable. Since

piston pumps are implemented, desired setpoint flow rates are correlated with pump drive speeds and a known displacement volume. Flow sensor information is however used as additional information for state estimation and data reconciliation. Level sensors are installed in all feed tanks, tank X04, and the product tank and provide redundant measurements on respective liquid flow rates. The pressure of the high pressure section is monitored with PICA06 and PICA18 enabling also control.
Temperature of reactor and settler are monitored with TIRC01 and TIRC02 respectively and controlled using corresponding thermostats W01 and W02. Additionally, temperature measurements are applied in all main process paths to control trace heating elements and enable the calculation of fluid properties, such as component densities. Surfactant feed tank stirrer SIRC01 and reactor stirrer SIRC02 are both operated at constant speeds of 30 % and 25 % of maximum speed respectively. Thus, sufficient mixing of surfactant and microemulsion, as well as proper gassing in the reactor are ensured.

Tab. 4.2: Installed actuators in the mini-plant. Information is given on application, range, and intended control action.

Tag	Actuator	Range	Effect
P01	Pump	$0 \ldots 1100\,\mathrm{mL\,h^{-1}}$	Alkene feed
P02	Pump	$0 \ldots 400\,\mathrm{mL\,h^{-1}}$	Catalyst feed
P03	Pump	$0 \ldots 400\,\mathrm{mL\,h^{-1}}$	Surfactant feed
P05	Pump	$0 \ldots 1100\,\mathrm{mL\,h^{-1}}$	Emulsion recycle
P06	Pump	$0 \ldots 1100\,\mathrm{mL\,h^{-1}}$	Oil recycle
P07	Pump	$0 \ldots 400\,\mathrm{mL\,h^{-1}}$	Water recycle
RV1	Control valve	$0 \ldots 100\,\%$	Level X04
RV6	Control valve	$0 \ldots 100\,\%$	Pressure reactor
W01	Thermostat	$20 \ldots 120\,^{\circ}\mathrm{C}$	Temperature reactor
W02	Thermostat	$20 \ldots 120\,^{\circ}\mathrm{C}$	Temperature settler

The automation concept and visualization of the entire mini-plant is realized in Siemens SIMATIC PCS 7. Hence, a base level automation has been realized including alarm logging, notifications, as well as sequential routines for safe shut-down in case of severe system failure or critical alarms. Due to safety restrictions, this base automation is not affected by any applied optimal process control method and all control loops adhere to specified limitations of process values. The graphical user interface of the automation system is exemplarily shown in Fig. 4.6. Here, the main high pressure section is depicted, where control actions regarding reaction pressure and temperature, settler temperature, or recycle ratio can be made. Additionally, a webcam feed of the phase separation state including level detection and concentration soft-sensor is provided. In an upper task bar other visualization frames can be selected to operate different parts of the plant, such as the feed section, plant inertization, permission handling, or general status observation.

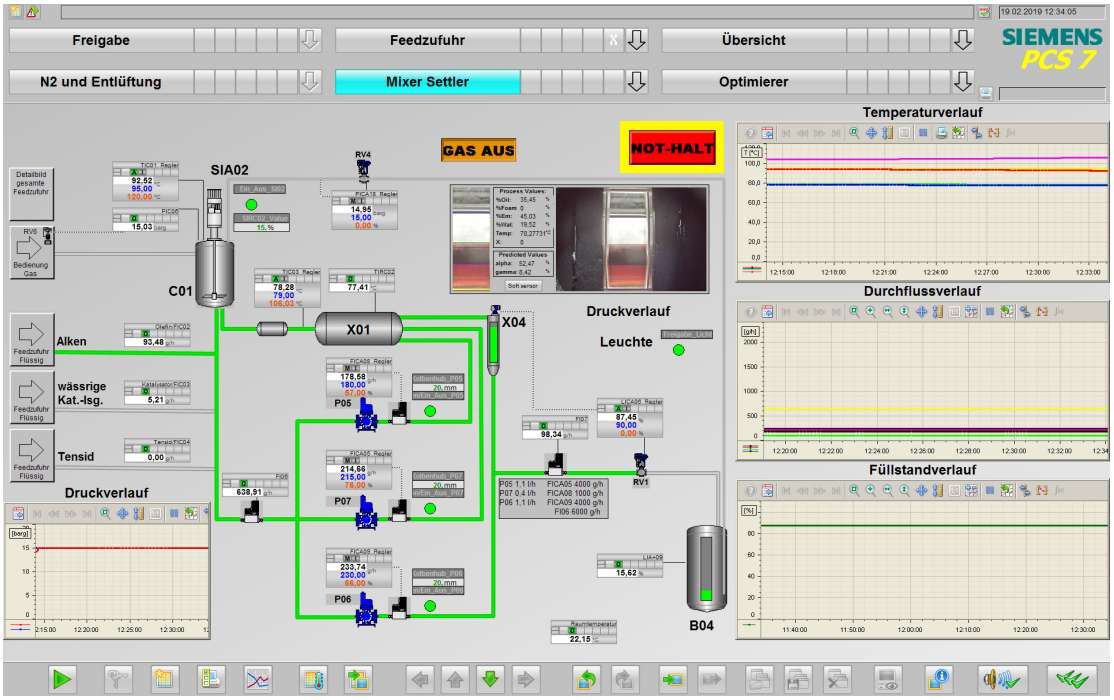

Fig. 4.6: Visualization of the process automation of the mini-plant. Main control frame for the high pressure section is shown.

4.2.2 Automated Phase Level Detection

From the systematic system analysis, the observation of the developed fractions of the phase volumes in the settler was identified as additional mandatory measurement to enable the application of a soft-sensor for the surfactant concentration. For this purpose, an ATEX zone 2 specified high definition webcam is installed. It is adjusted on the settler gauge glass and an opaque shielding is applied together with a spot light to guarantee defined lighting conditions.

For image evaluation and calculations, an own implementation in C++/Python is used (Alzate, 2018). In general, the different coloring and opacity of existing phases is exploited. The program sequence is depicted in Fig. 4.7 and starts with reading a frame from the webcam and cropping the image to the region of interest. It is smoothened and filtered with a Gaussian filter and then transformed into **H**ue **S**aturation **V**alue (HSV) color space. HSV is especially suitable here, since it is device independent and widely robust regarding changing lighting conditions (Ibraheem et al., 2012). The color detection is then sequentially performed on the image for the identification of all relevant phases. Necessary HSV color thresholds are provided from initial calibration. Additionally, a user interface has been programmed for on-the-fly re-calibration

in case the optical properties of the MES change. In the subsequent level detection step, the extent of the identified areas is then determined using canny edge detection on horizontal lines (Canny, 1986). Finally, detected level fractions are converted into volume fractions using the geometric information of the settler. The accuracy of this approach is generally considered to be high, as has been seen within first tests. However, a conservative assumption of a maximum measurement error of 5 % of the current value is assumed.

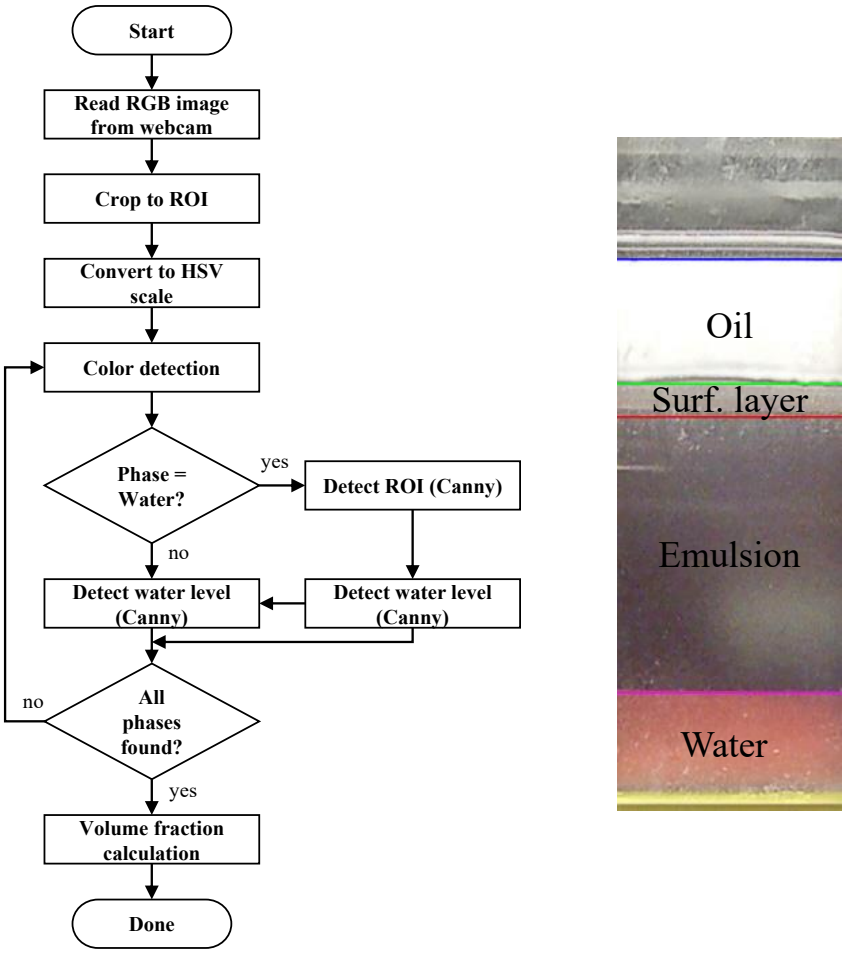

Fig. 4.7: Image processing script for detection of phase volume fractions and exemplary results.

4.2.3 Implemented and Applied Analytics

Due to the complexity of the chemical matrix of the MES, a multitude of analytical methods has been tested and further developed to enable tracking of reaction performance and distribution coefficients for the phase separation. In the following, respective analysis methods and procedures

for sample preparation are explained. Additionally, Tab. 4.3 provides a correlation matrix on type and online/offline applicability of used methods and the measurability of substances therein. This first of all states the poor or impossible measurability of the surfactant and water.

Tab. 4.3: Applied analytics and detectable substances. + good measurability; -no quantification possible. [1] Raman spectroscopy only applicable at constant optical properties of the mixture.

Component \ Method	offline		online	
	GC liquids	ICP-OES	Raman[1]	GC gasses
1-dodecene	+	-	+	
iso-dodecene	+	-	+	
Tridecanal	+	-	+	
iso-tridecanal	+	-	+	
Dodecane	+	-	-	
Marlipal® 24/70	-	-	-	
Water	-	-	-	
Rhodium catalyst	-	+	-	
SulfoXantPhos	-	+	-	
CO, H_2, N_2, O_2				+

Gas Chromatography

From all tested methods, gas chromatography for liquids offers the best applicability and is thus largely used. Nevertheless its application still requires advanced procedures:

The sample composition and especially the presence of water and surfactant have a large influence on the analysis results. Yet, only oily substances are traceable. Two configurations are used for liquid samples from the system: A Hewlett Packard HP 6890 GC equipped with a 1 m fused silica pre-column with 0.32 mm inner diameter and a separation column Agilent HP-5 (crosslinked 5% PH ME Siloxan, 30 m length, 0.32 mm inner diameter, 0.15 µm) is used for aqueous and surfactant rich samples. Oil phase samples are analyzed with an Agilent 7890A GC without pre-column and the same HP-5 column. For both, the analysis method is described in Sec. B.2

Sample preparation entails addition of nonane as internal standard (5 % of sample mass). Prepared samples are then fully dissolved in iso-propanol (dillution factor 6:1). A calibration has been performed for three different application cases and expected concentration ranges: reactor, oil, and water phase sampling. Corresponding results are listed in Tab. B.3. Resulting chromatograms are evaluated using an own implementation in Matlab. Here, the detector signal over time is analyzed and existing peaks are integrated. The assignment of components to peaks is then done based on expected retention time intervals and specific properties of component peaks (fronting/tailing). Afterwards, sample preparation and internal standard information is used for

correction before calculated peak areas are converted into mass fractions. Result data is then provided via an OPC DA interface in Matlab. This extensive procedure is necessary, because retention times of component are highly dependent on the chemical matrix of the samples. Thus, shifts are present with, e.g., increasing conversion in the mini-plant.

In addition, a micro-GC is applied to sample the composition of the gas phase of the reactor online. Information on that is found in Sec. B.2.

Raman Spectroscopy

Spectroscopic analytical methods offer real-time and in-situ measurement of the composition of a system. This is highly desired for the dynamic system and enables fast model updates. Regarding this, Raman spectroscopy is investigated and applied for mini-plant operations. To set up adequate calibration models for spectrum analysis, a test stand for the hydroformylation of 1-dodecene in microemulsions has been developed in collaboration with the Federal Institute for Materials Research and Testing (BAM). For reference measurements, several analytical tools, such as high field **N**uclear **M**agnetic **R**esonance (NMR), GC, and UV/vis have been implemented (see flow sheet in Fig. B.9). Satisfactory calibration models have been developed for 1-dodecene, its isomers, and tridecanal. Further information on the setup, applied multivariate data analysis, and model development can be found in our own contributions (Meyer et al., 2017a; Paul et al., 2017).

Pendant Drop Surface Tension Measurements

The analysis of surface tension is applied to determine the cmc of surfactant containing mixtures. This is relevant for the development of the phase separation model. Within this work, the pendant-drop method is used, in which the surface or interfacial tension is determined via the geometrical dimensions of a drop hanging from the exit of a capillary. The system DataPhysics OCA 20 with automated dosing is applied. The droplet size is captured with a digital camera and surface or interfacial tensions are calculated using the method described by (Jennings et al., 1988).

4.2.4 Communication Structure and Data Management

The targeted plant operation and application of model-based strategies for process control exhibits the necessary exchange of data between plant automation system, mini-plant equipment, and optimization platforms. Regarding this, a communication structure with different communication layers has been implemented. This is shown in Fig. 4.8 together with a flow diagram of

transferred information and used communication protocols for process automation. The aim is to avoid manual data transfer, enable information exchange in real-time, and ensure availability of necessary data at any element involved in the calculation of optimal plant trajectories. Three main communication and data exchange cycles are identified for the plant and discussed:

Mini-Plant – Distributed Control System

The DCS Siemens SIMATIC PCS 7 is applied for mini-plant automation and thus measurement values, sensor status information, and control actions are bidirectionally exchanged. Process data is then directly accessible on the **OS**. To ensure the availability of online data from the plant, an OPC DA (https://opcfoundation.org/) server is operated, providing read and write capabilities for process values, control setpoints, and sensor status information. This way, platform independent access on plant data and redundant archiving of process data in Matlab is possible.

Distributed Control System – Auxiliary Equipment / Sensor

Several *smart* sensors are applied to generate additional information on the plant's state. In case of applied GC analysis, concentration data is also provided within the process control system and stored with respective timestamps. For this purpose, a network connection of the GC result analysis station with the DCS is established via OPC. This procedure is analogous for the implemented image processing and surfactant soft-sensor. An external **Webcam Server** is installed, which operates the webcam in the mini-plant via Ethernet and performs the level detection described in Sec. 4.2.2. The current evaluation is then merged with real-time information on the settler temperature to calculate the corresponding mixture composition. Information on the fractions of phase volumes and concentrations is then written back to the plant via OPC. Additionally, current webcam frames and two **K**ey **P**erformance **I**ndicator (KPI) plots are provided to help plant operators to evaluate the current settler status of operation. These images are transferred to the **OS** via Ethernet and displayed in the DCS.

Distributed Control System – Optimizer

To apply online-optimization on the mini-plant, an external **Optimizer** workstation is set up. To identify the current plant's state, data on process variables and controls are read via OPC from the **OS** and applied for moving horizon state estimation. This comprises also soft-sensor and analytical data. The identified plant state is then used to calculate an optimal plant trajectory for the next 4 hours. The results are finally transferred back to the **OS**, which then applies gained optimal trajectories of setpoints on respective controllers.

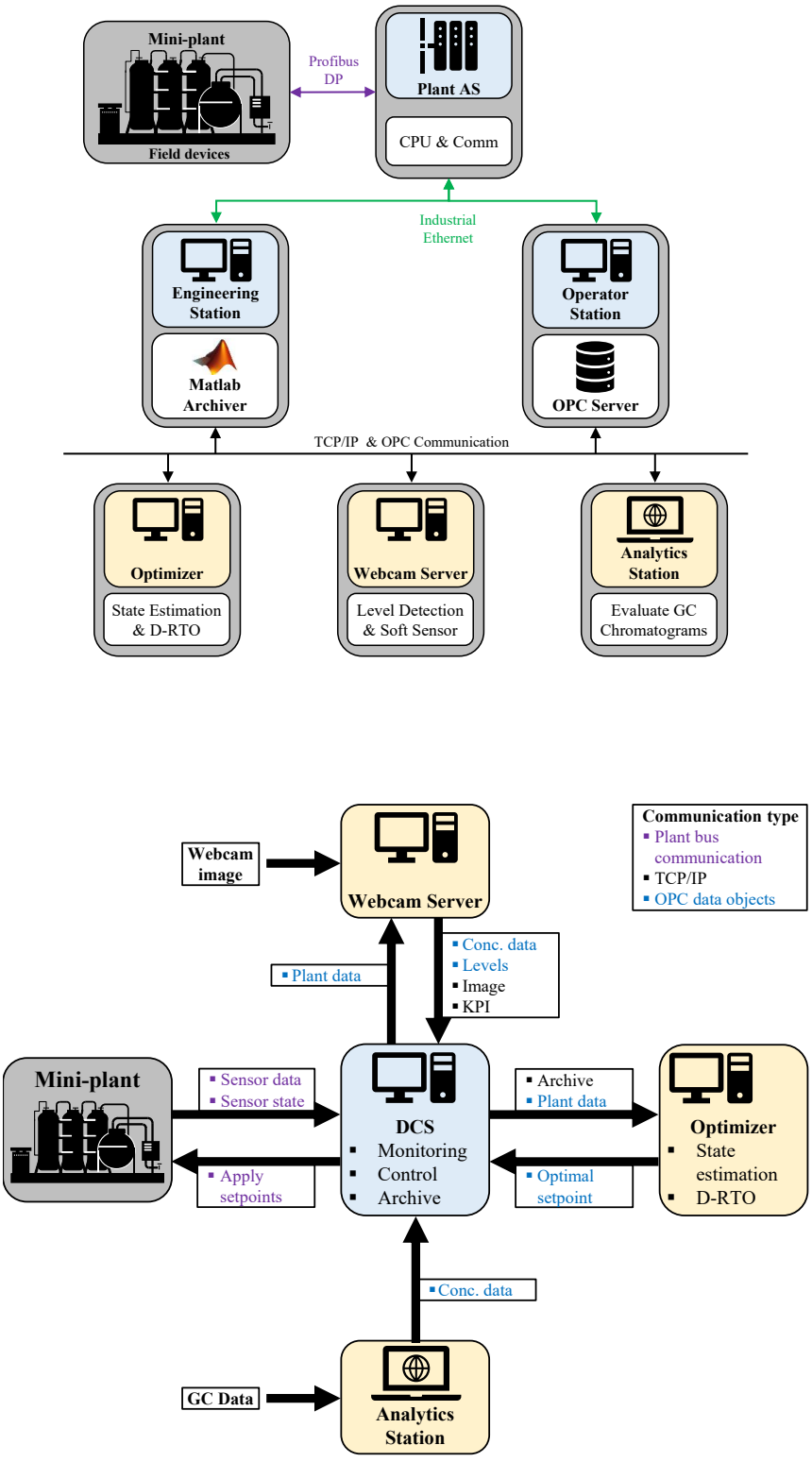

Fig. 4.8: Realized communication structure for process automation (top), information exchange and used communication protocols between mini-plant, DCS, additionally smart sensors, and model-based optimizer (bottom).

4.3 Development of the Dynamic Process Model

In this section, the dynamic model of the mini-plant for hydroformylation is presented. The two major features therein are an adapted mechanistic macro kinetic model for the hydroformylation reaction and a semi-empiric model for the dynamic three-phasic separation of MESs. The modeling itself has been carried out in the modeling environment MOSAICmodeling [1]. The developed DAE model and a discretized version are available as pdf [2].

4.3.1 General Structure and Scope of Modeling

In general, the model development focuses on model applicability for state estimation and dynamic (online) optimization. Hence, relevant dynamic phenomena within the mini-plant are to be entailed, but keeping model complexity as as low as possible. Due to the high complexity of the system and missing thermodynamic descriptions theoretically based predictive models are not attainable. Thus, the goal of the modeling is to find valid representations of identified operation regions for certain phenomena and the according dynamics for the transitions between operation modes. This includes:

- Overflow drainage of tanks with outlet activation
- Kinetic model including byproduct formation and reaction de/activation through syngas
- Three-phasic ME separation and respective component distribution
- Switching of settler outlet concentrations, according to separation state
- Three individual recycles with dead time behavior regarding concentration changes

Following the outlines in Sec. 2.4, the applied modeling techniques will focus on *reduced* first principles representations of mini-plant elements comprising the MESH(I) systematics and semi-empiric representations of relevant phenomena, especially the phase separation behavior.

To guide the discussion, Fig. 4.9 provides a modeling scheme, which holds the crucial elements of the technical mini-plant system relevant for modeling. Additionally, applied indices of components i (Tab. 4.4), units u, streams s (Tab. C.4) are introduced.

In the following, the focus is laid on key model functionalities and novel implementations. Hence, general definitions of equations, such as mass balances, sum relations, and auxiliary equations are summarized in the appendix C.2 and are not outlined here.

[1] http://mosaic-modeling.de/

[2] http://mosaic-modeling.de/?attachment_id=3489, http://mosaic-modeling.de/?attachment_id=3487

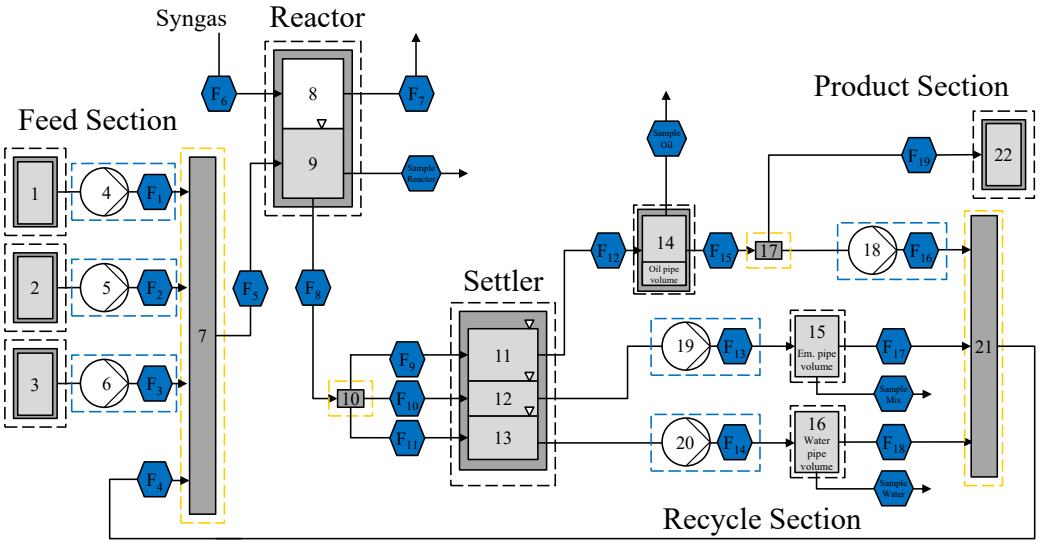

Fig. 4.9: Model scheme for the hydroformylation mini-plant. All relevant and modeled units, streams, and phases are depicted. Information on stream and unit indices can be found in Tab. C.4.

Tab. 4.4: Indexing of substances.

Component	Index *i*	**Component**	Index *i*
1-dodecene	1	CO	7
iso-dodecene	2	N_2	8
iso-tridecanal	3	H_2O	9
dodecane	4	Precursor: Rhacac$[CO]_2$	10
n-tridecanal	5	Ligand: SulfoXantPhos	11
H_2	6	Surfactant: Marlipal® 24/70	12

Assumptions

Basic assumptions for the model formulation are presented in the following. Predominantly, these are necessary to keep the model complexity low and ensure usability for optimization.

- **Neglect momentum balances, pressure drop, valves, and internals:** Only reactor pressure is of relevance. Flow data is widely measured.
- **Neglect energy balances and heat losses on units and pipes:** For the scope of modeling reactor and settler temperature are most important, which can be controlled tightly. Temperatures of flows are measured at relevant points in the mini-plant.
- **Pumps operate independent of pressure drop and counter pressure:** Piston pumps are operated well below max. pressure and hold linear characteristics (Bran+Luebbe, 2011).
- **Reaction only takes place in the reactor (Fig. 3.4)**
- **Tanks are assumed as cylinders**

- **Tanks are ideally mixed:** Stirrer used for reactor and surfactant tank. High mutual solubility of components in other tanks.
- **Neglect vapor-liquid-equilibria for non gaseous substances:** Relevant vapor pressures are low with respect to operation conditions and gas phase purge is very small with $10\,\mathrm{g\,h^{-1}}$. Hence only gas solubility is considered.
- **Gas dissolution for gases in liquids**: Instantaneous equilibrium is assumed.

Fluid Properties

Based on the made assumptions and simplifications for modeling of the mini-plant, only the compound densities are stated as relevant fluid properties. The calculation of densities is done separately for liquids and gasses. The former are computed via *DIPPR105*[3], which depends solely on temperature and parameters $a_i \dots d_i$. The latter uses a polynomial expression with parameters $a_i \dots e_i$ depending on temperature and pressure:

$$\rho(T)^L = \frac{a_i}{(b_i)^{1+(1-\frac{T}{c_i})^{d_i}}} \cdot M_i \tag{4.1}$$

$$\rho(T,p)^V = (a_i + b_i \cdot T + c_i \cdot p + d_i \cdot (T)^2 + e_i \cdot T \cdot p) \cdot M_i \tag{4.2}$$

Relevant parameters for each model component $i = 1 \dots 12$ have been fitted to experimental data or database correlations. Parameter data and data sources are listed in Tab. C.22. Here, 1-dodecene and its isomers, as well as tridecanal and its isomers are each handled as a single pseudo compound due to the lack of data. Also, all compounds of the catalyst solution are treated as pure water. In general, mixing effects on the density are omitted for this model and mixture densities are solely obtained from weighted pure substance densities. This assumption has been tested to satisfactory results with test mixtures of the microemulsion system.

Modeling of Dynamics, Reliable Switchovers, and Controller Equations

To capture the dynamics of the process for, e.g., the start-up procedure and discrete switching between the phase separation states, several switching functionalities need to be implemented. Regarding this, twice differentiable sigmoidal functions are introduced in Sec. 2.4.2 and are used as triggers for the activation of model functionalities. For example, the reactor outlet flow is only active, if the liquid level exceeds the level of the overflow pipe inlet. The difference between the actual level (Lvl) and the overflow setpoint (Lvl^{SP}) is then used as argument for the sigmoid to enable switching functionality. However, with outlet stream activation, Lvl is regulated to

[3]DIPPR Project 801, https://www.aiche.org/dippr/projects/801 [Access: 2019-03-04]

be at Lvl^{SP}. For this case, $Sigmoid(Lvl^{SP} - Lvl) \approx 0.5$ applies. Thus, a $0 \rightarrow 1$ switching of model elements is not ensured and drawbacks such as violated component mass balances and continuously *jumping* or *hanging* triggers occur (see standard case in Fig. 4.10).

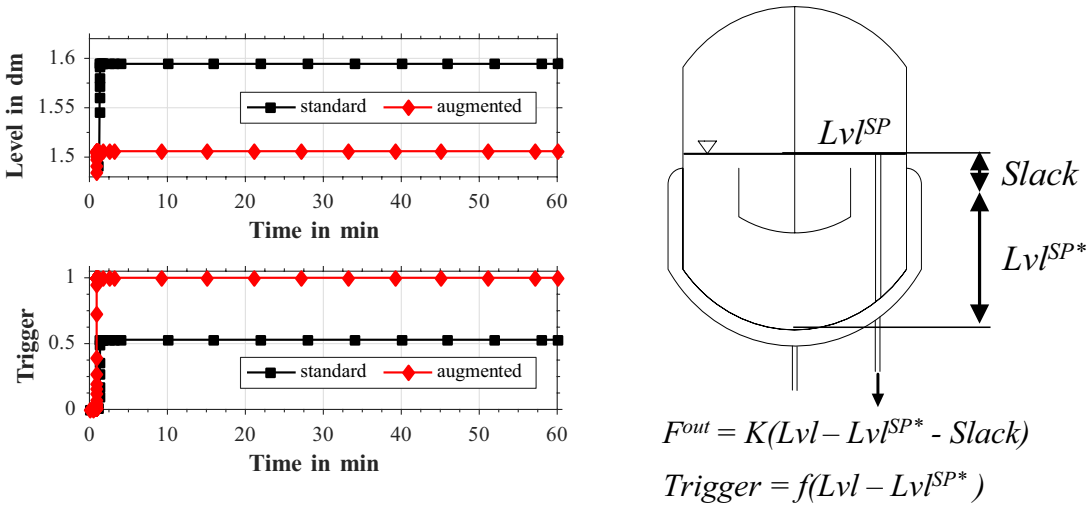

Fig. 4.10: Left: comparison of the trigger functionality for the standard and augmented sigmoidal function implementation. Trigger switching at a setpoint level of 1.5 dm desired. Right: level setpoint and slack configuration.

To overcome this hurdle, the implementation of sigmoidal functions for outlet flow triggering is augmented with a *Slack* variable:

$$TRIG = \frac{1}{2} + \frac{\frac{1}{2} \cdot (Lvl - Lvl^{SP*})}{\sqrt{(Lvl - Lvl^{SP*})^2 + \varepsilon}} \tag{4.3}$$

$$F^{Out} = \underbrace{KP \cdot (Lvl - Lvl^{SP})}_{Proportional\ Part} + \overbrace{KI \cdot I}^{Integral\ Part} \tag{4.4}$$

$$\frac{dI}{dt} = (Lvl - Lvl^{SP}) \cdot TRIG \tag{4.5}$$

$$Lvl^{SP} = Lvl^{SP*} + Slack \tag{4.6}$$

Firstly, the trigger function is defined, applying a modified setpoint level Lvl^{SP*} for the argument. The outlet stream definition F^{Out} could be formulated according Torricelli's law or a control equation. For model simplification, a PI-controller is proposed for F^{Out}. This ensures the physically driven increase or decrease of the outlet stream according to the current superelevation of the level and likewise avoids lasting control errors of the tank levels (integral behavior). A general definition for F^{Out} and the necessary differential equation for the differential part I of

the controller is given in Eq. (4.4)-4.5. The differential part of the controller equation is then augmented with the respective trigger, serving as *anti-windup*.

With the augmented control deviation $(Lvl - Lvl^{SP*} - Slack)$ of the PI-controller, the outlet stream ensures a level $Lvl^{SP*} + Slack$ – the desired setpoint in the tank. However, the argument of the trigger already switches to active at the lower level Lvl^{SP*}. Figure 4.10 emphasizes this stabilization of the switching functionality. For the augmented case, the sigmoidal function stays at the desired value of 1 and in contrast to the standard case, the respective tank level stabilizes at the desired setpoint $L^{SP} = 1.5\,\text{dm}$. Additionally, *min-operators*, already introduced in Eq. (2.4), are applied on F^{Out} to enforce strictly positive (and physically valid) outlet flows.

This strategy is applied throughout the model and results in significantly improved accuracy, since non-physical overfull tanks, negative flows, or wrongly truncated concentrations are avoided.

4.3.2 Feed Section

According to the mini-plant sections, firstly the feed section is modeled following Fig. 4.11.

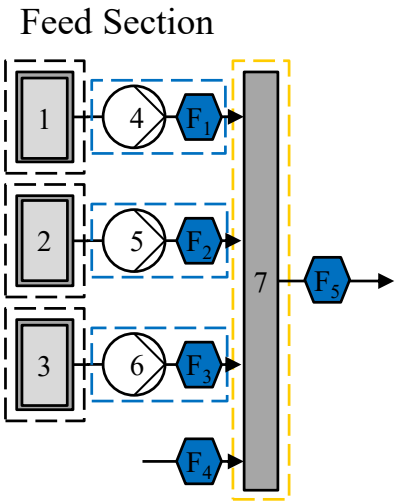

Fig. 4.11: Model scheme for the feed section.

The feed tanks itself (units 1-3) are implemented to link the available level sensor data from the plant to the model and allow for additional validation of feed streams $F_{s=1...3}$. Additionally, the feed streams are merged together with the total recycle stream $F_{s=4}$ in unit 7, the feed mixer. Following the proposed modeling systematics the component mass balances (**M**ass **B**alance (MB)) are set up for feed tanks and feed mixer (Eq. (C.13)-C.14).

The total feed streams $F_{s=1...3}$ result from the feed pump operation, represented by the application of desired setpoints $F^{SP}_{s=1...3}$. As a special feature, the feed streams are modified to account for all relevant operation modes of the plant: start-up/filling, full recycle, and the continuous operation. Hence, continuous transitions are enabled. Here, $TRIG^{PlantFill}_{Rec}$ identifies and switches on the filling status of the plant. F^{Conti}_{Feed} then represents the total feed to the plant in continuous operation mode, while $w^{i,Conti}_{Feed}$ are multipliers to adjust the total feed stream composition. The latter are specified according to the current calculated composition of the oily product stream.

$$F_s = F^{SP}_s \cdot (1 - TRIG^{PlantFill}_{Rec}) + F^{Conti}_{Feed} \cdot w^{Conti}_{Feed,s} \cdot TRIG^{PlantFill}_{Rec}, \qquad s = \{1 \dots 3\} \tag{4.7}$$

4.3.3 First Principles Model of the Reactor Unit

With the implementation of the hydroformylation kinetics, the reactor is one of the most important model elements. The modeling is done according to Fig. 4.12 and is subdivided into the actual unit modeling and the formulation of a suitable reaction kinetic in the next section.

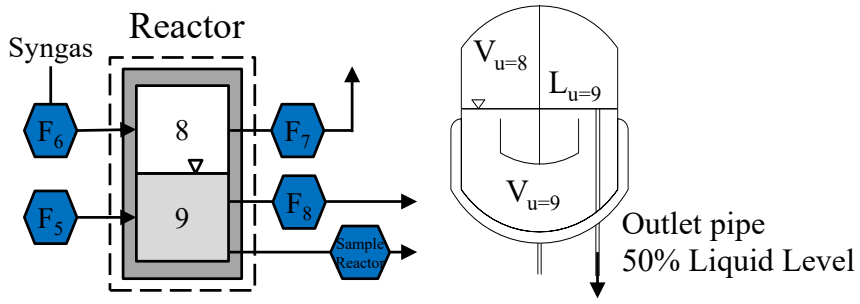

Fig. 4.12: Model scheme for the reactor.

Two hold-ups are relevant for his unit, the liquid phase, where the hydroformylation reaction takes place and a gas phase. The mass balance in Eq. (4.8) covers gas and liquid phase, relevant streams, a liquid sample purge $F^{Reactor}_{Sample,i}$, and the relevant reaction rates r_i of components. Additionally, the total component hold-up is subdivided according the existing phases:

$$\frac{\mathrm{d}HU^{Reactor}_i}{\mathrm{d}t} = F_{s=6,i} - F_{s=7,i} + F_{s=5,i} - F_{s=8,i} - F^{Reactor}_{Sample,i} + M_i \cdot L_{u=9} \cdot A_{u=9} \cdot r_i \tag{4.8}$$

$$HU^{Reactor}_i = HU^{L}_{u=9,i} + HU^{V}_{u=8,i} \tag{4.9}$$

The liquid drain from the reactor $F_{s=8}$ is activated using the afore described sigmoidal switching functions on the level $L_{u=9}$ (see right image in Fig. 4.12). The drain is thus set to be the sum of

the reactor feed and $F_{u=9}^{Lvl}$. The latter is an overflow regulation stream, designed as a PI-controller according to the deliberations in Sec. 4.3.1.

$$F_{s=8} = TRIG_{u=9}^{Lvl} \cdot F_{s=5} + F_{u=9}^{Lvl} \tag{4.10}$$

Related to the gas phase, the inlet and outlet streams $F_{s=6}$, $F_{s=7}$ are given below. $F_{s=7}^{Conti}$ is a design variable, setting the purge of gas phase from the reactor. This purge is required since the solubility of H_2 in the reaction mixture is higher than the solubility for CO. Hence, shifts in the composition of the gas phase are expected for a continuous operation. $F_{s=6}$ then specifies the feed stream of gas to the plant as the sum of purge stream setpoint and a regulation stream $F_{u=8}^{Gas}$. This is again defined as PI-controller, working on the deviation between current reactor pressure and its setpoint $p_{u=8}^{SP}$. Using Eq. (4.14) - 4.16, the gas feed composition can be switched between nitrogen and syngas feed, using an activation trigger $TRIG_{u=8}^{Gas}$.

$$F_{s=6} = F_{u=8}^{Gas} + F_{s=7}^{Conti} \tag{4.11}$$

$$F_{s=7} = F_{s=7}^{Conti} \tag{4.12}$$

$$p_{u=8}^{SP} = p^{Start} + TRIGGER_{u=9}^{Lvl} \cdot p^{Conti} \tag{4.13}$$

$$w_{s=6,i=6} = w_{s=6,i=6}^{SP} \cdot TRIG_{u=8}^{Gas} \tag{4.14}$$

$$w_{s=6,i=7} = w_{s=6,i=7}^{SP} \cdot TRIG_{u=8}^{Gas} \tag{4.15}$$

$$w_{s=6,i=8} = 1 - TRIG_{u=8}^{Gas} \tag{4.16}$$

The reactor pressure itself is calculated from the hold-up of the gas phase using the ideal gas law. Accordingly, the partial pressures for CO and H_2 are calculated in Eq. (4.18).

$$\sum_{i=1}^{Ni} \left(\frac{HU_{u=8,i}^{V}}{M_i}\right) = \frac{p_{u=8} \cdot 100 \cdot \left(V^{Reactor} - A_{u=9} \cdot \left(L_{u=9}\right)\right)}{R \cdot T_{u=9}} \tag{4.17}$$

$$\frac{HU_{u=8,i}^{V}}{M_i} = \frac{p_i^{V} \cdot 100 \cdot \left(V^{Reactor} - A_{u=9} \cdot \left(L_{u=9}\right)\right)}{R \cdot T_{u=9}} \qquad with\ i = \{6,7\} \tag{4.18}$$

This simplified approach is chosen, since only pressure and composition of the gas are relevant, assuming still moderate pressures. Also, other compounds are rather high boiling liquids applied at a reaction temperature of 95 °C. No significant partial pressures of these substances in the gas phase are expected. With a sufficiently large gas purge, the composition is then assumed to be constant, while physically correct mole numbers of gasses for gas hold-up and streams are not of interest. However, the gas solubility is relevant and its modeling described in Sec. 4.3.5.

4.3.4 Development of an Adapted Kinetic Model

Within this work, the proposed workflow for the formulation of adapted kinetic models for systems with inherent additional influences (see Sec. 2.3.4) is applied to generate a suitable kinetic model and gain a sufficiently precise representation of the reaction kinetics. This is mandatory since up to now no suitable kinetic models for reactions in microemulsions are documented in the literature.

Step 0: Model and Data Acquisition

Within the *Collaborative Research Center InPROMPT*, extensive studies on the reaction mechanism of the hydroformylation of 1-dodecene have been conducted. This resulted in the reaction network presented in Fig. 3.1 and a detailed (semi-)mechanistic kinetic model derived by (Kiedorf et al., 2014). The derivation of respective rate equations Eq. (4.19) - 4.24 for target *and* side reactions is based on a general methodology explained by Murzin et al. (2016) and considers the Wilkinson catalytic cycle (Fig. 2.11). The rate index $r = \{1 \dots 6\}$ denotes the reaction path according to Fig. 3.1 with 1: r_{Iso}, 2: r_{HydA}, 3: r_{HydB}, 4: r_{HyfoA}, 5: r_{HyfoB}, 6: r_{HyfoC}. Concentrations $c_{u=9,i=1\dots5}$ then represent the reactants: 1-dodecene (1), iso-dodecene (2), iso-tridecanal (3), dodecane (4), and tridecanal (5). Additionally, Eq. (4.25) gives a rate expression for the catalyst pre-equilibria, defining the concentration of active catalyst at current precursor concentration c_{cat} and dissolved gas concentrations of H_2 $c_{u=9,i=6}$ and CO $c_{u=9,i=7}$.

$$r^0_{r=1} = \psi_{cat} \cdot \frac{k^{ref}_{r=1} \cdot \exp(-\frac{E_{r=1}}{R} \cdot (\frac{1}{T_{u=9}} - \frac{1}{T^{ref}})) \cdot (c_{u=9,i=1} - \frac{c_{u=9,i=2}}{K^{eq}_{r=1}})}{(1 + K_{r=1,e=1} \cdot c_{u=9,i=1} + K_{r=1,e=2} \cdot c_{u=9,i=2})} \tag{4.19}$$

$$r^0_{r=2} = \psi_{cat} \cdot k^{ref}_{r=2} \cdot \exp(-\frac{E_{r=2}}{R} \cdot (\frac{1}{T_{u=9}} - \frac{1}{T^{ref}})) \cdot c_{u=9,i=2} \cdot c_{u=9,i=6} \tag{4.20}$$

$$r^0_{r=3} = \psi_{cat} \cdot \frac{k^{ref}_{r=3} \cdot \exp(-\frac{E_{r=3}}{R} \cdot (\frac{1}{T_{u=9}} - \frac{1}{T^{ref}})) \cdot c_{u=9,i=2} \cdot c_{u=9,i=6} - \frac{c_{u=9,i=4}}{K^{eq}_{r=3}}}{(1 + K_{r=3,e=1} \cdot c_{u=9,i=1} + K_{r=3,e=2} \cdot c_{u=9,i=4} + K_{r=3,e=3} \cdot c_{u=9,i=6})} \tag{4.21}$$

$$r^0_{r=4} = \psi_{cat} \cdot k^{ref}_{r=4} \cdot \exp(-\frac{E_{r=4}}{R} \cdot (\frac{1}{T_{u=9}} - \frac{1}{T^{ref}})) \cdot c_{u=9,i=2} \cdot c_{u=9,i=6} \cdot c_{u=9,i=7} \tag{4.22}$$

$$r^0_{r=5} = \psi_{cat} \cdot \frac{k^{ref}_{r=5} \cdot \exp(-\frac{E_{r=5}}{R} \cdot (\frac{1}{T_{u=9}} - \frac{1}{T^{ref}})) \cdot c_{u=9,i=1} \cdot c_{u=9,i=6} \cdot c_{u=9,i=7}}{(1 + K_{r=5,e=1} \cdot c_{u=9,i=1} + K_{r=5,e=2} \cdot c_{u=9,i=5} + K_{r=5,e=3} \cdot c_{u=9,i=6})} \tag{4.23}$$

$$r^0_{r=6} = \psi_{cat} \cdot k^{ref}_{r=6} \cdot \exp(-\frac{E_{r=6}}{R} \cdot (\frac{1}{T_{u=9}} - \frac{1}{T^{ref}})) \cdot c_{u=9,i=1} \cdot c_{u=9,i=6} \cdot c_{u=9,i=7} \tag{4.24}$$

$$\psi_{cat} = \frac{c_{cat}}{(1 + K_{cat,e=1} \cdot c_{u=9,i=7} + K_{cat,e=2} \cdot \frac{c_{u=9,i=7}}{c_{u=9,i=6}})} \tag{4.25}$$

$$K^{eq}_r = \exp(\frac{\Delta G_r}{R \cdot T_{u=9}}) \qquad with\ r = \{1,3\} \tag{4.26}$$

$$\Delta G_{r=3} = (-126.28 + 0.13 \cdot T + 6.8 \cdot (10)^{-6} \cdot (T)^2) \cdot (10)^3 \tag{4.27}$$

The component reaction rates r_i in Eq. (4.28)-Eq. (4.32) are expressed as the summarized reaction rates r_r and are applied for mass balances (Eq. (4.8)). For now, a batch reactor system (lab) is considered for later parameter estimation. This initial model is denoted as $Model_0$ further on.

$$1-\text{dodecene}: \quad \frac{\mathrm{d}c_{i=1}}{\mathrm{d}t} = r_{i=1} = -r^0_{r=1} - r^0_{r=3} - r^0_{r=5} - r^0_{r=6} \tag{4.28}$$

$$\text{iso}-\text{dodecene}: \quad \frac{\mathrm{d}c_{i=2}}{\mathrm{d}t} = r_{i=2} = r^0_{r=1} - r^0_{r=2} - r^0_{r=4} \tag{4.29}$$

$$\text{iso}-\text{tridecanal}: \quad \frac{\mathrm{d}c_{i=3}}{\mathrm{d}t} = r_{i=3} = r^0_{r=4} + r^0_{r=6} \tag{4.30}$$

$$\text{dodecane}: \quad \frac{\mathrm{d}c_{i=4}}{\mathrm{d}t} = r_{i=4} = r^0_{r=2} + r^0_{r=3} \tag{4.31}$$

$$\text{tridecanal}: \quad \frac{\mathrm{d}c_{i=5}}{\mathrm{d}t} = r_{i=5} = r^0_{r=5} \tag{4.32}$$

The model provides five liquid reactant concentrations $c_{i=1}$ - $c_{i=5}$ as measurable model states. Temperature, catalyst concentration, and pressure are then relevant controls or input variables. Hereof, reaction pressure is linked to the gas solubility model in Sec. 4.3.5 to provide concentrations of CO and H_2 in the liquid phase. The multitude of adjustable kinetic parameters can be classified as: activation energies E_r, pre-exponential factors k_r^{ref}, reaction equilibrium coefficients K_r^{eq}, related to the respective Gibbs reaction energies ΔG_r, and lumped inhibition constants $K_{r,e}$, which are linked to reactant concentrations. This totals in 23 parameters for which Kiedorf et al. (2014) provide an initial set estimated from experimental data for the hydroformylation of 1-dodecene in a thermomorphic solvent system, using BiPhePhos as ligand.

Step 1: Kinetic Information and Parameter Estimation for $\mathbf{Model_0}$

Having prepared $Model_0$, it is now verified that the initial model structure is suitable for the new application case: hydroformylation in MES using SulfoXantPhos as ligand.

Hereof, kinetic experiments were conducted with variation of the afore mentioned inputs $T_{u=9}$, c_{cat}, and $p_{u=9}$. Dynamic trajectories of the concentrations $c_{i=1}$-$c_{i=5}$ are tracked with sampling and GC analysis (see Tab. C.5 for list of experiment designs). The experiments were performed by Tobias Hamerla and Tobias Pogrzeba at Department of Chemistry, Technische Universität Berlin, using a 100 mL batch autoclave. Information on catalyst preparation, the experimental setup, and analytics can be found elsewhere (Pogrzeba et al., 2015; Pogrzeba et al., 2017a). Subsequently, a parameter estimation is performed on the gathered kinetic data using $Model_0$. For this purpose, the framework for parameter estimation with subset selection and quantification of relevant uncertain parameters (Sec. 2.4.3) is used. The implementation is done in Matlab, using *lsqnonlin* as solver for optimizatio (PE) and *ode15s* for solving the **O**rdinary **D**ifferential **E**quation (system) (ODE) (see Sec. C.2 for additional information):

Initially, parameter initials and bounds are specified. Here, the parameter set presented by Kiedorf et al. (2014) is used with rather large intervals around the parameter initials to guarantee a feasible solution of the PE problem. Due to the non-linearity of the model, a global solution of the parameter estimation cannot be guaranteed and several local minima are possible depending on parameter initials. Thus, a parameter sampling is applied, using the *Hammersley Sequence Sampling* (Hammersley, 1960; Diwekar et al., 1997). It is carried out on logarithmic scaling to ensure an appropriate distribution of the samples in the parameter space, since bounds are spanning several orders of magnitude. In total 5000 samples are tested on a pre-run of *lsqnonlin* with a maximum of five iterations. The sample showing the smallest RSME is then used for the actual parameter estimation. The applied parameter bounds, the calculated best initial guess, and the final set of estimated parameters can be found in Tab. C.6.
The final solution is obtained with an RSME of 0.0229 and visualized in Fig. 4.13 through a

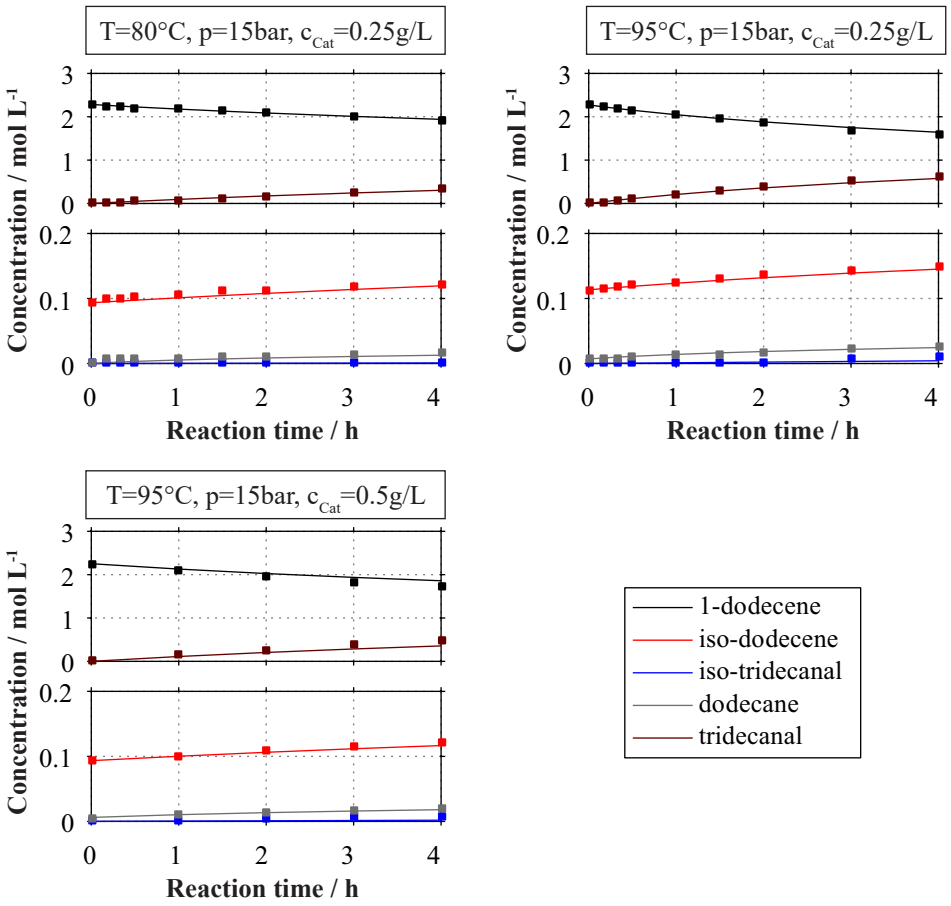

Fig. 4.13: Comparison of experimental data (symbols) and $Model_0$ (lines) for varied temperatures and catalyst concentrations. Further experimental conditions have been kept constant. Max. error from max. analytical error: $\pm 0.08\,\mathrm{mol\,L^{-1}}$.

comparison of experimental data and model kinetic trajectories for different reaction temperatures and catalyst concentrations. In each case, a very good agreement is found and it can be stated, that $Model_0$ generally is suitable to represent the kinetics of the hydroformylation in the regarded microemulsion system. However, this statement is limited to the varied set of inputs for $Model_0$ ($T_{u=9}$, c_{cat}, $p_{u=9}$) and a fixed composition of the microemulsion used for experiments.

Step 2: Influence Identification

The next step of the workflow deals with the analysis of the desired application and identification of additional influences on the reaction performance not incorporated in $Model_0$. This has already been done in Sec. 3.3 with respect to the applied microemulsion system and application in a mini-plant. From this discussion, the surfactant concentration γ and the ligand to metal ratio $L:M$ are shown to be most relevant. Variations of both are typically eminent for the mini-plant operation with internal recycles. The relevance of these additional influence factors becomes apparent in Fig. 4.14. Here, the amount of surfactant and the ligand to metal ratio are changed and compared to the model trajectories obtained from $Model_0$. In both cases, large deviations on the concentration profiles of 1-dodecene and tridecanal are obvious. Additionally, the increased isomerization for $L:M = 2$ is not covered by the model.

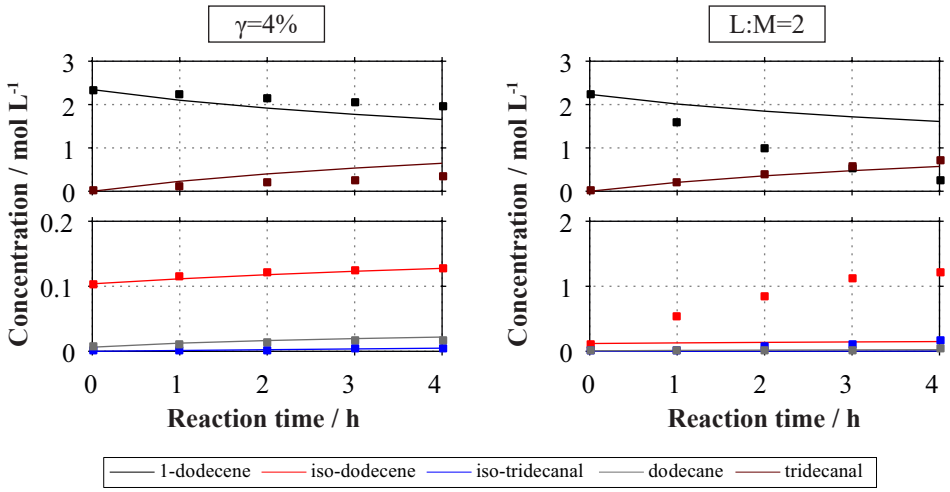

Fig. 4.14: Comparison of experimental data (symbols) and $Model_0$ (lines) at ligand and surfactant concentrations differing from standard standard mixture composition ($\gamma_0 = 8\,\%$, $LM = 4$). Max. error from max. analytical error: $\pm 0.08\,\mathrm{mol\,L^{-1}}$.

Step 3: Model Update and Parameter Estimation for $\mathbf{Model_{real}}$

Now, the effect of these additional influences is quantified with additional kinetic experiments. Mathematical formulations to adapt reaction rate equations in $Model_0$ are derived thereof:

Surfactant concentration: Figure 3.6 shows an increase of conversion over the surfactant concentration. It is assumed, that all reaction rates are increased uniformly, since the overall reaction selectivity does not change. A suitable power law expression is therefore given. Therein, $c_{i=12}$ is the surfactant concentration in $\mathrm{mol\,L^{-1}}$ and ${}^{n^{Surfactant}}$ an adjustable parameter to account for disproportionality:

$$r_r = c_{i=12}^{\;n^{Surfactant}} \cdot r_r^0 \tag{4.33}$$

Ligand to metal ratio: In this case, a step-wise transition of the reaction performance is observed (Fig. 3.3). Below a critical ratio, 1-dodecene conversion increases by a factor of roughly 3. At the same time, selectivity drops significantly. This effect is due to the already discussed shifting catalyst equilibria. A closer look at kinetic data reveals that isomerization of 1-dodecene is increased by a factor of roughly 6. Concurrently, also the hydroformylation reactions are accelerated (terminal and branched aldehyde), yet less pronounced. To account for this, the implementation of a sigmoidal function into the kinetic model is proposed:

$$r_r = (1 + \frac{k_r^{LM}}{1 + \exp(-(K^{LM} - \frac{n_{i=11,u=9}}{n_{i=10,u=9}}) \cdot P_r^{trig})}) \cdot r_r^0 \tag{4.34}$$

Here, $n_{i=11,u=9}$ and $n_{i=10,u=9}$ are the amount of ligand and catalyst precursor, respectively. K^{LM} is an adjustable parameter defining the *threshold* of the ligand to metal ratio, at which the sigmoidal takes action. k_r^{LM} then represents the *enhancement factor* for the corresponding rate equation and P_r^{trig} then adjusts the slope of the sigmoidal function. This adaption is then applied on the rate equations for the isomerization and all hydroformylation reactions. Thus, together with Eq. (4.33) a new adapted kinetic model $Model_{real}$ for the hydroformylation of 1-dodecene in microemulsions is obtained, containing six additional adjustable parameters:

$$r_{r_1}^* = c_{i=12}^{\;n^{Surfactant}} \cdot (1 + \frac{k_r^{LM}}{1 + \exp(-(K^{LM} - \frac{n_{i=11,u=9}}{n_{i=10,u=9}}) \cdot P^{trig})}) \cdot r_{r_1}^0, \quad r_1 = \{1,4,5,6\} \tag{4.35}$$

$$r_{r_2}^* = c_{i=12}^{\;n^{Surfactant}} \cdot r_{r_2}^0, \quad r_2 = \{2,3\} \tag{4.36}$$

Subsequently, another parameter estimation is performed on the updated set of experiments listed in Tab. C.7. The procedure is analogous to the PE for $Model_0$, using the final estimated parameters for $Model_0$ as initials. For the six newly introduced parameters, initials and assumptions on bounds are derived from experimental data. The applied parameter bounds and best initial set retrieved from Hammersley sampling are again listed in the appendix (Tab. C.8). At this point it has to be noted, that the PE is again performed on the full set of parameters to account for the structural change in the kinetics and additional experimental data.

The final solution is obtained with an RSME of 0.0313 and Tab. C.9 listing the obtained parameters together with information on their identifiability. The final active set of parameters conclusively includes $K_{cat,e=1}$, which influences the amount of available active catalyst in the system and thus all reaction rates. With $K_{r=5,e=2}$, an inhibition factor is also included, since it influences the predominant hydroformylation reaction rate. However, due to the rather small set of experimental data and high parameter colinearity, the number of identifiable parameters is very small and thus it is not surprising that the obtained parameter values differ significantly from the ones found for $Model_0$. Interestingly though, obtained activation energies are still in physically reasonable orders of magnitude and in good accordance to the values found by (Kiedorf et al., 2014). Especially, the activation energy for the hydroformylation of the terminal olefin obtained with $E_{r=5} = 57.9\,\mathrm{kJ\,mol^{-1}}$ is in good accordance with literature data collected for the applied catalyst in microemulsions ($59\,\mathrm{kJ\,mol^{-1}}$, (Pogrzeba et al., 2017a)) and single phase systems ($57.12\,\mathrm{kJ\,mol^{-1}}$, (Bhanage et al., 1997)).

To visualize these results, Fig. 4.15 and Fig. 4.16 are provided. Both plots demonstrate the successful adaptation of the initial kinetic model. The influences of surfactant and ligand to metal ratio are displayed adequately and deviations between model prediction and experiments are widely below 10 %. However, concentrations of iso-dodecene are slightly underestimated for the reference case ($T = 95\,^{\circ}\mathrm{C}$) and reduced surfactant concentration ($\gamma = 4\,\%$). This is partly explained by experiments not depicted here, showing the opposite deviation. In case of reduced ligand to metal ratio $L:M = 2$, $Model_{real}$ gains an adequate prediction of highly increased isomerization.

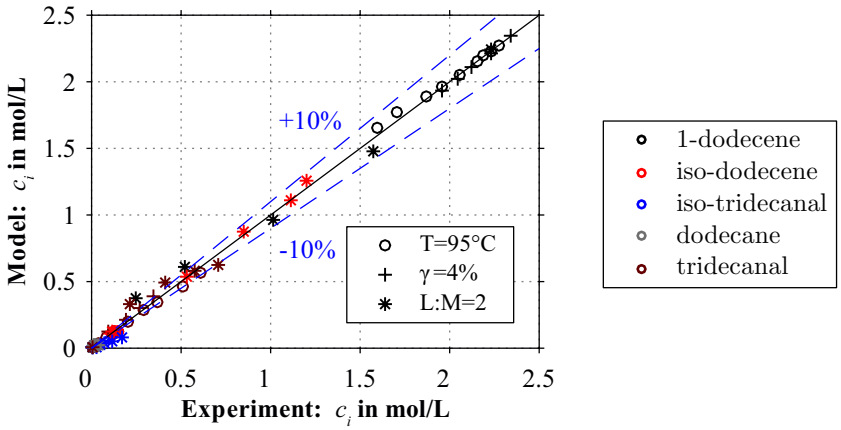

Fig. 4.15: Parity plot adapted kinetics: $T = 95\,^{\circ}\mathrm{C}$ reference experiment, $L:M = 2$ variation ligand to metal ratio, $\gamma = 4\,\%$ variation surfactant concentration. Max. error: $\pm 0.08\,\mathrm{mol\,L^{-1}}$.

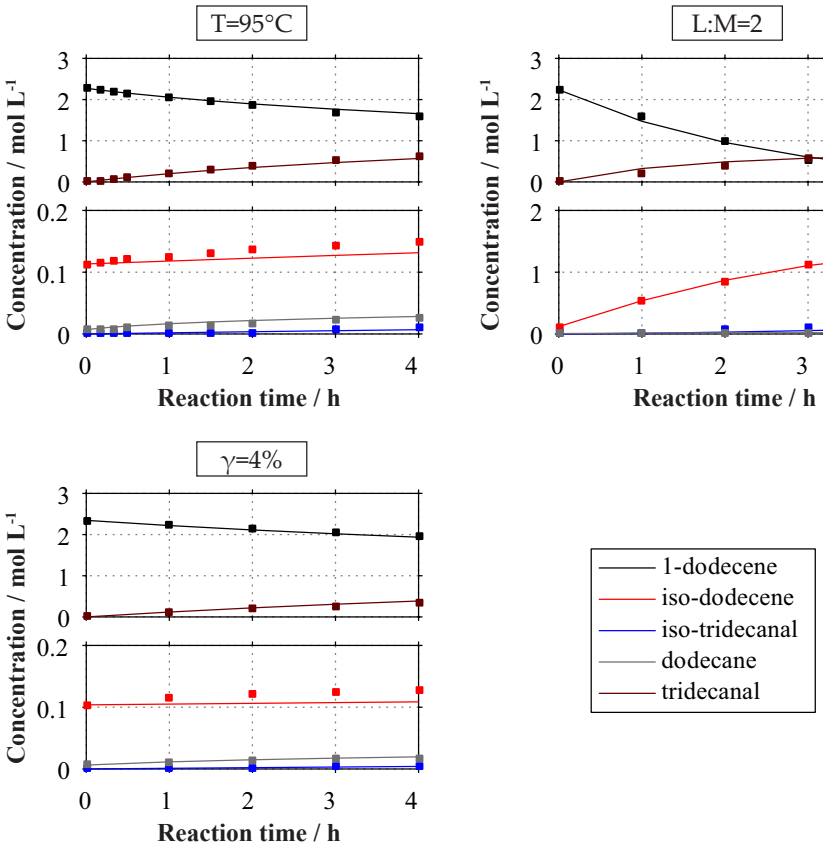

Fig. 4.16: Comparison of experimental data (symbols) and the adapted kinetic model (lines) for experiments: $T = 95\,^{\circ}\mathrm{C}$ reference experiment, $L:M = 2$ variation of ligand to metal ratio, $\gamma = 4\,\%$ variation of surfactant concentration. Max. error from max. analytical error: $\pm 0.08\,\mathrm{mol\,L^{-1}}$.

4.3.5 Gas Solubility Model

CO and H_2 are main reactants for the hydroformylation reaction. Hence, their solubility in the liquid phase of the reactor needs to be modeled adequately. Regarding this, Bernas et al. (2010, p. 618) state, that "organic synthesis reactions are in most cases considered to be slow or very slow compared to the diffusion processes. In the ultimate case, this means that the gas–liquid reaction system can be treated as a pseudo-homogeneous system; just the solubilities of the gas-phase components are included in the model". An according model formulation for the hydroformylation of propene, based on reactive films, yielded very good accordance of model simulations and experimental data. For long-chained alkenes, even lower reaction rates are found and thus kinetic limitations should be dominant and mass transfer can be omitted (Wender et al., 1956). For the system at hand, this is confirmed with Fig. A.2, since the reaction rate is found to be independent from the *gassing* stirrer speed.

From a thermodynamic point of view, the gas liquid equilibrium can be modeled using Henry's law for all gasses in each liquid component. However, literature data are limited to H_2 and CO solubility in water at high pressure. For CO, solubility data are only partially available for some oil phase compounds (Vogelpohl et al., 2013; Vogelpohl et al., 2014). Moreover, the effect of microemulsion structure and phase behavior on gas solubilities is widely unknown. Thus investigations on the gas solubility in the MES have been carried out in cooperation with Max Lemberg, Department of Biochemical and Chemical Engineering, TU Dortmund. Therein, the gas solubility has been measured for varying concentrations α, γ, and product content Y, as well as state variables T and p. Hence, the solubility is determined as a mixture property:

Experimental Procedure

The experiments were performed using a view cell for high pressures up to 400 bar. The system is temperature-controlled and allows for variable volumes between 27.5 and 59.6 mL. A detailed description of the test stand, sample preparation, and experimental procedure can be found in (Vogelpohl et al., 2013; Bardas, 2015). Two series of experiments were performed for CO and syngas respectively, varying the mixture composition according to Tab. 4.5. For each mixture, at minimum two pressure setpoints between 10 and 30 bar were tested at 85 °C and 105 °C. Microemulsion mixtures were prepared from distilled water, 1-dodecene, tridecanal, and Marlipal® 24/70. Syngas is used in a molar composition of 1:1.

Tab. 4.5: Composition of prepared samples for gas solubility experiments.

Exp.	1	2	3	4	5	6	7	8	9	10	11
α / %	50	50	50	50	50	50	50	40	40	60	60
γ / %	8	8	8	10	6	10	6	10	6	10	6
Y / %	0	20	40	0	0	40	40	40	40	40	40

Note that due to experimental limitations, the solubility of hydrogen cannot be measured directly. Instead, it is derived from the syngas solubility, assuming a constant molar ratio of CO and H_2 of 1:1 and no interactions in the liquid phase:

$$x^L_{Syngas}(p_{u=8}) = x_{i=7}(p^V_{i=7}) + x_{i=6}(p^V_{i=6}) \tag{4.37}$$

Model Formulation

The collected data are in the appendix (Tab. C.10, Tab. C.11) and further used to derive an empirical model for the mole fractions of CO and H_2. Five inputs α, γ, Y, T, and p are given, for which a polynomial model is formulated. For this, firstly the gathered data is evaluated regarding

the variation of a single input at constant remaining variables to identify appropriate polynomial orders. This is subsequently done for all inputs and combinations of inputs. Respective polynomial parameters are obtained from a nonlinear regression in Matlab and finally the model structure is tested for overfitting using additional test data. Subsequently, the following model structure is obtained:

$$\begin{aligned} x_{i=7} =& p^V_{i=7} \cdot P_{i=7,Sol=1} + T \cdot P_{i=7,Sol=2} + \alpha \cdot P_{i=7,Sol=3} + \gamma \cdot P_{i=7,Sol=4} + Y \cdot P_{i=7,Sol=5} \\ &+ \gamma^2 \cdot P_{i=7,Sol=6} + Y^2 \cdot P_{i=7,Sol=7} + p^V_{i=7} \cdot T \cdot P_{i=7,Sol=8} + p \cdot \alpha \cdot P_{i=7,Sol=9} \\ &+ p^V_{i=7} \cdot \gamma \cdot P_{i=7,Sol=10} + p^V_{i=7} \cdot Y \cdot P_{i=7,Sol=11} + T \cdot \alpha \cdot P_{i=7,Sol=12} \\ &+ T \cdot \gamma \cdot P_{i=7,Sol=13} + T \cdot Y \cdot P_{i=7,Sol=14} + \alpha \cdot Y \cdot P_{i=7,Sol=15} \end{aligned} \tag{4.38}$$

$$\begin{aligned} x_{i=6} =& p_{u=8} \cdot P_{i=6,Sol=1} + T \cdot P_{i=6,Sol=2} + \alpha \cdot P_{i=6,Sol=3} + \gamma \cdot P_{i=6,Sol=4} + Y \cdot P_{i=6,Sol=5} \\ &+ (\gamma)^2 \cdot P_{i=6,Sol=6} + (Y)^2 \cdot P_{i=6,Sol=7} + p_{u=8} \cdot T \cdot P_{i=6,Sol=8} + p_{u=8} \cdot \alpha \cdot P_{i=6,Sol=9} \\ &+ p_{u=8} \cdot \gamma \cdot P_{i=6,Sol=10} + p_{u=8} \cdot Y \cdot P_{i=6,Sol=11} + T \cdot \alpha \cdot P_{i=6,Sol=12} \\ &+ T \cdot \gamma \cdot P_{i=6,Sol=13} + T \cdot Y \cdot P_{i=6,Sol=14} + \alpha \cdot Y \cdot P_{i=6,Sol=15}) - x_{i=7} \end{aligned} \tag{4.39}$$

$$with\ \alpha = \alpha_{s=8},\ \gamma = \gamma_{s=8},\ Y = Y_{s=8},\ T = (T_{u=9} - 273.15)$$

The regression results are shown in the 3-D plot in Fig. 4.17. Here the experimental data is shown together with the model for CO and H_2. Additionally, parity plots are supplied in Fig. 4.18. These indicate an acceptable model accuracy, especially under consideration of test data used for model validation. Finally, obtained parameters are given in Tab. C.12.

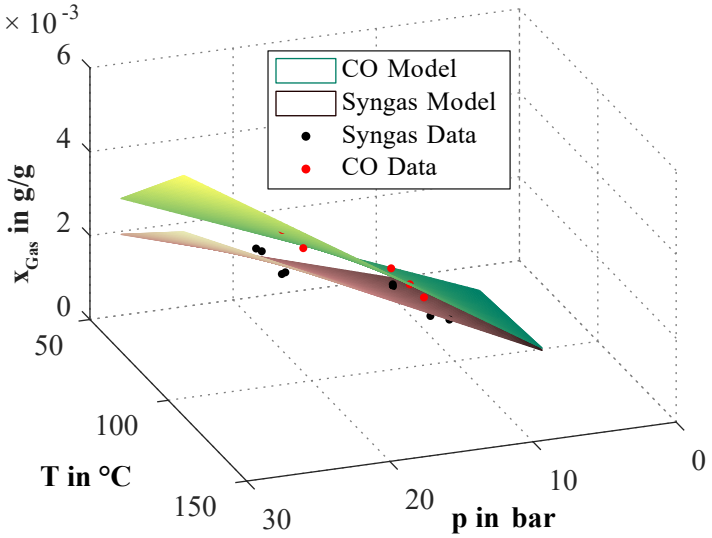

Fig. 4.17: Comparison of modeled solubility of CO and syngas with experimental data.

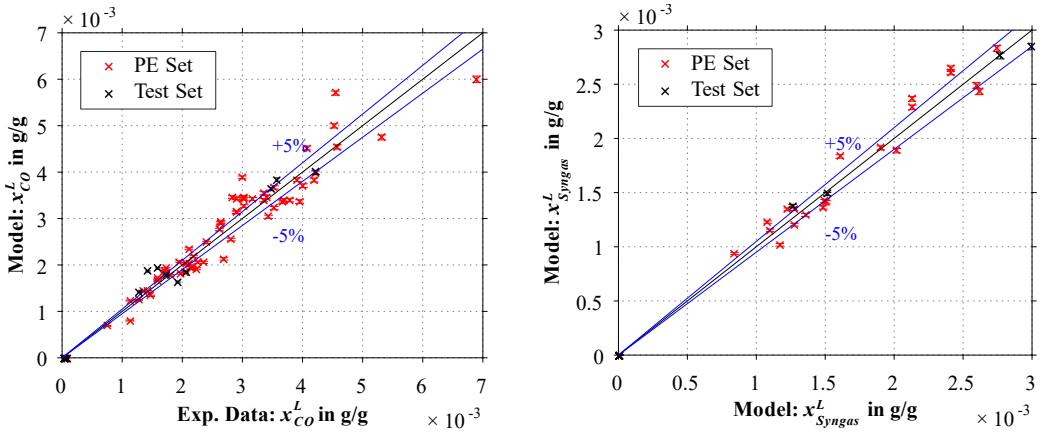

Fig. 4.18: Parity plot for the solubility of CO and syngas in the reaction mixture.

4.3.6 Phase Separation Model and Soft-Sensor Development

Following the system analysis in Sec. 3.4, a feasible mini-plant operation is only possible for maintaining three-phasic separation of the microemulsion. As a key element of this thesis, a respective phase separation model is derived to track this separation operation region and describe the component distribution therein. Hence, a profound description of phase compositions and valid component mass balances are mandatory for such a model. One core part for that is a soft-sensor to account for missing measurements of relevant states in the mini-plant (Sec. 3.4.5). The general modeling approach is depicted in Fig. 4.19 and combines the specific features of the three-phasic separation of the microemulsion derived from theory (Sec. 2.1.3) and the analysis of the actual system behavior. The fundamental idea is that for given constant temperature and pressure and occurring three-phasic miscibility gap, the component concentrations in the forming phases are constant. Only the fractions of phase volumes are changing according to the initial position within the miscibility gap (see top left in Fig. 4.19). With this idea in mind, optically accessible phase levels can be correlated with the integral concentrations of the mixture (phase state soft-sensor). In a second step, the composition of the individual phases is to be specified. The main idea here is to focus on the excess phases, thus the upper oily and lower aqueous phase of the separated ME. The composition of these phases is dominated by the two-phase oil-water system and the exceptionally low surfactant concentrations defined by the cmc.
Combining these two approaches results in a fully determined model for the phase separation. Relevant component concentrations used in the model adhere to the set of relevant sensitive influences on the phase separation system from Tab. 3.5: oil to water ratio α, surfactant concentration γ, and yield Y. These are used to uniquely identify the mixture composition for application of the phase separation model. In mini-plant model nomenclature those are given as:

$$\alpha_{s=8} \cdot \left(\sum_{i=1}^{5} w_{s=8,i} + w_{s=8,i=9}\right) = \sum_{i=1}^{5} w_{s=8,i}, \qquad \gamma_{s=8} = w_{s=8,i=12} \tag{4.40}$$

$$Y_{s=8} \cdot \sum_{i=1}^{5} w_{s=8,i} = w_{s=8,i=5}, \qquad Y_{s=8}^{mol} \cdot \sum_{i=1}^{5} \frac{w_{s=8,i}}{M_i} = \frac{w_{s=8,i=3}}{M_{i=3}} + \frac{w_{s=8,i=5}}{M_{i=5}} \tag{4.41}$$

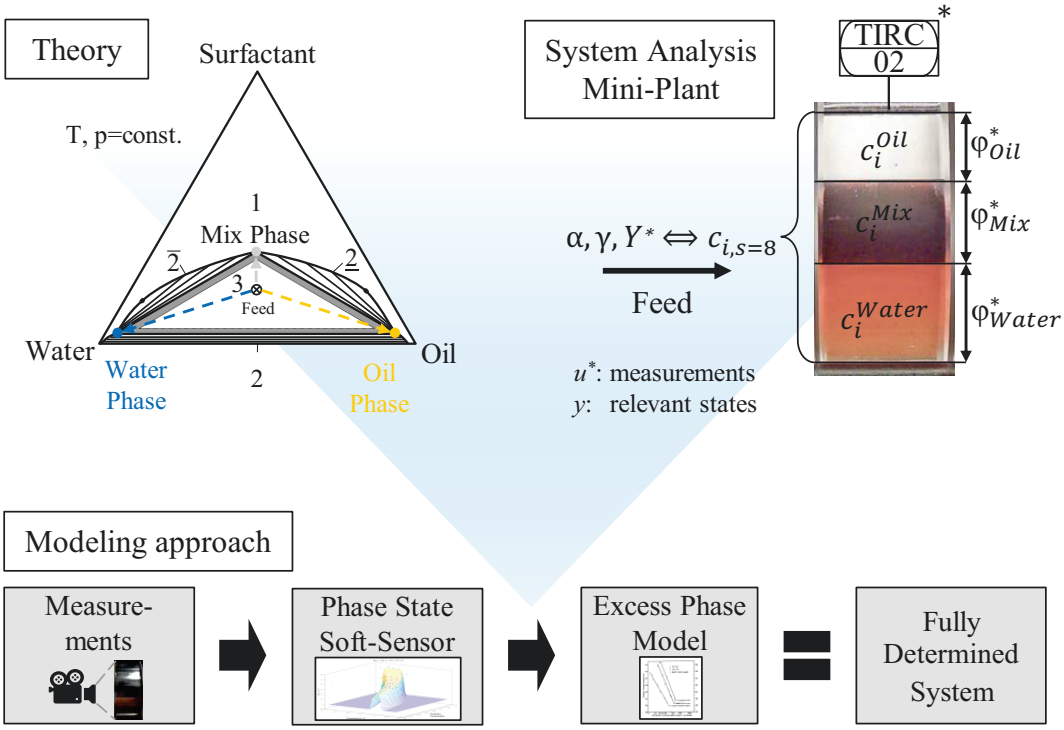

Fig. 4.19: General approach for the development of the phase separation model.

General assumptions for this phase separation model include disregarding separation dynamics, since the observed phase separation time is rather small in the operation region. Thus only the final *equilibrium* state is of interest and assumed to be reached in the settler. Additionally, radial or axial temperature gradients are omitted, since specific heating zones are supplied for the settler and the ratio of heat transfer area to volume is high.

Due to the lack of available fundamental models and with widely unknown fluid properties, empirical models based on experimental data are employed to describe observed system behavior. In accordance with deliberations in Sec. 2.4.1 polynomial models are generated, since the amount

of available data is still limited and prevents the application of more sophisticated data-driven modeling techniques. For this purpose, Matlab's *Curve Fitting* toolbox and the *poylfitn*[4] toolbox are used. In each case, test data or cross validation is applied to prevent overfitting.

Phase Volume Fraction Model and Concentration Soft-Sensor

The first part of the phase separation modeling aims for an empiric description of *Kahlweit's Fish* and the corresponding fractions phase volumes. For mini-plant operation, two aspects are of interest: given a mixture concentration, in which temperature interval does the three-phase separation occur? Which fractions of phase volumes are present at specific temperatures? This is systematically derived from the gathered experimental information of the full mapping of the phase separation system in Sec. 3.4.6.

Temperature boundaries

The data is firstly classified into separation states (Fig. 3.8) to identify the operation region (three-phase separation). Of importance therein is a suitable oil phase volume fraction >10 % to always ensure feasible product capture for mini-plant operation. Transition states from the three to the two-phasic separation are however excluded from this set, because the formation of dense surfactant layers is observed here. These layers represent undesired local accumulations, which impede mini-plant operation.

Subsequently, temperature limits for the operation region are obtained for sampled mixtures. These are then merged into polynomial models for an upper bound Th^{PhS} in Eq. (4.42) and lower bound Tl^{PhS} in Eq. (4.43) respectively. The corresponding parameters are listed in Tab. C.13 Figure 4.20 shows the model surfaces in comparison to the experimental results. Here, especially the steep descent of the T-γ model plane and the rather small width of *Kahlweit's Fish* are in good accordance with identified dependencies in Fig. 3.11.

$$\begin{aligned} Th^{PhS} =& P^{Th,PhS}_{ps=1}\cdot 1 + P^{Th,PhS}_{ps=2}\cdot\alpha + P^{Th,PhS}_{ps=3}\cdot\gamma + P^{Th,PhS}_{ps=4}\cdot Y + P^{Th,PhS}_{ps=5}\cdot\alpha\cdot\gamma + P^{Th,PhS}_{ps=6}\cdot\gamma\cdot Y \\ &+ P^{Th,PhS}_{ps=7}\cdot\alpha\cdot\gamma\cdot Y + P^{Th,PhS}_{ps=8}\cdot\alpha^2 + P^{Th,PhS}_{ps=9}\cdot\gamma^2 + P^{Th,PhS}_{ps=10}\cdot Y^2 \end{aligned} \tag{4.42}$$

$$\begin{aligned} Tl^{PhS} =& P^{Tl,PhS}_{ps=1}\cdot 1 + P^{Tl,PhS}_{ps=2}\cdot\alpha + P^{Tl,PhS}_{ps=3}\cdot\gamma + P^{Tl,PhS}_{ps=4}\cdot Y + P^{Tl,PhS}_{ps=5}\cdot\alpha\cdot\gamma + P^{Tl,PhS}_{ps=6}\cdot\gamma\cdot Y \\ &+ P^{Tl,PhS}_{ps=7}\cdot\alpha\cdot\gamma\cdot Y + P^{Tl,PhS}_{ps=8}\cdot\alpha^2 + P^{Tl,PhS}_{ps=9}\cdot\gamma^2 + P^{Tl,PhS}_{ps=10}\cdot Y^2 \end{aligned} \tag{4.43}$$

$$with\ \alpha = \alpha_{s=8},\ \gamma = \gamma_{s=8},\ Y = Y_{s=8},\ T = (T_{Settler} - 273.15)$$

[4] https://www.mathworks.com/matlabcentral/fileexchange/34765-polyfitn [Access: 2019-03-14]

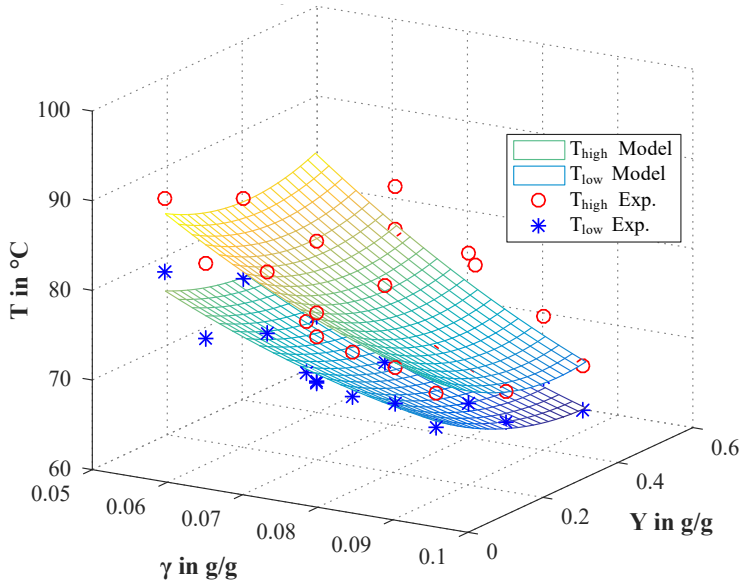

Fig. 4.20: Model surface plots of the lower and upper boundary for temperature of the three-phase region depending on yield and surfactant concentration at constant oil to water ratio of 50 %.

Evolution of fractions of phase volumes

Next, the correlation of the initial mixture concentration and temperature with the fractions of phase volumes ($\alpha,\gamma = f(\Phi^{Oil},\Phi^{Mix},\Phi^{Water},T,Y)$) is modeled. This is a core functionality of the model, since it enables the crucial soft-sensing of concentrations from phase level data observed in the mini-plant's settler. To describe the modeling approach, Fig. 4.21 depicts experimental

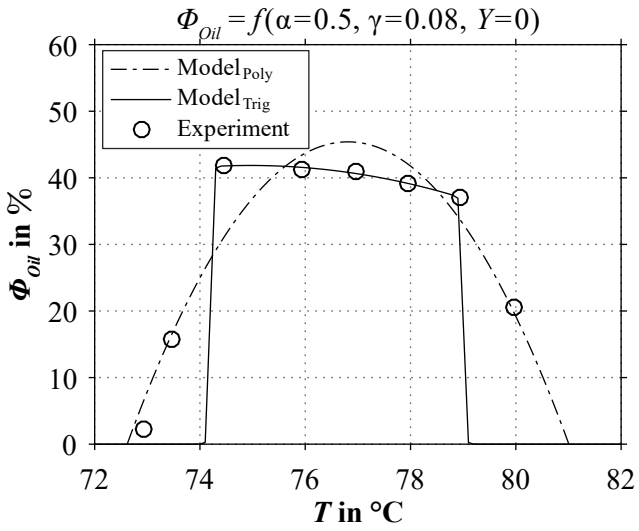

Fig. 4.21: Comparison modeling strategy for the phase volume fraction evolution: polynomial (Poly) and sigmoid augmented model (Trig).

data on the oil phase fraction for the standard mixture $\alpha = 50\,\%$ - $\gamma = 8\,\%$ - $Y = 0\,\%$. Yet again the main focus lies on an adequate representation of the three-phase separation for which high oil levels > 30 % are present in contrast to the border regions. This behavior is hard to capture with standard polynomial model structures and leads to larger deviations in the region of interest ($\text{Model}_{\text{Poly}}$).

Therefore, an augmented model structure is implemented using switching functions ($\text{Model}_{\text{Trig}}$). Using the model functions Tl^{PhS} and Th^{PhS} for the critical lower and upper boundary of temperature for the three-phase body, these can be augmented with sigmoidal functions to activate the formation of relevant phase fractions only within the three-phase region ($[Tl^{PhS},Th^{PhS}]$):

$$\begin{aligned}\Phi^{Phase} =&(P^{PhS,Phase}_{ps=1}\cdot 1 + P^{PhS,Phase}_{ps=2}\cdot T + P^{PhS,Phase}_{ps=3}\cdot \alpha + P^{PhS,Phase}_{ps=4}\cdot \gamma + P^{PhS,Phase}_{ps=5}\cdot Y\\ &+ P^{PhS,Phase}_{ps=6}\cdot T\cdot\alpha + P^{PhS,Phase}_{ps=7}\cdot \alpha\cdot\gamma + P^{PhS,Phase}_{ps=8}\cdot\gamma\cdot Y\\ &+ P^{PhS,Phase}_{ps=9}\cdot T\cdot\gamma + P^{PhS,Phase}_{ps=10}\cdot\alpha\cdot Y + P^{PhS,Phase}_{ps=11}\cdot T^2 + P^{PhS,Phase}_{ps=12}\cdot\alpha^2\\ &+ P^{PhS,Phase}_{ps=13}\cdot\gamma^2 + P^{PhS,Phase}_{ps=14}\cdot Y^2)\cdot TRIG^{PhS,Th}\cdot TRIG^{PhS,Tl}\end{aligned} \tag{4.44}$$

$$Phase = \{Oil, Water\},\ \alpha = \alpha_{s=8},\ \gamma = \gamma_{s=8},\ Y = Y_{s=8},\ T = (T_{Settler} - 273.15)$$

$$TRIG^{Th,PhS} = \frac{1}{1+\exp(500\cdot(T - Th^{PhS}))} \tag{4.45}$$

$$TRIG^{Tl,PhS} = \frac{1}{1+\exp(-500\cdot(T - Tl^{PhS}))} \tag{4.46}$$

Φ^{Oil} and φ^{Water} are then used to describe the behavior of respective fractions of the phase volumes depending on α, γ, T, and Y. For parameter fitting, solely data classified as three-phase region data and in accordance with Tl^{PhS} and Th^{PhS} are used. Again resulting parameters are listed in the appendix (Tab. C.14). Additionally, Fig. 4.22 provides a visualization of the models of φ^{Oil} and φ^{Water} for varied temperature and surfactant concentration. The experimental observation therein is widely captured by the model. The present deviations mainly result from partly inconsistent data in the border area of the three-phase region. This could be rectified by extended experimental studies including retries. However, phenomena identified in general for MES are well reproduced and in good agreement with theory presented in Sec. 2.1.3. For completeness it is noted, that the volume fraction of the emulsion phase φ^{Mix} is obtained from the subtraction of the excess phase volumes from the total volume of the separated system.

$$V^{L,tot}_{Settler} = (\varphi^{Oil} + \varphi^{Mix} + \varphi^{Water})\cdot V^{L,tot}_{Settler} \tag{4.47}$$

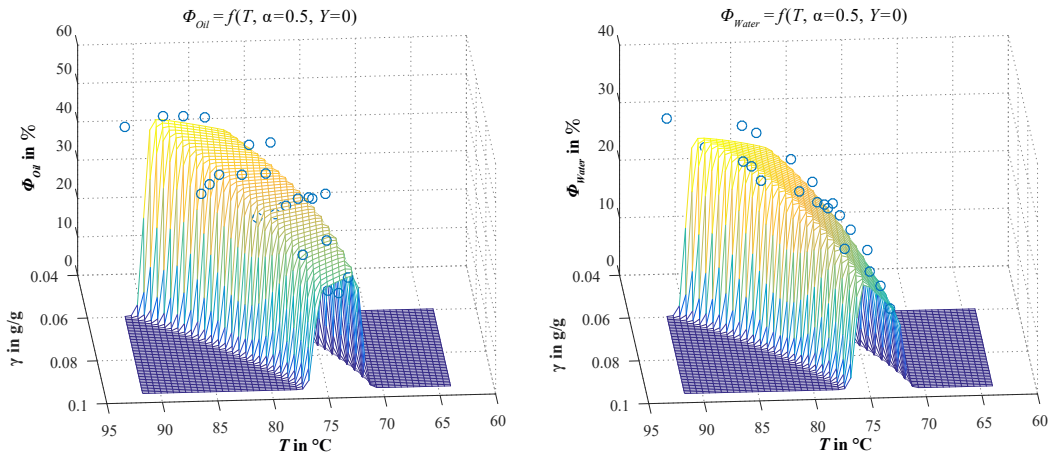

Fig. 4.22: Surface plots of the model of excess phase volume fractions for oily (left) and aqueous phase (right) at constant oil to water ratio and yield. Markers highlight experimental data.

Model of the Excess Phase Composition

The second part of the phase separation model now aims for the determination of component concentrations within the excess phases. Yet again, this is not an easy task, since all available analytical devices fail in determining surfactant and water concentrations. Hence, characteristic phenomena of MES are exploited. The idea and modeling procedure is sketched in Fig. 4.23. Firstly, a reduced set of key components is derived from the applied microemulsion system. The influence of dissolved gasses is neglected and water is assumed to be the main compound of the aqueous phase. Thus catalyst and ligand are basically not considered. Due to the very high reaction selectivities, 1-dodecene is assumed to be the main *nonpolar* oily compound subsidiary also for iso-dodecene and dodecane. Tridecanal is then considered as the main *polar* oily compound. The following modeling idea then is based on two main assumptions:

- As already presented in Sec. 2.1.3, the surfactant concentration in oily and aqueous excess phase are at the level of the cmc. For mixtures of nonionic surfactants, water, and long-chained oily substrates the cmcs are around 10^{-5} to $10^{-4}\,\mathrm{mol\,L^{-1}}$ (Rosen et al., 1982; Huibers et al., 1996).
- At these very small surfactant concentrations, the composition of excess phases is then mainly determined by the two-phasic oil-water miscibility gap below the three-phase body and compositions can be estimated by calculating the **L**iquid-**L**iquid-**E**quilibrium (LLE).

This means, that with the formulation of a cmc model and an appropriate LLE description both excess phases can be fully determined regarding their composition. This model formulation is then connected to the mini-plant model through a back calculation of the reduced set of key components into the full set of components *i*.

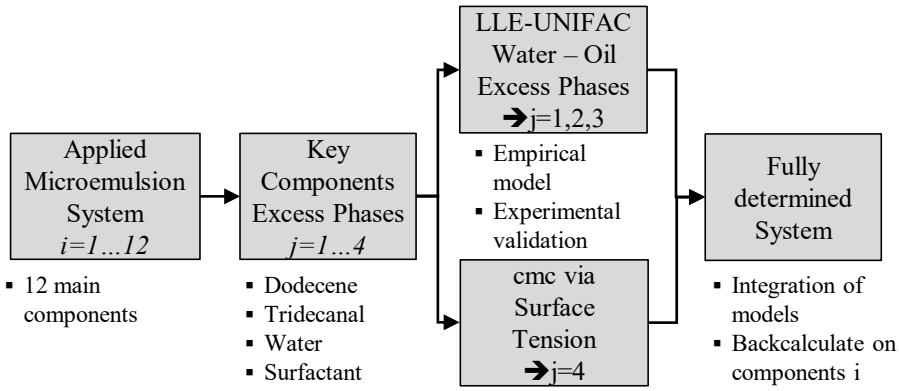

Fig. 4.23: Modeling strategy for the oil and water excess phase composition.

cmc model for surfactant concentrations

As already shown in Sec. 2.1.1, the cmc is accessible via surface tension measurements. Thus, extended experimental studies for the system at hand were conducted with representative *pure* oil and water phases:

- pure 1-dodecene as oily excess phase
- 60 wt.-% 1-dodecene – 40 wt.-% tridecanal as oily excess phase under reaction conditions
- water with 2.17 wt.-% sodium sulfate

It needs to be mentioned that the aqueous excess phase actually contains larger quantities of rhodium catalyst and ligand. In preliminary studies the influence of catalyst, ligand, and catalyst activation was tested against of exemplary systems water-sodium sulfate or water only. Similar values for the surface tension were obtained for catalyst containing aqueous solutions and water-sodium sulfate. Hence, the effect of sodium sulfate on thecmc is assumed to be predominant.

For each phase composition, successive dilutions for the surfactant concentration were tested at different temperatures. The obtained data are listed in the appendix in Tab. C.20 - C.21. cmc data for different temperatures are then computed and used to parameterize a model fit function for all investigated phase systems (bottom right in Fig. 4.24). The obtained results are in very good agreement with theory as an increase of cmc with rising temperatures can be observed for 1-dodecene, while the inverse case is present for water. This behavior is backed by the observations of Kahlweit et al. (1990). For the 1-dodecene/tridecanal system also a decrease of the cmc with temperature is observed, while values are still in the same order of magnitude as for pure 1-dodecene. This is rather unexpected and assumed to be due to the higher polarity of tridecanal. For the aqueous excess phase, the obtained cmc at 25 °C ($4.01 \cdot 10^{-5}$ g/g) is furthermore in good agreement with data presented by Rosen et al. (1982) ($5.59 \cdot 10^{-5}$ g/g for pure substance equivalent of Marlipal®, $C_{12}E_8$).

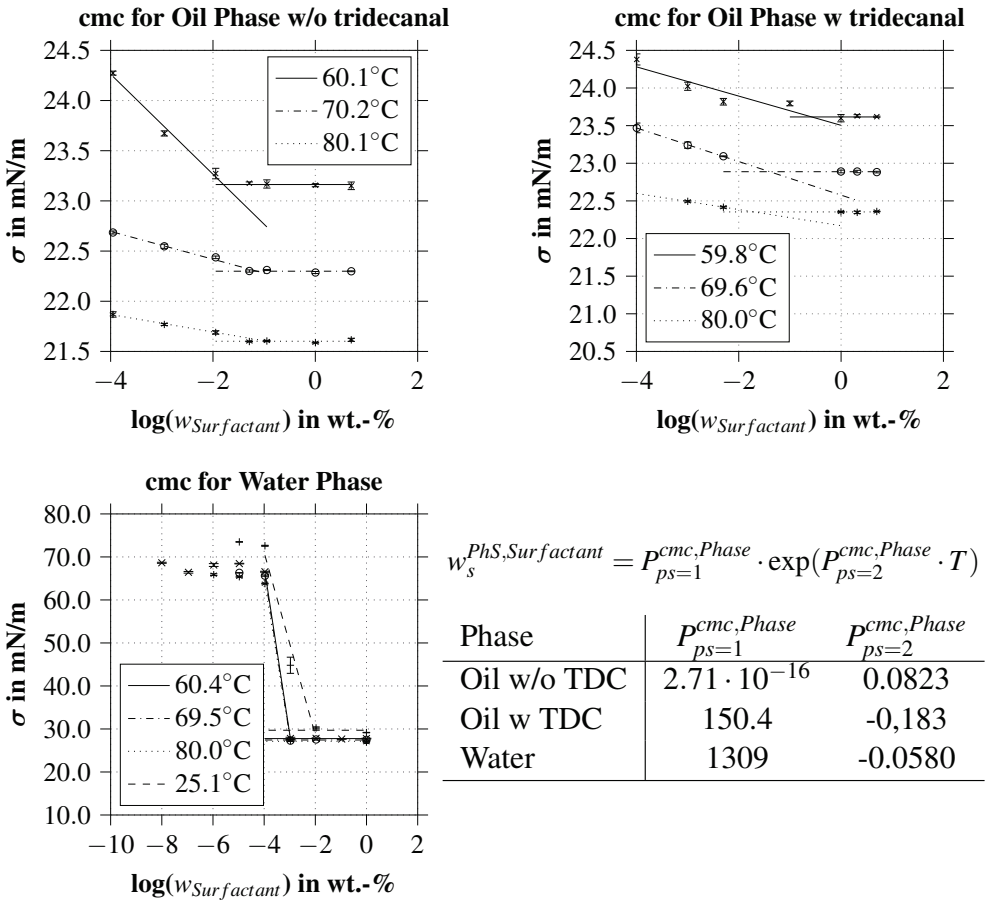

$$w_s^{PhS,Surfactant} = P_{ps=1}^{cmc,Phase} \cdot \exp(P_{ps=2}^{cmc,Phase} \cdot T)$$

Phase	$P_{ps=1}^{cmc,Phase}$	$P_{ps=2}^{cmc,Phase}$
Oil w/o TDC	$2.71 \cdot 10^{-16}$	0.0823
Oil w TDC	150.4	-0,183
Water	1309	-0.0580

Fig. 4.24: Experimental determination of cmc. The cmc is obtained at the intersection of descending and constant part of the surface tension. A fit function for the temperature dependent cmc $w_s^{PhS,Surfactant}$ is provided together with fitted parameters for each tested phase composition.

LLE surrogate model for excess phase composition

The next step then handles the determination of the oil and water amount in the excess phases. According to Fig. 2.3 and Fig. 2.4 the composition of this excess phases is dominated by the binary miscibility gap of oil and water. With respect to the very small surfactant concentrations (cmc) and the rather steep binodal expected for the water-1-dodecene/tridecanal miscibility gap, it is assumed that the composition of the excess phases can be approximated solely with the pseudo-binary LLE. This system is then given by water ($j = 1$) and a pseudo oily compound consisting of 1-dodecene ($j = 2$) and tridecanal ($j = 3$).

For this, the molar Gibbs enthalpy of the mixture *Mix* is defined:

$$g_{Mix} = \sum_{j=1}^{3} x_j \cdot g_j + RT\left(\sum_{j=1}^{3} x_j \cdot \ln(x_j)\right) + RT\left(\sum_{j=1}^{3} x_j \cdot \ln(\gamma_j)\right) \tag{4.48}$$

γ_j are the activity coefficients of the respective compounds, which account for the nonideal behavior of the mixture. As a first estimate, UNIFAC is used to calculate these activity coefficients, since necessary group contribution and interaction parameters are available from literature. Based on Eq. (4.48), separation and respective phase compositions at given temperature and yield are calculated using UNIFAC coefficients listed in the appendix in Sec. C.2.

The calculated equilibrium data is then used to set up a surrogate polynomial model of the form:

$$\begin{aligned} x_j^{Oil/Water} =& P_{ps=1}^{Conc,Oil/Water} \cdot T_{Settler} + P_{ps=2}^{Conc,Oil/Water} \cdot Y_{s=8}^{mol} + P_{ps=3}^{Conc,Oil/Water} \cdot T_{Settler} \cdot Y_{s=8}^{mol} \\ &+ P_{ps=4}^{Conc,Oil/Water} \cdot T_{Settler}^2 + P_{ps=5}^{Conc,Oil/Water} \cdot T_{Settler} \cdot Y_{s=8}^{mol\,2} \\ &+ P_{ps=6}^{Conc,Oil/Water} \cdot T_{Settler}^2 \cdot Y_{s=8}^{mol} + P_{ps=7}^{Conc,Oil/Water} \end{aligned} \tag{4.49}$$

Fitted parameters are listed in the appendix in Tab. C.15 and the results of LLE calculations and fitting of the surrogate model are visualized in Fig. 4.25. For both surface plots, the mole fraction of water x_{Water} in the water and oily excess phase is shown depending on temperature T and tridecanal content Y. In both cases, the correlation of x_{Water} with the inputs is physically consistent as a higher mutual solubility of water and oil is present for increased temperature and higher yields (meaning a higher oil phase polarity). The model has been further validated with a comparison to GC measurements of the oil phase collected from separated microemulsions. Considering the measurement accuracy and the very small concentrations to be measured, a qualitatively good agreement of model and experiment can be ensured.

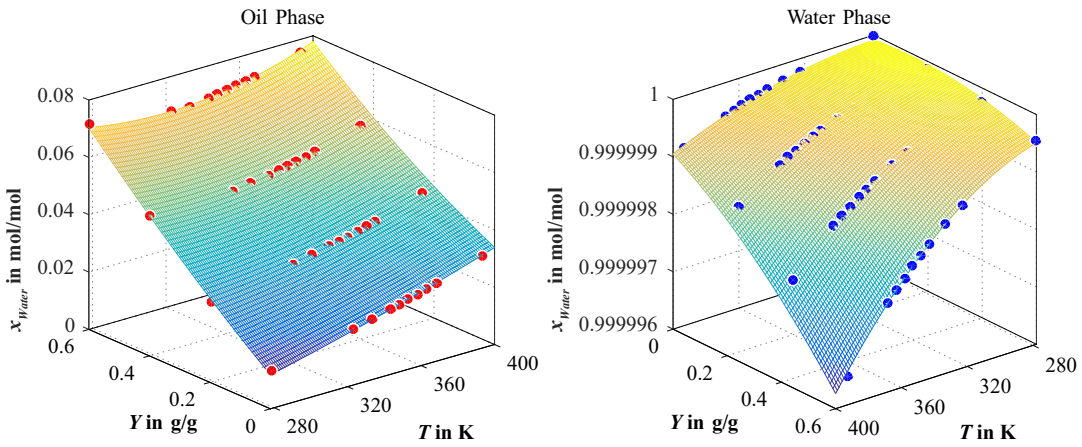

Fig. 4.25: Surface plots of polynomial surrogate model for content of water in the excess phases derived from UNIFAC (marker points).

Inference on full set of model concentrations

As a final step, the concentration information of the sub models for the excess phases is merged and subsequently transformed into the domain of the mini-plant model. Hence, the reduced set of component concentrations of the excess phases is back calculated to obtain the full set of all twelve components concentrations. Detailed outlines on that are waived at this point and the reader is referred to the given detailed procedure in Fig. C.10 and subsubsection C.2.

4.3.7 Settler Model for Dynamic Three-Phase Separation

The phase separation model is now implemented into a model of the settler. It is assumed, that the separation behavior is solely defined by the composition of the ME at the settler's inlet and its temperature. Thus, developed phase fractions are transported to the respective phase hold-ups already present in the settler. Additionally, diffusion between the phase hold-ups, as well as backmixing are neglected. This assumption is supported by rather large residence times in the settler applied for plant operation, the fast separation of the microemulsion within the three-phase region, and the lack of rigorous descriptions of mass transfer and fluid properties. Figure 4.26 shows the general idea: a splitter unit prior to the separation zone in the settler is applied. According to its composition and its temperature feed stream $F_{s=8}$ is separated into the individual phases of the microemulsion. These "phase streams" are then fed into respective independent phase hold-ups of the actual settler unit. Three respective phase drains are then provided. Though, these are not connected to a certain phase and the phase exiting via a certain drain can vary.

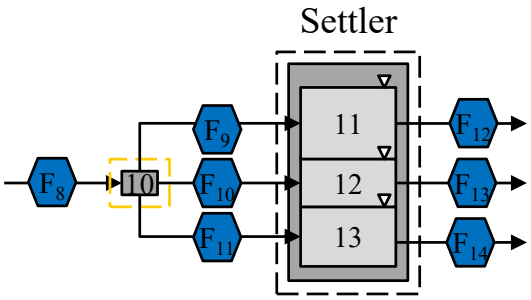

Fig. 4.26: Model scheme for the settler.

Splitter Module

The splitter unit $u = 10$ is represented by a component mass balance, showing the split of the reactor outlet into three phase streams: $s = 9$ oil phase, $s = 10$ mix/emulsion phase, $s = 11$ water

phase. The actual phase split is calculated using the model of the fractions of phase volumes presented above. Thus, Φ^{Oil} and Φ^{Water} are applied on the reactor outlet volume flow:

$$F_{s=8,i} = F^{Oil}_{s=9,i} + F^{Mix}_{s=10,i} + F^{Water}_{s=11,i} \tag{4.50}$$

$$\sum_{i=1}^{Ni} \frac{F^{Oil}_{s=9,i}}{\rho_{Settler,i}} = \Phi^{Oil} \cdot \sum_{i=1}^{Ni} \frac{F_{s=8,i}}{\rho_{Settler,i}} \tag{4.51}$$

$$\sum_{i=1}^{Ni} \frac{F^{Water}_{s=11,i}}{\rho_{Settler,i}} = \Phi^{Water} \cdot \sum_{i=1}^{Ni} \frac{F_{s=8,i}}{\rho_{Settler,i}} \tag{4.52}$$

Component mass streams $F^{Oil}_{s=9,i}$ and $F^{Water}_{s=11,i}$ are then calculated according to the model of the composition of the excess phases, using the concentration measures $w_s^{Oil,tot,PhS}$, $w_s^{PhS,Water,tot}$, and $w_s^{PhS,Surfactant}$ (see also Fig. C.10) as total oil, water, or surfactant content in$F^{Oil}_{s=9,i}$ and $F^{Water}_{s=11,i}$:

$$F^{Phase}_{s,i} \cdot (\sum_{i=1}^{5} F_{s=8,i}) = w_s^{Oil,tot,PhS} \cdot F_{s=8,i} \cdot F_s^{Phase} \qquad for\ i = \{1 \dots 5\} \tag{4.53}$$

$$F^{Phase}_{s,i} \cdot F_{s=8} = F_{s=8,i} \cdot F_s^{Phase} \qquad for\ i = \{6 \dots 8\} \tag{4.54}$$

$$F^{Phase}_{s,i=9} = w_s^{PhS,Water,tot} \cdot w_{cat}^{Water} \cdot F_s^{Phase} \tag{4.55}$$

$$F^{Phase}_{s,i=10} = w_s^{PhS,Water,tot} \cdot w_{cat}^{Rh} \cdot F_s^{Phase} \tag{4.56}$$

$$F^{Phase}_{s,i=11} = w_s^{PhS,Water,tot} \cdot w_{cat}^{Lig} \cdot F_s^{Phase} \tag{4.57}$$

$$F^{Phase}_{s,i=12} = w_s^{PhS,Surfactant} \cdot F_s^{Phase} \tag{4.58}$$

$$\text{Indexing} - \text{Oil Phase} : s = 9, Phase = Oil \qquad \text{Water Phase} : s = 11, Phase = Water$$

Exemplarily the amount of each oily reactant in water or oily excess phase is specified using Eq. (4.53). It is assumed, that the mass ratio of an oily compound $i = 1 \dots 5$ compared to the sum of all oily compounds is the same for the splitter feed and splitted streams. This general idea is then also adapted for dissolved gasses and the aqueous catalyst solutions. For the latter, a constant composition is assumed, set by w_{cat}^{Water}, w_{cat}^{Rh}, and w_{cat}^{Lig}. At this point it is highlighted that this also sets the catalyst loss towards the oil phase only being dependent on its water content. This set of equations provides a full determination of all mass fractions for both excess phases. The composition of the emulsion split stream is then a consequence of the mass balance.

First Principles Model of the Settler

The settler unit is modeled with three individual hold-ups. Thus, three mass balances are

implemented. Each phase hold-up is solely fed with the respective stream from the splitter unit ($F^{Oil}_{s=9,i}$, $F^{Mix}_{s=10,i}$, $F^{Water}_{s=11,i}$). However, the volume fraction of microemulsion phases might vary due to the current separation state, while the outlet positions of the settler unit are mechanically fixed. Thus, it is a priori not clear which phase is drawn from which settler drain. Regarding this, a continuous switching of the composition of settler outlet streams is implemented:

$$\frac{\mathrm{d}HU^{Oil,L}_{u=11,i}}{\mathrm{d}t} = F^{Oil}_{s=9,i} - (F_{s=12} \cdot TRIG^{Out,Oil}_{u=11} + F_{s=13} \cdot TRIG^{Out,Mix}_{u=11} + F_{s=14} \cdot TRIG^{Out,Water}_{u=11}) \cdot w^{Oil}_{u=11,i} \tag{4.59}$$

$$\begin{aligned}\frac{\mathrm{d}HU^{Mix,L}_{u=12,i}}{\mathrm{d}t} = {} & F^{Mix}_{s=10,i} - (F_{s=13} \cdot (1 - TRIG^{Out,Mix}_{u=11}) \cdot (1 - TRIG^{Out,Mix}_{u=13}) \\ & + F_{s=14} \cdot (1 - TRIG^{Out,Water}_{u=13}) \cdot (1 - TRIG^{Out,Water}_{u=11}) \\ & + F_{s=12} \cdot (1 - TRIG^{Out,Oil}_{u=11}) \cdot (1 - TRIG^{Out,Oil}_{u=13})) \cdot w^{Mix}_{u=12,i}\end{aligned} \tag{4.60}$$

$$\frac{\mathrm{d}HU^{Water,L}_{u=13,i}}{\mathrm{d}t} = F^{Water}_{s=11,i} - (F_{s=14} \cdot TRIG^{Out,Water}_{u=13} + F_{s=13} \cdot TRIG^{Out,Mix}_{u=13} + F_{s=12} \cdot TRIG^{Out,Oil}_{u=13}) \cdot w^{Water}_{u=13,i} \tag{4.61}$$

To visualize this implementation, Fig. 4.27 represents a scheme of the settler unit with three fixed outlets 1-3. Respective phase hold-ups are represented by the phase level L_{Oil}, L_{Em}, and L_{Water}, varying between 0 and the maximum level of the settler $L^{tot}_{Settler}$. Together with the level setpoints for the outlet drains $L^{SP,Outlet}_{Oil}$, $L^{SP,Outlet}_{Mix}$, and $L^{SP,Outlet}_{Water}$ the formulation of switching functions is possible like shown in the schematic drawing. Exemplarily $TRIG^{Out,Mix}_{u=13}$ is used to check, whether an enlarged water phase is present, which is superseding the emulsion phase at the middle drain. Consequently, this leads to a total of six switching functions. For the middle emulsion phase the logical statement applies that it is present at a certain outlet, if none of the other phases is present (no trigger active).

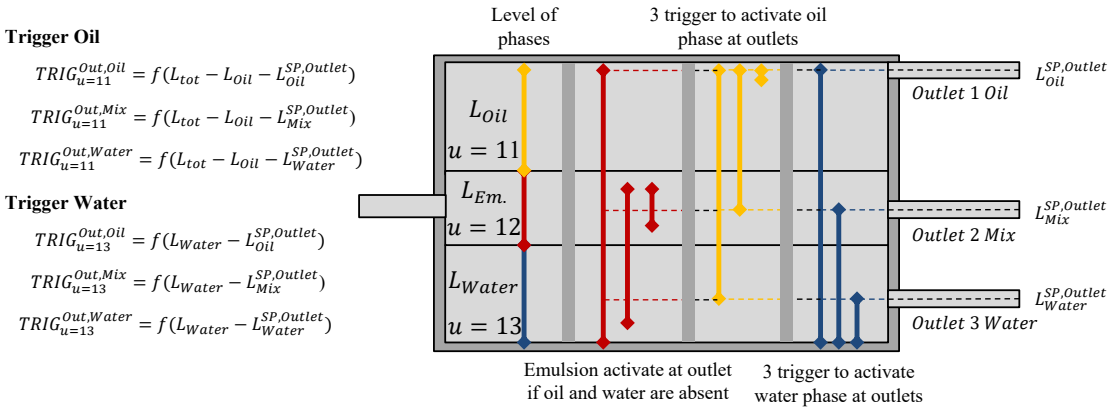

Fig. 4.27: Scheme for the dynamic activation of the drain of individual phases at the settler outlets.

The actual determination of the relevant phase levels L_{Oil}, L_{Em}, and L_{Water} is then done, assuming the geometry of the settler as a horizontal cylinder. Here, a polynomial surrogate is provided, since trigonometric equation for the volume of horizontal cylinders causes numerical instabilities and multiple possible solutions. Respective formulations are given in Sec. C.2 and respective volumes of the present phase hold-ups u are derived, using Eq. (C.9).

Finally, streams exiting the settler are introduced in Eq. (4.62)-4.64. These are determined by the control variables F_{Rec}^{Phase} representing the respective stream setpoints of recycle pumps. Since the top drain $F_{s=12}$ is an overflow, a sigmoid function $TRIG_{Settler}^{Lvl}$ is applied on total level of the settler activating $F_{Settler}^{Lvl}$. The remaining outlets are only activate, if sufficient liquid is fed to the plant, which is determined using $TRIG_{Rec}^{PlantFill}$ (see Sec. 4.3.8)

$$F_{s=12} = TRIG_{Settler}^{Lvl} \cdot F_{Rec}^{Oil} + F_{Settler}^{Lvl} \tag{4.62}$$

$$F_{s=13} = TRIG_{Rec}^{PlantFill} \cdot F_{Rec}^{Mix} \tag{4.63}$$

$$F_{s=14} = TRIG_{Rec}^{PlantFill} \cdot F_{Rec}^{Water} \tag{4.64}$$

4.3.8 Recycle and Product Section

At last, recycle and product section of the mini-plant model are reviewed. The main functionalities are derived following the modeling scheme in Fig. 4.28. Unit $u = 14$ represents the buffer

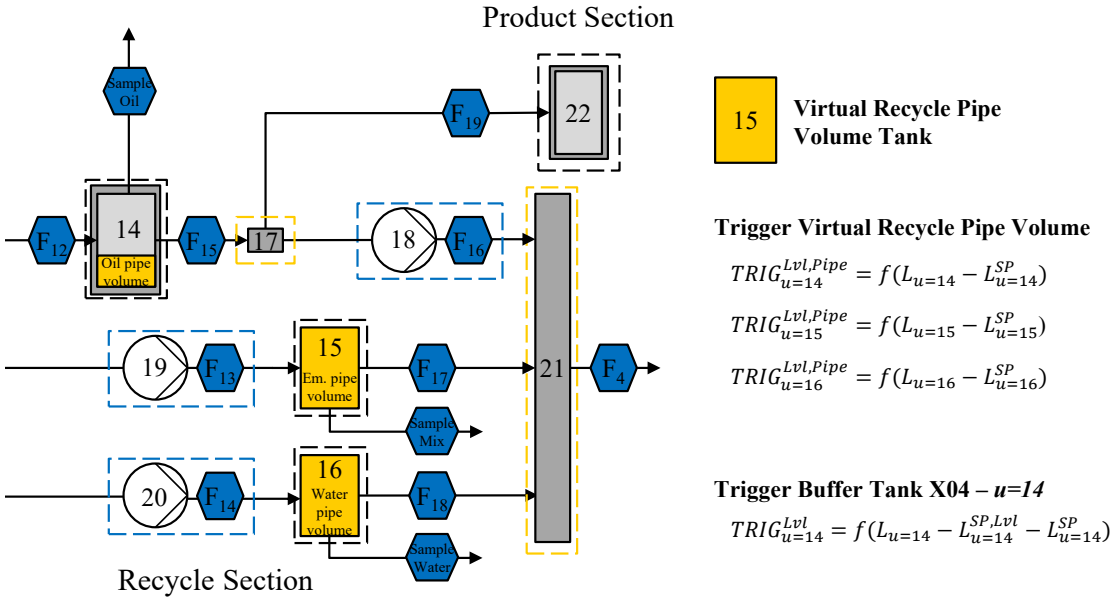

Fig. 4.28: Model scheme for the recycle and product section of the mini-plant.

tank X04 of the oil phase from which oil is either recycled back to the reactor or drawn off towards product tank $u = 22$ via splitter $u = 17$. Additionally, virtual tank volumes for each recycle stream are provided. The reason for that lies in the disadvantageous ratio of the overall mini-plant's liquid volume and volume of the recycle pipes, which can be calculated from Tab. B.2:

$$Volume\ ratio = \frac{V_{Tanks}}{V_{Recycle\ Pipes}} = 2.6$$

This means almost 30 % of the liquid volume of the plant is located inside the recycles' pipes. With the high dynamics of the system and high sensitivities of reaction and phase separation on concentrations it is mandatory to include the pipe volumes into the model. Ideally, this would be done with a dead time shift of concentrations of recycle streams entering the reactor. However, a feasible formulation of such a functionality for the use in optimization is challenging. Hence, virtual tanks $u = 14, Pipe$, $u = 15$, and $u = 16$ are implemented for respective recycle streams. For simplicity, these tanks are assumed to be ideally mixed.

Buffer Tank X04 and Virtual Recycle Volume Tanks

Therefore additional component mass balances for each relevant tank are supplied:

$$\begin{aligned}\frac{\mathrm{d}HU^{L}_{u=14,i}}{\mathrm{d}t} =& (w^{Oil}_{u=11,i} \cdot TRIG^{Out,Oil}_{u=11} + w^{Mix}_{u=12,i} \cdot (1 - TRIG^{Out,Oil}_{u=11}) \cdot (1 - TRIG^{Out,Oil}_{u=13}) \\ &+ w^{Water}_{u=13,i} \cdot TRIG^{Out,Oil}_{u=13}) \cdot F_{s=12} - F_{s=15,i} - F^{Oil}_{Sample,i} \end{aligned} \tag{4.65}$$

$$\begin{aligned}\frac{\mathrm{d}HU^{L}_{u=15,i}}{\mathrm{d}t} =& (w^{Oil}_{u=11,i} \cdot TRIG^{Out,Mix}_{u=11} + w^{Mix}_{u=12,i} \cdot (1 - TRIG^{Out,Mix}_{u=11}) \cdot (1 - TRIG^{Out,Mix}_{u=13}) \\ &+ w^{Water}_{u=13,i} \cdot TRIG^{Out,Mix}_{u=13}) \cdot F_{s=13} - F_{s=17,i} - F^{Mix}_{Sample,i} \end{aligned} \tag{4.66}$$

$$\begin{aligned}\frac{\mathrm{d}HU^{L}_{u=16,i}}{\mathrm{d}t} =& (w^{Oil}_{u=11,i} \cdot TRIG^{Out,Water}_{u=11} + w^{Mix}_{u=12,i} \cdot (1 - TRIG^{Out,Water}_{u=11}) \cdot (1 - TRIG^{Out,Water}_{u=13}) \\ &+ w^{Water}_{u=13,i} \cdot TRIG^{Out,Water}_{u=13}) \cdot F_{s=14} - F_{s=18,i} - F^{Water}_{Sample,i} \end{aligned} \tag{4.67}$$

The composition of entering streams for each tank is a consequence of the status of the phase separation in the settler and thus the already presented switching scheme of concentrations at the settler outlet drains is consequently implemented here. The respective total mass streams $F_{s=12\ldots14}$ have already been defined in Eq. (4.62)-4.64. Additionally, sample streams $F^{Oil}_{Sample,i}$, $F^{Mix}_{Sample,i}$, $F^{Water}_{Sample,i}$ are provided to account for liquid sampling during mini-plant operation.

The outlet streams for the virtual tanks then adhere to the presented overflow stream concept in Sec. 4.3.1. This way it is ensured, that these virtual tanks are always filled with the exact volume of respective pipes (see Sec. C.2).

Product split, product tank, and recycle mixer

The total level of X04 is used to control product purge to the product tank. Once the sigmoidal function $TRIG^{Lvl}_{u=14}$ for the level setpoint of X04 is active, product stream $F_{s=19}$ takes action. The total stream drawn from tank X04 is given by Eq. (4.69).

$$F_{s=19} = (F^{Lvl}_{u=14}) \cdot TRIG^{Lvl}_{u=14} \tag{4.68}$$

$$F_{s=15,i} = F_{s=16,i} + F_{s=19,i} \tag{4.69}$$

Finally, the product oil phase is collected in unit $u = 22$, for which again a mass balance is provided in Sec. C.2. This unit is provided in the model to include additional accurate level measurements. These are vital to validate data on the product stream. For completeness Eq. (C.22) represents the component mass balances around the recycle mixer, collecting all individual recycle streams into the total recycle $F_{s=4,i}$, which is fed back to the feed section.

4.4 Strategies for Optimal Operation

Following Fig. 4.1, several methods for enhancing and optimizing process operation are developed. These are tailored to cope with the identified operational challenges for hydroformylation in microemulsions. Hence, details on the implementation of an online-applicable soft-sensor for concentrations and the development of trajectories for optimal operation are presented in this section. In accordance with Fig. 2.20 the latter includes state estimation on multiple measurement rates and is implemented for online application on the mini-plant. Hence, an according communication and data handling scheme is presented. For these purposes the developed DAE model from Sec. 4.3 is applied in its discretized form using Lagrangian orthogonal collocation with shifted Radau roots of polynomial order three and finite elements as described by L. T. Biegler (2010, p. 290) (see Sec. C.4). Typically, a time horizon of 4 h is considered, using 16 finite elements. The resulting **A**lgebraic **E**quation system (AE) consists of 28720 equations.

4.4.1 Implementation of Surfactant Soft-Sensor

One of the major drawbacks for the reactive microemulsion systems is the immeasurability of surfactant concentrations. This severely complicates the operation of such a system, since high sensitivity of the phase separation to these concentrations (Fig. 3.11) and an overall small operation window (Tab. 3.5) are found. To overcome this hurdle, a soft-sensor is developed and implemented into the DCS. It is based on the model for the three-phase separation developed

in Sec. 4.3.6, which is connected to the optically accessible separation state. The graphical representation of this soft-sensor is shown in Fig. 4.29.

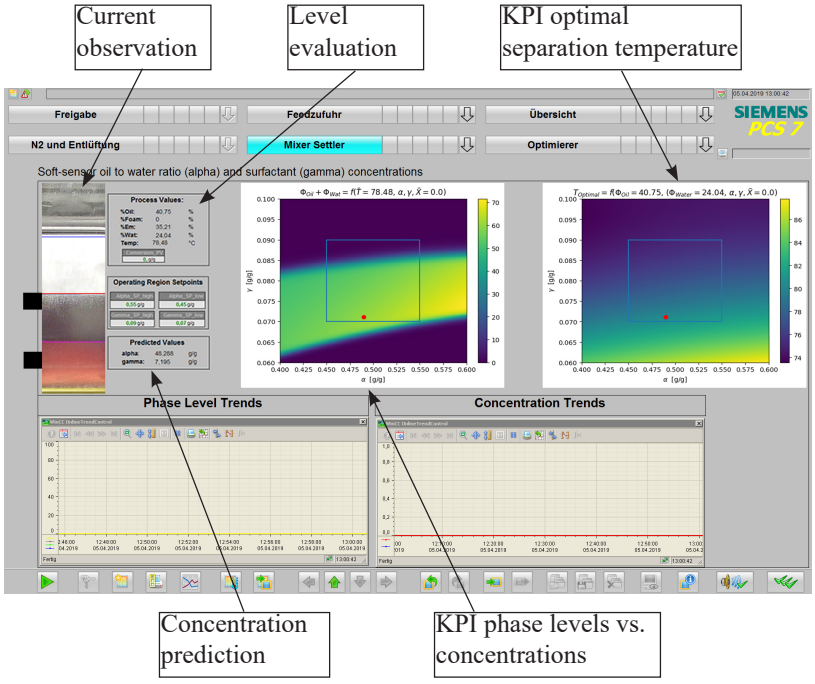

Fig. 4.29: DCS integration of the soft-sensor for phase separation and key performance indicators.

Observation and Level Detection

The setup consists of a webcam, which observes the phase separation in the gravity settler through a sight glass and thus provides the current separation state for the operator (**Current observation**). Thereof, the volume fraction of each present phase is calculated from the current webcam image (**Level evaluation**) using the script for automated level detection (Fig. 4.7).

Model-based Soft-Sensor

The desired **Concentration prediction** is calculated using the settler's temperature $T_{Settler}$ and the current reaction yield $Y_{s=8}$ measured by GC. The model of the phase separation is then reformulated to:

$$\alpha,\gamma = f(\phi^{Oil},\phi^{Mix},\phi^{Water},T,Y,P). \tag{4.70}$$

Thus, the otherwise inaccessible surfactant concentration γ and the oil to water ratio α are estimated. These calculated values are valid for the current state of the settler. They are assumed

to hold for its inlet zone, at which the separation mainly occurs (separation time $\approx$5 min $\ll$ residence time of settler). The calculation is performed on a webcam server (Fig. 4.8) running a Python script, which transfers results to the DCS via **O**pen **P**latform **C**ommunication (OPC). This evaluation is performed in real-time.

Key Performance Indicators

To further aid operators in evaluating the plant's state and derive control actions, two KPIs are provided. First of all, the KPI *Phase levels vs. concentrations* shows a contour plot of the cumulated volume fractions of phases Φ^{Oil} and Φ^{Water} depending on α and γ. Therein, the current operating point is marked with a red dot and the desired operation region is visualized according to user given setpoints. In Fig. 4.29, the yellow to green area indicates large volume fractions and thus stable three-phase separation in the settler. Based on the current operating point, the operator is then able to plan control actions, such as feed of surfactant or adjustment of the ratio of the three recycle streams in the plant. Hence, basic operation decisions can be derived to stabilize operation and especially maintain the vital three-phasic separation. This is further supported by the KPI *optimal separation temperature*, which provides information on ideal temperatures for phase separations. Both KPI contour plots are calculated using the presented phase separation model with respective user-defined or measured inputs.

4.4.2 Multi-Rate State Estimation

The development of optimal dynamic trajectories for the mini-plant requires the efficient and robust estimation of model states according to current and past measurements. Such a state estimation initially requires an analysis of the system regarding available measurements and their sensitivity on model states – the system's measurability (Def. 2.5). For dynamic problems, this typically yields a list of initials for the state variables, which are obtainable by state estimation and thus serve as respective manipulable variables. From that, a suitable estimator concept is derived considering the systems complexity regarding nonlinearity, available information on process noise or uncertainty, and differing sampling rates.

System and Measurability Analysis

The current operational state of the mini-plant is tracked via a multitude of sensors, which are subsequently discussed regarding their applicability for state estimation using the model of the mini-plant. From this, a suitable set of measurements is chosen. The selection considers first of all reliability of the measurements. Following Tab. 4.1, e.g., level sensors provide data of high

accuracy, while applied coriolis flow-meters show unreliable behavior if applied to the MES (see Fig. C.11). Also, the measurement should be represented in the model structure as a state variable or as part of the measurement model. Concentration information is typically of high value to determine compositions and close mass balances. However, they often come at the cost of delay and slow sampling rates. Based on these principles, a detailed discussion of applicable measurements is given in Sec. C.4. Tab. 4.6 summarizes these measurements, links them to model variables, and provides information on sampling frequency and measurement delay.

Tab. 4.6: Plant measurements used for the state estimation framework, sampling frequencies, and delays.

Measurement	Model Variable	Sampling Rate	Delay
Levels	$L_u, \quad u \in \{1,2,3,14,22\}$	1 s	-
Levels settler	$L_u, \quad u \in \{11-13\}$	2 min	-
Flows	$F_s, \quad s \in \{4,19\}$	1 s	-
Concentration reactor	$w_{s=8,i}, \quad i \in \{1,...,5\}$	1-2 h	45 min
Concentration oil phase	$w^{Oil}_{u=11,i}, \quad i \in \{1,...,5\}$	2-4 h	45 min
Concentration water phase	$w^{Water}_{u=13,i}, \quad i \in \{1,...,5\}$	4 h	45 min

Dynamic state estimation is set up as an optimization problem, which calculates initials of the model at t_0 setting them as manipulable variables. Therein, measurements and available control variables on a certain horizon $t_0 - t_{end}$ are used. These initials are represented by all component hold-ups (discretized system with collocation point $cp = 3$ at finite element $fe = 0$):

Tank hold-ups $u \in \{1,2,3\},\ i \in \{1,...,12\}$

- Feed: $HU_{u,fe=0,cp=3}$
- Reactor: $HU^{Reactor}_{i,fe=0,cp=3}$
- X04: $HU^{L}_{u=14,i,fe=0,cp=3}$
- Product tank: $HU^{L}_{u=22,i,fe=0,cp=3}$

Settler phases $i \in \{1,...,12\}$

- Oil: $HU^{L,Oil}_{u=11,i,fe=0,cp=3}$
- Mix: $HU^{L,Mix}_{u=12,i,fe=0,cp=3}$
- Water: $HU^{L,Water}_{u=13,i,fe=0,cp=3}$

Inaccessible or immeasurable initial of model state should be excluded from state estimation, since they are prone to cause ill-posed optimization problems regarding ill-conditioned Jacobian or Hessian matrices (Salau et al., 2014). For nonlinear models, the global verification of this *measurability* is very complex and intractable for every model state at every initial point. To nevertheless obtain (local) information thereon, a sensitivity case study is performed. Based on Def. 2.2, the objective function for state estimation only depends on $y_i = h(x_i)$, the model's measurement variables. Furthermore, the vector of the model states is given with $x_{k-N},...,x_k$. The main idea now is to analyze whether the manipulable variables (states at initial time point x_{k-N}) have a significant influence on the model's measurement variables y_i and thus on the objective function.

For this, matrix Θ is introduced, which contains the derivatives of the measurement vector $Y = [y_1, \ldots, y_{n_y}]$ with length n_y with respect to the initials of the states X_0 at $k-N$ with length n_x. Hereon, decisions can be made whether to exclude certain initials (manipulable variables) from the optimization problem. This case basically corresponds to a zero row in matrix 4.71.

$$\Theta = \begin{bmatrix} \frac{\partial y_1}{\partial x_{0,1}} & \cdots & \frac{\partial y_{n_y}}{\partial x_{0,1}} \\ \vdots & \ddots & \vdots \\ \frac{\partial y_1}{\partial x_{0,n_x}} & \cdots & \frac{\partial y_{n_y}}{\partial x_{0,n_x}} \end{bmatrix} \tag{4.71}$$

As an approximation of these derivatives, simulation studies are used. These are initialized at a standard continuous operation mode including reaction (similar to initials used for the case study in Sec. 5.2.5). The simulations are performed using the discretized model of the mini-plant with finite elements of the length $\Delta FE = 0.25$ h. For each derivative, the respective initial of the model state for time point $t = 0$ ($fe = 0$,_$cp = 3$) is altered and the simulation result compared to a reference simulation. The deviation between the resulting model measurements $y_{n_y,fe=1,cp=2}$ and the reference case $y^{ref}_{n_y,fe=1,cp=2}$ are then used to approximate the entries of matrix 4.71. The results are listed in Tab. C.26-C.27 showing the variation in percentages of $(y_{n_y,fe=1,cp=2} - y^{ref}_{n_y,fe=1,cp=2})$ normalized on the variation of the respective state variable $(x_{0,n_x,fe=0,cp=3} - x^{ref}_{0,n_x,fe=0,cp=3})$. Values smaller than 0.001 are set to zero. In addition to the already mentioned initials of the model state, also feed and recycle streams $F_s,\ s \in \{1,2,3,13,14,16\}$ and the settler temperature $T_{Settler}$ are included into the discussion (treated as adjustable for optimization). This is reasoned with the poor accuracy of flow sensors. Furthermore, $T_{Settler}$ only delivers local temperature information, which is prone to deviate from the mean temperature in the major separation zone.

Discussing the results, it is obvious that a larger set of model measurements is inaccessible. Thus, respective state initials need to be excluded from the set of manipulable variables. Exemplarily the measurability of surfactant, water, and catalyst component hold-ups is severely limited due to missing quality measurements. Apart from that, only hold-ups of the reaction compounds ($i \in \{1,...,5\}$) show relevant sensitivity on concentration measurements. Hence, the implementation of slow and delayed measurements from the GC is mandatory. In addition to that, matrix Θ also points out the importance of the surfactant soft-sensor. Focusing on $L^{Oil}_{u=11}$ and $L^{Water}_{u=13}$, high contributions of a significant number of state initials can be seen. The latter are in respect thereof also considered as necessary additional variables of the state estimation optimization problem.

Problem Statement and Estimator Structure

First of all, a choice of method for state estimation is done according to Sec. 2.5.2. Unlike MHE, filtering methods rely a corrector step, which requires an expression for process noise w_k according to Eq. (2.16) and the respective covariance matrix Q. Calculating process noise from physically correct model simulations is not practicable and moreover must be gathered in a function expressing process noise for every possible initial state of the model (Weigert et al., 2018). Since the true state of the regarded mini-plant is largely immeasurable, information on process noise $w(k)$ and respective covariances is not available. Thus, moving horizon state estimation based on an NLP formulation is deployed within this work, omitting process noise.

For MHE implementations, the choice of the horizon length is of importance due to computational burdens. It is to be set as short as possible but long enough to cover enough information content from plant measurements. The analysis of the system measurability revealed, that the slow concentration measurements are vital for estimating a large set of model states. Hence, it has to be ensured, that each estimation horizon at least covers one sample from each measurement position. Considering sampling rates and measurement delays in Tab. 4.6 a horizon of 4 h is thus chosen.

Additionally, assumptions for the formulation of the MHE are discussed: one major aspect are *arrival costs* ϕ, a corrector of the objective function to account for the influence of measurements prior to the estimation horizon. As already discussed in Sec. 2.5.2 their calculation is rather challenging. Using the inverse of the reduced Hessian of the NLP Lagrange from prior estimations, as proposed by López-Negrete et al. (2012), was tested in earlier applications of state estimation on the hydroformylation mini-plant model based on solely artificial data (Hoffmann et al., 2016). Despite promising results, arrival costs are however neglected in this work. Firstly, their influence on the state estimation result is diminished by larger estimation horizons, which is assumed to be true here. Secondly, the arrival costs directly influence the disturbance behavior of the estimator. In case previous estimates were falsified by large disturbances, ϕ then also introduces this *error* into the next estimation.

Concluding, the respective formulation of the optimization problem for the MHE is set up based on Def. 2.2:

Definition 4.1 (NLP Moving Horizon Estimation for Mini-Plant System):

$$\begin{aligned}\{\hat{E},\hat{x}(k-N+1),\ldots,\hat{x}(k)\} = \arg\min_{\{E,x(k-N+1),\ldots,x(k)\}} & f_{est} \\ s.t. \qquad & x(i+1) = F(x(i),u(i)) \\ & y(i) = h(x(i)) + v(i) \\ & c(z(i),x(i)) = 0 \\ & x^{LB} \leq x(i) \leq x^{UB}\end{aligned} \tag{4.72}$$

Here, E represents the vector of initials of the state variables, chosen based on the measurability analysis. Vector z corresponds to all system variables, which are neither differential state variables, nor measurements. $c(x,z)$ then is the respective equation system. Applying measurements from Tab. 4.6 the estimator function f_{est} can be set up to evaluate the deviation of model and measurement variables y. Thus, a respective objective function formulation is obtained.

Due to the complexity of the microemulsion system and experimental setup, the occurrence of sensor failure and large measurement errors is assumed to be frequently present during mini-plant operation. The handling of such gross error is tackled with the implementation of the Redescending Estimator (Eq. (2.28)) as robust M-estimator (f_{est}), as already introduced in Sec. 2.5.2. The Fair-Function (Eq. (2.27)) is then used as convex estimator to initialize the Redescending Estimator. The implementation of both functions for the regarded system is shown in the following:

Definition 4.2 (Objective function formulation using Fair-Function):

$$\begin{aligned} f_{est,FF} = & \sum_{u}\sum_{k=1}^{48} C_{FF}^2 \cdot \Lambda_{L_u}(k) \left[\frac{|\frac{L_u(k)-\hat{L}_u(k)}{\sigma_{L_u}}|}{C_{FF}} - \ln\left(1 + \frac{|\frac{L_u(k)-\hat{L}_u(k)}{\sigma_{L_u}}|}{C_{FF}}\right)\right] \\ & + \sum_{s}\sum_{k=1}^{48} C_{FF}^2 \cdot \Lambda_{F_s}(k) \left[\frac{|\frac{F_s(k)-\hat{F}_s(k)}{\sigma_{F_s}}|}{C_{FF}} - \ln\left(1 + \frac{|\frac{F_s(k)-\hat{F}_s(k)}{\sigma_{F_s}}|}{C_{FF}}\right)\right] \\ & + \sum_{m}\sum_{i=1}^{5}\sum_{k=0}^{48} C_{FF}^2 \cdot \Lambda_{w_{m,i}}(k) \left[\frac{|\frac{w_{m,i}(k)-\hat{w}_{m,i}(k)}{\sigma_{w_{m,i}}}|}{C_{FF}} - \ln\left(1 + \frac{|\frac{w_{m,i}(k)-\hat{w}_{m,i}(k)}{\sigma_{w_{m,i}}}|}{C_{FF}}\right)\right], \\ u \in \{1,2,3,9,11,13,14,22\}, \quad & s \in \{4,19\}, \quad m \in \{s=8,\, u=11,\, u=13\}, \quad C_{FF} = 6. \end{aligned} \tag{4.73}$$

Definition 4.3 (Objective function formulation using Redescending-Estimator):

$$
\begin{aligned}
f_{est,RE} = & \sum_{u}\sum_{k=1}^{48}\Lambda_{L_u}(k)\cdot\left[-c_1\left(1-\frac{2}{1+exp\left(-2\cdot\kappa_1\left(\frac{L_u(k)-\hat{L}_u(k)}{\sigma_{L_u}}\right)^2\right)}\right)\right. \\
& \left.-c_2\left(1-\frac{2}{1+exp\left(-2\cdot\kappa_2\left(\frac{L_u(k)-\hat{L}_u(k)}{\sigma_{L_u}}\right)^2\right)}\right)\right] \\
& +\sum_{s}\sum_{k=1}^{48}\Lambda_{F_s}(k)\cdot\left[-c_1\left(1-\frac{2}{1+exp\left(-2\cdot\kappa_1\left(\frac{F_s(k)-\hat{F}_s(k)}{\sigma_{F_s}}\right)^2\right)}\right)\right. \\
& \left.-c_2\left(1-\frac{2}{1+exp\left(-2\cdot\kappa_2\left(\frac{F_s(k)-\hat{F}_s(k)}{\sigma_{F_s}}\right)^2\right)}\right)\right] \\
& +\sum_{m}\sum_{i=1}^{5}\sum_{k=0}^{48}\Lambda_{w_{m,i}}(k)\cdot\left[-c_1\left(1-\frac{2}{1+exp\left(-2\cdot\kappa_1\left(\frac{w_{m,i}(k)-\hat{w}_{m,i}(k)}{\sigma_{w_{m,i}}}\right)^2\right)}\right)\right. \\
& \left.-c_2\left(1-\frac{2}{1+exp\left(-2\cdot\kappa_2\left(\frac{w_{m,i}(k)-\hat{w}_{m,i}(k)}{\sigma_{w_{m,i}}}\right)^2\right)}\right)\right],
\end{aligned}
\tag{4.74}
$$

$u \in \{1,2,3,9,11,13,14,22\}, \quad s \in \{4,19\}, \quad m \in \{s=8, u=11, u=13\},$

$a_{RE}=1,\ b_{RE}=2,\ c_{RE}=4$ according to Def. 2.4.

These definitions enforce the usability of all available mini-plant measurements and are designed in such a way, that the availability of measurements is handled using the parameter Λ:

$$
\Lambda(k) = \begin{cases} 0, & \text{no measurement at collocation point k given} \\ 1, & \text{measurement at collocation point k given} \end{cases} \tag{4.75}
$$

This way, the objective function can be used for every estimation horizon, even if time points of measurements are shifted or the number of available measurements is changing. Furthermore, Λ can be used to apply weighting on the elements of the objective functions.

Multi-Rate Implementation and Framework Algorithm

In the remainder of this section an algorithmic framework for the implementation of state estimation using multi-rate measurements is presented. Key aspects are the efficient exploitation of available plant measurements and the robust calculation of state estimates. Firstly, the handling of differing sampling rates is discussed. This is important, since for the given objective function the influence of slow and thus seldom measurements on the result of the estimation is small. The framework itself is then presented as an implementation in AMPL ((Fourer et al., 1997)), using IPOPT ((Wächter, 2002)) and CONOPT[5].

Initial concept - simultaneous usage of all measurements:
As a first approach, all measurements are used for the formulation of the objective function. Their influence is then weighted using the parameter $\Lambda_{Measurement}(k)$, which is divided by the sum of available data points per measurement in the time horizon.

$$\frac{\Lambda_{Measurement}(k)}{\sum_{j=0}^{48}\Lambda_{Measurement}(j)} \tag{4.76}$$

This approach is consequently applied on the presented estimators. Additionally, the vector optimization variables E is set according to the measurability analysis results in Tab. C.26-C.27. State estimation is then firstly applied based on a simulation study, from which artificial measurement data was generated considering the standard deviation from the respective real plant sensors. Exemplarily, Fig. 4.30 depicts the estimation result for one fast level measurement (level oil phase) and one slow concentration measurement (1-dodecene concentration reactor).

It is apparent, that for the fast measurement a very good agreement between measurement and estimation is achieved, which is moreover in good agreement with the model trajectory from the reference simulation. However, for the slow concentration measurement, a large constant positive offset is visible. In this case, the influence of fast level and flow measurements on the objective function of the estimator still dominates and the adjustment of manipulable variables (mainly component hold-ups) is performed accordingly. This behavior is highly undesirable and might be tackled by further scaling of the objective function formulations. This however is not assumed to be robust regarding all possible estimation scenarios.

[5] http://www.conopt.com/

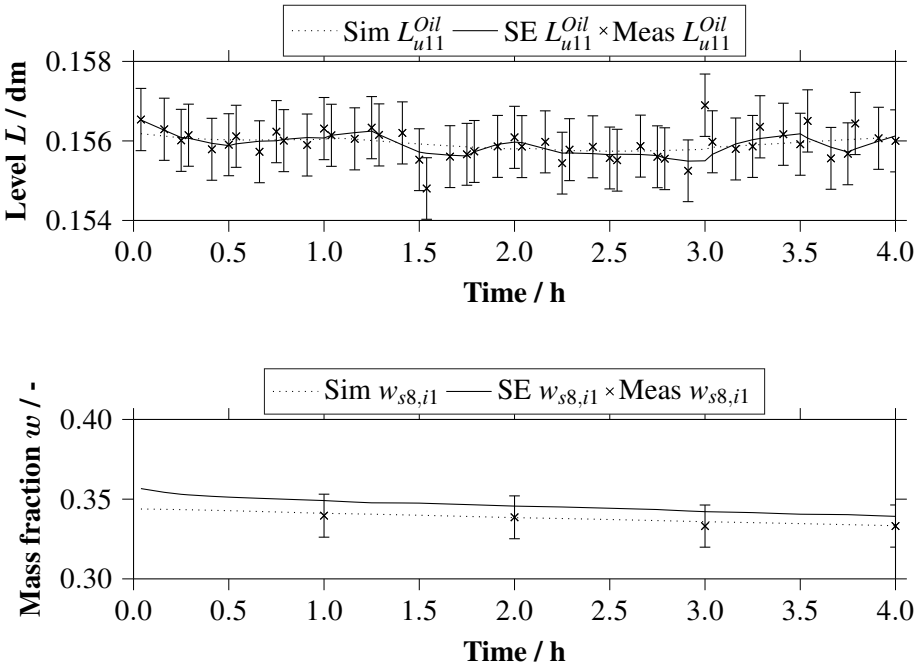

Fig. 4.30: Results for state estimation simultaneously considering fast and slow measurements. Measurements are derived from a reference simulation, which is also shown for comparison. Shown are the settler oil level L_{u11}^{Oil} and 1-dodecene $w_{s8,i1}$ concentration in the reactor.

Final concept - sequential multi-rate state estimation:
Thus, it is proposed to separate the state estimation into two sequential steps: a first estimation on the fast measurements, followed by an estimation solely on slow concentration measurements to effectively incorporate their vital information. This concept is embedded into a larger state estimation framework, consisting of several initialization and re-simulation steps to ensure robustness and improve the convergence behavior. A flow diagram of the developed framework is shown in Fig. 4.31:

Step 0 - Initialization: An initial set of model parameters (1), controls for the current horizon from optimization (2), fast measurements for the current horizon (3), state initials (4), and a full set of state variables (5) is provided. Note that slow measurements are needed at a later point, thus measurement delay is efficiently bridged (dashed lines in Fig. 4.31). The application of these data sets for specific calculations is marked with numbered arrows.

Step 1 - Pre-simulation: At time point $t = 0\,\mathrm{h}$ only the initial state of the model is known. To improve robustness and convergence behavior it is vital to provide good starting values for the provided discretized model on the full horizon. To do that, the model is reduced to only a single finite element of small length. The remaining collocation points are then initialized with the same respective provided state initials. After solving this reduced model, results are collected

to initialize a simulation again on the next finite element. This is iteratively repeated, till the final length of the horizon is reached. The applied step size control additionally enforces the application of the correct control values according to the current position within the time horizon. The results are collected and interpolated to provide starting values and initials for the full time horizon of 16 finite elements of length $\Delta FE = 0.25$. As additional information, a flow chart of the developed simulation framework can be found in Sec. C.4.

Step 2 - Inner state estimation on fast measurements: The initial state estimation step is implemented using the objective function implementation from Def. 4.2 and 4.3. Here, the Fair Function serves as convex estimator to initialize the Redescending Estimator. The state estimation itself is performed only on the set of fast measurements resulting in the following measurement specifiers for the objective function formulation:

$$u \in \{1,2,3,9,11,13,14,22\}, \quad s \in \{4,19\} \tag{4.77}$$

The idea is to use this initial state estimation to determine the system regarding its phase separation state and flow configuration. This means, tank hold-ups and manipulable recycle streams are to be validated in accordance with the level measurements and observations of the phase separation. The oil to water ratio α however should be adjusted to meet the observed phase separation state (settler phase levels). To do this without affecting the actual oily compound concentrations, additional pseudo variables for the total oil content are introduced for reactor and all hold-ups of settler phases:

$$HU^{Reactor,Oil} = \sum_{i=1}^{5} HU_i^{Reactor}, \qquad HU_{u=11}^{L,Oil,Oil} = \sum_{i=1}^{5} HU_{u=11,i}^{L,Oil}, \tag{4.78}$$

$$HU_{u=12}^{L,Mix,Oil} = \sum_{i=1}^{5} HU_{u=12,i}^{L,Mix}, \qquad HU_{u=13}^{L,Water,Oil} = \sum_{i=1}^{5} HU_{u=13,i}^{L,Water} \tag{4.79}$$

The state estimation is then applied using the following set of manipulable variables E_{fast}:

$$E_{fast} = \{HU_{u,i},\}, \quad u \in \{1,2,3,14,22\}, \quad i \in \{1,2,3,4,5,9,10,11,12\} \tag{4.80}$$

$$\{HU_{Reactor}^{Oil}, HU_{u=11}^{L,Oil,Oil}, HU_{u=12}^{L,Mix,Oil}, HU_{u=13}^{L,Water,Oil}\} \tag{4.81}$$

$$\{HU_i^{Reactor}, HU_{u=11,i}^{L,Oil}, HU_{u=12,i}^{L,Mix}, HU_{u=13,i}^{L,Water}\}, \quad i \in \{9,10,11,12\} \tag{4.82}$$

$$\{F_s(k), T_{Settler}(k)\}, \quad k \in \{1,...,16\}, \quad s \in \{1,2,3,13,14,16\} \tag{4.83}$$

Note, that the adaption of uncertain settler temperature, feed and recycle streams is possible for each of the available 16 finite elements.

Step 3 - Re-simulation: Based on the results of this initial state estimation, again a simulation run is performed. Using the framework from step 1 a full set of starting values of high accuracy for the second state estimation step is generated.

Step 4 - Outer State estimation on slow measurements: The setup of the second state estimation step is aligned with step 2. In this case only the slow concentration measurements from the reactor and oil/water phase of the settler are used: $w_{s=8,i}$, $w^{Oil}_{u=11,i}$, $w^{Water}_{u=13,i}$, $\quad i \in \{1,..,5,\}$. The set of optimization variables E_{slow} in this case consists of the hold-ups of respective oily compounds in reactor and oil/water phase in the settler, which were previously combined into total oil phase hold-ups. To improve the robustness of the framework, an additional presolve of the state estimation using Fair Function is performed, before applying the Redescending Estimator.

$$E_{slow} = \{HU_i^{Reactor}, HU^{L,Oil}_{u=11,i}, HU^{L,Mix}_{u=12,i}, HU^{L,Water}_{u=13,i}\}, \quad i \in \{1,...,5\} \tag{4.84}$$

The application of this framework including information on robustness and computation time is shown for an artificial case study in Sec. 5.2.5 and for real mini-plant data in Sec. 5.3.3.

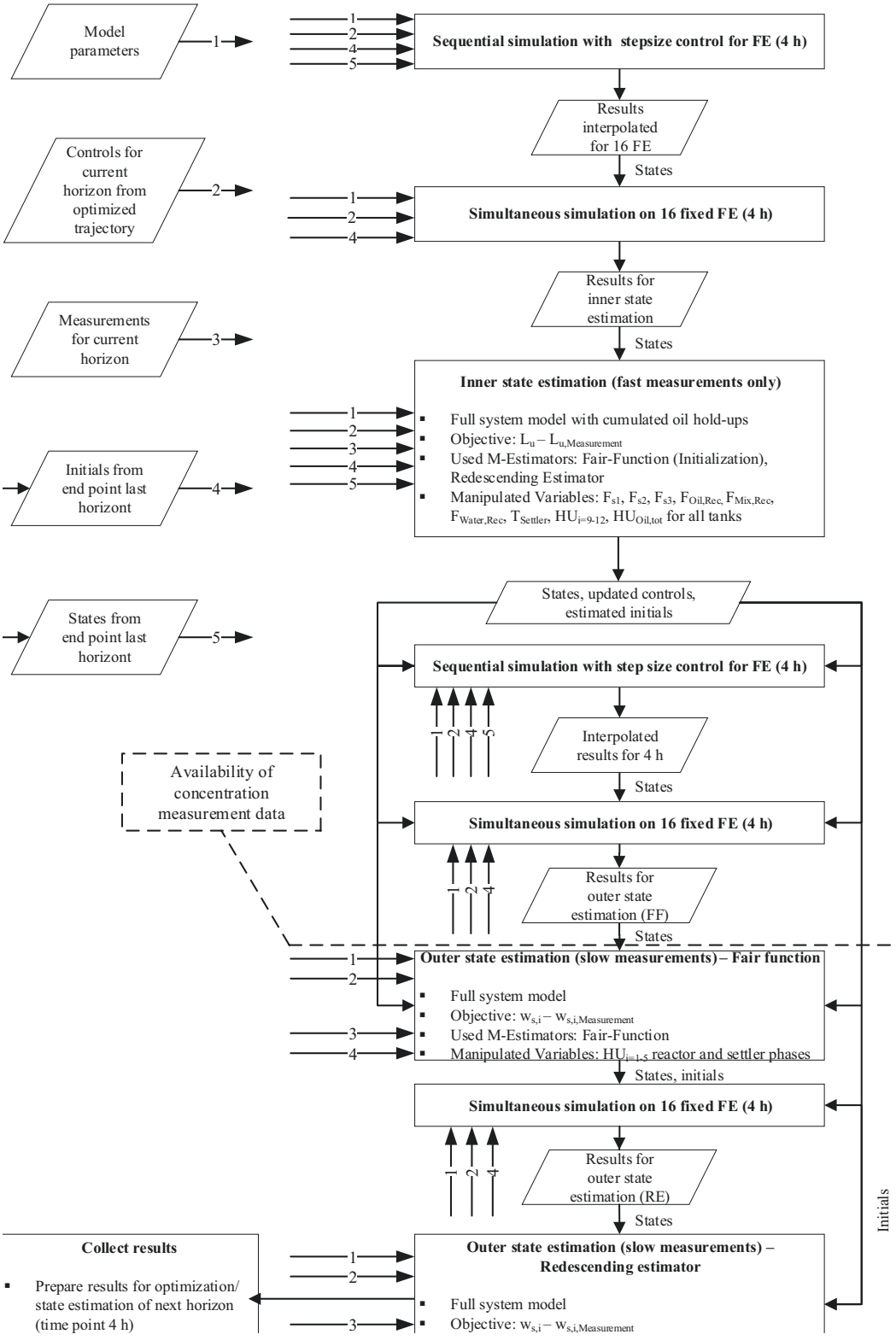

Fig. 4.31: Flow diagram of the developed framework for multi-rate state estimation including data handling and pre-solves. Figure adapted from Weigert (2017).

4.4.3 Dynamic Optimization

The application of dynamic optimization aims for the calculation of optimal trajectories to stabilize the mini-plant operation regarding reaction and phase separation performance. In principle this translates to an economic objective function regarding maximization of the product content in the product tank $HU_{u=22}$ since this is only possible with stable phase separation and adequate reaction control.

As a general requirement, optimization problems are constrained in such a way, that validity of especially the phase separation sub-model is ensured. This also means, that an optimization of the mini-plant operation from highly deteriorated states not covered by the presented dynamic model of the mini-plant is impossible. To initially avoid such a case, the introduction of a suitable formulation of the objective function and constraints is necessary. These are applied for optimizing different operation modes of the mini-plant, such as the start-up, stabilization of the plant operation, and the continuous operation with high yields of tridecanal. A generalized formulation of the optimization problem is given as:

$$\arg\min_{u} \quad \Phi_Y + \Phi_P + \Phi_\alpha + \Phi_\gamma + \Phi_\tau \tag{4.85}$$

$$s.t. \quad g(x,u,P) = 0 \tag{4.86}$$

$$0.4 \leq \alpha_{s=8} \leq 0.6 \tag{4.87}$$

$$0.06 \leq \gamma_{s=8} \leq 0.1 \tag{4.88}$$

$$0.1 \leq \phi^{Oil} \leq 1 \tag{4.89}$$

$$0.05 \leq \phi^{Water} \leq 1 \tag{4.90}$$

$$0.2 \leq \tau_{Settler} \leq 1 \tag{4.91}$$

$$u_{LB} \leq u \leq u_{UB} \tag{4.92}$$

Objective

As economically driven parts of the objective, Φ_Y and Φ_P represent the production of the target product tridecanal. Φ_Y represents the yield of tridecanal in the reactor. It is specifically relevant for start-up optimization, since in this phase the product tank is still empty and no sensitivity on the objective is present. Consequently, Φ_P is applied for trajectory optimization of the continuous operation. Here, the maximization of the actual amount of product collected from the plant is of interest. Using the weights W_Y and W_P these parts of the objective function can be activated or scaled.

$$\Phi_Y = -W_Y \cdot Y_{s=8} \tag{4.93}$$

$$\Phi_P = -W_P \cdot HU^L_{u=22,i=5} \tag{4.94}$$

Additionally, three penalties are added to the objective function to maintain desirable oil to water ratios (Φ_α) and surfactant concentrations (Φ_γ) in the reactor. In accordance with the range of validity of the kinetic model, the respective setpoints are chosen, using $\alpha^{SP}_{s=8} = 0.5\,\mathrm{g\,g^{-1}}$ and $\gamma^{SP}_{s=8} = 0.08\,\mathrm{g\,g^{-1}}$. Φ_τ enforces a suitable residence time for the settler of $\tau^{SP}_{Settler} = 0.5\,\mathrm{h}$. Costs for catalyst loss are indirectly represented by enforcing a stable operation of the phase separation. Referring to Sec. 4.3.6, the concentration of the catalyst in the oil phase of the settler is minimal and varies insignificantly with, e.g., temperature or higher yields. Hence, no significant impact on the objective function is expected.

$$\Phi_\alpha = +W_\alpha \cdot (\alpha_{s=8} - \alpha^{SP}_{s=8})^2 \tag{4.95}$$

$$\Phi_\gamma = +W_\gamma \cdot (\gamma_{s=8} - \gamma^{SP}_{s=8})^2 \tag{4.96}$$

$$\Phi_\tau = +W_\tau \cdot (\tau_{Settler} - \tau^{SP}_{Settler})^2 \tag{4.97}$$

Constraints

The objective function is subject to several constraints. Here, $\alpha_{s=8}$ and $\gamma_{s=8}$ are restricted with inequalities to the design space of the phase separation model. Moreover, inequalities for the success of the phase separation are deployed (minimum volume fractions of oil and water). This ensures that the three-phasic separation in the settler is maintained and optimized trajectories do not lead to infeasible separation states. The lower bounds on ϕ^{Oil} and ϕ^{Water} are applied well off the boundaries of the feasible region for separation with minimum 10 and 5 % volume fraction of oil and water respectively. This is meant to ensure stable phase separation operation at these bounds even under disturbance. Lastly, the residence time of the settler $\tau_{Settler}$ is constrained to a minimum of 12 min to ensure quality of separation. An upper bound of 1 h on the residence time is applied to avoid batch operation.

Controls

The optimizer is allowed to vary several controls u. These include the setpoints of feed and recycle streams $F^{SP}_{s=1...3}$, $F^{SP,Oil}_{s=13}$, $F^{SP,Mix}_{s=14}$, $F^{SP,Water}_{s=16}$, as well as reactor and settler temperature $T_{u=9}$ and $T_{Settler}$. Information on bounds and resulting degrees of freedom for the optimizer are given for respective applications in Chap. 5.

Application and Framework

Different formulations are used for different phases of the plant operation: start-up trajectories, as well as long-term offline trajectories are usually calculated in gPROMS® based on the **D**ifferential-**A**lgebraic **E**quation (system) (DAE) model of the plant.

For the application of **Dynamic R**eal-**T**ime **O**ptimization (D-RTO), an implementation in AMPL is used, based on the discretized mini-plant model. Thus, all above stated constraints apply at every collocation point cp and finite element fe. Controls are allowed to change in every finite element. Hence, the objective function is given as:

$$\min_{u} \quad \sum_{fe=1}^{16} \sum_{cp=0}^{3} \Phi_{Y,fe,cp} + \Phi_{P,fe,cp} + \Phi_{\alpha,fe,cp} + \Phi_{\gamma,fe,cp} + \Phi_{\tau,fe,cp} \tag{4.98}$$

For the calculation of optimal trajectories, a two-step procedure is implemented and shown in the sketch of the optimization framework in Fig. C.13. At the beginning of the optimization only the initial state at $t = 0\,\mathrm{h}$ is given. Thus, a pre-optimization is performed to initialize the model with variable controls on the full time frame of the current optimization step. This is done by initializing the length of the finite elements on a small value and subsequently enlarge it, while no objective function, but all constraints are provided. A step-size control is applied to ensure feasible solution for every enlargement step, till the final horizon length is reached. After that, the solution on the full horizon is taken and re-optimized, providing the above specified objective function.

4.4.4 Continuous Implementation of Optimal Control Strategies

To enable optimal operation of the mini-plant system, the online application of state estimation and trajectory optimization is desired. Key obstacle for that is the efficient coupling of state estimation and optimization, as well as the realization of necessary computation time to solve respective optimization problems.

Regarding this, Fig. 4.32 presents the calculation routine and scheduling for the D-RTO framework developed for the hydroformylation mini-plant. Therein, two major aspects are shown. Firstly, dashed boxes mark time horizons, on which specific data sets, such as reconciled or estimated data or optimal trajectories of plant controls are given. Respective calculation time frames are then marked with boxes (full line). For the given application, time intervals are set to $t_{k+1} - t_k = 2\,\mathrm{h}$.

Initially, D-RTO assumes the availability of a first set of optimized plant controls given on horizon $\{t_0 - t_3\}$. Starting at time point t_3, state estimation (**SE 1**) on available plant data for

horizon $\{t_0 - t_2\}$ is performed using the algorithm in Fig. 4.31. The first inner estimation step is using only fast measurements from the plant (full line in **Measurements 1**). Subsequently, the outer state estimation is performed on the slow measurements (squares), when the last concentration information for time point t_2 is available after passing its delay due to sampling. This results in **Validated Measurements /Model State Estimate 1** for $\{t_0 - t_2\}$. The state of the model at t_2 is then passed as initial to a simulation step (**Sim 1**). This simulates the trajectory of the mini-plant for time horizon $\{t_2 - t_3\}$ (**Simulated Trajectory 1**), still given the initial optimal trajectory of controls. This step is crucial, as it is the projection of the future plant behavior based on the state estimation, which is necessary to generate required computation time for all calculation steps. Subsequently, the optimization **Opt 1** is started, calculating optimal trajectories of control setpoints of the plant for $\{t_3 - t_4\}$ based on the model state at t_3 given by the **Simulation Trajectory 1**. After the optimization is finished and **Opt. Trajectory 1** is available, one D-RTO loop is complete. The framework is now restarted on a shifted time frame $\{t_3 - t_4\}$.

In general, all calculations blocks in one D-RTO loop are executed within a time frame of 2 h. Afterwards, the optimized trajectory for the next horizon must be available. To increase the robustness of this approach regarding online application, several instances of the framework are started in parallel and partially also on shifted time horizons. This way the chance to obtain at least one feasible optimal trajectory and consistent estimates of the model state is maximized. Of course this does not ensure success of the D-RTO in case the plant has drifted out of bounds of the validity of the mini-plant model. In this case, process operation still has to be recovered manually. However, back up strategies are provided to aid this process, such as offline long-term trajectories from start-up optimization, as well as the already introduced soft-sensor and its KPIs.

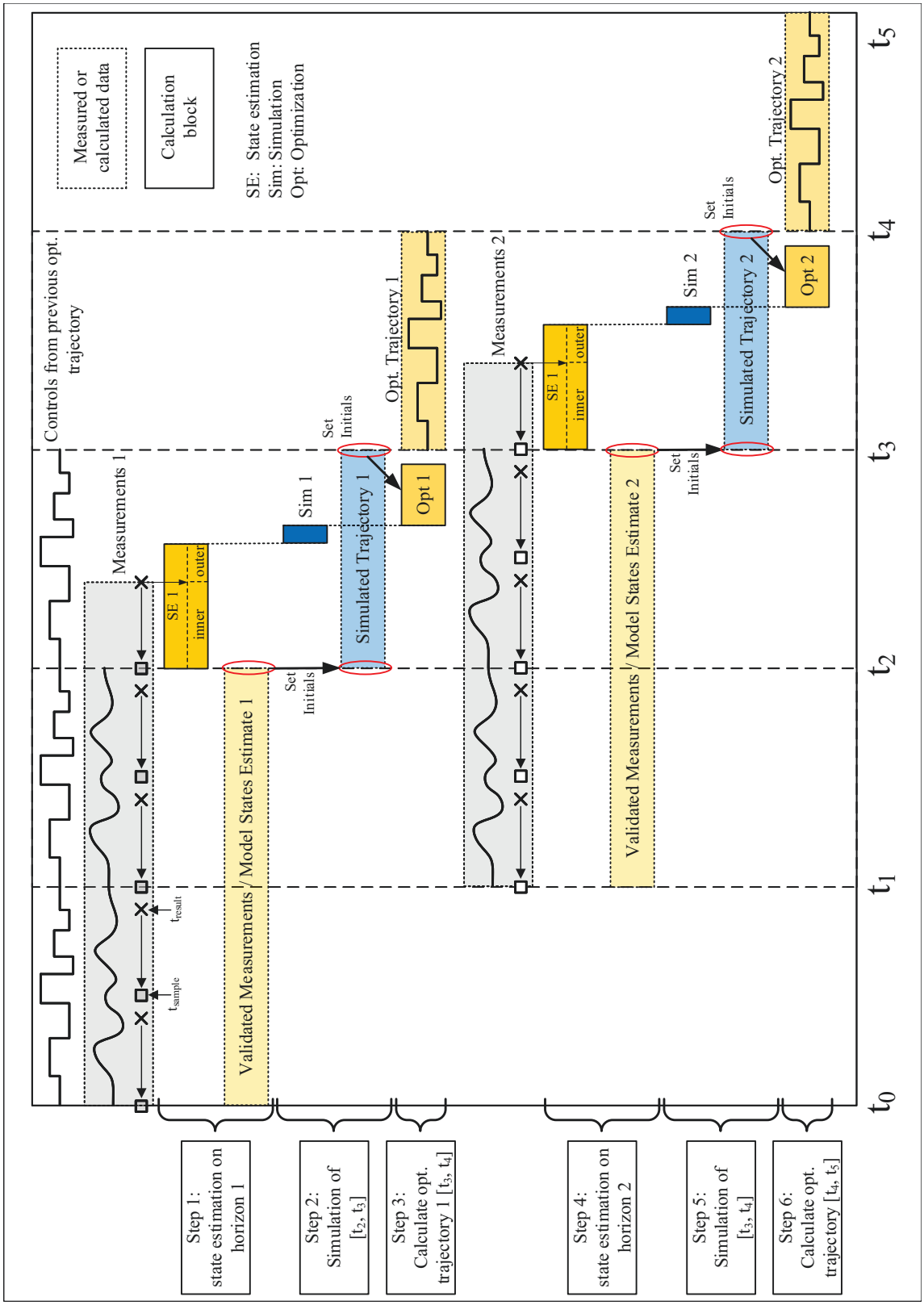

Fig. 4.32: Calculation routine and time frames for the continuous calculation of optimal trajectories. Displayed are the time frames for available measured and calculated data, as well as calculation time blocks for state estimation, simulation, and optimization.

5 Proof of Concept: Mini-Plant Operation Results and Application of Optimal Control Strategies

Within this chapter, mini-plant operation results are presented in order to provide a proof of concept for the hydroformylation of 1-dodecene in microemulsions. First of all, results of conventional mini-plant operations without model-based control strategies and respective identified challenges are presented. Based on mini-plant data, developed model-based elements, analytics, and optimal control strategies are evaluated regarding applicability and possible operation improvement. After that, a successful realization of a continuous plant operation is presented. Finally, the developed D-RTO scheme is tested and evaluated.

5.1 Conventional Unassisted Mini-Plant Operation and Identification of Operational Challenges

Results on a conventional mini-plant run are used to generally investigate the operability and viability of the concept of homogeneous catalysis in MES and the developed mini-plant system. Gathered long-term operation results represent a base case for comparison to later on applied improvements of operation and optimization. From that, several key aspects are raised for evaluation. An assessment of the mini-plant operation characteristics is used to discuss the process operability regarding steady state behavior, disturbance behavior, and system dynamics. Connected to this, reaction performance and success of the phase separation are looked at. Hence. it is checked, whether applied process conditions yield expected results. Secondly, reaction and phase separation are assessed regarding controllability and disturbance behavior. Operational challenges are identified and discussed. This is done to answer the important question, whether the observed process behavior can be explained by already known phenomena of the system and thus could be coped with by improving process design and operation.

5.1.1 Conditions and Standard Operation Modes

The first long-term mini-plant campaign (**Plant Op 1**) lasted for 167 h, following the schedule in Tab. 5.1. Experimental conditions and results were already presented in (Illner et al., 2016c; Illner et al., 2016b). The plant is continuously operated in a three-shift system with 3 operators per shift. After startup, the mini-plant can be operated in two basic operation modes: a continuous operation with an applied continuous feed of alkene and respective product drain towards the product tank. In case no feed is present all separated phases from the settler are fully recycled to the reactor. This (semi-) batch mode is applied for either stabilization of the phase separation or fast increase of reaction yield.

Reaction Conditions

According to the previously identified optimal reaction conditions, the reactor was operated at 15 bar gauge and 95 °C. The feed strategy was chosen to ensure a composition in the reactor according to the reference experiment in Fig. 3.2: of 46 wt.-% 1-dodecene and catalyst solution each, as well as 8 wt.-% Marlipal® 24/70. Accordingly, the catalyst solution was prepared applying 96.81 wt.-% water, $6.34 \cdot 10^{-2}$ wt.-% [Rh(acac)$(CO)_2$], 0.96 wt.-% SulfoXantPhos, and 2.17 wt.-% Na_2SO_4. During operation, the stirrer speed was kept above 600 rpm to ensure proper emulsification and gassing.

Operation Schedule

As stated by (Illner et al., 2016c), "the mini-plant operation was divided into several operation modes, in order to influence the reaction by manipulating feed rate, product purge, and residence time". First of all, the system was inertization with N_2. Afterwards, alkene, catalyst solution, and surfactant were fed into the plant. The applied operation schedule is shown in Tab. 5.1.

Tab. 5.1: Operation schedule for the mini-plant operation **Plant Op 1** and applied fixed controls for several operation modes (SP1-SP4).

	SP 1	SP 2	SP 3	SP 4
Operating hour / h	0-97	97-109	109-125	125-167
Operation mode	continuous	full recycle	continuous	continuous
$\tau_{Reactor}$ / h	0.32	2.00	1.85	1.82
$\tau_{Settler}$ / h	0.47	3.00	2.73	2.68
$\tau_{Reaction}$ / h	2.00	5.80	7.09	7.01
Total recycle rate / g/h	1500	250	250	250
Recycle ratio oil:mix:water	0.19:0.57:0.24	0.40:0.20:0.40	0.40:0.28:0.32	0.24:0.52:0.24
Feed rate alkene / g/h	100	0	30	30

After start-up, **SP 1** was initially started in full recycle mode to stabilize the phase separation and test the recycle operation. At 20 h, the reaction was initiated by feeding syngas and switching to continuous operation at a high alkene feed rate. **SP 2** was then used to increase the yield of tridecanal in a full recycle operation, before entering the continuous operation at a lower feed rate of 30 g/h in **SP 3**. Finally, **SP 4** investigated the influence of changed recycle ratios on the performance of separation and reaction. In addition, Tab. 5.1 provides information on residence times for reactor, settler, and the reaction. The residence time of the reaction is defined to enable the comparison of the reaction performance in the plant with lab experiments. The formulation includes the effect of internal recycles and is further described in Sec. D.1.

To aid the discussion of results, data on the applied controls and respective measurement data are furthermore given: reactor pressure, temperature, and settler temperature profiles are shown in Fig. 5.1. Figure D.15 depicts measured feed rates. Figure 5.2 shows recycle streams and recycle ratios calculated from setpoint data (Fig. D.16). It is apparent that several adjustments of the recycle ratio and related to that, also the settler temperature were made. This is especially true for **SP 1** and related to the stabilization of phase separation during reaction and recycle operation. The setpoint changes were made manually using heuristics derived from first lab-scale experiments. Moreover it has to be mentioned, that rather large offsets between applied pump setpoints and actual flow measurements are present. Especially for the recycle streams this is due to fluid properties of the emulsion.

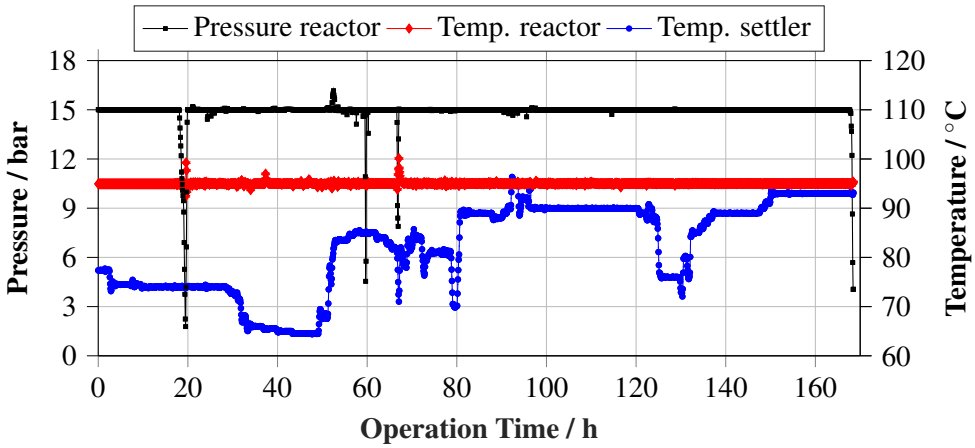

Fig. 5.1: Operation schedule conventional mini-plant campaign: system pressure and temperatures.

Disturbances

Following Illner et al. (2016c) “unavoidable systematic or random disturbances and their impact on the process have to be considered” to evaluate the operation data. “Concentration measurements (...) were carried out via offline gas chromatography implying manual sampling. Hence, the total liquid amount inside the plant was reduced each time and needed to be replenished according to the extracted components”. A total of 30 g was extracted every hour, which equals roughly 1.2 % of the total liquid amount in the plant’s high pressure section. Hence, these masses were re-fed based on the analysis result from GC to diminish the influence of sampling from the plant. Moreover, it is noted, that a pump failure of the water recycle occurred at the beginning of **SP 2**, which led to a hold and standby phase of approx. 20 h.

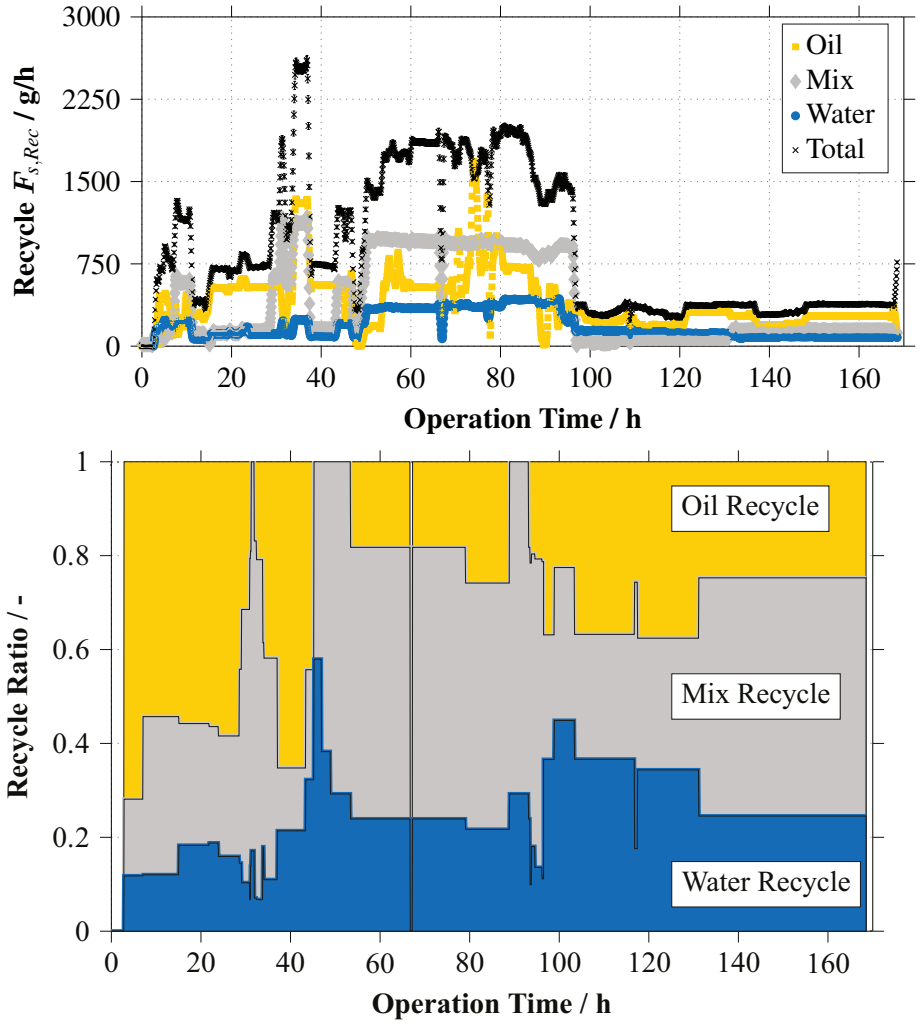

Fig. 5.2: Operation schedule conventional mini-plant campaign: measured recycle rates to the reactor and the recycle ratio per stream setpoint are given.

5.1.2 Mini-Plant Operation Results

Reaction Performance

Firstly, the reaction performance is discussed regarding conversion of 1-dodecene X_{s8} and yield of tridecanal Y_{s8} in the reactor. Definitions of these reaction performance indicators are given in Sec. D.1. Figure 5.3 then shows conversion and yield for the horizon of plant operation. Mark ups for the respective operation setpoint and the theoretically achievable reaction yield according to the applied residence time of reaction and lab references (Fig. 3.2) are additionally supplied. Figure 5.4 provides the corresponding concentration profiles of all reactants.

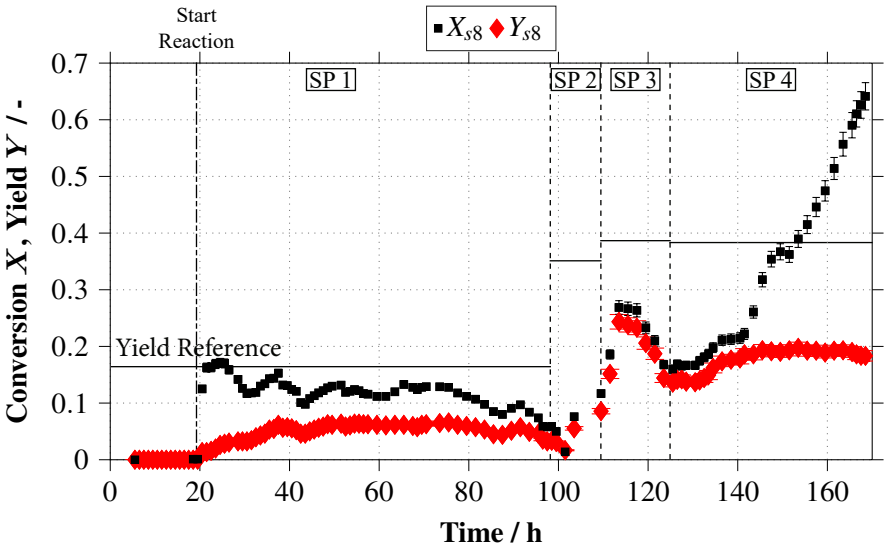

Fig. 5.3: Operation results conventional mini-plant campaign: total conversion of 1-dodecene X_{s8} and yield of tridecanal Y_{s8} in reactor.

In general, a successful realization of the hydroformylation reaction in the mini-plant is found. Significant amounts of the target product **Tri**d**ec**anal (TDC) were observed throughout all operation modes. However, in comparison to the reference yield, it is obvious that firstly the reaction performance is severely dampened within the mini-plant and secondly the chemo-selectivity regarding TDC is severely lower. With the reaction start at $t = 20\,\text{h}$, the reaction immediately starts with the conversion of 1-dodecene, which peaks at 17 % after 5 h. Simultaneously, the formation of tridecanal starts, but is outperformed by the isomerization reaction (tridecanal:iso-dodecene 2.5:15 wt.-% after 5 h). With ongoing continuous operation and a feed rate of 100 g/h alkene, the reaction performance stabilizes around 60 h with a yield of 6.2 % and a conversion of 12 %. At the end of **SP 1** the conversion drops significantly, while TDC yield only lightly decreases. Here, leakage at the water recycle pump led to a loss of aqueous phase and catalyst. Consequently, the reaction activity decreased.

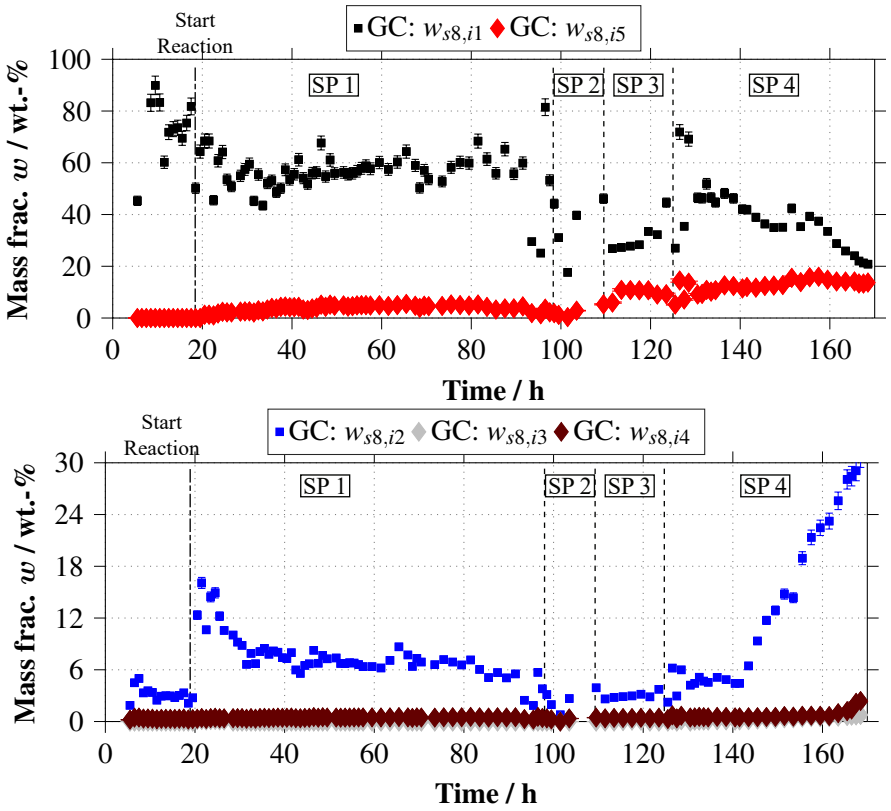

Fig. 5.4: Operation results conventional mini-plant campaign: reactant mass fractions in reactor. $w_{s=8,i}$ 1-dodecene ($i = 1$), iso-dodecene ($i = 2$), iso-TDC ($i = 3$), dodecane ($i = 4$), TDC ($i = 5$).

The reasons for this bad reaction performance are analyzed based on Sec. 3.3. With the initial startup of the mini-plant and feeding of freshly prepared catalyst solution, a reduced ligand to metal ratio is not considered as reason for the shown byproduct formation. However, considering the observations of the settler's sight glass for the time horizon of **SP 1** in Fig. 5.5, it appears, that the catalyst was insufficiently activated at reaction initiation. The active (and selective) catalyst species is of a bright yellow color, while the inactivated catalyst is red. This indicates an insufficient supply of CO and thus inselective catalyst species were formed (compare to Fig. 3.4). To this end, the formation of iso-dodecene as byproduct is also an indicator for this hypothesis. With ongoing plant operation, the catalyst within the plant was successively activated, stabilizing the reaction performance.

Starting with **SP 2**, yield and conversion increased as expected for the full recycle operation and the subsequent continuous operation at low feed rate in **SP 3**. This resulted in an acceptable chemo-selectivity above 90 %. However, starting with hour 114 X_{s8} and Y_{s8} decreased despite otherwise unchanged controls. Referring to Fig. 5.5 a significant accumulation of emulsion or surfactant in the settler was observed, also trapping catalyst solution. This led to a drop of the

catalyst concentration in the reactor and subsequently reducing reaction rates. As a counter measure, the settler temperature was increased to 95 °C and the recycle ratio was changed to mainly recycling emulsion phase for **SP 4**. This initially resulted in increasing X_{s8} and Y_{s8}. However, starting with operating hour 142, again a severely high rate of isomerization was observed. This led to an almost linear conversion increase, while the yield of tridecanal remained almost unchanged. Again, changes in the catalytic system are indicated to cause this behavior. In this case, the residence time of the settler was set to a rather high value of 2.7 h with the fraction of the water recycle stream being at 0.24 of the total recycle. Hence, only small amounts of catalyst were recycled and a depletion of dissolved CO occurs in the settler. Again, this caused the formation of inselective catalyst species (see also Sec. 2.2). Additionally, the observations of the sight glass show a large amount of dense surfactant layers in the settler, which additionally inhibits vertical mass transfer of CO in the settler.

Separation Performance

The separation success for the mini-plant operation is evaluated by the purity of the oil phase, which is defined as the combined mass fraction of all oily compounds in the oil phase. Figure 5.5 shows a respective diagram with added pictures of the settler's sight glass at specific time points.

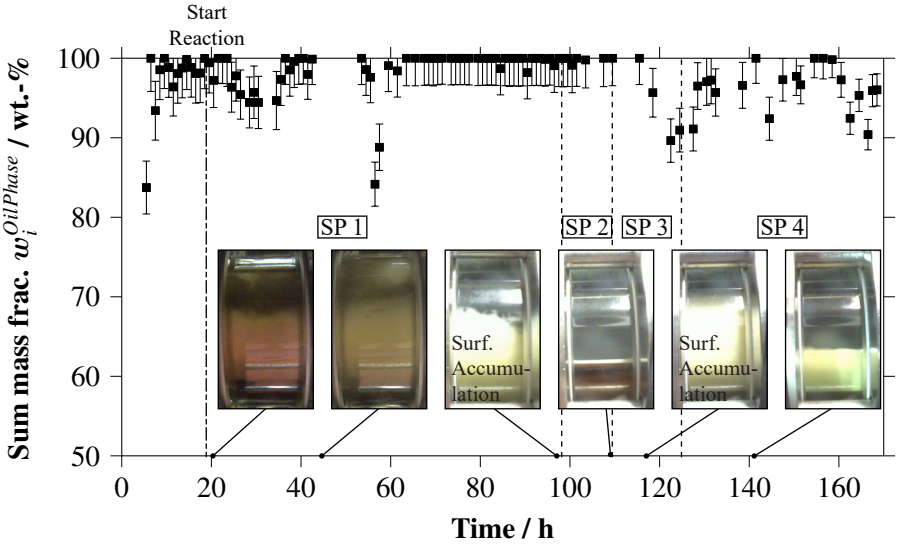

Fig. 5.5: Operation results conventional mini-plant campaign: quality of phase separation as total amount of oily compounds $i = 1 \ldots 5$ of settler oil phase. Additionally the visual observation from the camera system is given at specific time points.

Despite the already described partially perturbed operation the phase separation was in general stabilized to such an extend that good oil phase purities above 90 wt.-% were obtained. Especially

at the end of **SP 1** phase separation resulted in rather good quality of the oily excess phase close to 100 wt.-% mass fraction of oil. However, the occurrence of surfactant accumulation in the settler and applied counter measures (recycle ratio changes and settler temperature increase) decrease the purity of the oil phase significantly. Especially on temperature increase, larger quantities of surfactant dissolve in the oil phase (transition **SP3** to **SP4** in Sec. 4.3.6).

Conclusion and Operational Challenges

Concluding this mini-plant operation, a successful first realization of the hydroformylation of 1-dodecene in microemulsions is partially given. However, the expected reaction performance was not met since either target yield of tridecanal was not achieved or unexpected drops in selectivity occurred. The continuous phase separation in the settler was successfully initialized and allowed syphoning off of high purity oil. However, the actual control of the phase separation was rather challenging and fully based on system knowledge and heuristics. Frequent concentration shifts and substance accumulations in the plant appeared, which additionally affected the reaction performance. Moreover, measurements of recycle streams and operation of pumps were unreliable due to the fluid properties of the microemulsion. From the system analysis, these phenomena however are understood and can directly be linked to observations or control actions of the mini-plant operation. To this point, reliable and predictable long-term mini-plant operation is impossible and the application of strategies for improvement of process operation and unit design from Chap. 4 is advised.

5.2 Validation and Application of Strategies for Process Design & Operation

In this section the developed strategies to improve process design and operation are individually tested regarding applicability and validity for the technical mini-plant system. Thus, their potential for long-term continuous plant operation and benefit on process operability (suitable reaction performance and phase separation stabilization) are evaluated. This includes the developed adapted kinetic model, online testing of Raman spectroscopy for in-situ measurements of concentrations, and testing of the phase separation soft-sensor. Afterwards, the development of optimal mini-plant startup trajectories is presented alongside a case study on multi-rate moving horizon state estimation. Key element here is the developed dynamic mini-plant model from Sec. 4.3. In case no further information is given the model parameters and additional design variables of Sec. C.3 are applied therein.

5.2.1 Validation of Kinetic Model

The development of the adapted hydroformylation kinetics in Sec. 4.3.4 is based on lab-scale data. It is thus mandatory to validate this model with mini-plant data and ensure, that no additional phenomena appear during this scale-up (scale-up factor mini-plant - lab reactor ≈ 10).

Batch Operation

First of all, a batch experiment was performed: an initial reaction mixture was fed to the reactor according to Tab. 5.2. The mixture was then heated up and emulsified using a stirrer speed of 900 rpm. The reaction was then started by quickly feeding syngas.

Tab. 5.2: Feed composition and reaction conditions for batch reaction experiment in mini-plant.

Feed composition			**Reaction conditions**		
1-dodecene	45.99	wt.-%	Temperature	95	°C
Catalyst solution	46.01	wt.-%	Pressure	15	bar
Surfactant	8.00	wt.-%			
Conc. [Rh(acac)$(CO)_2$]	256.83	mg L^{-1}			
Molar ratio SX:Rh	5.016	-			
Total Mass	750.12	g			

Based on the given experimental conditions, a simulation of the reaction in the mini-plant was carried out in gPROMS® using the full mini-plant model and solution specifications given in Sec. D.2. Figure 5.6 compares resulting trajectories for a respective batch reaction with experimental data collected from GC sampling. For this, conversion and yield are depicted over the time horizon of the experiment of 6 h. In general, a very good agreement of experiment and simulation can be observed with a maximum deviation of 1.1 (conversion) and 1.6 percentage points (yield), which is within the range of measurement error. The deviation is largest for longer experimental duration due to the fact, that experimental data on larger time horizons for estimation of kinetic parameters was scarce and the kinetics thus yield a better fit on the typical time horizon (0-4 h for lab-scale experiments).

This is also evident for the profiles of mass fractions of reactants in Fig. 5.7. Larger mismatches are visible starting from $Time > 4$ h and especially for the byproducts iso-dodecene ($w_{s8,i2}$) and dodecane ($w_{s8,i4}$). However, adequate matching for the educt 1-dodecene ($w_{s8,i1}$) and target product tridecanal ($w_{s8,i5}$) is found and trends for the formation of (by-)products are predicted correctly. Thus the developed adapted kinetic model for the hydroformylation in microemulsions is considered as suitable for further application.

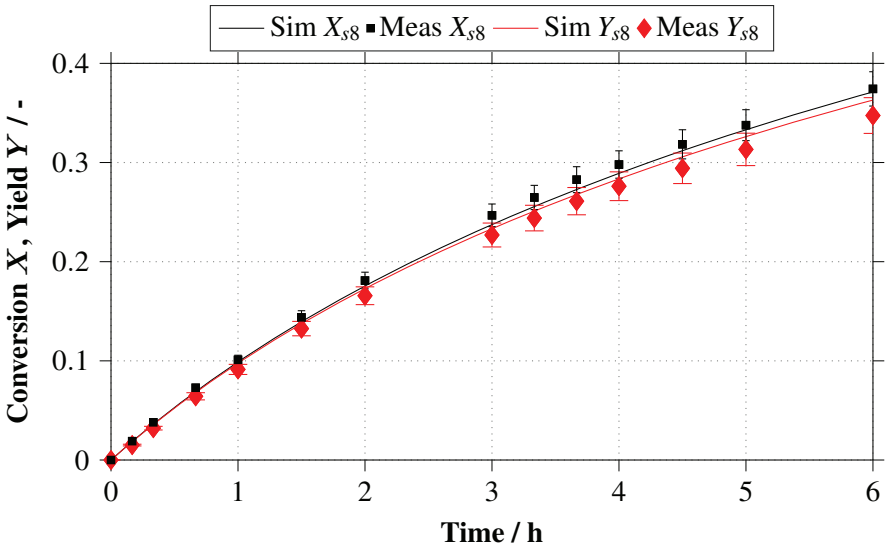

Fig. 5.6: Comparison mini-plant batch operation and simulation: conversion of 1-dodecene $X_{s=8}$ and TDC yield $Y_{s=8}$.

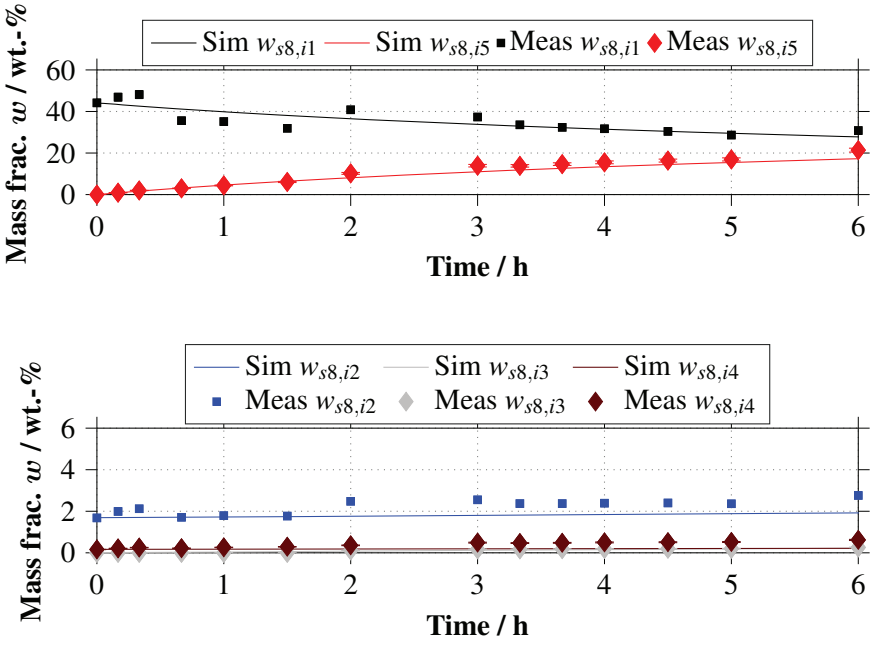

Fig. 5.7: Comparison mini-plant batch operation and simulation: mass fractions $w_{s=8,i}$ 1-dodecene ($i = 1$), iso-dodecene ($i = 2$), iso-tridecanal ($i = 3$), dodecane ($i = 4$), tridecanal ($i = 5$).

Continuous Operation - Plant Op 1

In addition to the batch experiment, a gPROMS® simulation study on the already shown mini-plant operation **Plant Op 1** is presented. The idea is to verify whether the kinetic model is capable of predicting the observed disturbed plant operation regarding byproduct formation and drop in selectivity. The model was initialized in accordance to the state of the mini-plant at operation time $t = 132\,\mathrm{h}$ and simulated for 24 h. Using the initial feed at startup and the obtained concentration information, a suitable total compound mixture of the plant was calculated according to Tab. 5.3. The simulation was then initialized as continuous operation adhering to the given reaction conditions and recycle operation in Tab. 5.1.

Tab. 5.3: Feed composition and reaction conditions for plant simulation of **Plant Op 1**.

Feed composition					
1-dodecene	36.54	wt.-%	Catalyst solution	47.31	wt.-%
Iso-dodecene	3.32	wt.-%	Surfactant	6.33	wt.-%
Iso-tridecanal	0.00	wt.-%	Conc. [Rh(acac)$(CO)_2$]	256.00	$\mathrm{mg\,L^{-1}}$
Dodecane	0.35	wt.-%	Molar ratio SX:Rh	1.00	-
Tridecanal	6.05	wt.-%			
Reaction conditions					
Temperature	95	°C	Pressure	15	bar

It was already mentioned, that the undesirable high residence time in the settler for setpoint **SP 4** can be linked to the observed drop of reaction selectivity due to depleting dissolved gas concentrations in the settler and potential formation of inselective catalyst species. Hence, the ligand to metal ratio is artificially set to 1 for this simulation to activate the *selectivity switch* in kinetic rate equations (Eq. (4.34)).

The result of this comparison is depicted in Fig. 5.8 for the conversion of 1-dodecene and the yield of tridecanal. Immediately with the start of the simulation, fast increasing conversion and yield are visible despite the continuous operation. This is mainly due to the increased reaction rates for the assumed low ligand to metal ratio. Surprisingly, the TDC yield shows a very good agreement with mini-plant data, predicting the plant trajectory with a maximum relative deviation of 4.3 %. In comparison, the trajectory for the conversion of 1-dodecene X_{s8} is only met in general. Relative deviations of plant data and simulation of $2.8 - 23.9\,\%$ are thus found. Here, the simulation predicts a smooth logarithmic behavior of the conversion, while plant data shows an initially slower logarithmic increase for operation hour $132 - 142\,\mathrm{h}$ and subsequent high linear increase of X_{s8}. In this case, larger amounts of iso-dodecene were formed. Several interfering influences on the catalytic system, such as gas supply to the catalyst and thus altered catalyst equilibria as well as concentration shifts are prone to result in such an observation.

Despite the inaccurate prediction of the dominant byproduct formation, this simulation study successfully shows that using the adapted kinetic model, the encountered undesired inselective reaction performance can be generally reproduced. This is very helpful in the context of optimization of process operation as these operation conditions can hence be avoided.

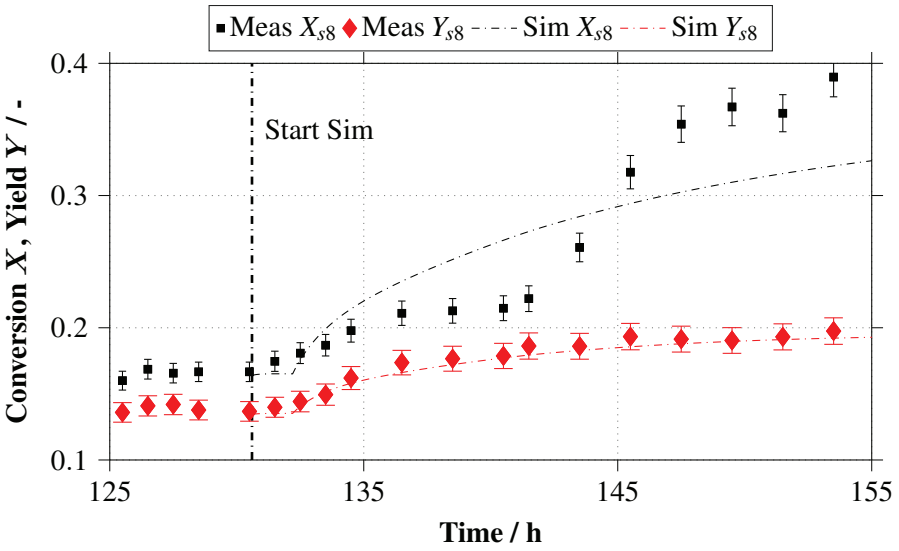

Fig. 5.8: Comparison mini-plant continuous operation and simulation: conversion $X_{s=8}$ and yield $Y_{s=8}$.

5.2.2 Applicability of Raman Spectroscopy

To overcome the hurdle of sampling dead times of offline liquid GC analysis and the reduced compound measurability, Raman spectroscopy was studied. As already presented in Sec. 4.2.3, a calibration test stand including NMR, GC, and UV/vis as reference analytics was developed. Dynamic experiments under process conditions with multiple probe geometries and with active hydroformylation reaction were thus performed (Meyer et al., 2017a). Based on the collected data, it was attempted to develop chemometric models of the deployed substances in the microemulsion and thus for in-situ measurements. The model development itself consists of spectral data pretreatment by standard normal variate transformation and detrending, followed by the formulation of **P**artial **L**east **S**quares (PLS) regression models for each compound (Paul et al., 2017). This way, suitable PLS1-models were obtained for 1-dodecene and tridecanal with *RSME* of internal cross validation of 2.51 and 2.93 wt-.%, respectively. Unfortunately dodecane, the surfactant, and water remained inaccessible due to missing unique Raman shifts.

The applicability was then also tested online during the mini-plant campaign **Plant Op 1**, applying a Raman immersion probe directly to the reactor outlet. The focus was put on testing

the given chemometric models for application in the technical mini-plant system and analysis of the robustness of the prediction regarding changes in process operation and disturbances. As a results, Fig. 5.9 shows a comparison of the concentration predictions obtained from Raman sampling (V) and GC for 24 h of operation. Additionally, information on the applied total recycle stream in g/h is given. It is apparent, that for the first 17 hours of operation, the Raman prediction does not meet the reference measurements obtained by GC. Larger amounts of tridecanal are returned, although the reaction was not yet started. However, after activating the reaction very good agreement of both methods is visible. The reason for this lies in the catalyst activation itself, for which the color of the reaction mixture changes from red to yellow. This also represents a drastic change in the optical properties of the reaction mixture, which affects the intensities of obtained Raman spectra. Given the fact, that the calibration models were set up for the reactive system, validity is thus also only gained after initiation of the reaction.

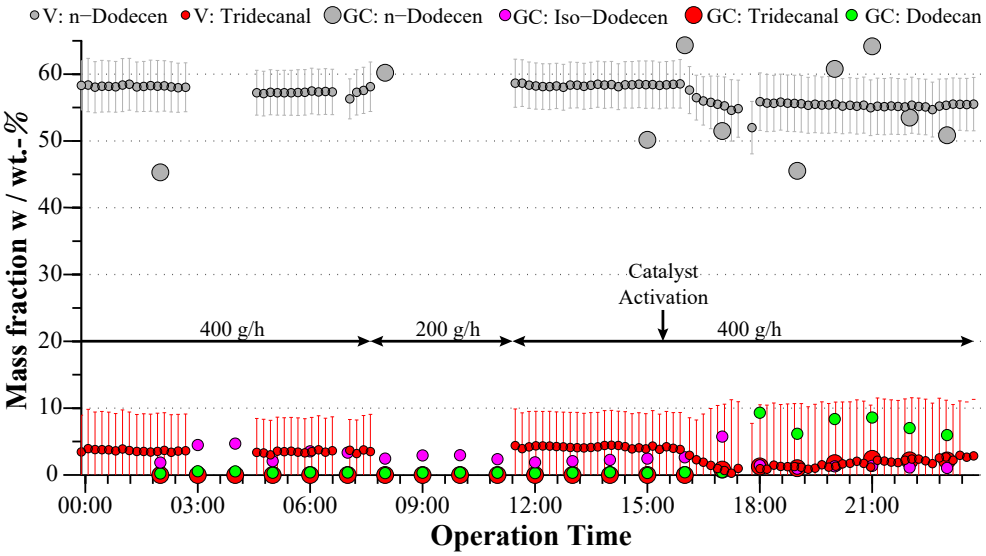

Fig. 5.9: Results Raman spectroscopy application for mini-plant operation **Plant Op 1** and comparison of Raman prediction (V) to GC.

Furthermore, several total failures of the method are visible (blank areas around 09:00 and 07:30-12:00). These are closely related to changes in the operation conditions, such as surfactant feeding or changed recycle ratios. In fact, at time point 07:30 the total mini-plant recycle was reduced to 200 g/h, which led to an immediate loss of applicability of the Raman model. However, when the initial total recycle of 400 g/h was restored, also utilizable spectra were regained. This phenomenon can be connected to the properties of the microemulsion. With changing operation conditions, several micelle configurations, microemulsion structures and turbidities of the reaction mixture are possible (Fig. 2.5). These also represent widely altered

optical properties of the mixture, which again influence the Raman spectra. One promising approach to overcome this obstacle is the coupling of chemometric model information with the optical properties of the mixtures. Methods like photon density wave spectroscopy or multi angle light scattering can be used to track the current microemulsion configuration and enable switching between different prediction models.

5.2.3 Application of Soft-Sensor and Phase Separation Model

Key element for obtaining observability and operability of the mini-plant is the developed soft-sensor for phase separation. Hence, it is mandatory to validate the operability and robustness of the developed approach on the mini-plant system and under reaction conditions.

Tracking of the State of the Phase Separation and Application of the Soft-Sensor

An application study on observations from a mini-plant is presented in Fig. 5.10. Sightglass observations of the mini-plant's settler are given together with detected levels for several operating states and disturbances of the phase separation.

Throughout all cases, the automated level detection script successfully gathered information on the volume fractions of the individual settler phases, regardless of the reaction state (cases 1 and 2) or disturbances. Case 3 shows a typical situation for continuous mini-plant operations, where surfactant clogging occurs at the inner sightglass surface due to heat loss to the environment. Case 4 then represents an operating condition close to the boundary between the three-phase and lower two-phase region, for which surfactant build-up occurs at the oil / emulsion interface (see Sec. 2.1.3). This additional liquid phase is also successfully mapped by level detection. Hence, a very good reliability and uptime of 98 % was ensured for various mini-plant campaigns of up to 100 h. In this context, a closer look is taken at the implemented phase separation KPIs. These are shown for case 1 and 4 at the bottom of Fig. 5.10. In both cases it was possible to calculate a respective fully described state of the separation model from detected volume fractions. Respective KPIs for volume fractions and phase separation temperature were then generated (Sec. 4.4.1). The former is essential for tracking the feasible operation region regarding α and γ given a constant temperature (large cumulated volume fractions Φ_{Oil}+Φ_{Water} indicate feasibility). For case 1, the current operating point is correctly located within the yellow to green area. For case 4 the boundary region is already reached. This corresponds to the also observed transition state towards the undesired two-phase region. The latter KPI provides information on the optimal phase separation temperature given the current composition in the settler. For case 1

and 4 physically meaningful results are obtained, which aligns with the identified sensitivities of α and γ on the optimal phase separation temperature, gathered in Tab. 3.5.

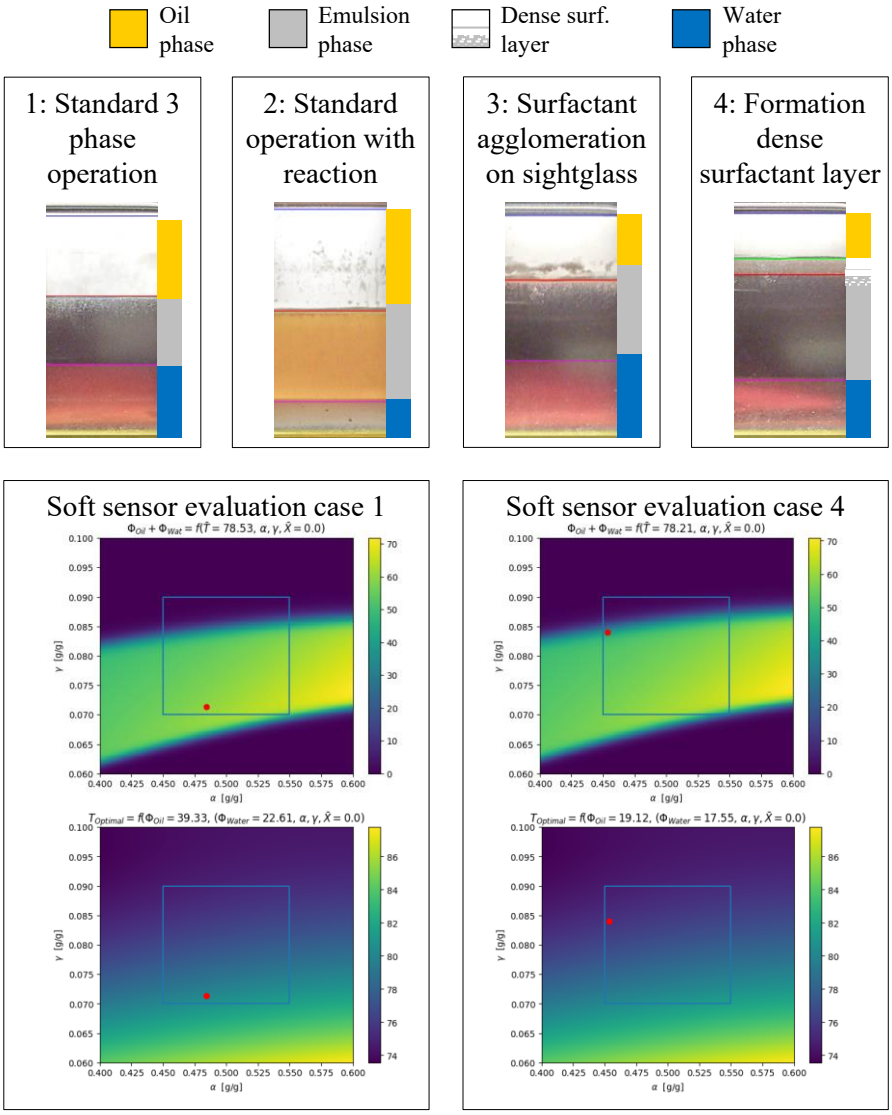

Fig. 5.10: Application case study of phase separation soft-sensor and phase separation model.

In addition to that, Fig. 5.11 sketches the online application of the soft-sensor for phase separation for the start-up process of the mini-plant. Here, reactor and settler were prefilled with a prepared reaction mixture, corresponding to a phase separation composition of $\alpha = 0.482\,\mathrm{g\,g^{-1}}$ and $\gamma = 0.072\,\mathrm{g\,g^{-1}}$. Initial phase separation was obtained at an optimal separation temperature of $T^{Opt} = 78.5\,^{\circ}\mathrm{C}$ (observation for time point 13:35). Since the initial composition is known, a direct comparison with the model response is possible. Here, a very good agreement is found

with a minimal relative deviation of 0.95 % and 0.55 % for α and γ, respectively. Subsequently, the recycle was started to establish a full recycle operation with stable phase separation at a composition setpoint of $\alpha = 0.5\,\mathrm{g\,g^{-1}}$ and $\gamma = 0.08\,\mathrm{g\,g^{-1}}$. To achieve this, frequent adjustments of the volumetric ratio of recycle streams were deployed.

For time point 16:15 this actually led to a significant shift of the settler composition, but rather undesired separation state with formed dense surfactant layers. Even with a KPI assisted opera-

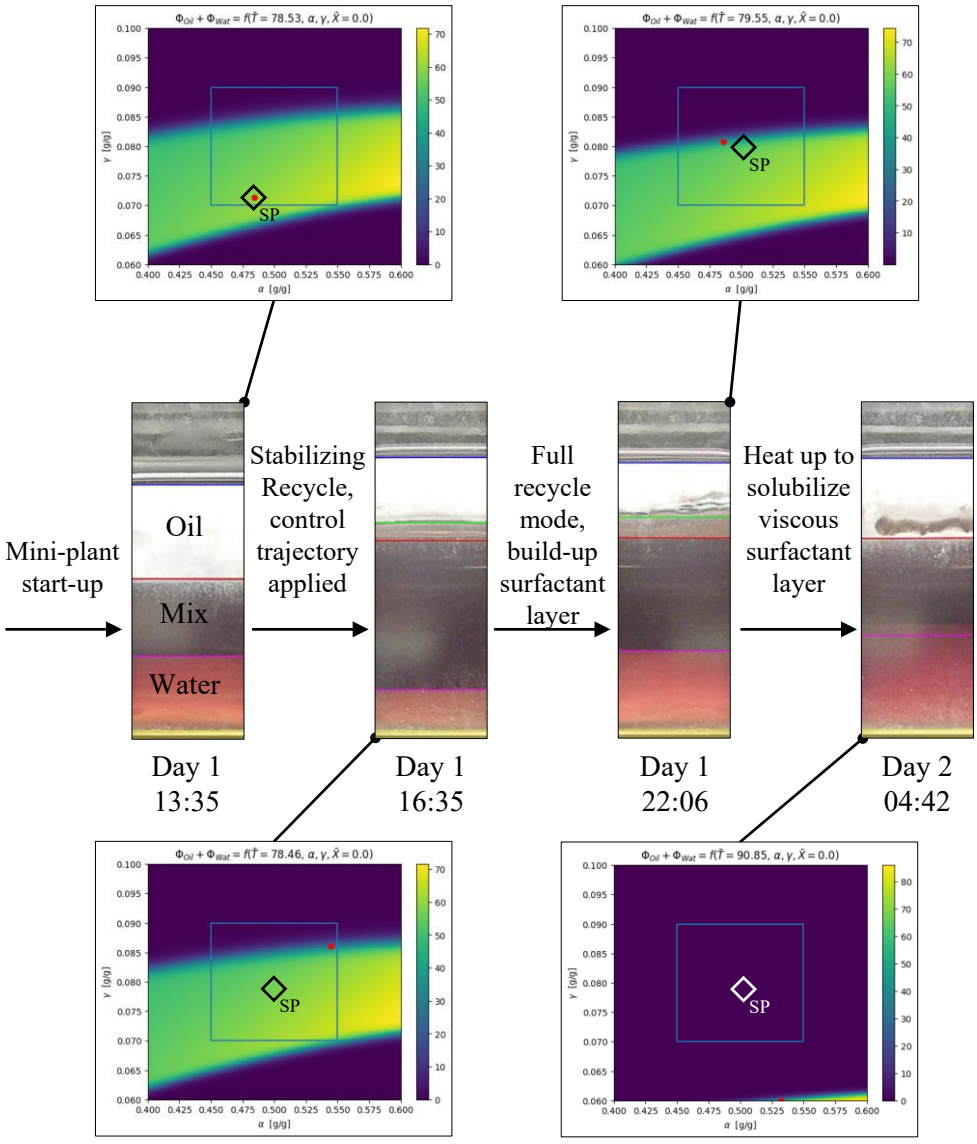

Fig. 5.11: Online tracking of the phase separation state for a mini-plant campaign using the phase separation soft-sensor and additional KPIs.

tion strategy, it was not possible to avoid this. Surfactant build-up slowly commenced despite the phase separation soft-sensor indicating a feasible operation. The reason for this was already explained for Fig. 3.13 and is related to pre-separation of the system before entering the settler. According to the coalescence behavior of MEs this likely results in accumulations of surfactant. This microemulsion specific challenge is to be tackled with the modified mixer-settler unit shown in Fig. 4.5, which was not yet operational at this point. As a countermeasure, the settler temperature was slightly increased to 79.5 °C to enhance separation performance and account for the reduced surfactant concentration at the inlet of the settler (accumulation inside settler). Until time point 22:06 this strategy yielded successful phase separation and stabilization of the settler's composition close to the desired setpoint. To re-homogenize the accumulated surfactant, it was then decided to significantly increase the settler temperature. This led to a complete dissolution of the accumulated surfactant until 04:42 (Day 2). However, with this unspecific separation state of the microemulsion (interlaced with dissolution and diffusion processes), the applicability of the soft-sensor for phase separation was lost.

Concluding it can be stated, that the developed concept of a model-based soft-sensor for surfactant concentration and phase separation tracking is a feasible approach to enable operation of microemulsion based processes with internal recycling. However, with the current development stage of the phase separation model and with respect to the technical operability of such systems it is mandatory to enforce well defined separation conditions for the microemulsion: phase separation must occur at a suitable and constant temperature out of a fully mixed state.

5.2.4 Development of Optimal Start-Up Trajectories

To this point, mini-plant operation and especially control of the phase separation is not satisfactory. It is thus worth to investigate the potential of dynamic optimization regarding the critical start-up of the mini-plant and transfer into continuous operation. A respective optimization problem was already formulated in Sec. 4.4.3. Main focus therein is on the stabilization of the phase separation and maximizing the product formation.

Initialization and Evaluation of Start-Up Strategies

Following Weber (2007), guiding principles apply for the start-up of chemical plants. Ideally, all units in the process are started separately. If reaction and separation steps are present, the latter should be started first. Afterwards operating units are step-wise coupled until to entire plant is operating. For the microemulsion system, these principles are not feasible, since larger concentration shifts and transient operations on starting and connecting individual units are

present. Control of the phase separation step is thus considered to be highly challenging. Thus optimized start-up strategies tailored to the current mini-plant configuration are proposed:

From a practical point of view, the initial filling of the mini-plant using variable feed streams is impractical and leads to fatal deviations in the resulting composition of the mixture. It is thus favorable to operate continuously at fixed feed rates. This way initial concentrations in reactor and settler can be realized more precisely. Hence, only a fixed feed composition and fixed feed rates apply for optimization. After plant filling, the optimizer is allowed to activate the reaction (syngas feed) and increase conversion towards a predefined target value of $X_{s8} = 30\,\%$. This represents the expected reaction conversion for a continuous operation with an alkene feed rate of $30\,\mathrm{g\,h^{-1}}$. Based on this, three start-up case studies are developed:

- **Full recycle**: After plant filling, recycle and reaction are directly activated. At target conversion, alkene feed and thus continuous operation is activated (sigmoidal switch).
- **Conti:** To avoid control actions and transient mini-plant states, the alkene feed is activated together with recycle and reaction.
- **TDC Feed:** Tridecanal is already fed to the plant on start-up. Thus target conversion is present from the beginning and the continuous operation mode can directly be initiated.

Manipulable variables, i.e., controls are specified in accordance with mini-plant actuators (Tab. 4.2) and are given by setpoints for the three feed and recycle streams, as well as reactor and settler temperature. Corresponding initial values and bounds are listed in Tab. D.28. The time horizon for each optimization scenario was set to 70 h with piece-wise constant control intervals of 1 h. The optimization problems were set up and solved in gPROMS® using the DAE mini-plant model and solution specifications given in Sec. D.2. Depending on the initialization, optimization problems were solved typically within 10 s and at maximum within 30 min CPU time. The resulting control trajectories for all three cases are given in Tab. D.29-D.30.

Figure 5.12 compares resulting trajectories on conversion of 1-dodecene. For all scenarios, feasible solutions are obtained, which adhere to the specified constraints. However, the results obviously vary regarding the objective of minimum time until continuous operation at target conversion is achieved. For the case **TDC Feed** the target conversion applies from the beginning and only stabilization of phase separation and recycle is necessary. In contrast, significantly longer start-up times of 15 hours and 46 hours apply for **Full recycle** start-up and the **Conti** mode. Hence, the addition of tridecanal for filling of the plant is recommended for economic optimality and reduction of transient operating states. Nevertheless, throughout this work full recycle start-up is favored due to the very high cost and poor market availability of tridecanal.

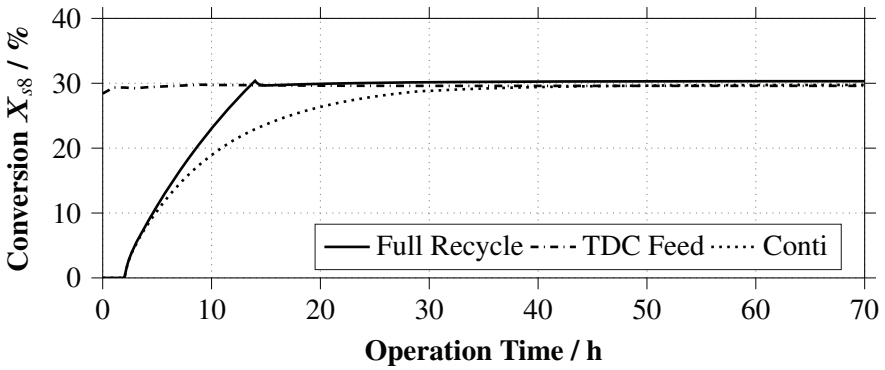

Fig. 5.12: Reaction conversion for three different start-up optimization scenarios.

Optimization Results - Full Recycle Start-Up

Fig. 5.13 shows the feed streams of alkene, catalyst solution, and surfactant. After the initial filling of the plant from operation hour 0 until 1, the feed is stopped and the plant is operated in full recycle mode with recycle pumps active (see Fig. 5.15). The alkene feed is then activated at around operation hour 15 and kept constant for the rest of the optimization horizon. Catalyst and surfactant feed remained near zero (approx. 0.05 $\mathrm{g\,h^{-1}}$ and 0.03 $\mathrm{g\,h^{-1}}$), thus no larger replen-

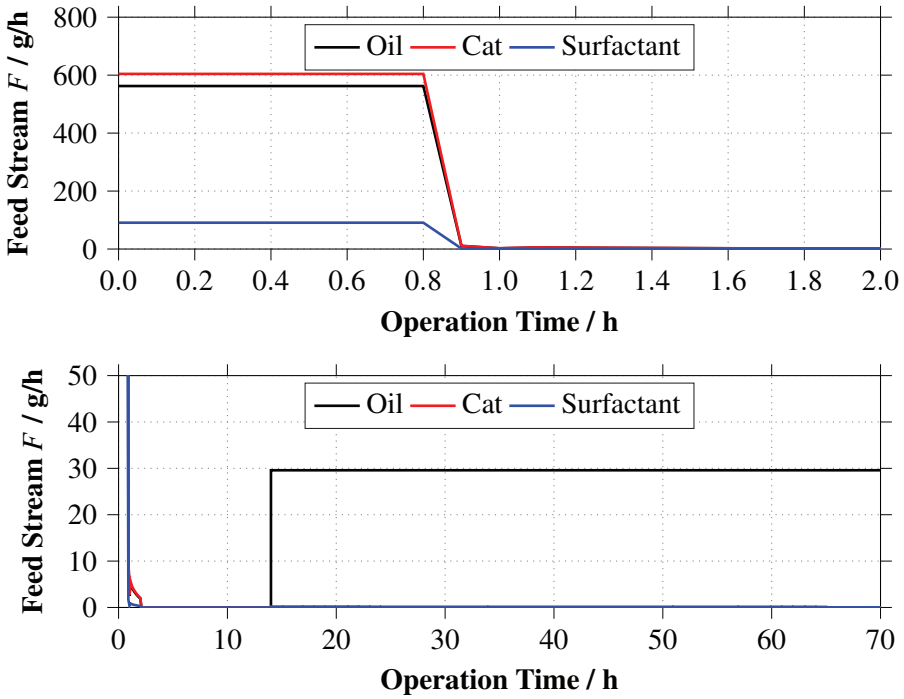

Fig. 5.13: Optimal start-up trajectory: controller setpoints for feed streams.

ishing of catalyst or surfactant is necessary to ensure the composition of the reaction mixture of approx. $\alpha = 0.5\,\mathrm{g\,g^{-1}}$ and $\gamma = 0.08\,\mathrm{g\,g^{-1}}$. This is also in perfect agreement with expected substance loss via the oily product stream $F_{s=19}$ (see model for composition of excess phases Sec. 4.3.6). However, for longer operating times replenishing of surfactant is recommended due to its high influence on the phase separation. To avoid concentration spikes and larger disturbances, feed devices such as syringe pumps are considered to enable small steady flows.

Most relevant for optimization of the mini-plant start-up is phase separation initiation and stabilization throughout all transient operating state. To this end, Fig. 5.14 presents the levels of the settler phases over time for two different cases: a simulation study with fixed recycle setpoints, as well as results from the presented start-up optimization. Starting the recycle with fixed setpoints of streams leads to significant concentration shifts in reactor and settler, since different pipe volumes apply for each individual recycle. Consequently, the simulation study states a

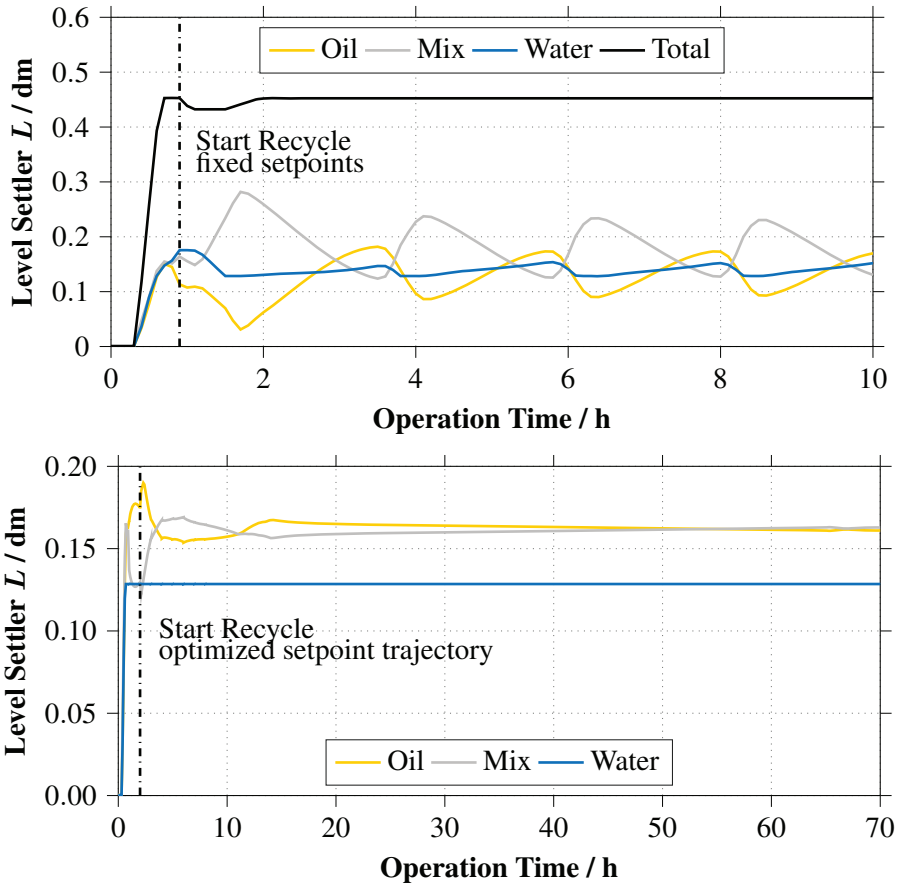

Fig. 5.14: Top: Simulated plant start-up: settler level fluctuations and phase separation failure, no optimization applied. Bottom: Optimal start-up trajectory with resulting settler phase levels.

situation, which was frequently encountered during first mini-plant runs: the phase separation is lost within less than 30 min and the level of the mixed phase increases to a maximum. Interestingly, an oscillatory behavior is then established. At some point after prolonged recycling of the emulsion phase the desired phase separation is regained and lost again. In contrast, the optimized trajectories signal stable phase separation throughout to whole start-up process. Here, large fractions of the aqueous and oily excess phase are present. However, from operation hour 0 until 15 several transitions of especially levels oil and mix phase can be found. For this time frame, recycle initiation and full recycle operation with fast increase of reaction conversion occurs. Thus concentration shifts are prone to alter the phase separation performance. However, with the applied control actions on recycle streams and temperature of the settler shown in Fig. 5.15, the feasible operation region for the three-phasic separation can still be maintained. By consequence, optimal recycle trajectories show frequent setpoint adjustments in this time frame. The drastic reduction of the oil phase recycle at around operation hour 15 is caused by the alkene feed. Regarding the settler temperature, a step-wise reduction is found for the start-up and reaction initiation phase. This is in perfect agreement with the identified influence of tridecanal on the optimal separation temperature (reduction).

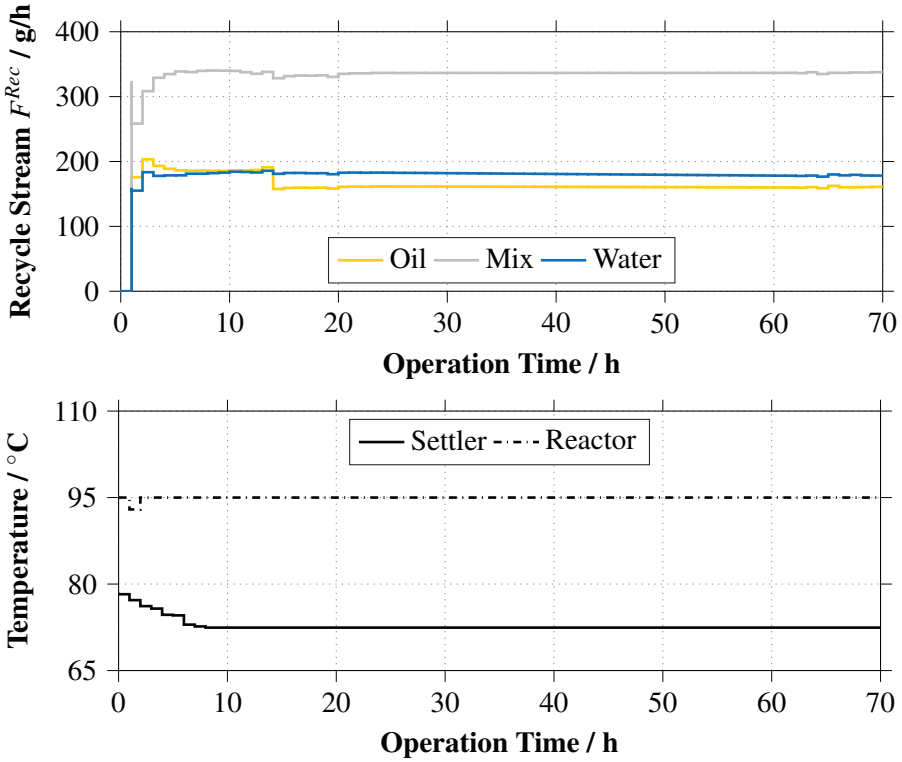

Fig. 5.15: Optimal start-up trajectory: controller setpoints for recycle streams, reactor, and settler temperature.

In general, control actions obtained from the optimization results are rather smooth and respective value changes are generally below 14 % of the previous setpoint. The developed optimal start-up trajectories are thus regarded feasible for application on the mini-plant.

5.2.5 Case Study Multi-Rate Moving Horizon State Estimation

The aim of the case study is to verify, that under the given model structure and measurements with according sampling rates appropriate and physically meaningful model states can be generated using the framework in Sec. 4.4.2. Thus, correct prediction of the (future) plant trajectories is strived for, which further enables optimization of control actions.

Reference Simulation and Measurement Data

An excerpt from the presented optimal start-up trajectory is used as a reference simulation study. Here, the full-recycle mode for operation time $t = [10,14]$ h is used. It provides an already established recycle with stable phase separation, which is the desired case of application for the state estimation. With the continuous reaction at least some transient behavior is included to account for dynamics. From this simulation, measurement data is generated. Measurement error is added according to the relative standard deviation of the respective sensor Tab. 4.1. Additionally, gross error is randomly added. The composed data set is summarized in Tab. 5.4.

Tab. 5.4: Properties of artificial measurement data for the case study on state estimation. STD: standard deviation.

Measurement	Interval	rel. STD / %	No. gross errors
L_{u1}	collocation point (<4 min)	1.67	6
L_{u2}	collocation point (<4 min)	1.67	0
L_{u3}	collocation point (<4 min)	1.67	0
L_{u11}^{Oil}	collocation point (<4 min)	1.67	0
L_{u13}^{Water}	collocation point (<4 min)	1.67	0
L_{u14}	collocation point (<4 min)	1.67	6
L_{u22}	collocation point (<4 min)	1.67	6
F_{s4}	collocation point (<4 min)	1.57	0
F_{s19}	collocation point (<4 min)	1.57	6
$w_{s8,i}$ $i \in \{1,\ldots,5\}$	1 h	4.0-4.4	0
$w_{u11,i}^{Oil}$ $i \in \{1,\ldots,5\}$	4 h	2.3-2.4	0
$w_{u13,i}^{Water}$ $i \in \{1,\ldots,5\}$	4 h	3.2-3.9	0

State Estimation Calculations

The state estimation is implemented in AMPL® using the framework shown in Fig. 4.31. For this, the fully discretized model is exported as AMPL® code using MOSAICmodeling. All calculation steps are performed given the hardware and solver specifications in Sec. D.2. As initial values for all variables the respective solution from the reference simulation at $t = 10\,\mathrm{h}$ is supplied alongside trajectories of all controls of the model (pump setpoints, temperatures). For the specified estimation horizon of 4 h, a feasible solution is attained within 230 CPU seconds, which is a very good result considering online application of the framework. Supporting information on the calculation times for respective simulation and optimizations steps can be found in Tab. 5.5. At this point, it is noted that the convergence behavior significantly depends on the choice of solver and its parameters. It has been found, that especially the interior point solver IPOPT suffers from variables converging towards their respective bounds and from bad choices for the barrier parameter (Wächter, 2002). Hence, CONOPT was preferred as optimization solver and provided satisfactory performance for various initializations of the respective NLP.

Tab. 5.5: CPU time for the state estimation case study. All calculation steps according to framework in Fig. 4.31 are listed. SE: State Estimation, FF: Fair Function, RE: Redescending Estimator.

Step	CPU Seconds Solver	CPU Seconds incl. AMPL Process
Initial sequential simulation	6.77	9.06
Simultaneous simulation	4.92	4.92
Inner SE - FF	85.01	85.04
Inner SE - RE	65.30	65.40
Simultaneous simulation	9.47	11.91
Sequential simulation	2.51	2.51
Outer SE - FF	25.24	25.26
Simultaneous simulation	3.71	3.81
Outer SE - RE	22.49	22.56
Total	225.44	230.47

Results of the State Estimation

To discuss the results of the case study, a comparison of the resulting estimation, used measurement data, and the reference simulation is shown. Generally, a very good agreement of results from state estimation and the model simulation is visible. This is especially prominent for the levels of feed tanks $L_{u1} - L_{u3}$ in Fig. 5.16, even under the influence of gross error in measurements of L_{u1}. For levels of oil and water phase in Fig. 5.16, a similar result is obtained. However, the oil level shows minor divergence at the beginning of the time horizon, which is related to adjustment of the initial hold-up of the oil phase (manipulable variables for optimizer).

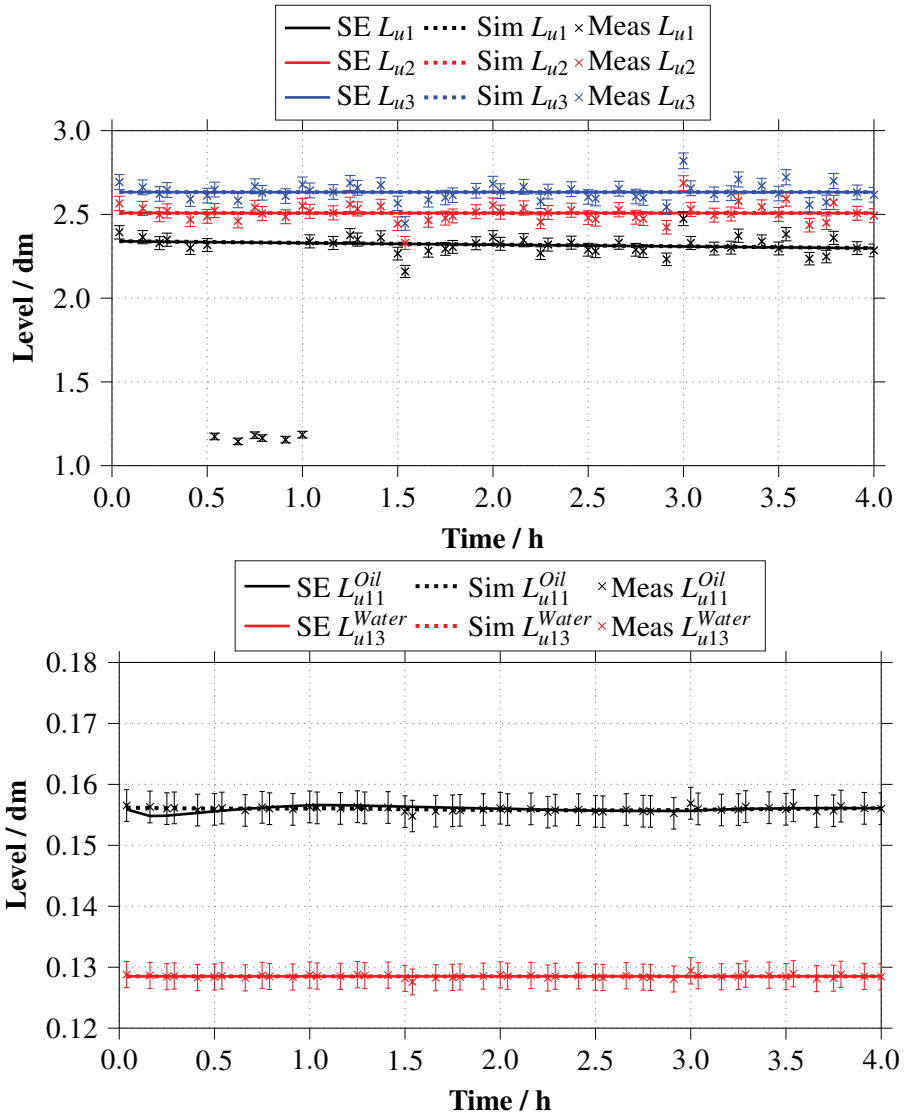

Fig. 5.16: State estimation case study: results for levels of feed tanks (top) and levels of settler excess phases (bottom).

The results for the phase separation-related variables is shown in Fig. 5.17. Again, reference values from simulation are met with high accuracy. No concentration drifts or shifted ratios of recycle streams are found. Hence, it is possible to obtain valid states of the phase separation over time given only experimental data on reactant concentrations, level information, and evaluated fractions of phase volumes from the soft-sensor. This implies that the developed structure of the phase separation model is appropriate to obtain full sets of valid initials of the model only given the rather reduced information content of the measurements.

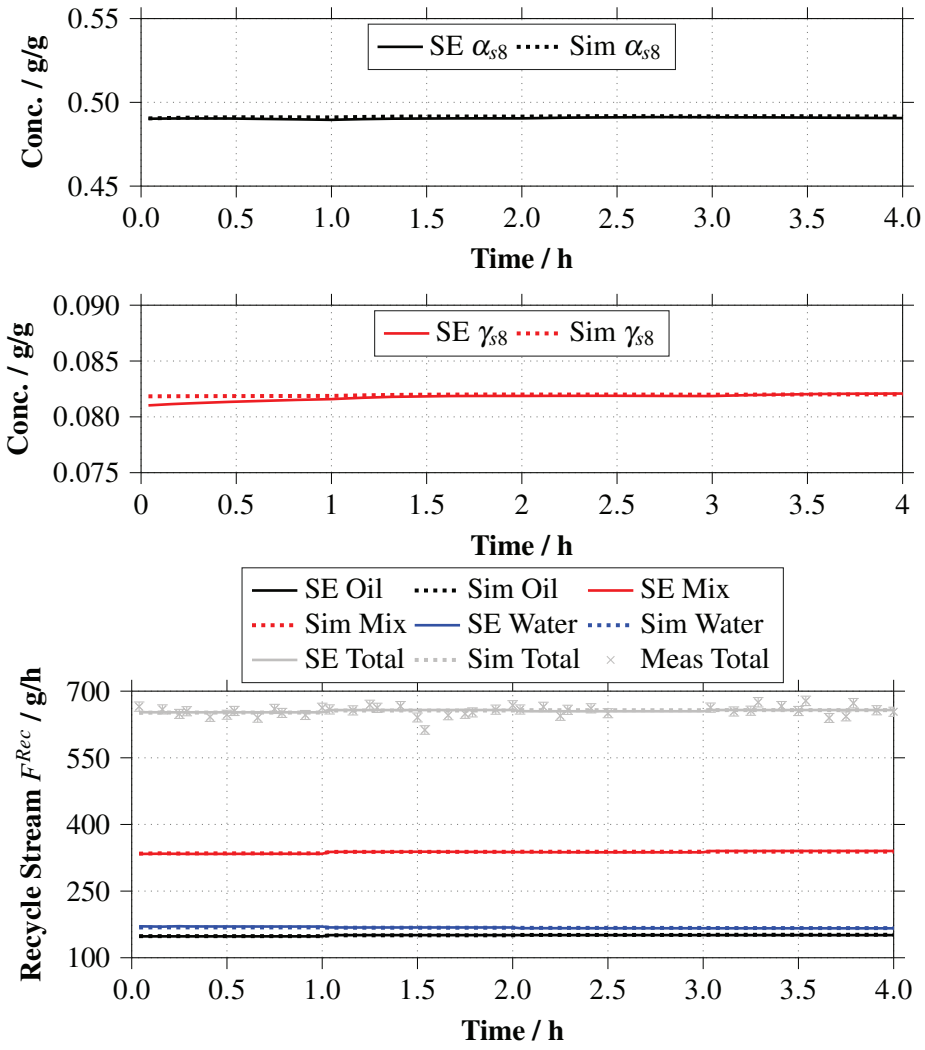

Fig. 5.17: State estimation case study: results for oil to water ratio α_{s8} and surfactant concentration γ_{s8} (top), as well as recycle streams (bottom).

Finally, also the reaction performance, as well as compositions in reactor and the settler's phases are captured correctly, as can be seen from Fig. 5.18. Despite scarce measurement data, estimation results for the main reaction educt, product, and byproducts are in good agreement with the reference from simulation. No deterioration of concentration profiles by the dominating influence of, e.g., fast level measurements is visible (see discussion in Sec. 4.4.2). Hence, the developed sequential state estimation framework with individual handling and incorporation of fast and slow measurements is considered as suitable for the desired application.

However, despite this very promising results it has to be emphasized, that the applicability of the developed multi-rate state estimation framework is limited by the availability of a valid set of initial values. The initial state of the model at $t = 0$ must adhere to a feasible phase separation and established recycle. In addition, provided controls for a respective estimation horizon must be feasible and cannot be set freely. If this is given, online application of state estimation for the mini-plant system is possible and further coupling with optimization for the development of optimal control trajectories according to Fig. 4.32 is encouraged.

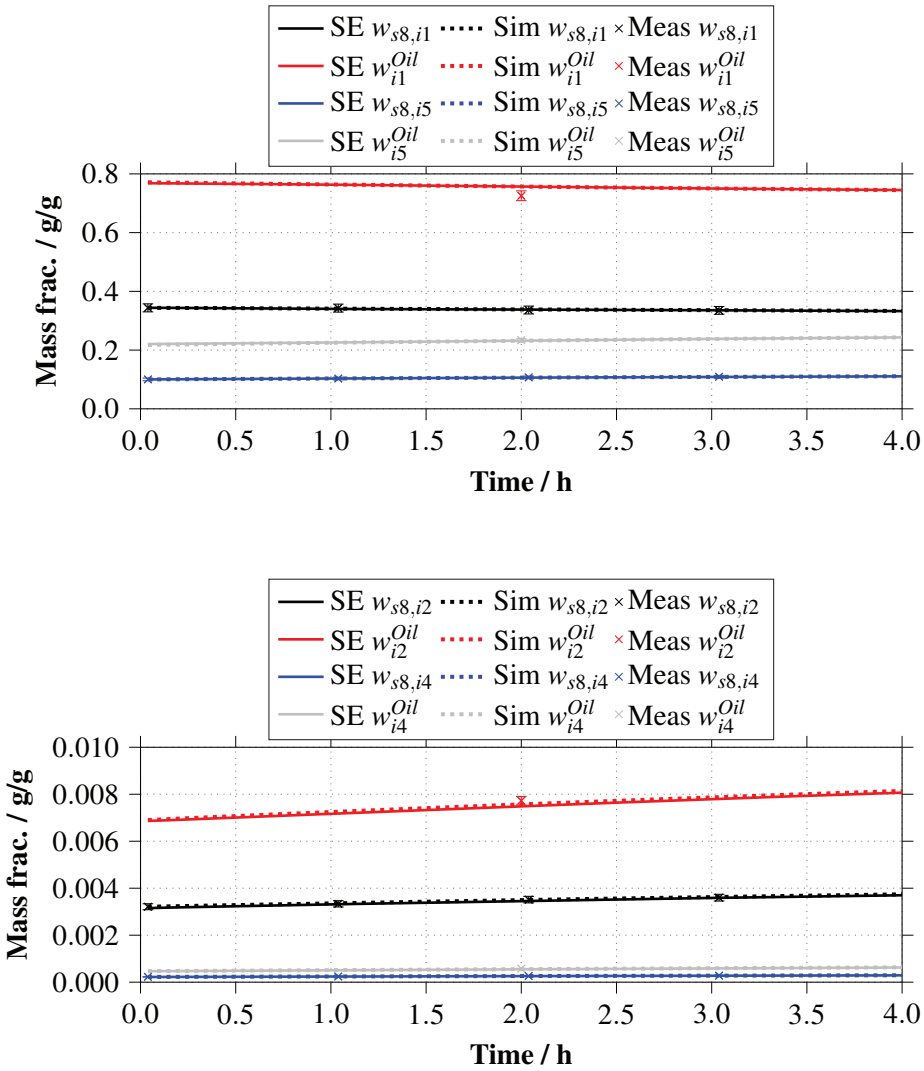

Fig. 5.18: State estimation case study: results for mass fractions of 1-dodecene (w_{i1}), iso-dodecene (w_{i2}), dodecane (w_{i4}), and tridecanal (w_{i5}) in reactor ($s8$) and settler oil phase (Oil).

5.3 Successful Realization of Continuous Operation

In this section, the realization of a successful long-term mini-plant campaign is presented. Cornerstone for its realization are the applied results from the systematic analysis of the microemulsion system, developed plant design improvements, and model-assisted operation strategies:

Modifications of Process Design on the mini-plant were made in accordance with Sec. 4.1.1. This includes adding a second rushton turbine to the reactor for improved mixing, as well as a gas phase purge. In contrast to previous plant operations, the settler volume was reduced to 0.45 L and check valves were implemented in the recycle to avoid backflow. However, the developed mixer-settler unit was not yet deployed in this campaign.

Process Operation was assisted by an optimal start-up trajectory as well as all precise data on necessary feed masses based on plant dimensions and information on phase separation. Additionally, the model of the phase separation was provided to aid decisions on control actions.

5.3.1 Conditions and Operation Strategy - Plant Op 2

The mini-plant was continuously operated over a total of 180 h in a three-shift system with 18 operators. Reaction conditions and covered operation modes are given with:

Reaction Conditions

Again, the reactor was operated at 15 bar gauge and per default at 95 °C. The target reactor composition was set according to the reference experiment in Fig. 3.2 to each 46 wt.-% 1-dodecene/ and catalyst solution, as well as 8 wt.-% Marlipal® 24/70. Accordingly, the catalyst solution was prepared with 98.96 wt.-% water, $6.48 \cdot 10^{-2}$ wt.-% [Rh(acac)$(CO)_2$], 0.98 wt.-% SulfoXantPhos, and 2.17 wt.-% Na_2SO_4. During operation, the stirrer speed was kept above 750 rpm to ensure proper emulsification and gassing.

Operation Schedule

The operation is subdivided into six modes (SP) presented in Tab. 5.6. Several goals were pursued for this plant operation. Firstly, a fast start-up and realization of continuous operation at target reaction yield was strived for. Hence, after initial feeding of substances to the plant **SP 1** was used to establish the recycle and obtain a stable phase separation. In contrast to the suggested optimal start-up trajectory, no syngas was fed to the plant to keep the operation flexible and avoid additional influences on the phase separation. At operating hour 19, operation

in full recycle was established and the reaction was started by feeding syngas. Reaction yield was increased over 24 h, before the continuous operation was established with a feed rate of 1-dodecene of 28 $g\,h^{-1}$ in **SP 3**. This operation mode was tested for 66 h before perturbation experiments were started for **SP 4** - **SP 6**. Here, the response of reaction performance and phase separation were tested regarding the reduction of the residence time of the settler (**SP 4**), shifts in the recycle ratio (**SP 5**), and elevated reaction temperatures (**SP 6**).

Tab. 5.6: Operation schedule for mini-plant operation and applied fixed controls for several operation modes (SP1-SP4) for successful mini-plant campaign **Plant Op 2**.

	SP 1	SP 2	SP 3
Operating hour / h	0-19	19-43	43-109
Operation mode	start-up full recycle	full recycle	continuous
$\tau_{Reactor}$ / h	0.85	0.64	0.45
$\tau_{Settler}$ / h	0.64	0.48	0.34
$\tau_{Reaction}$ / h	-	7.1	7.1
$T_{Reactor}$ / °C	95	95	95
Total recycle rate / g/h	600	800	1100
Recycle ratio oil:mix:water	0.25:0.50:0:25	0.25:0.50:0:25	0.18:0.5:0.32
Feed rate alkene / g/h	0	0	28
Reaction status	inactive	active	active
	SP 4	SP 5	SP 6
Operating hour / h	109-126	126-154	154-172
Operation mode	continuous with residence time shift	continuous with recycle ratio shift	continuous with temperature shift
$\tau_{Reactor}$ / h	1.2	0.62	0.45
$\tau_{Settler}$ / h	0.90	0.47	0.34
$\tau_{Reaction}$ / h	8.0	7.4	7.1
$T_{Reactor}$ / °C	95	95	105
Total recycle rate / g/h	400	800	1100
Recycle ratio oil:mix:water	0.25:0.5:0.25	0:4:0.2:0.4	0.18:0.5:0.32
Feed rate alkene / g/h	28	28	28
Reaction status	active	active	active

To aid the discussion, data on the applied controls and respective measurement data are given: Fig. D.17 shows measured feed rates. Figure 5.19 depicts recycle stream measurements and the recycle ratio calculated from setpoint data (Fig. D.18). Reactor pressure, temperature, and settler temperature are given in Fig. 5.20.

In contrast to **Plant Op 1**, profiles for recycle streams and settler temperature are rather smooth and transitions are mainly limited to setpoint changes according to the operation schedule. Hence, the applied control strategy and adjusted plant design significantly improved plant observability and operability. After start-up and recycle initiation (**SP 1**), stable configurations of recycle streams have been observed and respective flow measurements indicate quasi-steady state operation for full recycle and continuous operation with reaction. Except for a heating period around

operating hour 60 to counter emerging surfactant accumulations, settler temperature adjustments were likewise minimal during this time (**SP 2/3**). For **SP 5**, the recycle operation was partly deteriorated by blockage of the recycle of the emulsion phase. This was however expected, since a step experiment with a unfavorable recycle ratio was performed. A proper continuous operation was regained on switching back to feasible setpoints for recycle streams in **SP 6**.

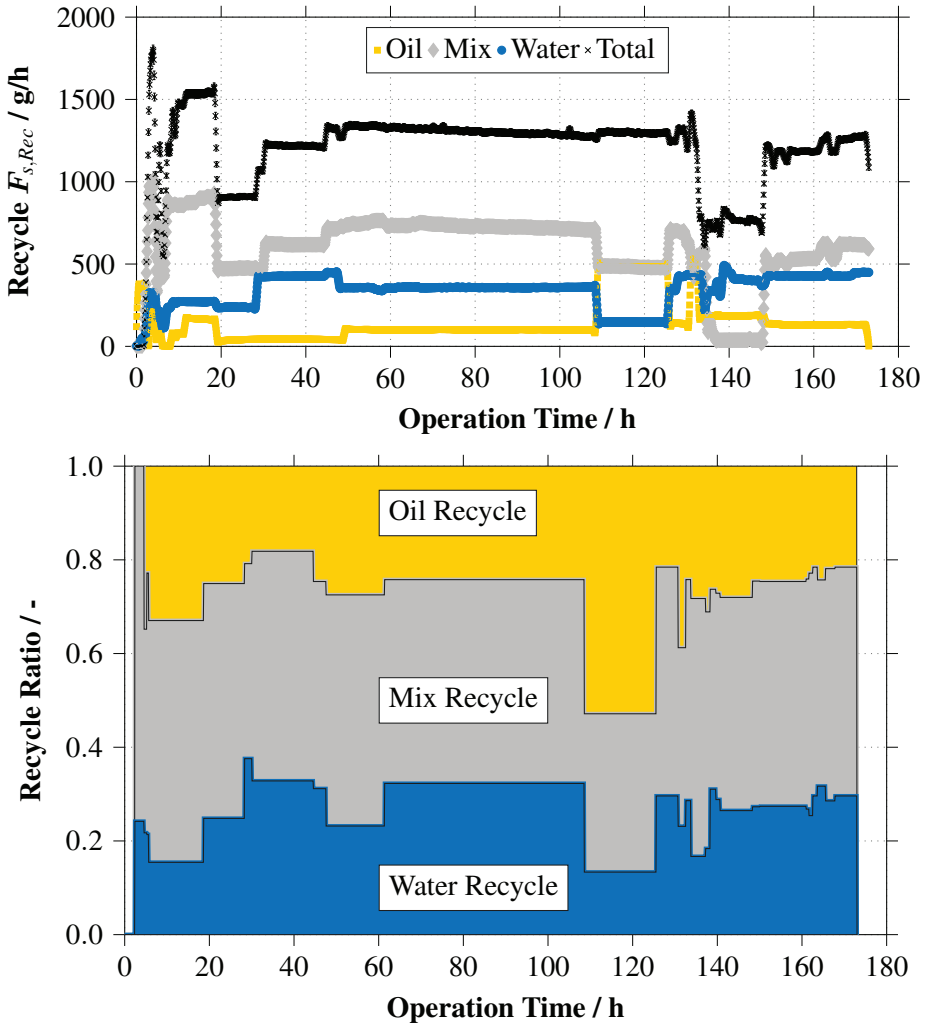

Fig. 5.19: Operation schedule Successful mini-plant campaign: measured recycle rates and the recycle ratio per stream setpoint are given.

5.3.2 Proof of Concept: Long-Term Mini-Plant Results

Reaction and phase separation results are presented in the following. Together they prove the concept of hydroformylation in microemulsions.

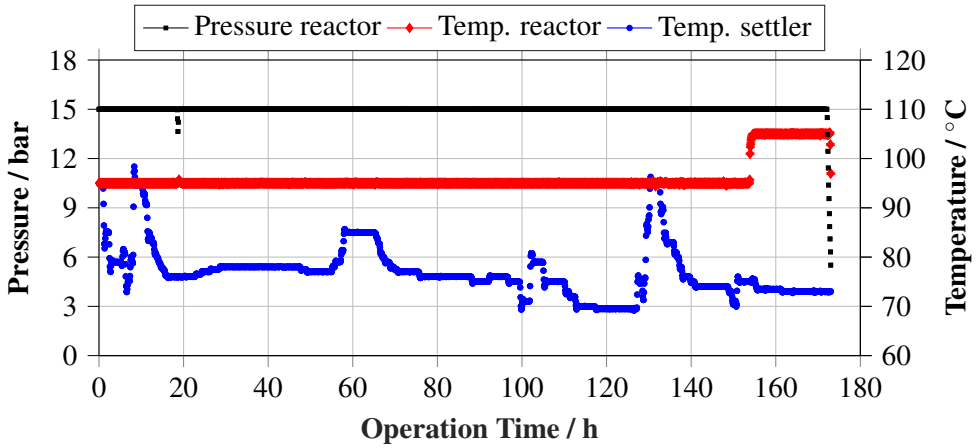

Fig. 5.20: Operation schedule successful mini-plant campaign: system pressure and temperatures.

Reaction Performance

The reaction performance is discussed regarding the conversion of 1-dodecene X_{s8}, yield of tridecanal Y_{s8}, and selectivities of the reaction S_{s8}^{TDC} and $S_{s8}^{n/iso}$.[1] Figure 5.21 and 5.22 present respective results with mark ups of setpoints of operation and theoretically achievable reaction yield (Fig. 3.2). Additionally, Fig. D.19 provides the concentration profiles of all reactants.

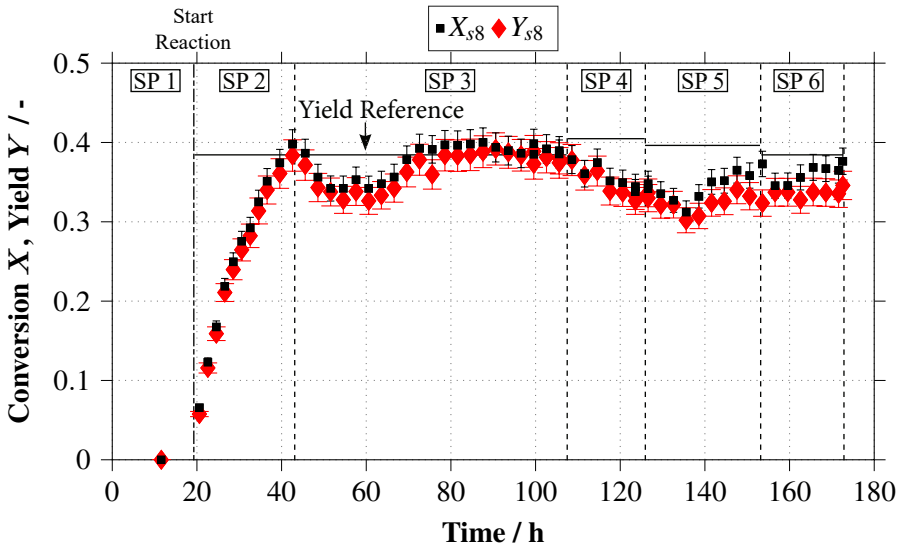

Fig. 5.21: Operation results successful mini-plant campaign: total conversion of 1-dodecene X_{s8} and yield of tridecanal Y_{s8} in reactor.

The hydroformylation reaction was successfully established in the mini-plant with syngas feed. For the full recycle operation **SP 2** yield and conversion increase rapidly and almost congru-

[1] Respective definitions can be found in the appendix Sec. D.1.

ently. This hints to an exceptionally good chemo-selectivity of around 92 %. Thus, immediate activation of the rhodium catalyst complex and formation of its active and selective species was achieved on reaction initiation.

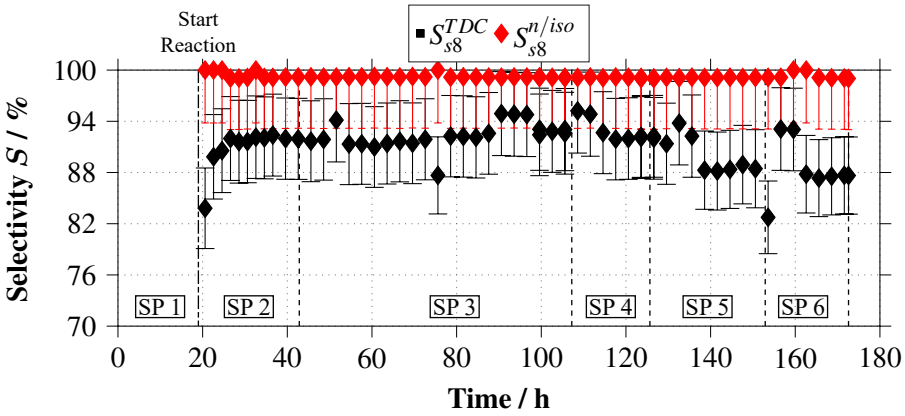

Fig. 5.22: Operation results successful mini-plant campaign: reaction selectivity towards TDC S_{s8}^{TDC} and n/iso selectivity $S_{s8}^{n/iso}$ in reactor.

As an outstanding result, the yield of tridecanal at the end of **SP 2** meets the predicted reference of $Y_{s8} = 38.5\,\%$ from model calculations almost perfectly. Looking at the optimal start-up trajectory from Fig. 5.12, a yield of approx. $Y_{s8}^{Opt,FR} = 28\,\%$ after 12 h of full recycle operation is found. For the same operational state, mini-plant results also show a very good agreement with a TDC yield above 27 %. In the following continuous operation in **SP 3** yield and conversions initially decreased due to the introduction of the 1-dodecene feed. Additionally, as already mentioned, emerging surfactant accumulation in the settler appeared around operating hour 60. This possibly reduced the surfactant concentration in the reactor and thus impeded reaction performance. After recovery and proceeding continuous operation, X_{s8} and Y_{s8} increased and stabilized at 38.8 % and 37.1 %, respectively. Again reaction yield is in perfect agreement with the reference from lab and model calculations.

For **SP 4** to **6** the reaction performance worsened and the yield dropped significantly by 10 percentage points until operating hour 140. For **SP 4** the residence time of the settler was doubled to test the influence on the reaction (expected catalyst deactivation and formation of inselective species at high residence times, as in **Plant Op 1**). However, this was not fully confirmed within this mini-plant run, as only catalyst activity was reduced. Chemo and n/iso-selectivity remained at favorably high values. It is likely, that starting surfactant accumulations in the settler led to a decreasing reaction performance: for **SP 5** failure of the surfactant rich recycle stream of the mix phase was encountered, which significantly reduced the surfactant concentration in the reactor. On resolving this issue and establishing stable recycle and phase separation for **SP 6**, X_{s8} and Y_{s8}

increased again and evened out at 35.6 % and 32.4 % without reaching their respective reference values. However, this does not exclude complete recovery of the reaction performance with further commencing stable continuous operation and homogenization of the system.

Throughout the whole mini-plant operation both chemo- and n/iso-selectivity were exceptionally high at values above 91 % and 99 %, respectively. Thus, no significant byproduct formation occurred, which is also confirmed seeing the profiles of reactant concentrations for the reactor in Fig. D.19. Minor reduction of the chemo-selectivity towards 88 % however is found starting in the middle of **SP 5**. Again, afore discussed disturbances for the process operation are assumed to cause this. For **SP 6** a reduced selectivity is however excepted, since the reaction temperature was increased to 105 °C. Here, higher byproduct formation was already stated in lab experiments.

Separation Performance

To evaluate the quality of the separation, Fig. 5.23 shows the purity of the oil phase purity over the entire operation time with photos from the settler's sight glass. Generally, it was possible to maintain the desired three-phasic separation of the microemulsion for the entire operation of the mini-plant. This enabled the efficient recycling of catalyst, surfactant, as well as separation of the oil phase for product collection. Again, this is emphasized by the given settler images. Purities of the oil phase above 95 % are widely found. These are generally in the range of expected values from the phase separation model. Again the surfactant represents most of the impurities. Significant decreases of the purity of the oil phase are found for the heat-up phase

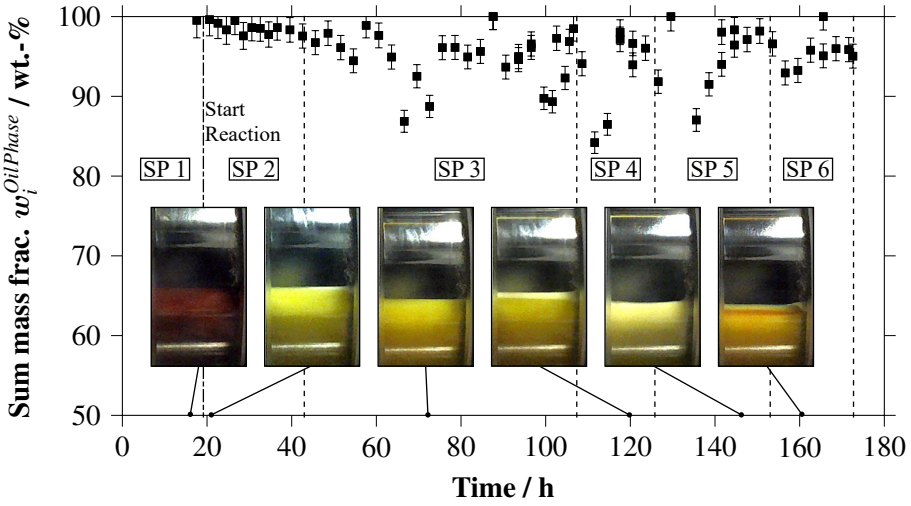

Fig. 5.23: Operation results successfull mini-plant campaign: phase separation quality as total amount of oily compounds $i = 1 \ldots 5$ of settler oil phase. Additionally the visual observation from the camera system is given at specific time points.

around operating hour 60. Here, larger amounts of surfactant are dissolved in the oil phase. This was at least qualitatively measurable via GC. A similar case occurred starting with operating hour 130. There, again a heat-up of the settler was initiated (see Fig. 5.20).

Conclusion

Concluding, the results of operation represent a milestone towards a valid proof of concept for the hydroformylation of 1-dodecene in microemulsions in a continuously operated plant. A successful transfer of the hydroformylation reaction from lab to mini-plant was achieved. All responses of the reaction performance influenced by conditions of the process operation can be explained with the collected knowledge from the system analysis and predictions from developed models. No further phenomena have been observed and hence the application of microemulsion or liquid multiphase reaction media in general is encouraged.

5.3.3 D-RTO Application Case Study

Having the proof of concept of the stable and efficient mini-plant operation, the developed D-RTO-framework from Fig. 4.32 is evaluated. A case study is performed on results and measurements of this operation **Plant Op 2**. No online application of this framework was done due to availability of the plant as well as the high effort and costs for an operation. It is however used for comparison of results from state estimation and optimization with obtained mini-plant measurements. Thus, feasibility of the approach and gained optimal trajectories can be tested.

Case Study and Data Preparation

The case study is prepared from an excerpt of the continuous operation for **SP 3** for the time frame of $t \in [76,88]$ h. This results in three 4 h-horizons, on which the framework was applied and respective mini-plant measurements were used. To generate a valid set of model states x at the beginning of each time horizon, a simulation of the full mini-plant model was set up in accordance with mini-plant measurements (levels, concentrations, temperatures, pressure). This way, a trajectory of state variables for a continuous operation over 12 h was generated. As an excerpt Tab. 5.7 presents the chosen initial reactor composition (estimated from feed calculations and GC), setup of the settler's phase separation state (settler image), and setpoints of the recycle streams. Settler temperature and recycle streams were obtained from the model evaluation to ensure steady state as observed in the mini-plant.

Tab. 5.7: Specifications for initial mini-plant model state used for D-RTO case study on **Plant Op 2**.

Reactor composition $w_{s=8,i}$ / wt.-%							
$i=1$	32.55	$i=2$	3.55	$i=3$	0.42	$i=4$	0.65
$i=5$	18.41	$i=6$	0.002	$i=7$	0.006	$i=8$	0.00
$i=9$	35.43	$i=10$	0.02	$i=11$	0.35	$i=12$	8.55

Settler and Recycle			
F_{Rec}^{Oil} / g h^{-1}	383.95	Φ^{Oil} / %	47.55
F_{Rec}^{Mix} / g h^{-1}	395.43	Φ^{Water} / %	13.84
F_{Rec}^{Water} / g h^{-1}	394.88	$T_{Settler}$ / °C	345.90

Table 5.8 then lists the measurements used for state estimation. The data were partially provided by simulation. The optimization was implemented as specified in Sec. 4.4.3 with listed formulation of the objective function and constraints. Setpoint values for the given objective function penalties are given with: $\alpha_{s=8}^{SP} = 0.6\,\mathrm{g\,g^{-1}}$, $\gamma_{s=8}^{SP} = 0.085\,\mathrm{g\,g^{-1}}$, and $\tau_{s=8}^{SP} = 0.5\,\mathrm{h}$. This corresponds to the initial steady state solution of the simulation, which is to be maintained.

Tab. 5.8: Properties of measurement data for the D-RTO case study. *: mini-plant data only partially available, filled with simulation data. STD: relative standard deviation.

Measurement	Interval	rel. STD / %	Source
L_{u1}	collocation point (<4 min)	1.67	Mini-plant
L_{u2}	collocation point (<4 min)	1.67	Mini-plant
L_{u3}	collocation point (<4 min)	1.67	Mini-plant
L_{u11}^{Oil}	collocation point (<4 min)	1.67	Mini-plant*
L_{u13}^{Water}	collocation point (<4 min)	1.67	Mini-plant*
L_{u14}	collocation point (<4 min)	1.67	Simulation
L_{u22}	collocation point (<4 min)	1.67	Simulation
F_{s4}	collocation point (<4 min)	1.57	Simulation
F_{s19}	collocation point (<4 min)	1.57	Simulation
$w_{s8,i}$ $i \in \{1,\ldots,5\}$	2-3 h	4.0-4.4	Mini-plant
$w_{u11,i}^{Oil}$ $i \in \{1,\ldots,5\}$	4 h	2.3-2.4	Mini-plant
$w_{u13,i}^{Water}$ $i \in \{1,\ldots,5\}$	4 h	3.2-3.9	Mini-plant

D-RTO Results

The D-RTO scheme from Fig. 4.32 was implemented in AMPL® using the fully discretized model. All calculations were performed given the hardware and solver specifications in Sec. D.2. For the specified horizon of 4 h, feasible solutions were attainable within 72 min (example horizon 1: state estimation - 735 CPU seconds; optimization - 3535 CPU seconds), which is a very good result considering online application of the framework. Again the convergence behavior significantly depends on the choice of solver and its parameters and CONOPT is

preferred as optimization solver and provides satisfactory performance for various initializations of respective NLPs. The most time consuming step in the D-RTO is the pre-optimization step (Fig. C.13) used to initialize the dynamic optimization. Improvement of runtime in this sequential script is however easily attainable by finding more suitable loop control parameters.

As a key result, Fig. 5.24 shows the reaction yield and trajectories of conversion from state estimation, optimization, and actual plant measurements for all three D-RTO horizons. Starting from the measurement data for each horizon, a successful estimation of a corresponding model trajectory was possible and plant measurements are met precisely. This is further supported by the gained validation results of the reactor composition (Fig. 5.25), surfactant concentration and oil to water ratio (Fig. D.20), as well as levels of the settler's excess phases (Fig. D.21).

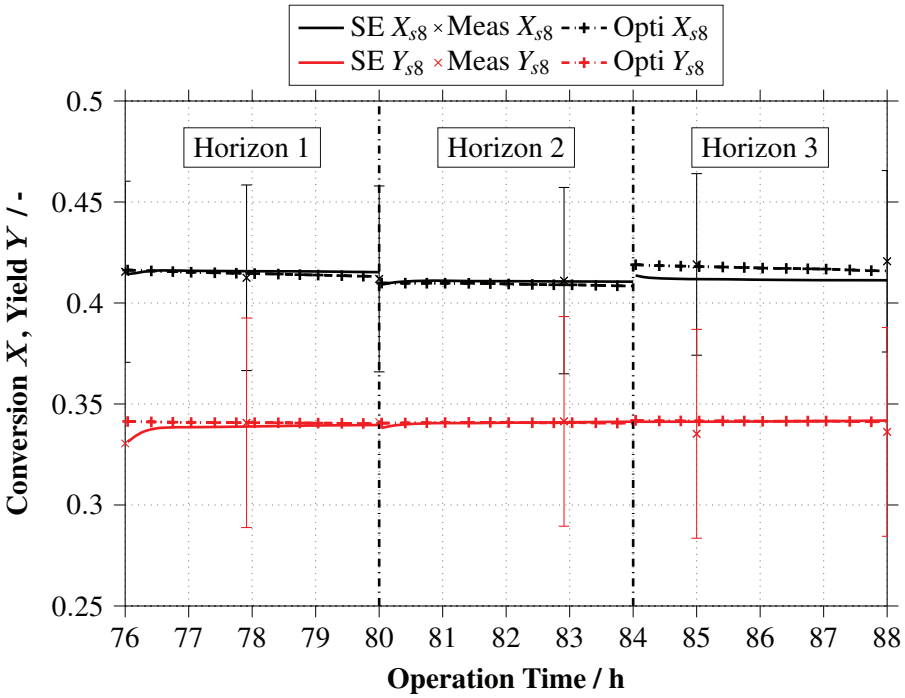

Fig. 5.24: Results for the D-RTO case study on SP 3 of Plant Op 2 for reaction yield Y_{s8} and conversion X_{s8}. Trajectories from state estimation (SE) and optimization (Opti) are compared with measurement data (Meas).

Determined optimal trajectories then again meet the performed mini-plant operation. Except from small improvements on conversion in horizon 3 no further enhancement of the reaction performance was obtained via optimization. Thus, acquired optimal trajectories of controls should be similar to actually applied setpoints for mini-plant controllers. In Fig. D.22, this can be confirmed with a comparison of trajectories of settler and reactor temperature. In addition Fig. D.21 depicts a similar result for the levels of phases in the settler.

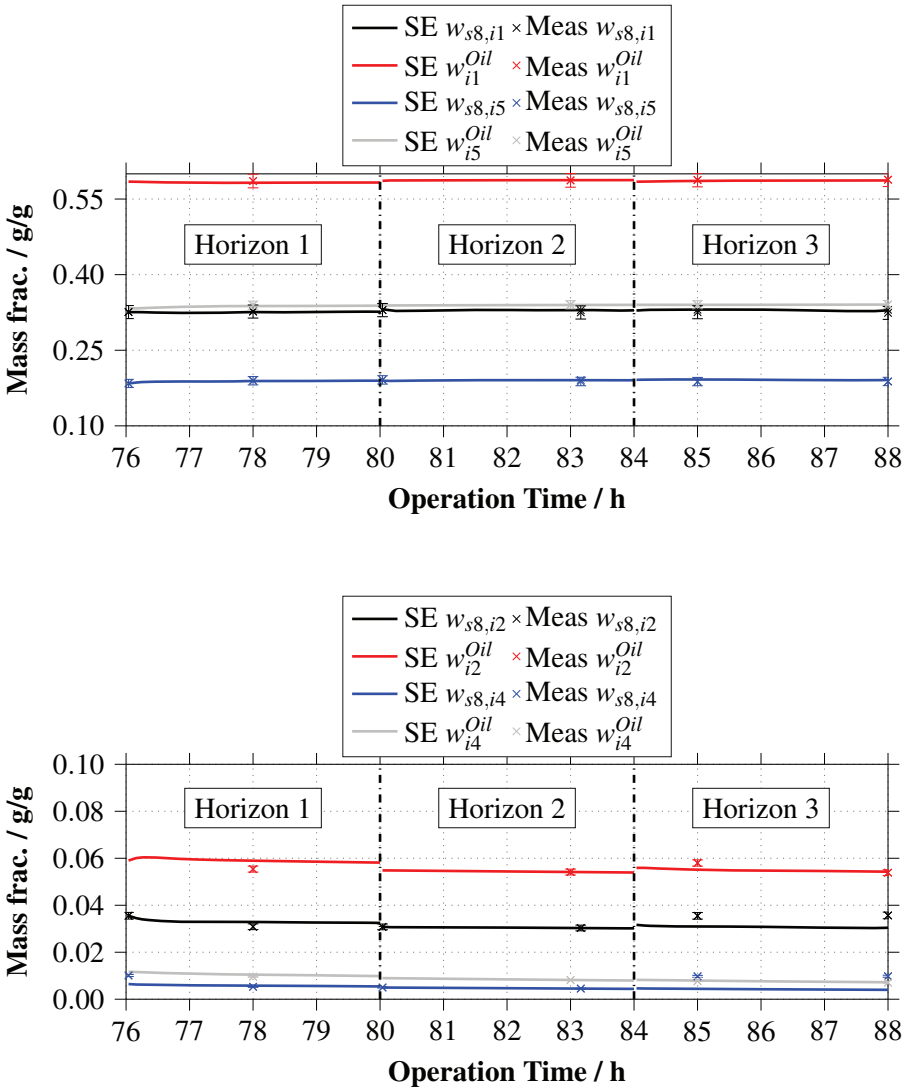

Fig. 5.25: Results for the D-RTO case study on SP 3 of Plant Op 2 for reactant concentrations 1-dodecene ($i = 1$), iso-dodecene ($i = 2$), iso-tridecanal ($i = 3$), dodecane ($i = 4$), tridecanal ($i = 5$) for reactor (Oil)and settler oil phase (Oil). Measurements (Meas) are supplied for comparison.

These results are very promising regarding two aspects: first of all, the conducted mini-plant operation shows a close to optimal performance. Secondly, the online calculation of optimal trajectories is possible and likely yields feasible results given the current structure of the dynamic model of the mini-plant. However, applicability and feasibility of solutions from the D-RTO-scheme have yet to be shown online for plant operations. Furthermore, reliable and timely convergence has to be shown for applying erroneous mini-plant data. However, with these first promising results such future work is strongly encouraged.

6 Conclusions and Future Directions

6.1 Conclusions

There are a number of reasons, why novel innovative reaction media such as microemulsions are still not applied at larger scale in industry and even most academic applications are limited to lab-scale systems. A major obstacle lies in the not well understood thermodynamic nature and overall complexity of such mixtures. Related to this, a strong interaction between the microemulsion and the way reactions therein work exists, further complicating their application. The transfer of a complex reaction system from the lab into continuous mini- or pilot-plants is further impeded, in case phase separation for additive recycling needs to be considered in addition to reaction steps. Here, the complexity of such mixtures poses several operational challenges making their operation infeasible.

To overcome this situation, a systematic approach for the rigorous analysis of multiphase reaction media and subsequent development of tailored process design and model-based optimal process control strategies has been introduced. Within this thesis, the procedure was applied on the hydroformylation of 1-dodecene in microemulsions aiming for a successful realization of this novel process concept in a continuously operated mini-plant. Initially, the rigorous system analysis focused on the two critical aspects as well as their mutual interaction: firstly, the performance of the hydroformylation in the microemulsion system and additional relevant influences for process operation. Secondly, the phase separation behavior was systematically studied using parallel lab-scale and mini-plant experiments. The main focus here was on the rigorous quantification of influences for feasible operation regions as well as the controllability of the quality of the phase separation regarding available measurements. This way, a ranking of critical challenges, which hinder successful process operation, was obtained. Here, a strong influence of the formulation of the microemulsion and phase separation performance in the mini-plant on the reaction was found. Furthermore, controllability of the phase separation significantly suffers from a lack of measurability of the surfactant concentration. In addtion, very high sensitivities of various (partially immeasurable) system parameters on the phase separation apply.

Several tailored solution strategies have been developed to counter these issues. Process design modifications of reactor, settler geometry, and recycle configuration have been implemented. Several advanced process analytical tools, such as Raman spectroscopy were evaluated to increase measurability of key influences. As a fundamental aspect, model-based optimal process control strategies are implemented to enable the efficient tracking of the mini-plant state and calculate optimal trajectories. Cornerstone for this is a developed fully dynamic mini-plant model with an adapted macrokinetic model for the hydroformylation reaction and a first time implementation of a model for the three phasic separation of microemulsions. Based thereon, several methods have been set up to assist process operation and enable a stable continuous operation: a soft-sensor for the tracking of surfactant concentrations; a framework for moving horizon state estimation; supply of optimal start-up trajectories; and an implementation for dynamic real-time optimization. Model structure and developed methods have been validated with mini-plant test runs and largely proved applicable.

Finally, these results were used to realize a long-term mini-plant operation of 180 h, which provided a proof of concept for the hydroformylation of 1-dodecene in microemulsions. Control of the critical phase separation step was tested for different operation modes and overall good oil phase purities of up to 99.5 % (amount of oily components in the separated oil phase) were obtained. The reaction performance gained a product yield of up to 38 % with a chemo selectivity of 92 % at steady-state (>30 h), which is in perfect agreement with lab-scale investigations. For this operation no online application of D-RTO was done. However, a respective case study on real mini-plant data showed feasibility of the approach regarding calculation time and obtained control trajectories. Overall, a successful transfer of the hydroformylation reaction from lab to mini-plant was achieved. All responses of the reaction and phase separation to process conditions can be explained with the collected knowledge from the system analysis. The developed mini-plant model has been proven applicable to predict the system behavior and thus encourages further online application of D-RTO.

The presented advancements are thus considered ready for the transfer on other multiphase reaction media and potentially decrease process development time. To this end, the reader is referred to an already successful transfer of the methodology for the methoxycarbonylation of 1-dodecene in a two-phase system by Illner et al. (2018c).

6.2 Future Directions

Based on the presented work, several points are raised to be discussed in future work. First of all, the developed systematic approach for rigorous analysis of multiphase reaction media for process design and operation is yet to be tested on different multiphase media and other reactions. Thereof, further generalization of this method should be obtained. To initially aid the formulation of optimal reaction media, strategies for the selection of solvent systems and additives for a given reaction are desirable. As a first approach, heuristics on the thermodynamic properties of solvent systems can be used together with key experiments.

To fully enable Raman spectroscopy in multiphase media, relations between spectral information and the mixture's optical properties must be resolved. Inline reaction monitoring is achievable by combining the tracking of the emulsion configuration with prediction models, which incorporate these configurations of the emulsion.

Regarding the process design and application of the hydroformylation in microemulsions, a thorough test of the developed mixer-settler unit (Fig. 4.5) is required. Close attention has to be given on the effective prevention of build-up of a surfactant layer in the settler. The performance of the phase separation should be compared to model predictions and lab reference data. Finally, the realized process should be driven towards sustainability by the investigation of bio-based feedstocks, such as fatty acid methyl esters.

The current mini-plant model can be improved in many ways. First of all, the phase separation dynamics (Φ^{Phase} over time) should be incorporated. Moreover, the model of the phase separation currently assumes three individual hold-ups. Hence, major improvements are possible regarding the implementation of axial and radial dispersion (partial DAE system). Also, a combination of experimental data and computational fluid dynamics, from which surrogate models can be derived, is feasible (Misra et al., 2018). Additionally, the provided model of the composition of the excess phases is based on first simplified UNIFAC calculation. To increase accuracy of respective phase equilibria the influence of present electrolytes and additives should be incorporated by suitable activity models or equations of state.

The developed multi-rate moving horizon state estimation framework up to now neglects process noise as contribution to the objective function. Since the estimation of process noise or model uncertainty is challenging, workarounds must be found. One way would be to improve model accuracy online via parameter estimation. Exemplarily, state estimation, model prediction results, and plant data can be used to track the plant-model mismatch over time and trigger re-estimation of model parameters.

List of References

Abe, M. (1996). Microemulsions in enhanced oil recovery - middle-phase microemulsion formation with some typical anionic surfactants. In: *Industrial Applications of Microemulsions*. Ed. by C. Solans, H. Kunieda. 1st ed. Vol. 6. 4. CRC Press. Chap. 14, 279–304. ISBN: 9780824797959 (cit. on p. 9).

Ahmad, A., Gao, W., Engell, S. (2019). A study of model adaptation in iterative real-time optimization of processes with uncertainties. *Computers & Chemical Engineering* 122, 218–227. DOI: 10.1016/j.compchemeng.2018.08.001 (cit. on p. 38).

Alexandrova, S., Marsheva, M., Spasic, A., Saboni, A. (2018). The influence of surfactants on the drainage and rupture of mobile liquid films between drops: A parametric numerical study. *Journal of Chemical Technology and Metallurgy* 4.53, 664–673 (cit. on p. 18).

Ali, J. M., Hoang, N. H., Hussain, M., Dochain, D. (2015). Review and classification of recent observers applied in chemical process systems. *Computers & Chemical Engineering* 76, 27–41. DOI: 10.1016/j.compchemeng.2015.01.019 (cit. on p. 39).

Alzate, A. (2018). Design of an Automatic Method for the Soft-sensing of the Surfactant Concentration in a Mini-plant of Hydroformylation of Long-chain Alkenes in Microemulsions. *Master's Thesis*. Politecnico Di Milano (cit. on p. 75).

Anastas, P. T., Warner, J. (2000). *Green Chemistry: Theory and Practice*. Ed. by P. T. Anastas. Oxford University Press Inc. 148 pp. ISBN: 9780198506980. URL: https://www.ebook.de/de/product/3263211/paul_t_anastas_john_warner_green_chemistry_theory_and_practice.html (cit. on p. 1).

AspenProperties V10 (2019). *Density Calculation using Database PURE36 and Peng-Robinson as EOS*. Aspen Technology Inc. (cit. on pp. 72, C-19).

Atkins, P., Paula, J. (2010). *Physikalische Chemie*. Ed. by P. Atkins, J. Paula. Wiley-VCH Verlag GmbH. ISBN: 9783527315468 (cit. on p. 9).

Auch-Schwelk, B., Kohlpaintner, C. (2001). Die technische Anwendung wasserlöslicher Katalysatoren: Zweiphasenkatalyse. *Chemie in unserer Zeit* 35.5, 306–312. DOI: 10.1002/1521-3781(200110)35:5%3C306::AID-CIUZ306%3E3.0.CO;2-9 (cit. on p. 2).

Bahrmann, H., Bach, H., Frey, G. (2013). Oxo Synthesis. In: *Ullmann's Encyclopedia of Industrial Chemistry*. Ed. by B. Elvers. Wiley-VCH Verlag GmbH & Co. KGaA. DOI: 10.1002/14356007.a18_321.pub2 (cit. on p. 1).

Bard, Y. (1973). *Nonlinear parameter Estimation*. Ed. by Y. Bard. Academic Press Inc. (cit. on pp. 34, 35).

Bardas, U. (2015). Messung von Gaslöslichkeiten in mizellaren Reaktionssystemen. *Master's Thesis*. Technische Universität Dortmund (cit. on pp. 95, C-10).

Bau, U., Baumgärtner, N., Seiler, J., Lanzerath, F., Kirches, C., Bardow, A. (2019). Optimal operation of adsorption chillers: First implementation and experimental evaluation of a nonlinear model-predictive-control strategy. *Applied Thermal Engineering* 149, 1503–1521. DOI: 10.1016/j.applthermaleng.2018.07.078 (cit. on p. 37).

Behr, A., Obst, D., Westfechtel, A. (2005). Isomerizing hydroformylation of fatty acid esters: Formation of ?-aldehydes. *European Journal of Lipid Science and Technology* 107.4, 213–219. DOI: 10.1002/ejlt.200401123 (cit. on p. 2).

Bera, A., Mandal, A. (2014). Microemulsions: a novel approach to enhanced oil recovery: a review. *Journal of Petroleum Exploration and Production Technology* 5.3, 255–268. DOI: 10.1007/s13202-014-0139-5 (cit. on p. 9).

Berger, R. (1986). Koaleszenzprobleme in chemischen Prozessen. *Chemie Ingenieur Technik* 58.6, 449–456. DOI: 10.1002/cite.330580602 (cit. on p. 29).

Bernas, A., Wärnå, J., Mäki-Arvela, P., Murzin, D. Y., Salmi, T. (2010). Kinetics and mass transfer in hydroformylation-bulk or film reaction?. *The Canadian Journal of Chemical Engineering*, n/a–n/a. DOI: 10.1002/cjce.20330 (cit. on p. 94).

Besora, M., Maseras, F. (2018). Microkinetic modeling in homogeneous catalysis. *Wiley Interdisciplinary Reviews: Computational Molecular Science* 8.6, e1372. DOI: 10.1002/wcms.1372 (cit. on p. 29).

Bhaduri, S., Mukesh, D. (2014). *Homogeneous Catalysis - Mechanisms and Industrial Applications*. Ed. by S. Bhaduri, D. Mukesh. John John Wiley & Sons, Inc. (cit. on p. 29).

Bhanage, B., Divekar, S., Deshpande, R., Chaudhari, R. (1997). Kinetics of hydroformylation of 1-dodecene using homogeneous HRh(CO)(PPh3)3 catalyst. *Journal of Molecular Catalysis A: Chemical* 115, 247–257 (cit. on p. 93).

Bhosekar, A., Ierapetritou, M. (2018). Advances in surrogate based modeling, feasibility analysis, and optimization: A review. *Computers & Chemical Engineering* 108, 250–267. DOI: 10.1016/j.compchemeng.2017.09.017 (cit. on p. 32).

Biegler, L. T., Grossmann, I. E., Westerberg, A. W. (1997). *Systematic methods for chemical process design*. Ed. by N. R. Amundson. Prentice Hall PTR (cit. on p. 65).

Biegler, L., Damiano, J. J., Blau, G. E. (1986). Nonlinear parameter estimation: A case study comparison. *AIChE Journal* 32.1, 29–45. DOI: 10.1002/aic.690320105 (cit. on p. 35).

Biegler, L., Yang, X., Fischer, G. A. G. (2015). Advances in sensitivity-based nonlinear model predictive control and dynamic real-time optimization. *Journal of Process Control* 30, 104–116. DOI: 10.1016/j.jprocont.2015.02.001 (cit. on pp. 36, 37).

Biegler, L., Zavala, V. (2009). Large-scale nonlinear programming using IPOPT: An integrating framework for enterprise-wide dynamic optimization. *Computers & Chemical Engineering* 33.3, 575–582. DOI: 10.1016/j.compchemeng.2008.08.006 (cit. on pp. 36, 37).

Biegler, L. T. (2010). *Nonlinear Programming*. Society for Industrial and Applied Mathematics. DOI: 10.1137/1.9780898719383 (cit. on p. 111).

Biegler, L. T. (2018). New directions for nonlinear process optimization. *Current Opinion in Chemical Engineering* 21, 32–40. DOI: http://dx.doi.org/10.1016/j.coche.2018.02.008 (cit. on pp. 31, 37).

Bohnet, M. (1976). Trennen nicht mischbarer Flüssigkeiten. *Chemie Ingenieur Technik* 48.3, 177–189. DOI: 10.1002/cite.330480303 (cit. on pp. 17, 29).

Boonme, P. (2007). Applications of microemulsions in cosmetics. *Journal of Cosmetic Dermatology* 6.4, 223–228. DOI: 10.1111/j.1473-2165.2007.00337.x (cit. on p. 9).

Börner, A., Franke, R. (2016). *Hydroformylation*. Ed. by A. Börner, R. Franke. Wiley-VCH Verlag GmbH & Wiley-VCH Verlag GmbH & Co. DOI: 10.1002/9783527677931 (cit. on pp. 2, 50).

Bowcott, J. E., Schulman, J. H. (1955). Emulsions Control of droplet size and phase continuity in transparent oil-water dispersions stabilized with soap and alcohol. *Zeitschrift für Elektrochemie* 59.4, 283–290. DOI: 10.1002/bbpc.19550590409 (cit. on p. 9).

Bran+Luebbe (2011). *NOVADOS H1 Metering Pumpe: Original technical manual*. SPX flow (cit. on p. 82).

Brown, C. K., Wilkinson, G. (1970). Homogeneous hydroformylation of alkenes with hydridocarbonyltris-(triphenylphosphine)rhodium(I) as catalyst.. *Journal of the Chemical Society A: Inorganic, Physical, Theoretical*, 2753. DOI: 10.1039/J19700002753 (cit. on p. 19).

Brunsch, Y., Behr, A. (2012). Temperature-Controlled Catalyst Recycling in Homogeneous Transition-Metal Catalysis: Minimization of Catalyst Leaching. *Angewandte Chemie International Edition* 52.5, 1586–1589. DOI: 10.1002/anie.201208667 (cit. on p. 4).

Büchi AG (2013). *Dokumentation Labor-Rührautoklav Typ 4/1.5 lt. Artikelnummer: 49.30974.0000.* (Cit. on p. B-1).

Burth, M., Verghese, G., Velez-Reyes, M. (1999). Subset selection for improved parameter estimation in on-line identification of a synchronous generator. *IEEE Transactions on Power Systems* 14.1, 218–225. DOI: 10.1109/59.744536 (cit. on p. 36).

Canny, J. (1986). A Computational Approach to Edge Detection. *IEEE Transactions on Pattern Analysis and Machine Intelligence* PAMI-8.6, 679–698. DOI: 10.1109/TPAMI.1986.4767851 (cit. on p. 76).

Cárdenas, D. C. L. (2016). Systematic evaluation of ill-posed problems in model-based parameter estimation and experimental design. *phdthesis*. Technische Universität Berlin (cit. on p. 36).

Caspari, A., Faust, J. M., Schäfer, P., Mhamdi, A., Mitsos, A. (2018). Economic Nonlinear Model Predictive Control for Flexible Operation of Air Separation Units. *IFAC-PapersOnLine* 51.20, 295–300. DOI: 10.1016/j.ifacol.2018.11.028 (cit. on p. 37).

Chen, C. Y., Joseph, B. (1987). On-line optimization using a two-phase approach: an application study. *Industrial & Engineering Chemistry Research* 26.9, 1924–1930. DOI: 10.1021/ie00069a034 (cit. on p. 38).

Chen, W., Bakshi, B. R., Goel, P. K., Ungarala, S. (2004). Bayesian Estimation of Unconstrained Nonlinear Dynamic Systems. *IFAC Proceedings Volumes* 37.1, 263–268. DOI: 10.1016/S1474-6670(17)38742-6 (cit. on p. 40).

Chen, Z. (2003). *Bayesian Filtering: From Kalman Filters to Particle Filters, and Beyond. techreport*. Communications Research Laboratory, McMaster University, Hamilton, Ontario, Canada (cit. on p. 40).

Cheng, H., Kontogeorgis, G. M., Stenby, E. H. (2002). Prediction of Micelle Formation for Aqueous Polyoxyethylene Alcohol Solutions with the UNIFAC Model. *Industrial & Engineering Chemistry Research* 41.5, 892–898. DOI: 10.1021/ie010072e (cit. on p. 11).

Cobelli, C., DiStefano, J. J. (1980). Parameter and structural identifiability concepts and ambiguities: a critical review and analysis. *American Journal of Physiology-Regulatory, Integrative and Comparative Physiology* 239.1, R7–R24. DOI: 10.1152/ajpregu.1980.239.1.R7 (cit. on p. 36).

Cordes, E. H., Dunlap, R. B. (1969). Kinetics of organic reactions in micellar systems. *Accounts of Chemical Research* 2.11, 329–337. DOI: 10.1021/ar50023a002 (cit. on p. 22).

Cornils, B., Hibbel, J., Konkol, W., Lieder, V., Much, J., Schmidt, V., Wiebus, E. (1982). Verfahren Zur Herstellung von Aldehyden. German. *patentde* DE3234701 (cit. on p. 2).

Cornils, B., Herrmann, W. A., Rasch, M. (1994). Otto Roelen, Pioneer in Industrial Homogeneous Catalysis. *Angewandte Chemie International Edition in English* 33.21, 2144–2163. DOI: 10.1002/anie.199421441 (cit. on p. 1).

Cornils, B., Kuntz, E. G. (1995). Introducing TPPTS and related ligands for industrial biphasic processes. *Journal of Organometallic Chemistry* 502.1-2, 177–186. DOI: 10.1016/0022-328X(95)05820-F (cit. on p. 2).

Danov, K. D., Valkovska, D. S., Ivanov, I. B. (1999). Effect of Surfactants on the Film Drainage. *Journal of Colloid and Interface Science* 211.2, 291–303. DOI: 10.1006/jcis.1998.5973 (cit. on p. 18).

Darby, M. L., Nikolaou, M., Jones, J., Nicholson, D. (2011). RTO: An overview and assessment of current practice. *Journal of Process Control* 21.6, 874–884. DOI: 10.1016/j.jprocont.2011.03.009 (cit. on pp. 36, 37).

Deibele, L., Schäfer, J.-P., Eltner, A. (2000). Rektifikation, Flüssig/Flüssig-Extraktion und Membrantechnik. *Chemie Ingenieur Technik* 72.12, 1487–1495. DOI: 10.1002/1522-2640(200012)72:12%3C1487::AID-CITE1487%3E3.0.CO;2-X (cit. on p. 17).

Deshpande, R., Kelkar, A., Sharma, A., Julcour-Lebigue, C., Delmas, H. (2011). Kinetics of hydroformylation of 1-octene in ionic liquid-organic biphasic media using rhodium sulfoxantphos catalyst. *Chemical Engineering Science* 66.8, 1631–1639. DOI: 10.1016/J.CES.2010.12.040 (cit. on p. 21).

Diwekar, U. M., Ulas, S. (1997). Sampling Techniques. *AIChE Journal* 43.2, 440–447. DOI: 10.1002/aic.690430217 (cit. on p. 90).

Dochain, D., Couenne, F., Jallut, C. (2009). Enthalpy based modelling and design of asymptotic observers for chemical reactors. *International Journal of Control* 82.8, 1389–1403. DOI: 10.1080/00207170802236085 (cit. on p. 39).

Drown, D. C., Thomson, W. J. (1977). Fluid Mechanic Considerations in Liquid-Liquid Settlers. *Industrial & Engineering Chemistry Process Design and Development* 16.2, 197–206. DOI: 10.1021/i260062a007 (cit. on p. 28).

Dwars, T., Paetzold, E., Oehme, G. (2005). Reactions in Micellar Systems. *Angewandte Chemie International Edition* 44.44, 7174–7199. DOI: 10.1002/anie.200501365 (cit. on p. 22).

E.L.B. (2011). *Liquid Level Measuring Instruments Series TK-304*. E.L.B. GmbH. URL: https://www.elb-bensheim.de/NewSite/static/document/datasheet/11/11-03-01-E_tk-30x_ex_allg_daten_1.pdf (cit. on p. 73).

Edgar, T. F., Himmelblau, D. M. (2001). *Optimization of Chemical Processes*. Ed. by E. Glandt. McGraw-Hill ACS Combinatorial Science (cit. on pp. 31, 32).

Endress+Hauser (2011a). *Technical Information Levelflex FMP50 Guided Level-Radar Level measurement in liquids - Version TI01000FEN_1311*. Endress+Hauser AG. URL: https://portal.endress.com/wa001/dla/5000327/6685/000/02/TI01000FEN%5C_1311.pdf (cit. on p. 73).

Endress+Hauser (2011b). *Technical Information Levelflex FMP51, FMP52, FMP54 Guided Level-Radar Level measurement in liquids - Version TI01001F/00/EN/13.11*. Endress+Hauser AG. URL: https://portal.endress.com/wa001/dla/5000327/6687/000/02/TI01001FEN%5C_1311.pdf (cit. on p. 73).

Esche, E., Müller, D., Wozny, G. (2014). Systematic approaches for model derivation for optimization purposes. In: *Proceedings of the 8th International Conference on Foundations of Computer-Aided Process Design – FOCAPD*. Ed. by M. R. Eden, J. D. Sirola, G. P. Twoler, 699–704 (cit. on p. C-1).

Evans, D., Yagupsky, G., Wilkinson, G. (1968). The reaction of hydridocarbonyltris(triphenylphosphine)rhodium with carbon monoxide, and of the reaction products, hydridodicarbonylbis(triphenylphosphine)rhodium and dimeric species, with hydrogen. *Journal of the Chemical Society A: Inorganic, Physical, Theoretical*, 2660. DOI: 10.1039/J19680002660 (cit. on p. 19).

Faber, R., Arellano-Garcia, H., Li, P., Wozny, G. (2007). An optimization framework for parameter estimation of large-scale systems. *Chemical Engineering and Processing: Process Intensification* 46.11, 1085–1095. DOI: 10.1016/j.cep.2007.02.019 (cit. on p. 38).

Flores, M. V., Voutsas, E. C., Spiliotis, N., Eccleston, G. M., Bell, G., Tassios, D. P., Halling, P. J. (2001). Critical Micelle Concentrations of Nonionic Surfactants in Organic Solvents: Approximate Prediction with UNIFAC. *Journal of Colloid and Interface Science* 240.1, 277–283. DOI: 10.1006/jcis.2001.7627 (cit. on p. 10).

Forrester, A. I. J., Sóbester, A., Keane, A. J. (2008). *Engineering Design via Surrogate Modelling - A Practical Guide*. Ed. by A. I. J. Forrester, A. Sóbester, A. J. Keane. John Wiley & Sons, Ltd (cit. on pp. 32, 35).

Fourer, R., Gay, D. M., Kernighan, B. W. (1997). *AMPL: A Modeling Language for Mathematical Programming (with AMPL Plus Student Edition for Microsoft Windows) (The Scientific Press Series)*. Cengage Learning. ISBN: 0894262327. URL: https://www.amazon.com/AMPL-Mathematical-Programming-Microsoft-Scientific/dp/0534509835?SubscriptionId=AKIAIOBINVZYXZQZ2U3A&tag=chimbori05-20&linkCode=xm2&camp=2025&creative=165953&creativeASIN=0534509835 (cit. on p. 119).

Franke, R., Selent, D., Börner, A. (2012). Applied Hydroformylation. *Chemical Reviews* 112.11, 5675–5732. DOI: 10.1021/cr3001803 (cit. on p. 2).

García-Sánchez, F., Eliosa-Jim'enez, G., Salas-Padrón, A., Hernández-Garduza, O., Ápam-Mart'inez, D. (2001). Modeling of microemulsion phase diagrams from excess Gibbs energy models. *Chemical Engineering Journal* 84.3, 257–274. DOI: 10.1016/S1385-8947(00)00285-0 (cit. on p. 22).

Gerlach, M., Wajid, D. A., Hilfert, L., Edelmann, F. T., Seidel-Morgenstern, A., Hamel, C. (2017). Impact of minor amounts of hydroperoxides on rhodium-catalyzed hydroformylation of long-chain olefins. *Catalysis Science & Technology* 7.7, 1465–1469. DOI: 10.1039/C7CY00244K (cit. on p. 50).

Gesellschaft Deutscher Chemiker, O. (2013). *Historische Stätten der Chemie - Otto Roelen*. online (cit. on p. 1).

Gmehling, J., Kolbe, B. (1992). *Thermodynamik (German Edition)*. Wiley-VCH. ISBN: 978-3527285471. URL: https://www.amazon.com/Thermodynamik-German-J-rgen-Gmehling/dp/3527285474?SubscriptionId=AKIAIOBINVZYXZQZ2U3A&tag=chimbori05-20&linkCode=xm2&camp=2025&creative=165953&creativeASIN=3527285474 (cit. on pp. C-13, C-14).

Goedheijt, M. S., Kamer, P. C., Leeuwen, P. W. van (1998). A water-soluble diphosphine ligand with a large 'natural' bite angle for two-phase hydroformylation of alkenes. *Journal of Molecular Catalysis A: Chemical* 134.1-3, 243–249. DOI: 10.1016/S1381-1169(98)00042-9 (cit. on p. 20).

Gorissen, D., Crombecq, K., Couckuyt, I., Dhaene, T., Demeester, P. (2010). A Surrogate Modeling and Adaptive Sampling Toolbox for Computer Based Design. *Journal of Machine Learning Research* 11, 2051–2055 (cit. on p. 32).

Grabow, K., Bentrup, U. (2014). Homogeneous Catalytic Processes Monitored by Combined in Situ ATR-IR, UV–Vis, and Raman Spectroscopy. *ACS Catalysis* 4.7, 2153–2164. DOI: 10.1021/cs500363n (cit. on p. 29).

Hamerla, T. (2014). Hydroformylierung langkettiger Olefine mit zweizähnigen Rhodium-Komplexen in mizellaren Lösungen und Mikroemulsionen. *PhD Thesis*. Technische Universität Berlin (cit. on pp. 22, 47).

Hamerla, T., Paul, N., Kraume, M., Schomäcker, R. (2013a). Aufklärung der Stofftransportwege in mizellaren Mehrphasenreaktionen am Beispiel der Hydroformylierung. *Chemie Ingenieur Technik*, n/a–n/a. DOI: 10.1002/cite.201300048 (cit. on p. 22).

Hamerla, T., Rost, A., Kasaka, Y., Schomäcker, R. (2013b). Hydroformylation of 1-Dodecene with Water-Soluble Rhodium Catalysts with Bidentate Ligands in Multiphase Systems. *ChemCatChem* 5.7, 1854–1862. DOI: 10.1002/cctc.201200744 (cit. on p. 4).

Hammersley, J. M. (1960). MONTE CARLO METHODS FOR SOLVING MULTIVARIABLE PROBLEMS. *Annals of the New York Academy of Sciences* 86.3, 844–874. DOI: 10.1111/j.1749-6632.1960.tb42846.x (cit. on p. 90).

Hampel, F. R. (1974). The Influence Curve and its Role in Robust Estimation. *Journal of the American Statistical Association* 69.346, 383–393. DOI: 10.2307/2285666 (cit. on p. 43).

Hangos, K., Cameron, I. (2001). *Process Modelling and Model Analysis*. Ed. by J. Perkins, G. Stephanopoulos. Academic Press (cit. on p. 31).

Hansen, P. C. (1987). The truncatedSVD as a method for regularization. *BIT* 27.4, 534–553. DOI: 10.1007/BF01937276 (cit. on p. 36).

Haumann, M., Koch, H., Hugo, P., Schomäcker, R. (2002). Hydroformylation of 1-dodecene using Rh-TPPTS in a microemulsion. *Applied Catalysis A: General* 225.1-2, 239–249. DOI: 10.1016/S0926-860X(01)00869-9 (cit. on pp. 3, 22).

Haumann, M., Riisager, A. (2008). Hydroformylation in Room Temperature Ionic Liquids (RTILs): Catalyst and Process Developments. *Chemical Reviews* 108.4, 1474–1497. DOI: 10.1021/cr078374z (cit. on p. 2).

Heck, R. F., Breslow, D. S. (1963). Carboxyalkylation Reactions Catalyzed by Cobalt Carbonylate Ion. *Journal of the American Chemical Society* 85.18, 2779–2782. DOI: 10.1021/ja00901a023 (cit. on p. 19).

Heck, R. F., Breslow, D. S. (1961). The Reaction of Cobalt Hydrotetracarbonyl with Olefins. *Journal of the American Chemical Society* 83.19, 4023–4027. DOI: 10.1021/ja01480a017 (cit. on p. 19).

Herrmann, W. A. (2002). *Chemie aus Leidenschaft: Pioniere, Visionäre, Patente - Festvortrag zum 75. Gründungsjubiläum der RUHRCHEMIE AGOberhausen, 28. Oktober 2002*. *techreport*. Technische Universität München. URL: http://aci.anorg.chemie.tu-muenchen.de/new/images/stories/ProfWAH/docs/pioniere.pdf (cit. on p. 1).

Hloucha, M., Küsters, E., Schorb, J., Prinz, D., Seipel, W., Wirtz, M. (2014). Use of microemulsions in cosmetic cleaning compositions. English. *United States Patent* US9656104B2 (Düsseldorf, DE) (cit. on p. 9).

Hoffmann, C., Illner, M., Müller, D., Esche, E., Wozny, G., Biegler, L. T., Repke, J.-U. (2016). Moving-horizon State Estimation with Gross Error Detection for a Hydroformylation Miniplant. In: *Computer Aided Chemical Engineering - Proceedings of the 26th European Symposium on Computer Aided Process Engineering*. Vol. 38. Elsevier, 1485–1490. DOI: 10.1016/B978-0-444-63428-3.50252-6 (cit. on pp. 42, 116).

Hohl, L., Kraume, M. (2018). The formation of complex droplets in liquid three phase systems and their effect on dispersion and phase separation. *Chemical Engineering Research and Design* 129, 89–101. DOI: 10.1016/j.cherd.2017.10.027 (cit. on p. 22).

Hohl, L., Paul, N., Kraume, M. (2016). Dispersion conditions and drop size distributions in stirred micellar multiphase systems. *Chemical Engineering and Processing: Process Intensification* 99, 149–154. DOI: 10.1016/j.cep.2015.08.011 (cit. on p. 18).

Hong, C. I., Kim, J., Choi, N., Shin, H., Yang, S., Kim, J., Lim, J., Kim, C. (2001). Microemulsions and uses thereof as nanoreactors or delivery vehicles. Englisch. *United States Patent Application* US6306434B1 (Decatur, IL) (cit. on p. 9).

Huibers, P. D. T., Lobanov, V. S., Katritzky, A. R., Shah, D. O., Karelson, M. (1996). Prediction of Critical Micelle Concentration Using a Quantitative Structure-Property Relationship

Approach. 1. Nonionic Surfactants. *Langmuir* 12.6, 1462–1470. DOI: 10.1021/la950581j (cit. on p. 102).

Ibraheem, N. A., Hasan, M. M., Khan, R. Z., Mishra, P. K. (2012). Understanding Color Models: A Review. *ARPN Journal of Science and Technology* 2.3, 265–275. ISSN: 2225-7217 (cit. on p. 75).

Illner, M., Müller, D., Esche, E., Schomäcker, R., Repke, J.-U. (2016a). Hydroformylierung in Mikroemulsionen - Anforderungen und Lösungsansätze im Miniplant-Betrieb. In: *Chemie Ingenieur Technik - Special Issue: ProcessNet-Jahrestagung und 32. DECHEMA-Jahrestagung der Biotechnologen 2016, Aachen, Germany*. Vol. 88. 9. Wiley, 1334–1334. DOI: 10.1002/cite.201650346 (cit. on p. 22).

Illner, M., Pogrzeba, T., Schmidt, M., Müller, D., Esche, E., Schomäcker, R., Repke, J.-U., Schomäcker, Wozny, G. (2016b). Hydroformylation of 1-dodecene in Microemulsions: Operation and Validation of Lab Results in a Miniplant. In: *Technical Transactions - Mechanics Issue 1-M (1) 2016*, 107–120. DOI: 10.4467/2353737XCT.16.011.4975 (cit. on pp. 4, 22, 66, 130).

Illner, M., Esche, E., Repke, J.-U. (2018a). Optimal Control of Surfactant containing Multiphase Systems - Challenges and Solution Strategies for a stable Mini-Plant Operation. In: *13th International Symposium on Process Systems Engineering (PSE 2018)*. Ed. by M. R. Eden, M. G. Ierapetritou, G. P. Towler. Vol. 44. Computer Aided Chemical Engineering 13. Elsevier, 739–744. DOI: 10.1016/B978-0-444-64241-7.50118-X (cit. on pp. 3, 14, 63).

Illner, M., Müller, D., Esche, E., Pogrzeba, T., Schmidt, M., Schomäcker, R., Wozny, G., Repke, J.-U. (2016c). Hydroformylation in Microemulsions: Proof of Concept in a Miniplant. *Industrial & Engineering Chemistry Research* 55.31, 8616–8626. DOI: 10.1021/acs.iecr.6b00547 (cit. on pp. 3, 14, 130, 132).

Illner, M., Schmidt, M., Pogrzeba, T., Urban, C., Esche, E., Schomäcker, R., Repke, J.-U. (2018c). Palladium-Catalyzed Methoxycarbonylation of 1-Dodecene in a Two-Phase System: The Path toward a Continuous Process. *Industrial & Engineering Chemistry Research* 57.27, 8884–8894. DOI: 10.1021/acs.iecr.8b01537 (cit. on pp. 3, 4, 166).

Ivanković, A. (2017). Review of 12 Principles of Green Chemistry in Practice. *International Journal of Sustainable and Green Energy* 6.3, 39. DOI: 10.11648/j.ijrse.20170603.12 (cit. on p. 1).

Jacquez, J. A., Greif, P. (1985). Numerical parameter identifiability and estimability: Integrating identifiability, estimability, and optimal sampling design. *Mathematical Biosciences* 77.1-2, 201–227. DOI: 10.1016/0025-5564(85)90098-7 (cit. on p. 36).

James, G., Witten, D., Hstie, T., Tibshirani, R. (2017). *An Introduction to Statistical Learning: with Applications in R*. Ed. by R. Tibshirani. Springer (cit. on p. 35).

Jeffreys, G. V., Davies, G. A., Pitt, K. (1970). Rate of coalescence of the dispersed phase in a laboratory mixer settler unit: Part I. *AIChE Journal* 16.5, 823–827. DOI: 10.1002/aic.690160521 (cit. on p. 28).

Jennings, J. W., Pallas, N. R. (1988). An efficient method for the determination of interfacial tensions from drop profiles. *Langmuir* 4.4, 959–967. DOI: 10.1021/la00082a030 (cit. on p. 78).

Ji, L., Rawlings, J. B. (2015). Application of MHE to large-scale nonlinear processes with delayed lab measurements. *Computers & Chemical Engineering* 80, 63–72. DOI: 10.1016/j.compchemeng.2015.04.015 (cit. on pp. 39, 40).

Jörke, A., Seidel-Morgenstern, A., Hamel, C. (2017). Rhodium-BiPhePhos catalyzed hydroformylation studied by operando FTIR spectroscopy: Catalyst activation and rate determining step. *Journal of Molecular Catalysis A: Chemical* 426, 10–14. DOI: 10.1016/j.molcata.2016.10.028 (cit. on p. 20).

Kahlweit, M. (1988). Microemulsions. *Science* 240.4852, 617–621. DOI: 10.1126/science.240.4852.617 (cit. on p. 9).

Kahlweit, M., Strey, R., Busse, G. (1990). Microemulsions: a qualitative thermodynamic approach. *The Journal of Physical Chemistry* 94.10, 3881–3894. DOI: 10.1021/j100373a006 (cit. on pp. 11, 15, 103).

Kahlweit, M., Strey, R., Firman, P., Haase, D., Jen, J., Schomaecker, R. (1988). General patterns of the phase behavior of mixtures of water, nonpolar solvents, amphiphiles, and electrolytes. 1. *Langmuir* 4.3, 499–511. DOI: 10.1021/la00081a002 (cit. on pp. 16, 18).

Kahlweit, M., Strey, R., Haase, D., Kunieda, H., Schmeling, T., Faulhaber, B., Borkovec, M., Eicke, H.-F., Busse, G., Eggers, F., Funck, T., Richmann, H., Magid, L., Söderman, O., Stilbs, P., Winkler, J., Dittrich, A., Jahn, W. (1987). How to study microemulsions. *Journal of Colloid and Interface Science* 118.2, 436–453. DOI: 10.1016/0021-9797(87)90480-2 (cit. on pp. 4, 17, 24).

Kahlweit, M., Strey, R. (1985). Phasenverhalten ternärer Systeme des Typs H2O – Öl – nichtionisches Amphiphil (Mikroemulsionen). *Angewandte Chemie* 97.8, 655–669. DOI: 10.1002/ange.19850970806 (cit. on pp. 12, 13, 24).

Keim, W. (2013). Oligomerization of Ethylene to alpha-Olefins: Discovery and Development of the Shell Higher Olefin Process (SHOP). *Angewandte Chemie International Edition* 52.48, 12492–12496. DOI: 10.1002/anie.201305308 (cit. on p. 4).

Kiedorf, G., Hoang, D., Müller, A., Jörke, A., Markert, J., Arellano-Garcia, H., Seidel-Morgenstern, A., Hamel, C. (2014). Kinetics of 1-dodecene hydroformylation in a thermomorphic solvent system using a rhodium-biphephos catalyst. *Chemical Engineering Science* 115, 31–48. DOI: 10.1016/j.ces.2013.06.027 (cit. on pp. 88–90, 93).

Klier, J., Tucker, C. J., Kalantar, T. H., Green, D. P. (2000). Properties and Applications of Microemulsions. *Advanced Materials* 12.23, 1751–1757. DOI: 10.1002/1521-4095(200012)12:23%3C1751::AID-ADMA1751%3E3.0.CO;2-I (cit. on p. 9).

Knickerbocker, B. M., Pesheck, C. V., Scriven, L. E., Davis, H. T. (1979). Phase behavior of alcohol-hydrocarbon-brine mixtures. *The Journal of Physical Chemistry* 83.15, 1984–1990. DOI: 10.1021/j100478a012 (cit. on p. 12).

Kramer, S., Gesthuisen, R., Engell, S. (2005). Fixed structure multirate state estimation. In: *Proceedings of the American Control Conference*. IEEE. DOI: 10.1109/ACC.2005.1470723 (cit. on p. 44).

Krämer, S., Gesthuisen, R. (2005). Multirate State Estimation using Moving Horizon Estimation. *IFAC Proceedings Volumes* 38.1, 1–6. DOI: 10.3182/20050703-6-CZ-1902.00654 (cit. on p. 40).

Kranenburg, M., Burgt, Y. E. M. van der, Kamer, P. C. J., Leeuwen, P. W. N. M. van, Goubitz, K., Fraanje, J. (1995). New Diphosphine Ligands Based on Heterocyclic Aromatics Inducing Very High Regioselectivity in Rhodium-Catalyzed Hydroformylation: Effect of the Bite Angle. *Organometallics* 14.6, 3081–3089. DOI: 10.1021/om00006a057 (cit. on p. 20).

Küpper, A., Diehl, M., Schlöder, J. P., Bock, H. G., Engell, S. (2009). Efficient moving horizon state and parameter estimation for SMB processes. *Journal of Process Control* 19.5, 785–802. DOI: 10.1016/j.jprocont.2008.10.004 (cit. on p. 40).

Langevin, D. (1986). Microemulsions and Liquid Crystals. *Molecular Crystals and Liquid Crystals* 138.1, 259–305. DOI: 10.1080/00268948608071764 (cit. on p. 13).

Leeuwen, P. W. N. M. van, Chadwick, J. C. (2011). *Homogeneous Catalysts*. Ed. by P. W. N. M. van Leeuwe. Wiley VCH Verlag GmbH. ISBN: 9783527323296. URL: https://www.ebook.de/de/product/14131574/john_c_chadwick_piet_w_n_m_van_leeuwen_homogeneous_catalysts.html (cit. on p. 4).

Li, C., Widjaja, E., Chew, W., Garland, M. (2002). Rhodium Tetracarbonyl Hydride: The Elusive Metal Carbonyl Hydride. *Angewandte Chemie* 114.20, 3939–3943. DOI: 10.1002/1521-3757(20021018)114:20%3C3939::AID-ANGE3939%3E3.0.CO;2-N (cit. on p. 20).

Liao, Y., Lucas, D. (2010). A literature review on mechanisms and models for the coalescence process of fluid particles. *Chemical Engineering Science* 65.10, 2851–2864. DOI: 10.1016/j.ces.2010.02.020 (cit. on p. 18).

Lindman, B., Stilbs, P. (2018). Molecular diffusion in Microemulsions. In: *Microemulsions: Structure and Dynamics*. Ed. by Friberg. CRC Press, 119–152. DOI: 10.1201/9781351074599 (cit. on p. 11).

López-Negrete, R., Biegler, L. T. (2012). A Moving Horizon Estimator for processes with multi-rate measurements: A Nonlinear Programming sensitivity approach. *Journal of Process Control* 22.4, 677–688. DOI: 10.1016/j.jprocont.2012.01.013 (cit. on pp. 39, 41, 44, 116).

López-Negrete, R., Patwardhan, S. C., Biegler, L. T. (2011). Constrained particle filter approach to approximate the arrival cost in Moving Horizon Estimation. *Journal of Process Control* 21.6, 909–919. DOI: 10.1016/j.jprocont.2011.03.004 (cit. on p. 41).

López, D. C., Barz, T., Körkel, S., Wozny, G. (2015). Nonlinear ill-posed problem analysis in model-based parameter estimation and experimental design. *Computers & Chemical Engineering* 77, 24–42. DOI: 10.1016/j.compchemeng.2015.03.002 (cit. on pp. 35, 36).

Lutz, E. F. (1986). Shell higher olefins process. *Journal of Chemical Education* 63.3, 202. DOI: 10.1021/ed063p202 (cit. on p. 4).

Markert, J., Brunsch, Y., Munkelt, T., Kiedorf, G., Behr, A., Hamel, C., Seidel-Morgenstern, A. (2013). Analysis of the reaction network for the Rh-catalyzed hydroformylation of 1-dodecene in a thermomorphic multicomponent solvent system. *Applied Catalysis A: General* 462-463, 287–295. DOI: 10.1016/j.apcata.2013.04.005 (cit. on p. 47).

Marquardt, D. W. (1963). An Algorithm for Least-Squares Estimation of Nonlinear Parameters. *Journal of the Society for Industrial and Applied Mathematics* 11.2, 431–441. DOI: 10.1137/0111030 (cit. on p. 35).

McBride, K., Sundmacher, K. (2019). Overview of Surrogate Modeling in Chemical Process Engineering. *Chemie Ingenieur Technik* 91.3, 228–239. DOI: 10.1002/cite.201800091 (cit. on p. 32).

Menger, F. M., Rizvi, S. A. A. (2011). Relationship between Surface Tension and Surface Coverage. *Langmuir* 27.23, 13975–13977. DOI: 10.1021/la203009m (cit. on p. 10).

Meyer, K., Ruiken, J.-P., Illner, M., Paul, A., Müller, D., Esche, E., Wozny, G., Maiwald, M. (2017a). Process spectroscopy in microemulsions—setup and multi-spectral approach for reaction monitoring of a homogeneous hydroformylation process. *Measurement Science and Technology* 28.3, 035501. DOI: 10.1088/1361-6501/aa54f3 (cit. on pp. 78, 140).

Misra, A., Bonamy, C., Souza, L. M. de, Hohl, L., Illner, M., Kraume, M., Repke, J.-U., Thévenin, D. (2018). A multi-fluid approach to simulate separation of liquid-liquid systems in a gravity settler. In: *Computer Aided Chemical Engineering - Proceedings of the 28th European Symposium on Computer Aided Process Engineering*. Elsevier, 31–36. DOI: 10.1016/B978-0-444-64235-6.50008-5 (cit. on p. 167).

Mitsos, A., Asprion, N., Floudas, C. A., Bortz, M., Baldea, M., Bonvin, D., Caspari, A., Schäfer, P. (2018). Challenges in process optimization for new feedstocks and energy sources. *Computers & Chemical Engineering* 113, 209–221. DOI: 10.1016/j.compchemeng.2018.03.013 (cit. on pp. 4, 29).

Mitsos, A., Lee, U., Recker, S., Skiborowski, M. (2019). Handbook of Green Chemistry: Online. In: ed. by P. T. Anastas. Wiley-VCH Verlag GmbH & Co. KGaA. Chap. Part 12. Conceptual Process Design and Process Optimization, 87–114. ISBN: 9783527628698. DOI: https://doi.org/10.1002/9783527628698.hgc137 (cit. on p. 31).

Miyagawa, C. C., Kupka, J., Schumpe, A. (2005). Rhodium-catalyzed hydroformylation of 1-octene in micro-emulsions and micellar media. *Journal of Molecular Catalysis A: Chemical* 234.1-2, 9–17. DOI: 10.1016/j.molcata.2005.02.013 (cit. on p. 3).

Müller, D., Esche, E., C., D. C. L., Wozny, G. (2014). An algorithm for the identification and estimation of relevant parameters for optimization under uncertainty. *Computers & Chemical Engineering* 71, 94–103. DOI: 10.1016/j.compchemeng.2014.07.007 (cit. on p. 36).

Müller, D., Esche, E., Pogrzeba, T., Illner, M., Leube, F., Schomäcker, R., Wozny, G. (2015). Systematic Phase Separation Analysis of Surfactant-Containing Systems for Multiphase Settler Design. *Industrial & Engineering Chemistry Research* 54.12, 3205–3217. DOI: 10.1021/ie5049059 (cit. on pp. 22–27, 57, 61, 70).

Müller, M., Kasaka, Y., Müller, D., Schomäcker, R., Wozny, G. (2013). Process Design for the Separation of Three Liquid Phases for a Continuous Hydroformylation Process in a Miniplant Scale. *Industrial & Engineering Chemistry Research* 52.22, 7259–7264. DOI: 10.1021/ie302487m (cit. on pp. 3, 22, 66).

Murzin, D., Salmi, T. (2016). *Catalytic Kinetics*. Ed. by D. Murzin, T. Salmi. 2nd ed. Elsevier Science (cit. on pp. 29, 88).

Myers, D. (2005a). Surfactant Science and Technology. In: *Surfactant Science and Technology*. Ed. by D. Myers. John Wiley & Sons, Inc. Chap. 4: Surfactants in Solution: Monolayers and Micelle, 107–159. ISBN: 9780471680246. DOI: 10.1002/047174607X.ch4 (cit. on p. 9).

Myers, D. (2005b). Surfactant Science and Technology. In: *Surfactant Science and Technology*. Ed. by D. Myers. John Wiley & Sons, Inc. Chap. 5: Higher-Level Surfactant Aggregate Structures: Liquid Crystals, Continuous Biphases, and Microemulsions, 107–159. ISBN: 9780-47168-0246. DOI: 10.1002/047174607X.ch4 (cit. on p. 11).

Nicholson, B., López-Negrete, R., Biegler, L. T. (2014). On-line state estimation of nonlinear dynamic systems with gross errors. *Computers & Chemical Engineering* 70, 149–159. DOI: 10.1016/j.compchemeng.2013.11.018 (cit. on pp. 40, 42).

NIST (2019a). *Thermophysical Properties of Carbon monoxide*. National Institute of Standards and Technology Chemistry Webbook. URL: https://webbook.nist.gov/cgi/fluid.cgi?ID=C630080&Action=Page (cit. on p. C-19).

NIST (2019b). *Thermophysical Properties of Hydrogen*. National Institute of Standards and Technology Chemistry Webbook. URL: https://webbook.nist.gov/cgi/fluid.cgi?ID=C1333740&Action=Page (cit. on p. C-19).

NIST (2019c). *Thermophysical Properties of Nitrogen*. National Institute of Standards and Technology Chemistry Webbook. URL: https://webbook.nist.gov/cgi/fluid.cgi?ID=C7727379&Action=Page (cit. on p. C-19).

Oetter, G., Hoffmann, H. (1988). Correlation between Interfacial Tension and Miceallar Structures. *Journal of Dispersion Science and Technology* 9.5, 459–492. DOI: 10.1080/01932698808944005 (cit. on p. 10).

Özyurt, D. B., Pike, R. W. (2004). Theory and practice of simultaneous data reconciliation and gross error detection for chemical processes. *Computers & Chemical Engineering* 28.3, 381–402. DOI: 10.1016/j.compchemeng.2003.07.001 (cit. on p. 42).

Padilla, R., Ruiz, M., Trujillo, W. (1996). Separation of liquid-liquid dispersions in a deep-layer gravity settler: Part I. Experimental study of the separation process. *Hydrometallurgy* 42.2, 267–279. DOI: 10.1016/0304-386X(95)00095-X (cit. on p. 28).

Palyska, W., Chmielewski, A. G. (1993). Solvent Extraction and Emulsion Separation in Magnetic Fields. *Separation Science and Technology* 28.1-3, 127–138. DOI: 10.1080/01496399308019482 (cit. on p. 25).

Paul, A., Meyer, K., Ruiken, J.-P., Illner, M., Müller, D.-N., Esche, E., Wozny, G., Westad, F., Maiwald, M. (2017). Process spectroscopy in microemulsions—Raman spectroscopy for online monitoring of a homogeneous hydroformylation process. *Measurement Science and Technology* 28.3, 035502. DOI: 10.1088/1361-6501/aa54f0 (cit. on pp. 78, 140).

Pogrzeba, T. (2018). Rhodium-catalysed hydroformylation of long-chain alkenes in aqueous multiphase systems: Kinetic studies and systematic process development. *PhD Thesis*. Technische Universität Berlin (cit. on p. 20).

Pogrzeba, T., Illner, M., Schmidt, M., Milojevic, N., Esche, E., Repke, J.-U., Schomäcker, R. (2019). Kinetics of hydroformylation of 1-dodecene in microemulsion systems using a rhodium sulfoxantphos catalyst. *Industrial & Engineering Chemistry Research*. DOI: 10.1021/acs.iecr.8b06157 (cit. on pp. 21, 29, 30, 47, 49, 50, A-1).

Pogrzeba, T., Müller, D., Illner, M., Schmidt, M., Kasaka, Y., Weber, A., Wozny, G., Schomäcker, R., Schwarze, M. (2016a). Superior catalyst recycling in surfactant based multiphase systems – Quo vadis catalyst complex?. *Chemical Engineering and Processing: Process Intensification* 99, 155–166. DOI: 10.1016/j.cep.2015.09.003 (cit. on pp. 22, 55).

Pogrzeba, T., Illner, M., Schmidt, M., Repke, J.-U., Schomäcker, R. (2017a). Microemulsion Systems as Switchable Reaction Media for the Catalytic Upgrading of Long-Chain Alkenes. *Chemie Ingenieur Technik* 89.4, 459–463. DOI: 10.1002/cite.201600140 (cit. on pp. 89, 93).

Pogrzeba, T., Müller, D., Hamerla, T., Esche, E., Paul, N., Wozny, G., Schomäcker, R. (2015). Rhodium-Catalyzed Hydroformylation of Long-Chain Olefins in Aqueous Multiphase Systems in a Continuously Operated Miniplant. *Industrial & Engineering Chemistry Research* 54.48, 11953–11960. DOI: 10.1021/acs.iecr.5b01596 (cit. on pp. 47, 57, 89).

Pogrzeba, T., Schmidt, M., Milojevic, N., Urban, C., Illner, M., Repke, J.-U., Schomäcker, R. (2017b). Understanding the Role of Nonionic Surfactants during Catalysis in Microemulsion Systems on the Example of Rhodium-Catalyzed Hydroformylation. *Industrial & En-*

gineering Chemistry Research 56.36, 9934–9941. DOI: 10.1021/acs.iecr.7b02242 (cit. on pp. 20, 22, 49, 52, A-1).

Pontes, K. V., Wolf, I. J., Embiruçu, M., Marquardt, W. (2015). Dynamic Real-Time Optimization of Industrial Polymerization Processes with Fast Dynamics. *Industrial & Engineering Chemistry Research* 54.47, 11881–11893. DOI: 10.1021/acs.iecr.5b00909 (cit. on p. 37).

Pruett, R. L. (1979). Hydroformylation. *Advances in Organometallic Chemistry*, 1–60. DOI: 10.1016/S0065-3055(08)60320-2 (cit. on p. 47).

Rao, C. V., Rawlings, J. B. (2000). Nonlinear Moving Horizon State Estimation. In: *Nonlinear Model Predictive Control*. Birkhäuser Basel, 45–69. DOI: 10.1007/978-3-0348-8407-5_3 (cit. on p. 41).

Rawlings, J. B., Bakshi, B. R. (2006). Particle filtering and moving horizon estimation. *Computers & Chemical Engineering* 30.10-12, 1529–1541. DOI: 10.1016/j.compchemeng.2006.05.031 (cit. on pp. 40, 41).

Ritter, E., Racheva, R., Storm, S., Müller, S., Ingram, T., Smirnova, I. (2016). Influence of Inorganic Salts on the Phase Equilibrium of Triton X-114 Aqueous Two-Phase Systems. *Journal of Chemical & Engineering Data* 61.4, 1496–1501. DOI: 10.1021/acs.jced.5b00821 (cit. on p. 16).

Roelen, O. (1938). Verfahren zur Herstellung von sauerstoffhaltigen Verbindungen. German. DE849548 (cit. on p. 1).

Rosen, M. J., Cohen, A. W., Dahanayake, M., Hua, X. Y. (1982). Relationship of structure to properties in surfactants. 10. Surface and thermodynamic properties of 2-dodecyloxypoly-(ethenoxyethanol)s, C12H25(OC2H4)xOH, in aqueous solution. *The Journal of Physical Chemistry* 86.4, 541–545. DOI: 10.1021/j100393a025 (cit. on pp. 15, 102, 103).

Rösler, T., Faßbach, T. A., Schrimpf, M., Vorholt, A. J., Leitner, W. (2018). Toward Water-Based Recycling Techniques: Methodologies for Homogeneous Catalyst Recycling in Liquid/Liquid Multiphase Media and Their Implementation in Continuous Processes. *Industrial & Engineering Chemistry Research* 58.7, 2421–2436. DOI: 10.1021/acs.iecr.8b04295 (cit. on p. 4).

Rost, A., Müller, M., Hamerla, T., Kasaka, Y., Wozny, G., Schomäcker, R. (2013). Development of a continuous process for the hydroformylation of long-chain olefins in aqueous multiphase systems. *Chemical Engineering and Processing: Process Intensification* 67, 130–135. DOI: 10.1016/j.cep.2012.10.001 (cit. on p. 47).

Salau, N. P., Trierweiler, J. O., Secchi, A. R. (2014). Observability analysis and model formulation for nonlinear state estimation. *Applied Mathematical Modelling* 38.23, 5407–5420. DOI: 10.1016/j.apm.2014.03.053 (cit. on pp. 44, 114).

Sandee, A. J., Slagt, V. F., Reek, J. N. H., Kamer, P. C. J., Leeuwen, P. W. N. M. van (1999). A stable and recyclable supported aqueous phase catalyst for highly selective hydroformylation of higher olefins†. *Chemical Communications* 17, 1633–1634. DOI: 10.1039/A903916C (cit. on p. 20).

Schlieper, L., Chatterjee, M., Henschke, M., Pfennig, A. (2004). Liquid-liquid phase separation in gravity settler with inclined plates. *AIChE Journal* 50.4, 802–811. DOI: 10.1002/aic.10075 (cit. on p. 28).

Schomäcker, R., Holmberg, K. (2009). Reactions in Organised Surfactant Systems. In: *Microemulsions: Background, New Concepts, Applications, Perspectives*. Ed. by C. Stubenrauch. John Wiley & Sons, Ltd. Chap. 5, 148–179. ISBN: 9781405167826. DOI: 10.1002/9781444305524.ch5 (cit. on pp. 9, 22).

Schulman, J. H., Hoar, T. P. (1943). Transparent Water-in-Oil Dispersions: the Oleopathic Hydro-Micelle. *Nature* 152, 102–103. DOI: 10.1038/152102a0 (cit. on p. 9).

Schulman, J. H., McRoberts, T. S. (1946). On the structure of transparent water and oil dispersions (solubilised oils). *Transactions of the Faraday Society* 42, 165–170. DOI: 10.1039/TF946420B165 (cit. on p. 9).

Schulman, J., Friend, J. (1949). Light scattering investigation of the structure of transparent oil-water disperse systems. II. *Journal of Colloid Science* 4.5, 497–509. DOI: 10.1016/0095-8522(49)90046-X (cit. on p. 9).

Schulman, J., Riley, D. (1948). X-ray investigation of the structure of transparent oil-water disperse systems.. *Journal of Colloid Science* 3.4, 383–405. DOI: 10.1016/0095-8522(48)90024-5 (cit. on p. 9).

Schulman, J. H., Stoeckenius, W., Prince, L. M. (1959). Mechanism of Formation and Structure of Micro Emulsions by Electron Microscopy. *The Journal of Physical Chemistry* 63.10, 1677–1680. DOI: 10.1021/j150580a027 (cit. on p. 9).

Schwuger, M.-J., Stickdorn, K., Schomaecker, R. (1995). Microemulsions in Technical Processes. *Chemical Reviews* 95.4, 849–864. DOI: 10.1021/cr00036a003 (cit. on p. 9).

Seader, J., Henley, E., Roper, D. (2011). *Separation Process Principles: Chemical and Biochemical Operations*. Ed. by J. Welter. 3rd ed. John Wiley & Sons, Inc. (cit. on p. 28).

Shylesh, S., Hanna, D., Mlinar, A., Kŏng, X.-Q., Reimer, J. A., Bell, A. T. (2013). In Situ Formation of Wilkinson-Type Hydroformylation Catalysts: Insights into the Structure, Stability, and Kinetics of Triphenylphosphine- and Xantphos-Modified Rh/SiO2. *ACS Catalysis* 3.3, 348–357. DOI: 10.1021/cs3007445 (cit. on p. 20).

Silva, S. M., Bronger, R. P. J., Freixa, Z., Dupont, J., Leeuwen, P. W. N. M. van (2003). High pressure infrared and nuclear magnetic resonance studies of the rhodium-sulfoxantphos catalysed hydroformylation of 1-octene in ionic liquids. *New Journal of Chemistry* 27.9, 1294. DOI: 10.1039/B306051A (cit. on p. 20).

Smith, A. R., Caswell, J. E., Larson, P. P., Cavers, S. D. (1963). Coalescence of drops in liquid-liquid extraction columns. *The Canadian Journal of Chemical Engineering* 41.4, 150–157. DOI: 10.1002/cjce.5450410404 (cit. on p. 17).

Smith, R. (2005). *Chemical Process Design and Integration*. Ed. by R. Smith. John John John Wiley & Sons, Inc. DOI: 10.1002/9783527621583 (cit. on p. 65).

Sorensen, D. C. (1982). Newton's Method with a Model Trust Region Modification. *SIAM Journal on Numerical Analysis* 19.2, 409–426. DOI: 10.1137/0719026 (cit. on p. 35).

Sottmann, T., Stubenrauch, C. (2009). Phase Behaviour, Interfacial Tension and Microstructure of Microemulsions. In: *Microemulsions: Background, New Concepts, Applications, Perspectives*. Ed. by C. Stubenrauch. John Wiley & Sons, Ltd. Chap. 1, 1–47. ISBN: 9781405167826. DOI: 10.1002/9781444305524.ch1 (cit. on pp. 11–14, 24).

Tadros, T. F. (2013). Emulsion Formation, Stability, and Rheology. In: *Emulsion Formation and Stability*. Wiley-VCH Verlag GmbH & Co. KGaA, 1–75. DOI: 10.1002/9783527647941.ch1 (cit. on p. 9).

Tatiraju, S., Soroush, M., Ogunnaike, B. A. (1999). Multirate nonlinear state estimation with application to a polymerization reactor. *AIChE Journal* 45.4, 769–780. DOI: 10.1002/aic.690450412 (cit. on p. 44).

Tekle, E., Ueda, M., Schelly, Z. A. (1989). Dynamics of electric field induced transient-phase separation in water-in-oil microemulsion. *The Journal of Physical Chemistry* 93.16, 5966–5969. DOI: 10.1021/j100353a005 (cit. on p. 25).

Tikhonov, A. N. (1963). On the solution of ill-posed problems and the method of regularizatio. *Dokl. Akad. Nauk SSSR* (cit. on p. 36).

Tinucci, L., Platone, E. (1990). Process for the catalytic hydroformylation of olefins. English, French. EP0380154A2 (cit. on p. 3).

Tolman, C. A. (1977). Steric effects of phosphorus ligands in organometallic chemistry and homogeneous catalysis. *Chemical Reviews* 77.3, 313–348. DOI: 10.1021/cr60307a002 (cit. on p. 20).

Torrealba, V. A., Johns, R. T. (2018). Microemulsion Phase-Behavior Equation-of-State Model Using Empirical Trends in Chemical Potentials. *SPE Journal* 23.03, 0819–0830. DOI: 10.2118/184555-PA (cit. on p. 22).

Toumi, A., Diehl, M., Engell, S., Bock, H., Schlöder, J. (2005). Finite Horizon Optimizing Control of advanced SMB Chromatographic Processes. *IFAC Proceedings Volumes* 38.1, 609–614. DOI: 10.3182/20050703-6-CZ-1902.01675 (cit. on p. 37).

Vijayan, S., Ponter, A. B. (1975). Drop/drop and drop/interface coalescence in primary liquid/liquid dispersion separators. *Chemie Ingenieur Technik - CIT* 47.18, 748–755. DOI: 10.1002/cite.330471803 (cit. on p. 18).

Vogelpohl, C., Brandenbusch, C., Sadowski, G. (2013). High-pressure gas solubility in multicomponent solvent systems for hydroformylation. Part I: Carbon monoxide solubility. *The Journal of Supercritical Fluids* 81, 23–32. DOI: 10.1016/j.supflu.2013.04.006 (cit. on p. 95).

Vogelpohl, C., Brandenbusch, C., Sadowski, G. (2014). High-pressure gas solubility in multicomponent solvent systems for hydroformylation. Part II: Syngas solubility. *The Journal of Supercritical Fluids* 88, 74–84. DOI: 10.1016/j.supflu.2014.01.017 (cit. on p. 95).

Vyve, F. V., Renken, A. (1999). Hydroformylation in reverse micellar systems. *Catalysis Today* 48.1-4, 237–243. DOI: 10.1016/S0920-5861(98)00378-2 (cit. on p. 3).

Wächter, A. (2002). An Interior Point Algorithm for Large-Scale Nonlinear Optimization with Applications in Process Engineering. *phdthesis*. Carnegie Mellon University (cit. on pp. 119, 151, D-5).

Wallace, S. C., Thomas, J. K. (1973). Reactions in Micellar Systems. *Radiation Research* 54.1, 49. DOI: 10.2307/3573865 (cit. on p. 22).

Warmeling, H., Janz, D., Peters, M., Vorholt, A. (2017). Acceleration of lean aqueous hydroformylation in an innovative jet loop reactor concept. *Chemical Engineering Journal* 330, 585–595. DOI: 10.1016/j.cej.2017.07.152 (cit. on p. 2).

Webb, P. B., Sellin, M. F., Kunene, T. E., Williamson, S., Slawin, A. M. Z., Cole-Hamilton, D. J. (2003). Continuous Flow Hydroformylation of Alkenes in Supercritical Fluid-Ionic Liquid

Biphasic Systems. *Journal of the American Chemical Society* 125.50, 15577–15588. DOI: 10.1021/ja035967s (cit. on p. 2).

Weber, K. H. (2007). *Inbetriebnahme verfahrenstechnischer Anlagen*. Springer-Verlag GmbH. ISBN: 978-3-540-34317-2. URL: https://www.ebook.de/de/product/11428651/klaus_h_weber_inbetriebnahme_verfahrenstechnischer_anlagen.html (cit. on p. 145).

Weigert, J. (2017). Entwicklung einer modellgestützten Plattform zur integrierten Messdatenvalidierung und Zustandsschätzung für eine Anlage zur Hydroformylierung in Mikroemulsionen. *Master's Thesis*. Technische Universität Berlin (cit. on p. 123).

Weigert, J., Illner, M., Esche, E., Repke, J.-U. (2018). Development of a State Estimation Environment for the Optimal Control of a Mini-plant for the Hydroformylation in Microemulsions. In: *Chemical Engineering Transactions*. Vol. 70, 973–978 (cit. on pp. 39, 40, 116).

Wender, I., Metlin, S., Ergun, S., Sternberg, H. W., Greenfield, H. (1956). Kinetics and Mechanism of the Hydroformylation Reaction. The Effect of Olefin Structure on Rate1. *Journal of the American Chemical Society* 78.20, 5401–5405. DOI: 10.1021/ja01601a064 (cit. on pp. 47, 94).

Wiese, K.-D., Obst, D. (2006). Hydroformylation. In: *Topics in Organometallic Chemistry*. Springer Berlin Heidelberg. Chap. 1, 1–33. DOI: 10.1007/3418_015 (cit. on p. 2).

WIKA (2009). *Operating instructions N-10 Pressure transmitter - Version 2147614.07 GB/D/F/E 04/2009*. WIKA Alexander Wiegand SE & Co. KG (cit. on p. 73).

Wilkinson, G., Evans, D., Osborn, J. A. (1968). Hydroformylation of alkenes by use of rhodium complex catalysts. *Journal of the Chemical Society A: Inorganic, Physical, Theoretical*, 3133. DOI: 10.1039/J19680003133 (cit. on pp. 19, 21).

Wille, S. (2013). Modellierung von Verteilungskoeffizienten in mizellaren Systemen und Mikroemulsionen zur Optimierung von Reaktionssystemen. *PhD Thesis*. Universität Erlangen-Nürnberg (cit. on p. 16).

Winsor, P. A. (1956). *Solvent Properties of Amphiphilic Compounds*. Butherworth & Co. DOI: 10.1002/lipi.19560581222 (cit. on pp. 9, 12, 13).

Wodrich, M. D., Busch, M., Corminboeuf, C. (2018). Expedited Screening of Active and Regioselective Catalysts for the Hydroformylation Reaction. *Helvetica Chimica Acta* 101.9, e1800107. DOI: 10.1002/hlca.201800107 (cit. on p. 20).

Wolf, I. J., Marquardt, W. (2016). Fast NMPC schemes for regulatory and economic NMPC – A review. *Journal of Process Control* 44, 162–183. DOI: 10.1016/j.jprocont.2016.05.002 (cit. on p. 37).

Wozny, G., Wendeler, H. (2006). Fluidverfahrenstechnik. In: ed. by R. Goedecke. R. Goedecke. Chap. 2, 86–165 (cit. on p. 32).

Zagajewski, M., Behr, A., Sasse, P., Wittmann, J. (2014). Continuously operated miniplant for the rhodium catalyzed hydroformylation of 1-dodecene in a thermomorphic multicomponent solvent system (TMS). *Chemical Engineering Science* 115, 88–94. DOI: 10.1016/j.ces.2013.09.033 (cit. on p. 2).

Zavala, V. M. (2008). Computational Strategies for the Optimal Operation of Large-Scale Chemical Processes. *phdthesis*. Carnegie Mellon University (cit. on p. 37).

Zhang, Z., Chen, J. (2015). Correntropy based data reconciliation and gross error detection and identification for nonlinear dynamic processes. *Computers & Chemical Engineering* 75, 120–134. DOI: 10.1016/j.compchemeng.2015.01.005 (cit. on p. 42).

Appendix A
Supporting Information - System Analysis & Experimental Setups

A.1 Kinetic Investigations of the Hydroformylation of 1-dodecene in Microemulsions

Additional kinetic experiments for the hydroformylation of 1-dodecene in microemulsions are given. The experiments were performed by Tobias Pogrzeba, Technische Universität Berlin, Department of Chemistry. The data was partially already published alongside descriptions of the experimental set-up in our own contributions (Pogrzeba et al., 2017b; Pogrzeba et al., 2019).

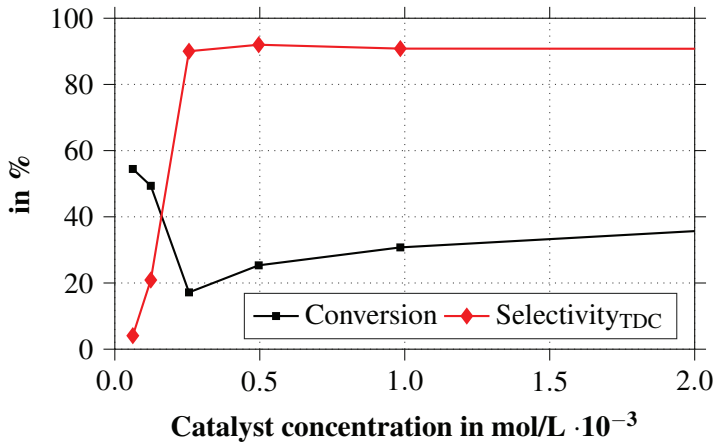

Fig. A.1: Influence of catalyst concentration on conversion and chemo selectivity towards the target product tridecanal for the hydroformylation of 1-dodecene. Experimental conditions: molar ratio SX:Rh 4:1, 2.4 mol L^{-1} 1-dodecene, 20 g water, 3.5 g Marlipal® 24/70, ($\alpha = 0.50$, $\gamma = 0.08$), 1 wt.-% Na_2SO_4, reaction volume = 50 mL. $p_R = 15$ bar syngas, $T_R = 95\,^{\circ}$C, stirrer speed = 1200 rpm, reaction duration: 4 h. Maximum error of analytical device: $\pm 3\,\%$.

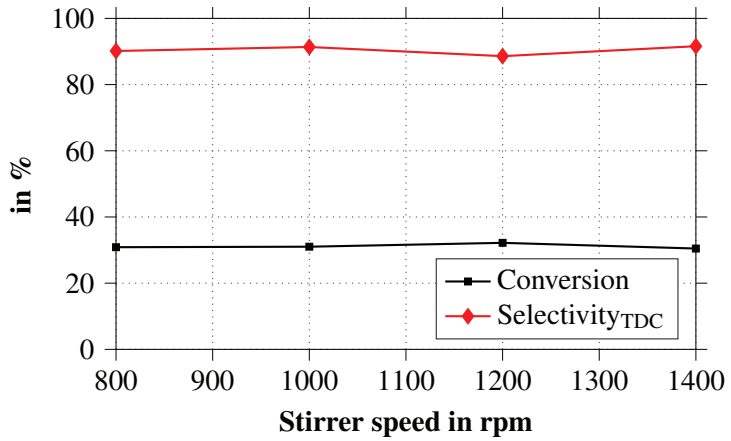

Fig. A.2: Influence of stirrer speed on conversion and chemo selectivity towards the target product tridecanal for the hydroformylation of 1-dodecene. Experimental conditions: Rh(acac)$(CO)_2$ = $1 \cdot 10^{-3}$ mol L^{-1}, molar ratio SX:Rh 4:1, 2.4 mol L^{-1} 1-dodecene, 20 g water, 3.5 g Marlipal® 24/70, ($\alpha = 0.50$, $\gamma = 0.08$), reaction volume = 50 mL. $p_R = 15$ bar syngas, $T_R = 95\,^{\circ}$C, reaction duration: 4 h. Maximum error of analytical device: $\pm 3\,\%$.

A.2 Experimental Procedures for the Systematic Phase Separation Analysis of the Microemulsion System

A.2.1 Setup and Procedure for Step 3 – Prescreening

Setup Glass Reactor

Experiments under elevated pressure and using synthesis gas are performed in a Parr Instruments® glass reactor of 450 mL volume. It is equipped with a gassing stirrer an heating jacket. The experimental setup is displayed in Fig. A.3. The respective experiments were partially performed in cooperation with Tobias Pogrzeba, Technische Universität Berlin, Department of Chemistry. Experimental investigation are conducted as follows:

1) The glass reactor is cleaned, inserted into its housing.
2) According the experimental plan, specified masses of 1-dodecene, tridecanal, Marlipal® 24/70, and aqueous catalyst are filled into the reactor.
3) After closing, the reactor is inertized and a final pressure test is conducted.
4) Without stirring, the thermostat is started and set to the desired temperature.
5) When reactor temperature is approaching its setpoint, the final pressure setpoint and respective gas composition is applied. Also the stirrer is activated.
6) If the temperature is stationary for 10 min, the stirrer is stopped and the camera simultaneously started to capture the phase level evolution in the vessel for 20 min.

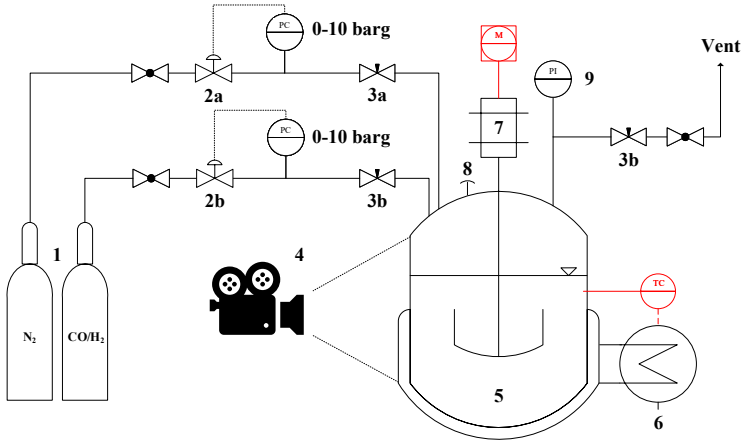

1 Gas containers
2 a/b Pressure regulators
3 a/b/c Needle valve
4 Camera system
5 Glass reactor
6 Thermostat with Pt100 sensor
7 Gassing stirrer and drive
8 Rupture disc
9 Pressure indicator

Fig. A.3: Experimental setup prescreening of the phase separation behavior. Glass reactor setup for tests including reaction and elevated pressure.

Setup Shake & Wait Experiments

Shake & Wait experiments are used as fast screening experiments. The experimental setup is displayed in Fig. A.4 and exploits fast screening in up to 8 test tubes, located in a water bath.

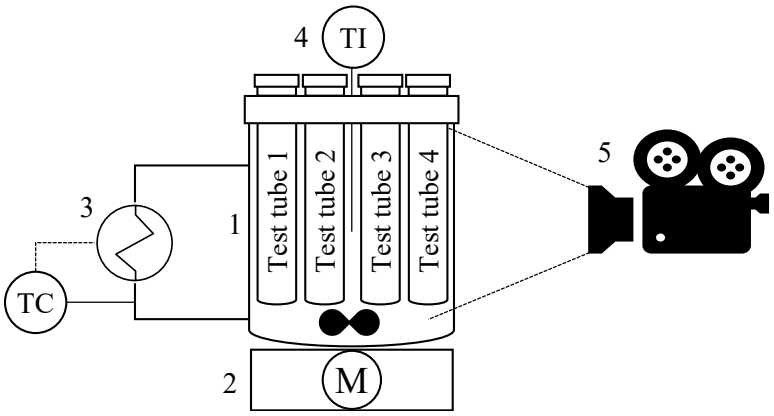

Fig. A.4: Experimental setup for Shake & Wait experiments. 1: thermostat bath glass vessel for up to 8 test tubes, 2: magnetic stirrer drive, 3: thermostat with internal temperature control, 4: Pt100 digital thermometer for temperature tracking, 5: camera for optical observation of the system.

The main screening procedure is then:

1) Prepare up to 8 test tubes with different microemulsion compositions in 20 mL vials.
2) Inertize and seal all vials and apply cover clamps.
3) After placing all test tubes in the water bath, thermostat and magnetic stirrer are started and a temperature setpoint is applied.

4) On stationary temperature, all test tubes are removed, vigorously shaken, and returned into the bath. The camera is simultaneously started to capture the phase level evolution in the test tubes for 20 min.

A.2.2 Setup and Procedure for Step 5 – Full System Mapping

All experiments for the full system mapping are carried out in small scale glass vessels of 25 and 40 mL, equipped with heating jacket and Pt100 temperature sensors. According to Fig. A.5, a magnetic stirrer drive is used for internal mixing of the samples and a thermostat with internal temperature control is used for heating of the samples. The procedure is then:

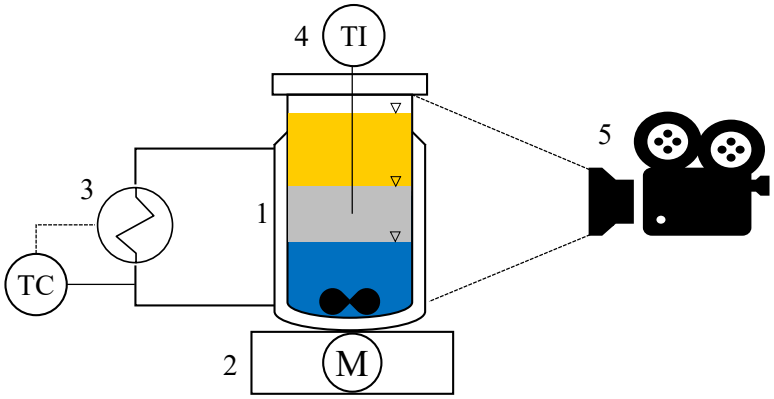

Fig. A.5: Experimental setup for the full factorial design phase separation mapping. 1: glass vessel with heating jacket, 2: magnetic stirrer, 3: thermostat with internal temperature control, 4: Pt100 digital thermometer for temperature tracking, 5: camera for optical observation.

1) 12 h before the experiment the aqueous catalyst solution is prepared.
2) Glass vessels are inertizes with nitrogen and closed with a cap including a septum.
3) According the experimental plan, specified masses of 1-dodecene, tridecanal, Marlipal® 24/70, and last the aqueous catalyst are filled into the vessel.
4) After adding a stirring bar, the mixture is carefully reinertized and the vessel closed tightly.
5) The glass vessel is positioned on the magnetic stirrer and connected to the thermostat.
6) The Pt100 temperature sensor is inserted into the mixture through the septum and a digital camera adjusted to correctly capture the phase level evolution in the glass vessel.
7) A temperature well below the three-phase region is set and the mixture stirred
8) If the temperature is stationary for 10 min, the stirrer is stopped and the camera simultaneously started to capture the phase level evolution in the vessel for 20 min.
9) Afterwards the temperature is increased by 1 K and stirrer activated.

10) The procedure is repeated from Step 8, till the upper boundary of the three-phase region is reached (vanishing oil phase or presence of dense surfactant layers).

The aim of this experimental procedure is to identify the location of the three phase region for each composition and accurately record the dynamic separation behavior and phase evolution at fixed temperatures. Captured movies are then converted into a series of images and evaluated using a Matlab®'s image processing toolbox to obtain time series of the relative phase volume fractions for each experimental setpoint. This information enables the development of a model for the desired three phasic separation of the microemulsion and a correlation of immeasurable surfactant concentrations to the phase state.

A.3 Experimental Results of the Systematic Phase Separation Analysis of the Microemulsion System

A.3.1 Analysis of Influence Factors on Separation Behavior

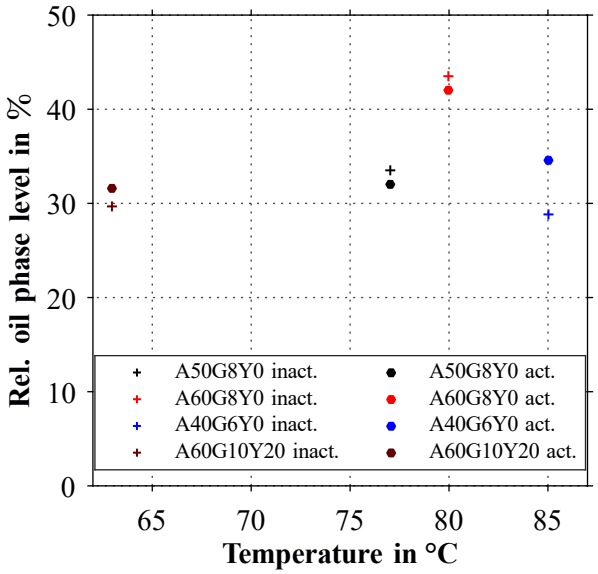

Fig. A.6: Comparison of oil phase levels with and without catalyst activation with syngas for different mixture compositions. Legend markers: A: α, G: γ, Y: Yield, with amount in wt.-%.

A.3.2 Experimental Plan and Results of Full System Mapping

Tab. A.1: Experimental plan and results of the full system mapping of the microemulsion system.

Concentration setpoint / %			**Concentration actual / %**			**Three phase region boundaries /** °C	
α	γ	Y	α	γ	Y	$\mathbf{T_l}$	$\mathbf{T_u}$
40.0	8.0	0.0	40.0	8.0	0.0	73.5	80.3
40.0	8.0	20.0	40.0	8.0	20.0	70.2	76.7
40.0	8.0	40.0	40.0	8.0	40.0	68.6	74.4
40.0	8.5	0.0	40.0	8.5	0.0	71.3	
40.0	8.5	20.0	40.0	8.7	20.0	65.6	69.6
40.0	8.5	40.0	40.0	8.6	40.0	63.9	68.1
40.0	9.0	0.0	40.0	9.1	0.0	72.0	77.9
40.0	9.0	20.0	39.9	9.0	20.0	68.1	74.4
40.0	9.0	40.0	40.0	9.0	40.0	65.8	72.7
40.0	9.5	0.0	40.0	9.6	0.0	70.2	75.0
40.0	9.5	20.0	39.9	9.6	20.0	66.3	71.1
40.0	9.5	40.0	40.0	9.6	40.0	62.7	67.8
50.0	6.0	0.0	50.0	6.0	0.0	83.3	91.6
50.0	6.0	20.0	50.0	6.0	19.9	78.8	87.8
50.0	6.5	0.0	50.0	6.5	0.0	76.8	85.1
50.0	6.5	20.0	50.0	6.6	19.9	72.1	78.2
50.0	6.5	40.0	50.0	6.4	40.2	74.8	
50.0	7.0	0.0	49.9	7.3	0.0	78.5	85.4
50.0	7.0	20.0	49.9	7.0	20.0	76.0	84.4
50.0	7.0	40.0	50.1	7.0	40.1		77.9
50.0	7.0	40.0	50.0	7.0	40.0	77.9	86.7
50.0	7.0	40.0	50.0	7.0	40.0	81.2	
50.0	7.0	40.0	50.0	7.0	40.0	74.2	81.9
50.0	7.5	0.0	49.9	7.8	0.0	74.7	80.5
50.0	7.5	20.0	49.9	7.5	20.0	68.6	73.2
50.0	7.5	40.0	50.1	7.3	40.1		74.6
50.0	7.5	40.0	50.0	7.7	40.0	67.1	72.0
50.0	8.0	0.0	50.0	8.0	0.0	73.9	81.8
50.0	8.0	20.0	49.1	7.9	20.0	72.1	80.7
50.0	8.0	40.0	50.0	8.1	40.1	71.2	79.4
50.0	8.0	40.0	50.0	8.0	40.0	72.3	80.5
50.0	8.5	0.0	50.0	8.5	0.0	73.0	77.9
50.0	8.5	20.0	49.1	8.5	20.0	68.8	74.1
50.0	8.5	40.0	50.0	8.5	40.0	65.5	74.0
50.0	8.5	40.0	50.0	8.7	40.1	64.9	71.9
50.0	9.0	0.0	50.0	9.0	0.0	73.1	77.0
50.0	9.0	20.0	50.0	9.0	20.0	69.2	72.1
50.0	9.0	40.0	49.2	9.0	40.0	68.1	74.9
50.0	9.5	0.0	50.0	9.6	0.0	71.0	74.9
50.0	9.5	20.0	50.0	9.5	20.0	67.7	71.1
50.0	9.5	40.0	49.2	9.5	40.0	65.1	70.0
60.0	6.0	0.0	60.0	6.0	0.0	82.9	
60.0	6.5	0.0	60.0	6.5	0.0	80.3	87.7
60.0	7.0	20.0	60.0	7.6	20.0	74.5	78.0
60.0	7.5	20.0	60.0	7.9	20.0	70.5	74.8
60.0	8.0	0.0	59.9	8.0	0.0	76.8	80.6
60.0	8.0	40.0	59.9	8.1	40.0	70.0	76.9
60.0	8.5	0.0	59.9	9.0	0.0	72.7	76.8
60.0	9.0	0.0	60.0	9.0	0.0	73.7	80.2
60.0	9.0	40.0	59.5	8.9	39.9	69.1	76.4
60.0	9.5	0.0	60.0	9.5	0.0	71.20	75.8
60.0	9.5	40.0	59.5	9.4	39.9	66.0	69.9

Appendix B
Supporting Information - Mini-plant & Analytics

B.1 Additional Information on Mini-Plant system

B.1.1 Geometries and Tank Volumes

Tab. B.2: Dimensions and volumes of mini-plant containers and piping systems.

Feed tanks B01-B03		**Buffer tank X04**	
Volume V	10.000 L	Volume V	0.260 L
Cross sectional area A	3.767 dm^2	Cross sectional area A	0.167 dm^2
Reactor C01[1]		**Recycle pipes**	
Volume V	1.500 L	Volume oil recycle V_{Rec}^{Oil}	0.096 L
Volume liquid V^{l}[2]	0.594 L	Volume emulsion recycle V_{Rec}^{Mid}	0.117 L
Cross sectional area A	0.554 dm^2	Volume water recycle V_{Rec}^{Water}	0.140 L
Level liquid L^{l}	1.072 dm	Volume mixed V_{Rec}^{Mix}	0.050 L
Settler X01		**Auxiliary tanks B04, B06**	
Volume V	0.449 L	Volume V	20.00 L
Diameter d	0.550 dm		
Level oil phase drain L^{Oil}	0.442 dm	**Total plant volume**	
Level emulsion phase drain L^{Mid}	0.215 dm	Total volume V^{tot}	2.35 L
Level water phase drain L^{Water}	0.129 dm	Total liquid volume $V^{tot,l}$	1.45 L

[1] Information from technical manual (Büchi AG, 2013)

[2] At 750 rpm stirrer speed

B.1.2 Semi-Automatized Reactor Sampling System - Design and Handling

The flow pattern of the sampling system is shown in the left diagram in Fig. B.7. Key component is a 6-way cross flow valve (element 3), in which pairs of inlets are connected to form the flow pattern (full and dashed line mark the possible valve positions). Starting with the fully empty system (1 bar nitrogen), the system is loaded with opening valve 1 and filled with fluid from the reactor, till a closed valve 5 (see blue lines left diagram). Due to pressure difference between reactor and sampling system, this filling is instantaneous. This way, the necessary dead volume of 9 mL(including then compressed N_2) is loaded in the dead volume loop between valve 3 and valve 5 and actual reactor sample is trapped in a 0.2 mL sample loop. Using nitrogen, the latter can be extracted into a vial using valve 4. Afterwards the dead volume is purged into a container using nitrogen and the system is depressurized.

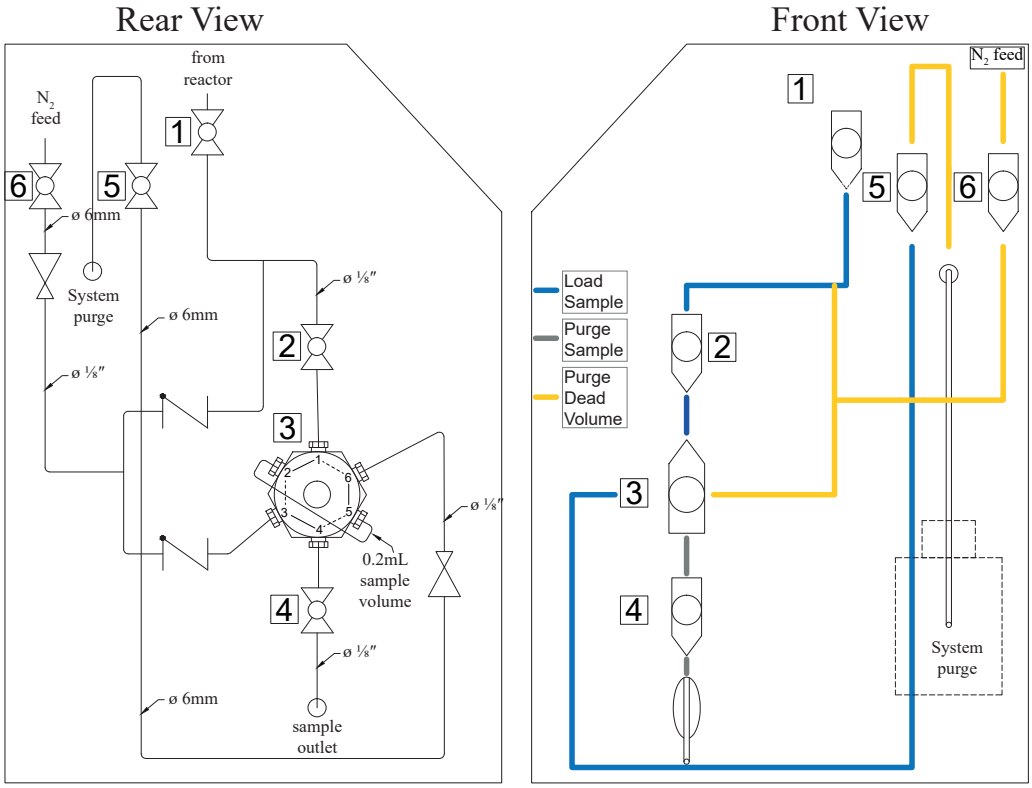

Fig. B.7: Semi-automatized sampling system for the reactor. Left: rear view with internal piping. Right: front view with operating elements and flow pattern.

B.1.3 Gas Purge Flow Pattern and Control for Mini-Plant System

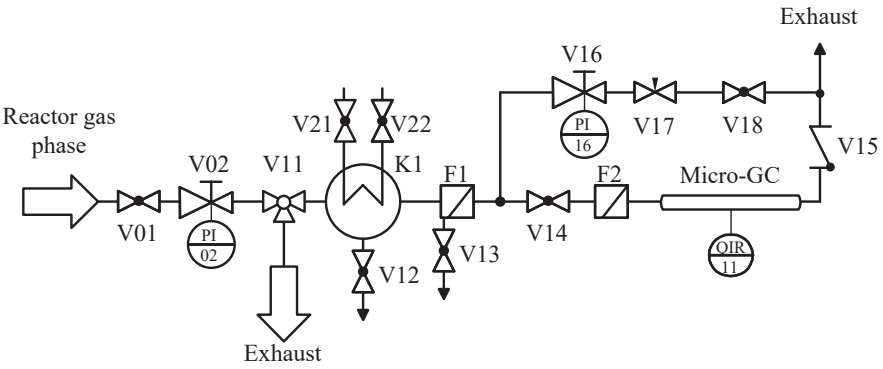

Fig. B.8: Integration of micro-GC into the mini-plant.

B.2 Additional Information Analytics & Experimental Methods

B.2.1 Gas Chromatography Analysis Method and Calibration Results

Gas Chromatography Calibration

Tab. B.3: GC calibration results with calibration factors P in wt.-% pA^{-1}, coefficient of determination R^2 in % and relative standard deviation STD in %. Iso-dodecene and iso-tridecanal are not available as analytical standards and are assumed to behave like the terminal molecule. Per calibration, 5 levels with triple determination were applied.

Compound	GC 7890A Oil Phase			GC HP 6890 Reactor phase			GC HP 6890 Water phase		
	P	R^2	STD	P	R^2	STD	P	R^2	STD
1-dodecene	$2.76 \cdot 10^{-3}$	99.7	0.30	$3.80 \cdot 10^{-3}$	99.8	1.97	$4.17 \cdot 10^{-3}$	99.9	1.20
iso-dodecene	$2.76 \cdot 10^{-3}$	99.7	0.32	$3.80 \cdot 10^{-3}$	99.8	1.90	$4.17 \cdot 10^{-3}$	99.9	1.94
Tridecanal	$3.41 \cdot 10^{-3}$	99.9	0.37	$4.16 \cdot 10^{-3}$	99.7	2.38	$5.33 \cdot 10^{-3}$	99.4	1.20
iso-tridecanal	$3.41 \cdot 10^{-3}$	99.9	0.37	$4.16 \cdot 10^{-3}$	99.7	2.38	$5.33 \cdot 10^{-3}$	99.4	1.20
Dodecane	$2.85 \cdot 10^{-3}$	99.9	0.36	$3.57 \cdot 10^{-3}$	99.9	2.24	$3.97 \cdot 10^{-3}$	88.7	1.50
Surfactant	$3.83 \cdot 10^{-2}$	61.6	54.2	$2.57 \cdot 10^{-1}$	25.7	-	-	-	-

Analysis Method

For both devices, a flame ionization detector operating at 300 °C and split/splitless injector working at 275 °C, 47.8 kPa, and 30:1 split ratio is used. The temperature program is set to 80 °C (3 min hold):10 °C min^{-1}:130 °C (2 min hold), 10 °C min^{-1}:150 °C (5 min hold), 35 °C min^{-1}:270 °C (9.5 min hold).

B.2.2 Gas Phase Gas Chromatography

The composition of the reactor gas phase is measured online using an ATEX zone 2 specified micro gas chromatograph Varian 490 GC. A Molsieve 5 Å column is used with argon as carrier gas. The implementation into the mini-plant is sketched in Fig. B.8. Gas phase from the reactor is first expanded to 2 bar using a pressure regulator. A condensation trap K1 and filter unit F1 are installed to separate condensable substances and particles to prevent damage to the GC or falsified results. A continuous gas phase purge of ≈10 g/h is enforced, from which the micro-GC draws samples. This way, the dead time between concentration changes in the reactor and its detection is kept low. The micro-GC was calibrated for the detection of the permanent gasses CO, H_2, N_2, and O_2 using two calibration levels (synthetic air, nitrogen, and syngas 1:1).

B.2.3 Pendant Drop Analysis for cmc Determination

For the determination of surfactant concentration dependent surface tensions ($\sigma - w^{Surfactant}$) via pendant drop initially several sampling solutions are prepared. Three general measurement series are prepared:

- pure 1-dodecene,
- 60mass.-% 1-dodecene and 40mass.-% tridecanal
- Water with 2wt.-% Na_2SO_4

To respective mixtures Marlipal 24/70 is added in known mass fractions. This way decadic dilution series are set up. Each sample is measured at three temperatures, whereby each experiment is repeated twice. Information on the experimental plan and concentration information can be obtained from Tab. C.20 - C.21.

B.2.4 Raman Calibration Test Stand with Reference Analytics

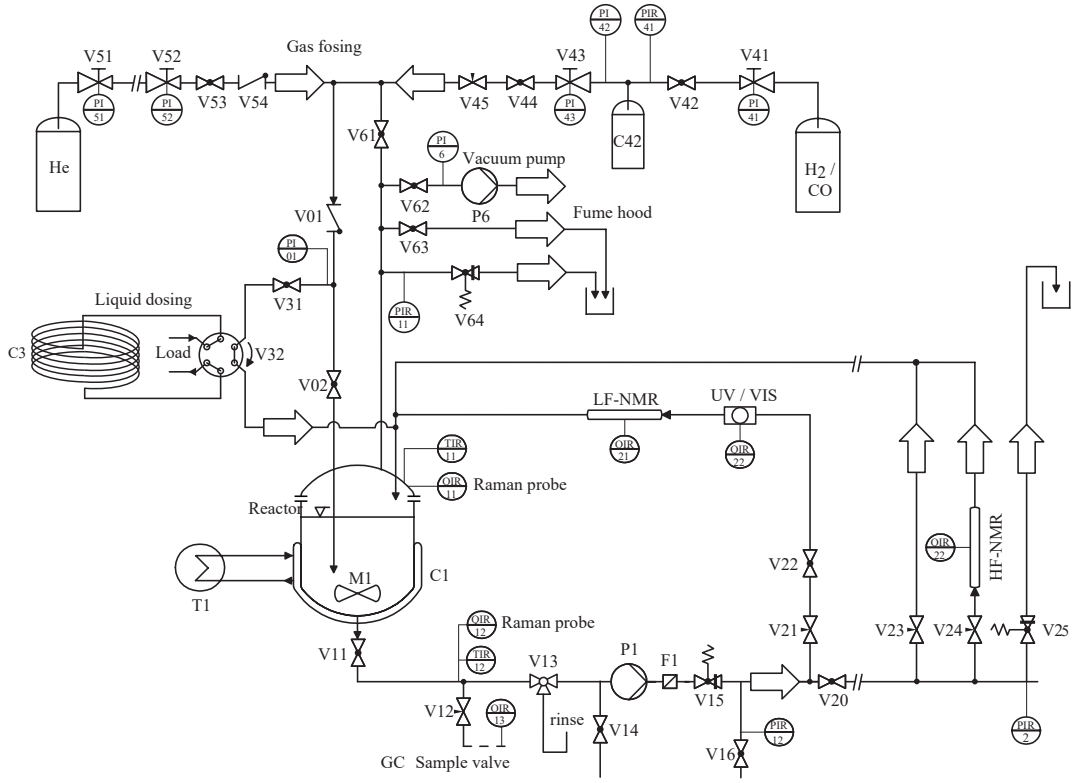

Fig. B.9: Calibration test stand for Raman spectroscopy, including various reference analytics.

B.3 Handling and Calculation of Measurement Errors

Within this thesis, measurement data from sensors or analytical devices is displayed together with information on respective measurement error, if available. Generally, the measurement error is shown as absolute standard deviation σ_i given the current measurement value using error bars. According to Tab. 4.1 information on measurement error is provided by sensor manufacturers in form of maximum sensor error according to the actual value. Throughout this work it is assumed that maximum error lie within the range of 3σ:

$$\sigma_i = \frac{max\ error}{3} \tag{B.1}$$

The calculation of the standard deviation of a variable Z, which is calculated by the already erroneous measurements x, y the Gaussian error propagation is applied. Here, the propagated error is obtained using the partial derivatives of Z regarding x and y and their respective errors. Using Eq. (B.2) this is done with applying the relative standard deviation of x and y to finally obtain $\bar{\sigma}_Z$:

$$\bar{\sigma}_Z = \sqrt{\left(\frac{\partial Z}{\partial x} \cdot \bar{\sigma}_x\right)^2 + \left(\frac{\partial Z}{\partial y} \cdot \bar{\sigma}_y\right)^2} \tag{B.2}$$

Appendix C
Supporting Information - Model Development & Optimal Process Control Strategies

C.1 Reformulations of Equations for Dynamic Models

Reformulations of equations used in (dynamic) process models are outlined and consequently applied on the derived mini-plant model in Sec. 4.3. Using these, common issues, such as occurring singularities, badly scaled Jacobians or indefinite Hessians are tackled. They are partly based on the suggestions by Esche et al. (2014).

Handling of singularities: A common issue for process models are divisions by zero due to roots in denominators $f_2(x) = 0$:

$$g(x) = \frac{f_1(x)}{f_2(x)} \qquad x \in \mathbb{R} \backslash 0 \tag{C.3}$$

To avoid this, several solutions are applied:

- Elimination of the fraction. This is suitable in case the relevant fraction is not part of a cascade of equations and can be handled separately:

$$f_2(x) \cdot g(x) = f_1(x) \qquad x \in \mathbb{R} \tag{C.4}$$

- In case this is not possible, the replacement of the fraction by a dummy variable is possible with the consequence of bloating the equation system

$$g(x) = f_3(x), \qquad f_2(x) \cdot f_3(x) = f_1(x) \tag{C.5}$$

- The combination of the smooth max(0,x) and min(x,0) operator can be deployed.

$$g(x) = \frac{f_1(x)}{max(min(f_2(x),\varepsilon),f_2(x))} \tag{C.6}$$

Root and power function approximations: Approximation of roots and power functions with noninteger exponents is useful, since values $\leq$ are not defined. The smooth max(0,x)-operator in Eq. (2.4) is deployed to enforce strictly positive arguments.

C.2 Dynamic Mini-Plant Model – Development and Formulations

Additional information on the mini-plant model is given regarding indexing, general and unit specific equation formulations

C.2.1 Indexing for the Dynamic Mini-Plant Model

Tab. C.4: Indexing of mini-plant units, specific hold-ups, and streams.

Unit	Index u	**Stream**	Index s
Feed tank 1-dodecene	1	Feed 1-dodecene	1
Feed tank catalyst solution	2	Feed catalyst solution	2
Feed tank surfactant	3	Feed surfactant	3
Feed pump 1-dodecene	4	Total recycle	4
Feed pump catalyst solution	5	Feed reactor	5
Feed pump surfactant	6	Gas feed reactor	6
Feed mixer	7	Gas purge reactor	7
Reactor - gas phase	8	Outlet reactor	8
Reactor - liquid phase	9	Split oil phase	9
Splitter phase separation	10	Split emulsion phase	10
Settler - oil phase	11	Split water phase	11
Settler - emulsion phase	12	Top outlet settler	12
Settler - water phase	13	Middle outlet settler	13
Buffer tank oil phase	14	Bottom outlet settler	14
Pipe volume emulsion phase	15	Outlet oil buffer tank	15
Pipe volume water phase	16	Oil phase recycle	16
Splitter oil phase	17	Emulsion phase recycle	17
Recycle pump oil phase	18	Water phase recycle	18
Recycle pump emulsion phase	19	Oil product	19
Recycle pump water phase	20		
Feed/recycle Mixer	21		
Product tank	22		

C.2.2 General Equation Definitions

At this point, reoccurring equations used within all parts of the model are presented once in a generic way. Firstly, sum relations are used on tank component hold-ups HU_u^{Phase} and component mass streams F_s:

$$HU_u^{Phase} = \sum_{i=1}^{Ni} HU_{u,i}^{Phase} \tag{C.7}$$

$$F_s = \sum_{i=1}^{Ni} F_{s,i} \tag{C.8}$$

The calculation of corresponding volumes and tank levels is done with Eq. (C.9). Component densities are calculated according Sec. 4.3.1. Liquid molar concentrations are derived from hold-up and volume variables:

$$V_u = A_u \cdot L_u = \sum_{i=1}^{Ni} \left(\frac{HU_{u,i}^{Phase}}{\rho_{u,i}}\right) \tag{C.9}$$

$$HU_{u,i}^{L} = A_u \cdot L_u \cdot M_i \cdot c_{u,i} \tag{C.10}$$

Mass fractions for hold-ups or streams are calculated using:

$$w_{u,i} \cdot HU_u^{Phase} = HU_{u,i}^{Phase} \tag{C.11}$$

$$w_{s,i} \cdot HU_u = F_{s,i} \tag{C.12}$$

C.2.3 Mass Balances Feed Section

$$\frac{\mathrm{d}HU_{u=1}^{L}}{\mathrm{d}t} = -F_{s=1} \qquad with\ u = s = \{1 \ldots 3\} \tag{C.13}$$

$$F_{s=5,i} = w_{s=1,i} \cdot F_{s=1} + w_{s=2,i} \cdot F_{s=2} + w_{s=3,i} \cdot F_{s=3} + F_{s=4,i} \tag{C.14}$$

$$\tag{C.15}$$

C.2.4 Development of an Adapted Kinetic Model

Additional information on the development of the adapted kinetic model for the hydroformylation in microemulsions is given. Especially applied kinetic datasets and parameter initials/ bounds are supplied for the performed parameter estimations of the initial and the adapted model.

Matlab framework

The Matlab implementation for parameter estimation on dynamic models includes several external packages. The *Hammersley Sequence Sampling* was carried out using the toolbox provided by John Burkardt: `https://people.sc.fsu.edu/ jburkardt/m_src/hammersley_dataset/hammersley_dataset.html`. An augmented version of the Matlab's *ode15s* is used for the calculation of the sensitivity matrix *S* for parameter sensitivity on the model states is used: `https://www.mathworks.com/matlabcentral/fileexchange/1480-sensitivity-analysis-for-odes-and-daes`

Additionally, following solver settings were used for *lsqnonlin*:

Code C.1: Solver options for lsqnonlin.

```
options = optimoptions(@lsqnonlin,...
'Algorithm','trustregion-reflective',...
'Diagnostics','on',...
'Display','iter-detailed',...
'DerivativeCheck','off',...
'FunValCheck','off',...
'Jacobian','off',...
'MaxFunEvals',20000,...
'MaxIter',1000,...
'TolFun',1e-10,...
'TolX',1e-10,...
'FinDiffRelStep', 7e-5, ...
'FinDiffType','forward');
```

C.2.4.1 Parameter Estimation on $Model_0$

Tab. C.5: Kinetic experiments used for parameter estimation of the initial reaction kinetics. Experimental controls T and p were kept constant and liquid sampling of reactants was carried out frequently (Data Points: sample amount).

No.	T °C	p bar	c_{Cat} g L^{-1}	LM -	m_{Surf} g	$m_{Dodecene}$ / g g	m_{tot} / g g	V mL	Data Points
1	68	15	0.26	4.00	3.50	20.00	43.45	49.94	9
2	72	15	0.26	3.94	3.50	20.00	43.51	50.00	9
3	75	15	0.27	3.85	3.50	20.00	43.54	50.03	9
4	80	15	0.26	4.01	3.50	20.00	43.49	49.98	9
5	85	15	0.25	4.08	3.51	20.02	43.54	50.03	9
6	90	15	0.26	3.93	3.51	20.01	43.70	50.02	8
7	95	15	0.26	4.01	3.50	20.00	43.59	50.08	9
8	95	15	0.26	4.04	3.50	20.00	43.50	49.99	9
9	95	15	0.25	4.12	3.52	19.99	43.72	49.98	8
10	95	15	0.26	3.90	3.50	20.00	43.67	49.99	7
11	95	15	0.26	3.90	3.50	20.00	43.67	49.99	7
12	95	15	0.26	3.90	3.50	20.00	43.67	49.99	7
13	95	15	0.26	3.90	3.50	20.00	43.67	49.99	7
14	95	15	0.26	3.90	3.50	20.00	43.67	49.99	3
15	95	15	0.26	3.90	3.50	20.00	43.67	49.99	3
16	95	15	0.26	3.90	3.50	20.00	43.67	49.99	3
17	95	15	0.26	3.90	3.50	20.00	43.67	49.99	3
18	95	15	0.25	4.12	3.52	19.99	43.55	49.98	9
19	95	15	0.26	3.91	3.52	20.02	43.76	50.09	8
20	95	15	0.25	4.12	3.52	19.99	43.72	49.98	8
21	95	15	0.12	4.03	3.50	20.00	43.58	49.98	5
22	95	15	0.52	3.99	3.50	20.00	43.83	49.98	5
23	95	20	0.26	4.10	3.50	20.58	44.11	50.60	9
24	100	15	0.26	4.00	3.51	20.00	43.51	50.00	9

Tab. C.6: Applied initial parameter values, lower (LB), and upper bound (UB) for the parameters parameter estimation of the initial reaction kinetics. The final set after parameter estimation is marked with **Final**.

Parameter	$\Delta G_{r=1}$ J/mol	$K_{cat,e=1}$ L/mol	$K_{r=1,e=1}$ L/mol	$K_{r=1,e=2}$ L/mol	$K_{r=3,e=1}$ L/mol	$K_{r=3,e=2}$ L/mol
Initial	$1.1 \cdot 10^{4}$	$1.4 \cdot 10^{4}$	$2.3 \cdot 10^{-3}$	$8.1 \cdot 10^{2}$	$1.4 \cdot 10^{-3}$	$2.5 \cdot 10^{4}$
LB	$1.1 \cdot 10^{-1}$	$1.0 \cdot 10^{-4}$	$3.9 \cdot 10^{-4}$	$2.3 \cdot 10^{-6}$	$2.7 \cdot 10^{-5}$	$7.1 \cdot 10^{-5}$
UB	$6.0 \cdot 10^{4}$	$1.0 \cdot 10^{6}$	$3.9 \cdot 10^{6}$	$2.3 \cdot 10^{7}$	$2.7 \cdot 10^{5}$	$7.1 \cdot 10^{5}$
Final	$3.7 \cdot 10^{0}$	$2.9 \cdot 10^{4}$	$2.1 \cdot 10^{-3}$	$2.3 \cdot 10^{3}$	$1.0 \cdot 10^{1}$	$2.4 \cdot 10^{4}$
Parameter	$K_{r=3,e=3}$ L/mol	$K_{r=5,e=1}$ L/mol	$K_{r=5,e=2}$ L/mol	$K_{r=5,e=3}$ L/mol	$k_{r=1}^{ref}$ L/(g h)	$k_{r=2}^{ref}$ $L^2/(g\,h\,mol)$
Initial	$6.3 \cdot 10^{-2}$	$7.9 \cdot 10^{-1}$	$5.6 \cdot 10^{3}$	$1.8 \cdot 10^{5}$	$7.1 \cdot 10^{0}$	$3.9 \cdot 10^{-4}$
LB	$1.3 \cdot 10^{-5}$	$5.8 \cdot 10^{-4}$	$3.0 \cdot 10^{-2}$	$1.2 \cdot 10^{-1}$	$7.0 \cdot 10^{-7}$	$7.0 \cdot 10^{-6}$
UB	$1.3 \cdot 10^{5}$	$5.8 \cdot 10^{7}$	$3.0 \cdot 10^{8}$	$1.2 \cdot 10^{9}$	$7.0 \cdot 10^{3}$	$7.0 \cdot 10^{4}$
Final	$3.3 \cdot 10^{0}$	$3.2 \cdot 10^{-1}$	$3.3 \cdot 10^{3}$	$1.1 \cdot 10^{5}$	$6.2 \cdot 10^{1}$	$4.6 \cdot 10^{0}$
Parameter	$k_{r=3}^{ref}$ $L^2/(g\,h\,mol)$	$k_{r=4}^{ref}$ $L^3/(g\,h\,mol^2)$	$k_{r=5}^{ref}$ $L^3/(g\,h\,mol^2)$	$k_{r=6}^{ref}$ $L^3/(g\,h\,mol^2)$	$K_{cat,e=2}$ -	$E_{r=1}$ J/mol
Initial	$1.7 \cdot 10^{3}$	$3.1 \cdot 10^{2}$	$1.7 \cdot 10^{7}$	$2.3 \cdot 10^{-4}$	$1.0 \cdot 10^{0}$	$1.4 \cdot 10^{5}$
LB	$1.4 \cdot 10^{-5}$	$6.0 \cdot 10^{-5}$	$5.0 \cdot 10^{-1}$	$6.0 \cdot 10^{-5}$	$1.0 \cdot 10^{-6}$	$1.4 \cdot 10^{3}$
UB	$1.4 \cdot 10^{7}$	$6.0 \cdot 10^{8}$	$5.0 \cdot 10^{9}$	$6.0 \cdot 10^{8}$	$1.0 \cdot 10^{3}$	$1.4 \cdot 10^{8}$
Final	$1.2 \cdot 10^{3}$	$5.4 \cdot 10^{2}$	$2.0 \cdot 10^{7}$	$3.7 \cdot 10^{-5}$	$1.2 \cdot 10^{2}$	$5.4 \cdot 10^{4}$
Parameter	$E_{r=2}$ J/mol	$E_{r=3}$ J/mol	$E_{r=4}$ J/mol	$E_{r=5}$ J/mol	$E_{r=6}$ J/mol	
Initial	$9.8 \cdot 10^{4}$	$7.8 \cdot 10^{4}$	$1.2 \cdot 10^{5}$	$7.3 \cdot 10^{4}$	$1.2 \cdot 10^{5}$	
LB	$1.0 \cdot 10^{3}$	$1.0 \cdot 10^{3}$	$1.0 \cdot 10^{3}$	$1.0 \cdot 10^{3}$	$1.0 \cdot 10^{3}$	
UB	$1.0 \cdot 10^{8}$	$1.0 \cdot 10^{8}$	$1.0 \cdot 10^{8}$	$1.0 \cdot 10^{8}$	$1.0 \cdot 10^{8}$	
Final	$1.4 \cdot 10^{5}$	$8.8 \cdot 10^{4}$	$9.9 \cdot 10^{4}$	$6.5 \cdot 10^{4}$	$1.7 \cdot 10^{6}$	

C.2.4.2 Parameter Estimation on $Model_{real}$

Tab. C.7: Kinetic experiments used for parameter estimation of the adapted reaction kinetics. Experimental controls T and p were kept constant and liquid sampling of reactants was carried out frequently (Data Points: sample amount).

No.	T °C	p bar	c_{Cat} g L^{-1}	LM -	m_{Surf} g	$m_{Dodecene}$ / g g	m_{tot} / g g	V mL	Data Points
1	68.00	15.00	0.26	4.00	3.50	20.00	43.45	49.94	9
2	85.00	15.00	0.25	4.08	3.51	20.02	43.54	50.03	9
3	85.00	15.00	0.26	4.03	3.50	20.00	43.68	50.00	3
4	90.00	15.00	0.26	3.93	3.51	20.01	43.70	50.02	8
5	95.00	15.00	0.52	4.00	3.50	20.00	43.83	49.98	5
6	95.00	15.00	0.13	4.03	3.50	20.00	43.57	49.98	5
7	95.00	15.00	0.26	4.01	3.50	20.00	43.59	50.08	9
8	95.00	15.00	0.26	4.04	3.50	20.00	43.50	49.99	9
9	95.00	15.00	0.25	4.12	3.52	19.99	43.72	49.98	8
10	95.00	15.00	0.26	3.90	3.50	20.00	43.67	49.99	7
11	95.00	15.00	0.26	3.90	3.50	20.00	43.67	49.99	7
12	95.00	15.00	0.26	3.90	3.50	20.00	43.67	49.99	7
13	95.00	15.00	0.26	3.90	3.50	20.00	43.67	49.99	7
14	95.00	15.00	0.26	3.90	3.50	20.00	43.67	49.99	3
15	95.00	15.00	0.26	3.90	3.50	20.00	43.67	49.99	3
16	95.00	15.00	0.26	3.90	3.50	20.00	43.67	49.99	3
17	95.00	15.00	0.26	3.90	3.50	20.00	43.67	49.99	3
18	95.00	15.00	0.25	4.12	3.52	19.99	43.55	49.98	9
19	95.00	15.00	0.28	4.00	0.41	20.02	40.60	46.77	5
20	95.00	15.00	0.27	4.01	0.81	20.03	41.01	47.21	5
21	95.00	15.00	0.27	3.98	1.67	20.00	41.84	48.07	5
22	95.00	15.00	0.26	4.00	2.55	20.00	42.72	48.99	5
23	95.00	15.00	0.26	3.91	3.52	20.02	43.76	50.09	8
24	95.00	15.00	0.25	4.00	4.45	20.00	44.62	50.99	5
25	95.00	15.00	0.24	4.00	7.06	20.00	47.23	53.73	5
26	95.00	15.00	0.26	2.00	3.50	20.00	43.59	49.99	5
27	95.00	15.00	0.26	3.00	3.50	20.00	43.63	49.99	5
28	95.00	15.00	0.25	4.12	3.52	19.99	43.72	49.98	8
29	95.00	15.00	0.27	4.78	3.49	20.06	43.76	50.06	8
30	95.00	15.00	0.26	6.08	3.50	19.93	43.68	49.90	8
31	95.00	15.00	0.25	7.14	3.52	20.00	43.86	50.06	8
32	95.00	15.00	0.27	7.68	3.49	20.03	43.85	50.02	8
33	95	20	0.26	4.10	3.50	20.58	44.11	50.60	9
34	100.00	15.00	0.26	4.00	3.51	20.00	43.51	50.00	9

Tab. C.8: Applied initial parameter values, lower (LB), and upper bound (UB) for the parameter estimation of the adapted reaction kinetics $Model_{real}$.

Parameter	$\Delta G_{r=1}$ J/mol	$K_{cat,e=1}$ L/mol	$K_{r=1,e=1}$ L/mol	$K_{r=1,e=2}$ L/mol	$K_{r=3,e=1}$ L/mol	$K_{r=3,e=2}$ L/mol
Initial	$5.0 \cdot 10^{4}$	$1.5 \cdot 10^{4}$	$3.0 \cdot 10^{-1}$	$5.0 \cdot 10^{-4}$	$1.5 \cdot 10^{0}$	$3.3 \cdot 10^{4}$
LB	$1.1 \cdot 10^{-1}$	$3.0 \cdot 10^{-4}$	$4.0 \cdot 10^{-4}$	$2.0 \cdot 10^{-6}$	$3.0 \cdot 10^{-5}$	$7.0 \cdot 10^{-5}$
UB	$6.0 \cdot 10^{4}$	$3.0 \cdot 10^{6}$	$4.0 \cdot 10^{6}$	$2.0 \cdot 10^{7}$	$3.0 \cdot 10^{5}$	$7.0 \cdot 10^{5}$
Parameter	$K_{r=3,e=3}$ L/mol	$K_{r=5,e=1}$ L/mol	$K_{r=5,e=2}$ L/mol	$K_{r=5,e=3}$ L/mol	$k_{r=1}^{ref}$ L/(g h)	$k_{r=2}^{ref}$ $L^2/(g\,h\,mol)$
Initial	$2.8 \cdot 10^{-4}$	$6.8 \cdot 10^{-3}$	$6.6 \cdot 10^{2}$	$2.3 \cdot 10^{4}$	$5.7 \cdot 10^{-1}$	$2.6 \cdot 10^{1}$
LB	$1.0 \cdot 10^{-5}$	$5.0 \cdot 10^{-3}$	$3.0 \cdot 10^{-2}$	$1.0 \cdot 10^{-1}$	$5.0 \cdot 10^{-7}$	$3.0 \cdot 10^{-6}$
UB	$1.0 \cdot 10^{5}$	$5.0 \cdot 10^{7}$	$3.0 \cdot 10^{8}$	$1.0 \cdot 10^{9}$	$5.0 \cdot 10^{3}$	$3.0 \cdot 10^{4}$
Parameter	$k_{r=3}^{ref}$ $L^2/(g\,h\,mol)$	$k_{r=4}^{ref}$ $L^3/(g\,h\,mol^2)$	$k_{r=5}^{ref}$ $L^3/(g\,h\,mol^2)$	$k_{r=6}^{ref}$ $L^3/(g\,h\,mol^2)$	$p_{r=1}^{trig}$ -	$p_{r=5}^{trig}$ -
Initial	$1.1 \cdot 10^{3}$	$3.3 \cdot 10^{3}$	$1.2 \cdot 10^{7}$	$6.3 \cdot 10^{-4}$	$1.2 \cdot 10^{1}$	$8.5 \cdot 10^{0}$
LB	$3.0 \cdot 10^{-3}$	$4.0 \cdot 10^{-7}$	$5.0 \cdot 10^{-1}$	$4.0 \cdot 10^{-6}$	$1.0 \cdot 10^{0}$	$1.0 \cdot 10^{0}$
UB	$3.0 \cdot 10^{7}$	$4.0 \cdot 10^{5}$	$5.0 \cdot 10^{9}$	$4.0 \cdot 10^{4}$	$1.0 \cdot 10^{2}$	$1.0 \cdot 10^{2}$
Parameter	K^{LM} -	$k_{r=1}^{LM}$ -	$k_{r=5}^{LM}$ -	$n^{Surfactant}$ -	$K_{cat,e=2}$ -	$E_{r=1}$ J/mol
Initial	$2.7 \cdot 10^{0}$	$6.0 \cdot 10^{1}$	$1.1 \cdot 10^{0}$	$1.1 \cdot 10^{0}$	$1.0 \cdot 10^{0}$	$1.4 \cdot 10^{5}$
LB	$2.0 \cdot 10^{0}$	$1.0 \cdot 10^{0}$	$1.0 \cdot 10^{0}$	$1.0 \cdot 10^{-6}$	$1.0 \cdot 10^{-3}$	$1.0 \cdot 10^{3}$
UB	$3.0 \cdot 10^{0}$	$8.0 \cdot 10^{1}$	$1.0 \cdot 10^{1}$	$1.1 \cdot 10^{0}$	$1.0 \cdot 10^{5}$	$1.0 \cdot 10^{8}$
Parameter	$E_{r=2}$ J/mol	$E_{r=3}$ J/mol	$E_{r=4}$ J/mol	$E_{r=5}$ J/mol	$E_{r=6}$ J/mol	
Initial	$1.0 \cdot 10^{5}$	$7.6 \cdot 10^{4}$	$1.2 \cdot 10^{5}$	$9.8 \cdot 10^{4}$	$1.3 \cdot 10^{5}$	
LB	$1.0 \cdot 10^{3}$	$1.0 \cdot 10^{3}$	$1.0 \cdot 10^{3}$	$1.0 \cdot 10^{3}$	$1.0 \cdot 10^{3}$	
UB	$1.0 \cdot 10^{8}$	$1.0 \cdot 10^{8}$	$1.0 \cdot 10^{8}$	$1.0 \cdot 10^{8}$	$1.0 \cdot 10^{8}$	

Tab. C.9: Final parameters for the adapted kinetic model of the hydroformylation in microemulsions. **SsS** denotes the final identifiable parameter set with 1: active for estimation and identifiable, 0: fixed parameter.

Parameter	$\Delta G_{r=1}$ J/mol	$K_{cat,e=1}$ L/mol	$K_{r=1,e=1}$ L/mol	$K_{r=1,e=2}$ L/mol	$K_{r=3,e=1}$ L/mol	$K_{r=3,e=2}$ L/mol
Value	$3.82 \cdot 10^{4}$	$4.51 \cdot 10^{4}$	$7.28 \cdot 10^{-1}$	$4.05 \cdot 10^{-5}$	$4.78 \cdot 10^{-1}$	$1.33 \cdot 10^{4}$
SsS	0	1	0	0	0	0
Parameter	$K_{r=3,e=3}$ L/mol	$K_{r=5,e=1}$ L/mol	$K_{r=5,e=2}$ L/mol	$K_{r=5,e=3}$ L/mol	$k_{r=1}^{ref}$ L/(g h)	$k_{r=2}^{ref}$ $L^2/(g\,h\,mol)$
Value	$1.03 \cdot 10^{3}$	$2.33 \cdot 10^{-2}$	$8.95 \cdot 10^{2}$	$4.42 \cdot 10^{4}$	$4.24 \cdot 10^{0}$	$5.60 \cdot 10^{-3}$
SsS	0	0	1	0	0	0
Parameter	$k_{r=3}^{ref}$ $L^2/(g\,h\,mol)$	$k_{r=4}^{ref}$ $L^3/(g\,h\,mol^2)$	$k_{r=5}^{ref}$ $L^3/(g\,h\,mol^2)$	$k_{r=6}^{ref}$ $L^3/(g\,h\,mol^2)$	$p_{r=1}^{trig}$ -	$p_{r=5}^{trig}$ -
Value	$1.74 \cdot 10^{4}$	$1.54 \cdot 10^{4}$	$9.95 \cdot 10^{7}$	$1.10 \cdot 10^{-2}$	$1.43 \cdot 10^{1}$	$1.13 \cdot 10^{1}$
SsS	0	0	0	0	0	0
Parameter	K^{LM} -	$k_{r=1}^{LM}$ -	$k_{r=5}^{LM}$ -	$n^{Surfactant}$ -	$K_{cat,e=2}$ -	$E_{r=1}$ J/mol
Value	$2.73 \cdot 10^{0}$	$6.69 \cdot 10^{1}$	$1.05 \cdot 10^{0}$	$1.03 \cdot 10^{0}$	$1.89 \cdot 10^{2}$	$4.08 \cdot 10^{4}$
SsS	0	1	0	0	0	0
Parameter	$E_{r=2}$ J/mol	$E_{r=3}$ J/mol	$E_{r=4}$ J/mol	$E_{r=5}$ J/mol	$E_{r=6}$ J/mol	
Value	$6.29 \cdot 10^{3}$	$1.05 \cdot 10^{5}$	$1.07 \cdot 10^{5}$	$5.79 \cdot 10^{4}$	$3.24 \cdot 10^{4}$	
SsS	0	0	0	0	0	

C.2.5 Gas Solubility Data and Model Parameters

Tab. C.10: Collected gas solubility data for CO for the microemulsion system. Data taken from the Master's Thesis in (Bardas, 2015).

Exp. No.	p bar	T °C	x $\% \cdot 10$	**Exp. No.**	p bar	T °C	x $\% \cdot 10$	**Exp. No.**	p bar	T °C	x $\% \cdot 10$
1	13.06	85.68	1.8654	2	22.5	85.07	3.6698	7	20.36	84.37	2.903
1	22.41	85.42	3.5464	2	14.96	94.81	2.4844	7	13.99	104.84	1.934
1	13.03	105.18	2.0269	2	22.38	94.94	3.8373	7	21.76	105.04	3.225
1	21.87	105.09	3.707	2	12.3	104.76	1.8372	8	31	84.89	3.462
4	12.7	84.15	1.725	2	21.9	104.98	3.9967	8	16.36	84.38	1.434
4	20.7	84.32	3.136	2	12.22	104.69	1.8547	8	23.5	84.56	2.349
4	12.63	95.39	1.774	2	21.89	104.88	3.9823	8	10.83	104.83	0.803
4	21.47	94.81	3.461	3	12.9	84.69	1.7807	8	17.61	104.96	1.634
4	12.66	104.73	1.822	3	24.03	84.47	3.8397	8	20.21	105.15	1.92
4	21.1	104.82	3.395	3	20.47	85.35	3.4261	8	25.16	104.85	2.548
5	13.37	85.3	1.924	3	7	85.2	0.6848	9	21.09	84.82	1.925
5	22.64	85.68	3.468	3	10.18	84.32	1.2415	9	14.38	105.53	1.335
5	12.33	84.82	1.86	3	14.92	84.33	2.0199	9	21.51	105.5	2.186
5	22.09	84.65	3.437	3	19.78	85.42	3.1297	10	15.3	84.89	3.887
5	14.53	94.37	2.073	3	29.62	84.63	4.9951	10	22.24	85.05	5.701
5	21.69	94.66	3.422	3	15.61	104.45	2.1296	10	14.09	104.35	3.395
5	15.49	104.72	2.056	3	21.67	104.67	3.3651	10	18.41	105.43	4.542
5	23.17	104.72	3.398	6	9.88	84.18	1.234	10	26.98	104.8	6
5	14.96	105	2.056	6	12.76	84.53	1.667	11	15.85	84.85	3.265
5	25.28	104.97	3.829	6	19.34	84.18	2.764	11	20.83	84.99	4.52
2	10.17	85.35	1.4241	6	13.71	105.39	1.947	11	14.62	105.14	3.037
2	22.19	85.39	3.635	6	21.33	105.45	3.357	11	21.96	104.97	4.747
2	42.3	85.45	7.3744	7	20.37	84.77	2.923				
2	10.49	84.98	1.4414	7	13.92	84.46	1.82				

Tab. C.11: Collected gas solubility data for syngas for the microemulsion system. Data taken from the Master's Thesis in (Bardas, 2015).

Exp. No.	p bar	T °C	x $\% \cdot 10$	**Exp. No.**	p bar	T °C	x $\% \cdot 10$	**Exp. No.**	p bar	T °C	x $\% \cdot 10$
1	12.71	85.06	1.422	4	22.28	104.15	2.848	6	20.45	104.73	2.431
1	22.36	85.02	2.762	4	12.22	104.82	1.363	7	12.09	85.01	1.153
1	12.9	84.71	1.487	4	22.6	104.85	2.849	7	21.39	85.07	2.287
1	22.27	84.64	2.83	2	10.85	85.2	1.228	7	12.09	104.72	1.293
1	12.72	85.46	1.347	2	14.55	104.33	1.913	7	21.13	104.93	2.489
1	21.88	85.45	2.612	2	21.84	104.24	2.978	9	12.48	85	0.938
4	12.69	85.08	1.379	6	12.85	85.47	1.346	9	22.3	85.06	1.834
4	22.15	84.3	2.645	6	20.4	85.52	2.365	9	13.86	104.75	1.018
4	10.87	104.58	1.204	6	12.88	104.68	1.411	9	22.84	104.31	1.887

Tab. C.12: Set of estimated model parameters for the gas solubility of CO and syngas in the microemulsion system fitted to the experimental data in Tab. C.11,Tab. C.10. **i=6** marks parameters used for calculating H_2 solubility from syngas data, **i=7** marks CO solubility. Final *RSME* of the least squares parameters estimation problem: $1.711 \cdot 10^{-4}$ for CO, $6.025 \cdot 10^{-5}$ for syngas.

Parameter	$P_{i,Sol=1}$	$P_{i,Sol=1}$	$P_{i,Sol=1}$	$P_{i,Sol=1}$	$P_{i,Sol=1}$
i=6	$-1.7718 \cdot 10^{-4}$	$1.7692 \cdot 10^{-5}$	$1.6934 \cdot 10^{-3}$	$-4.7302 \cdot 10^{-2}$	$4.3746 \cdot 10^{-4}$
i=7	$-6.4909 \cdot 10^{-5}$	$1.1885 \cdot 10^{-5}$	$1.0631 \cdot 10^{-3}$	$-2.7378 \cdot 10^{-2}$	$1.7599 \cdot 10^{-4}$
Parameter	$P_{i,Sol=6}$	$P_{i,Sol=7}$	$P_{i,Sol=8}$	$P_{i,Sol=9}$	$P_{i,Sol=10}$
i=6	$2.8638 \cdot 10^{-1}$	$1.5920 \cdot 10^{-3}$	$-1.7107 \cdot 10^{-7}$	$6.5328 \cdot 10^{-4}$	$5.3043 \cdot 10^{-4}$
i=7	$1.7476 \cdot 10^{-1}$	$9.2954 \cdot 10^{-4}$	$2.8881 \cdot 10^{-7}$	$2.9467 \cdot 10^{-4}$	$3.7274 \cdot 10^{-4}$
Parameter	$P_{i,Sol=11}$	$P_{i,Sol=12}$	$P_{i,Sol=13}$	$P_{i,Sol=14}$	$P_{i,Sol=15}$
i=6	$-7.2990 \cdot 10^{-6}$	$-1.4868 \cdot 10^{-5}$	$-3.0261 \cdot 10^{-5}$	$-1.2455 \cdot 10^{-5}$	$-1.1598 \cdot 10^{-4}$
i=7	$-4.1033 \cdot 10^{-5}$	$-9.9645 \cdot 10^{-6}$	$-3.8368 \cdot 10^{-5}$	$-6.9782 \cdot 10^{-6}$	$-8.2558 \cdot 10^{-5}$

C.2.6 Phase Separation Model and Settler

This section lists additional information on experimental data used for the development of the phase separation model, as well as the relevant parameter data obtained from parameter estimations. All data sets calculations are part of this work and have not been used elsewhere.

C.2.6.1 Phase Volume Fraction Model and Concentration Soft-Sensor

Temperature boundary model

Tab. C.13: Set of estimated model parameters for the temperature lower and upper limits Tl^{PhS}, Th^{PhS} of the three phase separation region fitted to experimental data. Final *RSME* of the least squares parameters estimation problem: 0.0153 for Tl^{PhS}, 0.0233 for Th^{PhS}.

Parameter	$P_{ps=1}^{Th/Tl,PhS}$	$P_{ps=2}^{Th/Tl,PhS}$	$P_{ps=3}^{Th/Tl,PhS}$	$P_{ps=4}^{Th/Tl,PhS}$	$P_{ps=5}^{Th/Tl,PhS}$
Th^{PhS}	1.0941	0.6654	-0.8914	-0.0592	-0.1839
Tl^{PhS}	0.8539	0.7439	-0.6604	-0.0216	-0.2412
Parameter	$P_{ps=6}^{Th/Tl,PhS}$	$P_{ps=7}^{Th/Tl,PhS}$	$P_{ps=8}^{Th/Tl,PhS}$	$P_{ps=9}^{Th/Tl,PhS}$	$P_{ps=10}^{Th/Tl,PhS}$
Th^{PhS}	-0.5121	0.3213	-0.3921	0.4019	0.5449
Tl^{PhS}	-0.4107	0.1716	-0.3769	0.3525	0.3837

Phase volume fraction model

Tab. C.14: Set of estimated model parameters for the phase volume fraction Φ^{Oil}, Φ^{Water} of the three phase separation region fitted to experimental data.

Parameter	$P_{ps=1}^{PhS,Oil/Water}$	$P_{ps=2}^{PhS,Oil/Water}$	$P_{ps=3}^{PhS,Oil/Water}$	$P_{ps=4}^{PhS,Oil/Water}$	$P_{ps=5}^{PhS,Oil/Water}$
Φ^{Oil}	-7.4938	8.8434	4.4609	7.9676	0.9389
Φ^{Water}	-1.7570	5.3831	1.7334	-2.3790	-0.4232
Parameter	$P_{ps=6}^{PhS,Oil/Water}$	$P_{ps=7}^{PhS,Oil/Water}$	$P_{ps=8}^{PhS,Oil/Water}$	$P_{ps=9}^{PhS,Oil/Water}$	$P_{ps=10}^{PhS,Oil/Water}$
Φ^{Oil}	-3.5048	-1.0631	-1.5553	-6.0463	-0.5099
Φ^{Water}	-3.2052	-0.5111	1.3168	2.4748	-0.5457
Parameter	$P_{ps=11}^{PhS,Oil/Water}$	$P_{ps=12}^{PhS,Oil/Water}$	$P_{ps=13}^{PhS,Oil/Water}$	$P_{ps=14}^{PhS,Oil/Water}$	*RSME*
Φ^{Oil}	-1.4631	0.1149	-2.0622	1.5102	0.055
Φ^{Water}	-2.6417	0.5308	0.4389	-0.3685	0.042

C.2.6.2 Settler Volume Surrogate Model Formulation

The trigonometric equation for the volume of a horizontal cylinder is given in Eq. (C.16). The solution of this equation causes numerical instabilities and multiple possible solutions are present due to the arccos function. Hence, a higher order polynomial surrogate is provided in Eq. (C.17).

$$V^{Settler}\left(L^{Settler}\right) = l^{Settler}\frac{d^{Settler\,2}}{2}\arccos\left(\frac{d^{Settler}-2L^{Settler}}{d^{Settler}}\right) - l^{Settler}\left(\frac{d^{Settler}}{2}-L^{Settler}\right)\sqrt{d^{Settler}L^{Settler}(L^{Settler})^2} \tag{C.16}$$

$$L_{Settler}^{Correlation} = 2.3652\cdot V_u - 16.6506\cdot V_u^2 + 94.6100\cdot V_u^3 - 284.1938\cdot V_u^4 + 424.8202\cdot V_u^5 - 246.1395\cdot V_u^6 \tag{C.17}$$

C.2.6.3 Model of Excess Phase Composition – Estimated Model Parameters

Tab. C.15: Model parameters for the polynomial surrogate model for the excess phase composition using $x_{s=9}^{PhS,Water}$, $x_{s=11}^{PhS,Water}$. Parameters fitted LLE data calculated using the γ-γ approach and UNIFAC as g^E model.

Parameter	$P_{ps=1}^{Conc,Oil/Water}$	$P_{ps=2}^{Conc,Oil/Water}$	$P_{ps=3}^{Conc,Oil/Water}$	$P_{ps=4}^{Conc,Oil/Water}$
$x_{s=9}^{PhS,Water}$	$-3.229\cdot10^{-5}$	$2.279\cdot10^{-1}$	$-1.063\cdot10^{-3}$	$2.497\cdot10^{-7}$
$x_{s=11}^{PhS,Water}$	$4.179\cdot10^{-8}$	$-1.913\cdot10^{-5}$	$1.526\cdot10^{-7}$	$-7.487\cdot10^{-11}$
Parameter	$P_{ps=5}^{Conc,Oil/Water}$	$P_{ps=6}^{Conc,Oil/Water}$	$P_{ps=7}^{Conc,Oil/Water}$	*RSME*
$x_{s=9}^{PhS,Water}$	$2.290\cdot10^{-4}$	$1.079\cdot10^{-6}$	$1.009\cdot10^{-3}$	$2.349\cdot10^{-4}$
$x_{s=11}^{PhS,Water}$	$-3.666\cdot10^{-9}$	$-3.065\cdot10^{-10}$	$1.000\cdot10^{0}$	$2.611\cdot10^{-8}$

C.2.6.4 Model of Excess Phase Composition – UNIFAC Parameters

UNIFAC parameters for the specified component system. The model formulation is done according the given equations in (Gmehling et al., 1992, p. 246 sqq).

Tab. C.16: v_{ik}: number of structural groups of type k in molecule i.

	Structural group	H_2O	CH_3	CH_2	CH_2=CH	CHO
Compound	v_{ik}	$k=1$	$k=2$	$k=3$	$k=4$	$k=5$
H_2O	$i=1$	1	0	0	0	0
$C_{12}H_{24}$	$i=2$	0	1	9	1	0
$C_{13}H_{26}O$	$i=3$	0	1	11	0	1

Tab. C.17: Relative van der Waals values for the present structural groups considering the UNIFAC model; taken from (Gmehling et al., 1992, p. 251).

Structural group	Main group	Sub group	Index	R_k	Q_k
H_2O	7	17	$k=1$	0,92	1,4
CH_3	1	1	$k=2$	0,9011	0,848
CH_2	1	2	$k=3$	0,6744	0,54
CH_2=CH	2	5	$k=4$	1,3454	1,176
CHO	10	21	$k=5$	0,998	0,948

Tab. C.18: a_{nm}: interaction parameter for pair structural group n and structural group m; taken from (Gmehling et al., 1992, p. 253).

Structural group	Structural group a_{nm} in K	H_2O $m=1$	CH_3 $m=2$	CH_2 $m=3$	CH_2=CH $m=4$	CHO $m=5$
H_2O	$n=1$	0	300	300	496,1	-257,3
CH_3	$n=2$	1318	0	0	86,02	677
CH_2	$n=3$	1318	0	0	86,02	677
CH_2=CH	$n=4$	270,6	-35,36	-35,36	0	448,75
CHO	$n=5$	232,7	505,7	505,7	56,3	0

C.2.6.5 Model of Excess Phase Composition – cmc Measurements

Tab. C.19: Experimental conditions and results on surface tension measurement for a simulated oily excess phase with tridecanal. w_{Surf}: mass fraction of Marlipal® 24/70.

w^{Marl} mass − %	θ °C	$\sigma_{m=1}$ mN/m	$\sigma_{m=2}$ mN/m	$\sigma_{m=3}$ mN/m	$\sigma_{m=4}$ mN/m	$\bar{\sigma}$ mN/m
0.0	59.80	24.659	24.535	24.470	X	**24.555**
0.0001018	59.80	24.481	24.351	24.307	X	**24.380**
0.001008	59.80	23.970	24.002	24.097	X	**24.023**
0.005013	59.80	23.874	23.811	23.767	X	**23.817**
0.010020	59.80	X	X	X	X	**X**
0.0997	59.80	23.792	23.835	23.758	X	**23.795**
0.995	59.80	23.533	23.648	23.615	X	**23.599**
2.066	59.80	23.642	23.606	23.640	X	**23.629**
4.985	59.80	23.613	23.613	23.629	X	**23.618**
0.0	69.60	23.633	23.552	23.675	23.589	**23.612**
0.0001018	69.60	23.561	23.428	23.421	X	**23.470**
0.001008	69.60	23.290	23.189	23.243	X	**23.241**
0.005013	69.60	23.092	23.087	23.100	X	**23.093**
0.010020	69.60	X	X	X	X	**X**
0.0997	69.60	X	X	X	X	**X**
0.995	69.60	22.912	22.868	22.892	X	**22.891**
2.066	69.60	22.912	22.873	22.886	X	**22.890**
4.985	69.60	22.882	22.870	22.896	X	**22.883**
0.0	80.00	22.689	22.671	22.729	22.704	**22.698**
0.0001018	80.00	22.641	22.564	22.589	X	**22.598**
0.001008	80.00	22.498	22.502	22.482	X	**22.494**
0.005013	80.00	22.416	22.402	22.430	X	**22.416**
0.010020	80.00	X	X	X	X	**X**
0.0997	80.00	X	X	X	X	**X**
0.995	80.00	22.361	22.350	22.349	X	**22.353**
2.066	80.00	22.361	22.325	22.356	X	**22.347**
4.985	80.00	22.363	22.356	22.360	X	**22.360**

Tab. C.20: Experimental conditions and results on surface tension measurement for a simulated oily excess phase without tridecanal. w_{Surf}: mass fraction of Marlipal® 24/70.

w^{Surf} mass − %	θ °C	$\sigma_{m=1}$ mN/m	$\sigma_{m=2}$ mN/m	$\sigma_{m=3}$ mN/m	$\sigma_{m=4}$ mN/m	$\bar{\sigma}$ mN/m
0.0	60.05	24.486	24.548	24.661	24.596	**24.573**
0.000111	60.05	24.284	24.245	24.290	X	**24.273**
0.001120	60.05	23.641	23.672	23.704	X	**23.672**
0.011300	60.05	23.334	23.206	23.277	X	**23.272**
0.051400	60.05	23.194	23.165	23.170	X	**23.176**
0.113	60.05	23.114	23.180	23.212	X	**23.169**
0.514	60.05	X	X	X	X	**X**
1.006	60.05	23.176	23.153	23.140	X	**23.156**
2.020	60.05	X	X	X	X	**X**
5.041	60.05	23.097	23.179	23.175	X	**23.150**
0.0	70.15	22.939	22.893	22.857	22.848	**22.884**
0.000111	70.15	22.671	22.706	22.678	X	**22.685**
0.001120	70.15	22.527	22.576	22.540	X	**22.548**
0.011300	70.15	22.455	22.424	22.434	X	**22.438**
0.051400	70.15	22.305	22.313	22.286	X	**22.301**
0.113	70.15	22.317	22.304	22.313	X	**22.311**
0.514	70.15	X	X	X	X	**X**
1.006	70.15	22.272	22.293	22.294	X	**22.286**
2.020	70.15	X	X	X	X	**X**
5.041	70.15	22.303	22.293	22.300	X	**22.299**
0.0	80.05	21.948	21.981	21.937	21.957	**21.956**
0.000111	80.05	21.861	21.840	21.905	X	**21.869**
0.001120	80.05	21.781	21.756	21.770	X	**21.769**
0.011300	80.05	21.670	21.712	21.685	X	**21.689**
0.051400	80.05	21.602	21.598	21.597	X	**21.599**
0.113	80.05	21.599	21.611	21.602	X	**21.604**
0.514	80.05	X	X	X	X	**X**
1.006	80.05	21.589	21.590	21.582	X	**21.587**
2.020	80.05	X	X	X	X	**X**
5.041	80.05	21.632	21.620	21.595	X	**21.616**

Tab. C.21: Experimental conditions and results on surface tension measurement for a simulated aqueous excess phase. w_{Surf}: mass fraction of Marlipal® 24/70.

w_{Surf} mass $-$ %	θ °C	$\sigma_{m=1}$ mN/m	$\sigma_{m=2}$ mN/m	$\sigma_{m=3}$ mN/m	$\bar{\sigma}$ mN/m
0.0	60.35	68.959	68.906	68.971	**68.945**
0.00000001069	60.35	68.811	68.564	68.537	**68.637**
0.0000001074	60.35	66.649	66.177	66.456	**66.427**
0.000001068	60.35	68.266	67.659	68.428	**68.118**
0.00001070	60.35	68.444	68.364	68.540	**68.449**
0.0001072	60.35	66.406	66.665	66.602	**66.558**
0.001063	60.35	27.743	27.488	28.157	**27.796**
0.01067	60.35	27.858	27.818	27.775	**27.817**
0.1073	60.35	27.703	27.697	27.594	**27.665**
0.992	60.35	27.873	27.776	27.671	**27.773**
0.0	69.45	67.481	67.322	67.497	**67.433**
0.00000001069	69.45	X	X	X	**X**
0.0000001074	69.45	X	X	X	**X**
0.000001068	69.45	X	X	X	**X**
0.00001070	69.45	66.276	66.376	66.261	**66.304**
0.0001072	69.45	65.494	65.829	65.602	**65.642**
0.001063	69.45	27.079	27.258	27.542	**27.293**
0.01067	69.45	27.474	27.774	27.423	**27.557**
0.1073	69.45	X	X	X	**X**
0.992	69.45	27.682	27.417	27.270	**27.456**
0.0	80.00	65.766	65.214	65.131	**65.370**
0.00000001069	80.00	X	X	X	**X**
0.0000001074	80.00	X	X	X	**X**
0.000001068	80.00	65.786	66.147	65.704	**65.879**
0.00001070	80.00	65.391	65.248	65.535	**65.391**
0.0001072	80.00	63.818	63.869	63.699	**63.795**
0.001063	80.00	27.130	27.388	27.539	**27.352**
0.01067	80.00	X	X	X	**X**
0.1073	80.00	X	X	X	**X**
0.992	80.00	27.107	26.828	26.803	**26.913**
0.0	25.10	73.087	72.865	73.041	**72.998**
0.00000001069	25.10	X	X	X	**X**
0.0000001074	25.10	X	X	X	**X**
0.000001068	25.10	X	X	X	**X**
0.00001070	25.10	73.455	73.520	73.506	**73.494**
0.0001072	25.10	72.436	72.672	72.679	**72.596**
0.001063	25.10	42.377	45.108	46.948	**44.811**
0.01067	25.10	29.975	30.571	30.179	**30.242**
0.1073	25.10	X	X	X	**X**
0.992	25.10	29.105	29.219	29.171	**29.165**

C.2.6.6 Model of Excess Phase Composition – Back Calculation on Full Set of Model Concentrations

The concentration information of the excess phase sub model for cmc and LLE is subsequently transformed into the domain of the mini-plant model, using the following correlations:

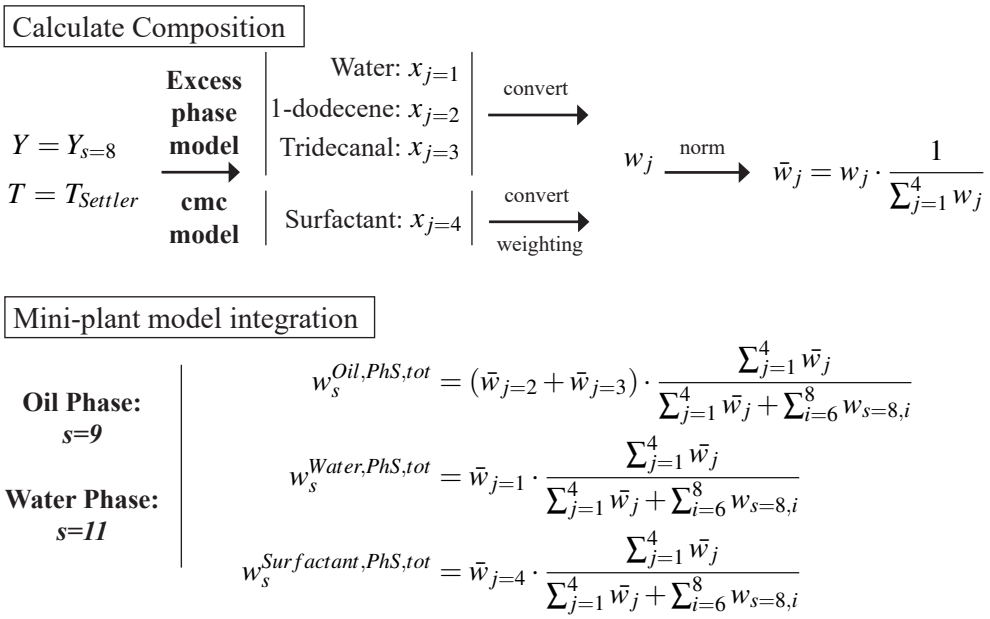

Fig. C.10: Normalization of concentrations obtained from the excess phase model and integration into the mini-plant model.

Using the correlation shown in Fig. 4.24, the cmc for idealized pure phases of 1-dodecene, tridecanal, and water is calculated. These data are then weighted with respective actual amounts of 1-dodecene, tridecanal, and water derived from LLE calculations to obtain an approximation of the cmc of the excess phases within the MES. Afterwards, this surfactant mass fraction $w_{j=4}$ is combined with the corresponding excess phase mass fractions $w_{j=1...3}$ to normalized mass fractions $\bar{w}_j$ to enforce summation to 1. These are then transformed into the relevant concentrations measures for the general mini-plant model, whereby again a normalization is performed to account for the mass fractions of dissolved gasses $w_{s=8,i=6...8}$. Note, that due to simplicity the latter are assumed to be equal to the values found in the reactor.

C.2.7 Recycle and Product Section – Additional Equations

Outlet streams virtual tanks

Outlet streams for the virtual tanks are set up according to the overflow stream concept in Sec. 4.3.1. In case of the buffer tank X04 this is slightly adapted, since the virtual pipe volume is included into this unit. Thus, two level setpoints exist for this unit. $L^{SP}_{U=14}$ is used to specify the level representing the oil recycle pipe volume. Once X04 is filled to this point, trigger $TRIG^{Lvl,Pipe}_{u=14}$ is activated and oil recycle pump operation is possible via the model-wise implemented setpoint stream F^{Oil}_{Rec}:

$$F_{s=16} = F^{Oil}_{Rec} \cdot TRIG^{Lvl,Pipe}_{u=14} \tag{C.18}$$

$$F_{s=17} = F^{Lvl}_{u=15} \tag{C.19}$$

$$F_{s=18} = F^{Lvl}_{u=16} \tag{C.20}$$

Mass balances product tank and recycle mi

$$\frac{\mathrm{d}HU^{L}_{u=22,i}}{\mathrm{d}t} = F_{s=19,i} \tag{C.21}$$

$$F_{s=4,i} = F_{s=16,i} + F_{s=17,i} + F_{s=18,i} \tag{C.22}$$

C.3 Dynamic Mini-Plant Model – Additional Information

Additional information on the mini-plant model is given regarding applied parameters, controls, fluid properties, and design variables.

C.3.1 Fluid Properties Information for Mini-Plant Model

Tab. C.22: Parameters for density correlations of liquids and gasses. Liquid density parameters are estimated for fixed pressure of 15 bar. *: parameters for Marlipal® 24/70 are estimated from its pure substance analogon octaethylene glycol monododecyl ether ($C_{12}E_8$). Component index provided in Tab. 4.4.

Compound i	a_i	b_i	c_i	d_i	e_i	Reference
Liquid						
1, 2	2.2849	0.6276	471.5315	0.8054		(AspenProperties V10, 2019)
4	2.2849	0.6276	471.5315	0.8054		(AspenProperties V10, 2019)
3, 5	0.1069	0.1457	748.4016	0.1976		(AspenProperties V10, 2019)
9-11	0.0515	0.0294	455.3277	0.0188		(AspenProperties V10, 2019)
12*	0.1200	0.2330	857.6999	0.3103		(AspenProperties V10, 2019)
Gaseous						
6	0.2895	−0.0017	0.0698	$2.450\cdot10^{-6}$	$-1.016\cdot10^{-4}$	(NIST, 2019b)
7	0.3096	−0.0018	0.0722	$2.683\cdot10^{-6}$	$-1.076\cdot10^{-4}$	(NIST, 2019a)
8	0.3068	−0.0018	0.0719	$2.650\cdot10^{-6}$	$-1.067\cdot10^{-4}$	(NIST, 2019c)

C.3.2 Mini-Plant Model - Parameters, Design Variables, and Controls

Tab. C.23: Feed tank composition for mini-plant model.

Alkene feed $w_{s=1,i}$							
$i=1$	0.96	$i=2$	0.04	$i=3$	0.00	$i=4$	0.00
$i=5$	0.00	$i=6$	0.00	$i=7$	0.00	$i=8$	0.00
$i=9$	0.00	$i=10$	0.00	$i=11$	0.00	$i=12$	0.00
Catalyst feed $w_{s=2,i}$							
$i=1$	0.00	$i=2$	0.00	$i=3$	0.00	$i=4$	0.00
$i=5$	0.00	$i=6$	0.00	$i=7$	0.00	$i=8$	0.00
$i=9$	0.989501	$i=10$	0.000648	$i=11$	0.009851	$i=12$	0.00
Surfactant feed $w_{s=3,i}$							
$i=1$	0.00	$i=2$	0.00	$i=3$	0.00	$i=4$	0.00
$i=5$	0.00	$i=6$	0.00	$i=7$	0.00	$i=8$	0.00
$i=9$	0.00	$i=10$	0.00	$i=11$	0.00	$i=12$	1.00

Tab. C.24: Controller and trigger parameters.

Controller Parameters		**Trigger Parameters**	
$KP_{u=8}$	1350 g/dmh	$\varepsilon_{u=9}$	10^{-10} -
$KP_{u=9}$	5350 g/dmh	$\varepsilon_{u=11}$	10^{-10} -
$KI_{u=8}$	1200 g/dmh^2	$\varepsilon_{u=13}$	10^{-10} -
$KI_{u=9}$	2200 g/dmh^2	$\varepsilon_{u=14}$	10^{-10} -
$KP_{Settler}$	0 g/dmh	$\varepsilon_{u=15}$	10^{-10} -
$KI_{Settler}$	500000 g/dmh^2	$\varepsilon_{u=16}$	10^{-10} -
$KP_{u=14}$	500000 g/dmh	ε_{Feed}	10^{-10} -
$KP_{u=15}$	500000 g/dmh	$\varepsilon_{Settler}$	10^{-10} -
$KP_{u=16}$	500000 g/dmh	ε_{Rec}	10^{-10} -
$KI_{u=14}$	5317 g/dmh^2	$P^{trig}_{u=9}$	1 -
$KI_{u=15}$	5317 g/dmh^2	$P^{trig}_{u=14}$	10 -
$KI_{u=15}$	5500 g/dmh^2	$P^{trig}_{u=15}$	10 -
$Slack^{Control}_{u=9}$	10^{-5} -	$P^{trig}_{u=16}$	10 -
$Slack^{Control}_{u=9}$	10^{-5} -	P^{trig}_{Feed}	5000 -
$Slack^{Control}_{u=14}$	10^{-5} -	P^{trig}_{Rec}	5000 -
$Slack^{Control}_{u=15}$	10^{-5} -	$P^{PhS,trig}_{Settler}$	5000 -
$Slack^{Control}_{u=16}$	10^{-5} -	$P^{trig}_{Settler}$	500000 -

Tab. C.25: Design variables for volumes and setpoint level.

Feed and product tanks		**Plant Filling**	
$A_{u=1...3}$	3.7668 dm	$V^{SP,tot}_{Settler}$	0.44851
$A_{u=22}$	3.7668 dm	$V^{SP,tot}_{Rec}$	0.40311
Reactor			
$V^{Reactor}$	1.1731	$L^{SP}_{u=9}$	1.0018 dm
$Slack^{Lvl}_{u=9}$	0.07 -	$A_{u=9}$	0.5542 dm
Settler		**Recycle**	
$L^{SP,tot}_{Settler}$	0.4423 dm	$L^{SP}_{u=14}$	0.7137 dm
$L^{Oil,SP}_{u=11}$	0.03 dm	$L^{Lvl}_{max,u=14}$	1.7878 dm
$L^{Mix,SP}_{u=11}$	0.2349 dm	$L^{SP}_{u=15}$	0.8399 dm
$L^{Water,SP}_{u=11}$	0.3238 dm	$L^{SP}_{u=16}$	0.9510 dm
$L^{Oil,SP}_{u=13}$	0.44 dm	$Slack^{Lvl,Pipe}_{u=14}$	0.1 -
$L^{Mix,SP}_{u=13}$	0.2147 dm	$Slack^{Lvl,Pipe}_{u=15}$	0.1 -
$L^{Water,SP}_{u=13}$	0.1285 dm	$Slack^{Lvl,Pipe}_{u=16}$	0.1 -
$Slack^{Lvl}_{Settler}$	0.02 -	$A_{u=14}$	0.1438 dm
		$A_{u=15}$	0.1438 dm
		$A_{u=16}$	0.1438 dm

C.4 Optimal Operation Strategies: State Estimation and Dynamic Optimization

C.4.1 Orthogonal Collocation

Applied Radau roots for orthogonal polynoms

$$\{\tau_0;\tau_1;\tau_2;\tau_3\} = \{0{,}000000;0{,}155051;0{,}644949;1{,}000000\} \tag{C.23}$$

Discretization of function $x(t)$ with $t \in [t_0,t_{max}]$:

$$x|_{\tau_i} = a_i \tag{C.24}$$

$$\dot{x}|_{\tau_i} = \left(\sum_{j=0}^{K} a_j \cdot \frac{\partial l_j}{\partial \tau}|_{\tau_i}\right) \cdot \left(\frac{1}{t_{max}-t_0}\right) \tag{C.25}$$

Matrix of first derivatives of Langrangian polynoms using Radau roots:

$$\begin{aligned} \partial L_{JI} &= \begin{bmatrix} \frac{\partial l_0}{\partial \tau}|_{\tau_0} & \cdots & \frac{\partial l_3}{\partial \tau}|_{\tau_0} \\ \vdots & \ddots & \vdots \\ \frac{\partial l_0}{\partial \tau}|_{\tau_3} & \cdots & \frac{\partial l_3}{\partial \tau}|_{\tau_3} \end{bmatrix} \\ &= \begin{bmatrix} -9{,}0000010080 & 10{,}0488101064 & -1{,}3821424037 & 0{,}3333333053 \\ -4{,}1393887736 & 3{,}2247461916 & 1{,}1678398419 & -0{,}2531972599 \\ 1{,}7393879671 & -3{,}5678400771 & 0{,}7752546483 & 1{,}0531974615 \\ -3{,}0000002520 & 5{,}5319724150 & -7{,}5319723310 & 5{,}0000001680 \end{bmatrix} \end{aligned} \tag{C.26}$$

C.4.2 Multi-Rate State Estimation

C.4.2.1 Analysis of Available Measurements and measurability analysis

In the following, available measurements of the mini-plant and their applicability for state estimation are discussed.

- **Level measurements:** Available for feed tanks, X04, product tank, and all settler phases via soft-sensor. Very low variances are obtained.
- **Temperature measurements:** Reactor $T_{u=9}$ and settler temperature $T_{Settler}$ are fixed as parameters in the model. The former is assumed to be ideally controlled by the base

automation. $T_{Settler}$ is varied for plant operations and might deviate from the mean temperature in the major separation zone of the settler. It is thus applicable as manipulable variable for state estimation.

- **Pressure measurements:** Pressure measurements are available at high accuracy. It is assumed that pressure is ideally controlled and is not part of the state estimation.
- **Flow measurements:** The usefulness of flow measurements is severely limited, since applied coriolis flow-meters show unreliable behavior applied to the MES (see Fig. C.11). This is especially true for recycle streams. Pure substance feed streams are reliable at higher flow rates, which however are only applied at plant start-up. Only the oil phase product stream $F_{s=19}$ and the total recycle stream $F_{s=4}$ are considered as available measurements for state estimation.
- **Concentration measurements reactor gas-phase:** A fixed reactor gas feed composition is enforced by a gas purge. Respective model states are thus fixed as parameters.
- **Concentration measurements:** Liquid phase concentration measurements are infrequently available for reactor, settler oil phase, and water phase. However, only 1-/iso-dodecene, n-/iso-tridecanal, and dodecane are measurable with acceptable deviations.

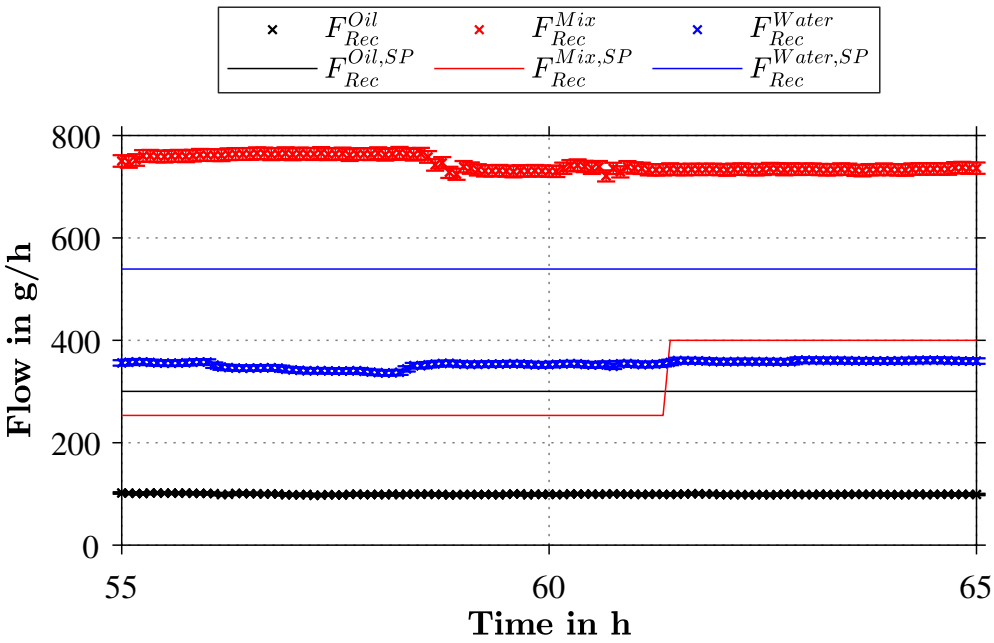

Fig. C.11: Comparison of recycle stream measurements from a mini-plant campaign and respective setpoint values calculated from the applied pump frequency.Error bars given according to sensor specifications.

C.4.2.2 Analysis of Measurability

Tab. C.26: Approximation of the sensitivity of model states on model measurements $\left|\frac{\delta y}{\delta x}\right|$ based on model simulations. Values < 0.001 are excluded. Gray overlay indicates vanishing influence of model states on all measurements. Light-gray overlay indicated sensitivity only on slow concentration measurements.

Variables at t_0	F_{x19}	L_{u11}^{Oil}	L_{u13}^{Water}	L_{u1}	L_{u2}	L_{u3}	L_{u14}	L_{u22}	$w_{u11,i1}^{Oil}$	$w_{u11,i2}^{Oil}$	$w_{u11,i3}^{Oil}$	$w_{u11,i4}^{Oil}$	$w_{u11,i5}^{Oil}$	$w_{s8,i1}$	$w_{s8,i2}$	$w_{s8,i3}$	$w_{s8,i4}$	$w_{s8,i5}$	$w_{u13,i1}^{Water}$	$w_{u13,i2}^{Water}$	$w_{u13,i3}^{Water}$	$w_{u13,i4}^{Water}$	$w_{u13,i5}^{Water}$
$HU_{u11,i1}^{L,Oil}$	0.111							0.094	0.152	0.440	0.437	0.439	0.441	0.009	0.025	0.023	0.024	0.025	0.002	0.007	0.006	0.007	0.007
$HU_{u11,i2}^{L,Oil}$									0.004	0.607	0.004	0.004	0.004		0.031					0.004			
$HU_{u11,i3}^{L,Oil}$											0.607					0.030					0.004		
$HU_{u11,i4}^{L,Oil}$												0.609					0.030					0.004	
$HU_{u11,i5}^{L,Oil}$	0.031							0.028	0.148	0.147	0.146	0.147	0.458	0.008	0.008	0.007	0.007	0.024	0.001	0.002	0.002	0.002	0.006
$HU_{u11,i6}^{L,Oil}$	0.063							0.004															
$HU_{u11,i7}^{L,Oil}$	0.076							0.004															
$HU_{u11,i8}^{L,Oil}$																							
$HU_{u11,i9}^{L,Oil}$									0.001	0.001	0.001	0.001	0.001										
$HU_{u11,i10}^{L,Oil}$																							
$HU_{u11,i11}^{L,Oil}$																							
$HU_{u11,i12}^{L,Oil}$																							
$HU_{u12,i1}^{L,Mix}$	0.074	0.283	0.007					0.044		0.002			0.002	0.016	0.007	0.007	0.007	0.007	0.001	0.004	0.004	0.004	0.004
$HU_{u12,i2}^{L,Mix}$		0.003								0.004					0.023					0.003			
$HU_{u12,i3}^{L,Mix}$											0.004					0.023					0.003		
$HU_{u12,i4}^{L,Mix}$												0.004					0.023					0.003	
$HU_{u12,i5}^{L,Mix}$	0.015	0.083	0.002					0.013	0.001				0.003	0.002	0.002	0.002	0.002	0.021	0.001	0.001	0.001	0.001	0.004
$HU_{u12,i6}^{L,Mix}$	0.104	0.032						0.004															
$HU_{u12,i7}^{L,Mix}$	0.125	0.039						0.005															
$HU_{u12,i8}^{L,Mix}$																							
$HU_{u12,i9}^{L,Mix}$	0.094	0.337	0.007					0.052		0.001	0.004	0.003		0.009	0.009	0.009	0.009	0.009					
$HU_{u12,i10}^{L,Mix}$																							
$HU_{u12,i11}^{L,Mix}$		0.003																					
$HU_{u12,i12}^{L,Mix}$	0.038	0.214	0.023					0.021						0.004	0.002	0.002	0.002	0.003					
$HU_{u13,i1}^{L,Water}$																			0.657				
$HU_{u13,i2}^{L,Water}$																				0.655			
$HU_{u13,i3}^{L,Water}$																					0.651		
$HU_{u13,i4}^{L,Water}$																						0.652	
$HU_{u13,i5}^{L,Water}$																							0.656
$HU_{u13,i6}^{L,Water}$	0.039	0.017	0.020					0.003						0.002	0.002	0.002	0.002	0.002					
$HU_{u13,i7}^{L,Water}$	0.047	0.021	0.024					0.004						0.002	0.002	0.002	0.002	0.002					
$HU_{u13,i8}^{L,Water}$																							
$HU_{u13,i9}^{L,Water}$	0.082	0.544	0.608					0.076		0.002	0.005	0.003		0.004	0.004	0.005	0.004	0.004	0.633	0.633	0.634	0.634	0.633
$HU_{u13,i10}^{L,Water}$																							
$HU_{u13,i11}^{L,Water}$		0.005	0.006																0.006	0.007	0.007	0.007	0.006
$HU_{u13,i12}^{L,Water}$																							
F_{x1}	1.022	0.007	0.019	0.001				0.009	0.002	0.006	0.006	0.006	0.006	0.023	0.015	0.016	0.016	0.014	0.002	0.010	0.009	0.010	0.009
F_{x2}	0.009																						
F_{x3}																							
F_{x13}	0.065	0.162	0.020								0.003	0.002		0.031	0.026	0.026	0.025	0.027					
F_{x14}	0.169	0.136	0.179							0.001	0.002	0.002		0.072	0.069	0.069	0.067	0.071		0.002	0.005	0.004	0.001
F_{x16}	0.230	0.065	0.106								0.003	0.001		0.090	0.079	0.074	0.074	0.083					

Tab. C.27: Continued: approximation of the sensitivity of model states on model measurements $\left|\frac{\delta y}{\delta x}\right|$ based on model simulations. Values < 0.001 are excluded. Gray overlay indicates vanishing influence of model states on all measurements. Light-gray overlay indicated sensitivity only on slow concentration measurements.

Variables at t_0	F_{s19}	L_{u11}^{Oil}	L_{u13}^{Water}	L_{u1}	L_{u2}	L_{u3}	L_{u14}	L_{u22}	$w_{u11,i1}^{Oil}$	$w_{u11,i2}^{Oil}$	$w_{u11,i3}^{Oil}$	$w_{u11,i4}^{Oil}$	$w_{u11,i5}^{Oil}$	$w_{s8,i1}$	$w_{s8,i2}$	$w_{s8,i3}$	$w_{s8,i4}$	$w_{s8,i5}$	$w_{u13,i1}^{Water}$	$w_{u13,i2}^{Water}$	$w_{u13,i3}^{Water}$	$w_{u13,i4}^{Water}$	$w_{u13,i5}^{Water}$
$HU_{i1}^{Reactor}$	3.376	0.049	0.241				0.001	0.203	0.089	0.264	0.260	0.265	0.261	0.429	0.297	0.325	0.324	0.273	0.087	0.371	0.379	0.378	0.366
$HU_{i2}^{Reactor}$	0.037	0.005	0.006					0.002	0.002	0.323	0.007	0.006	0.002	0.003	0.697	0.036	0.031	0.003	0.004	0.282	0.004	0.003	0.004
$HU_{i3}^{Reactor}$	0.002										0.328					0.698					0.288		
$HU_{i4}^{Reactor}$	0.003											0.323					0.684					0.284	
$HU_{i5}^{Reactor}$	1.000	0.103	0.129					0.057	0.081	0.083	0.082	0.083	0.250	0.082	0.103	0.114	0.111	0.590	0.088	0.085	0.085	0.085	0.376
$HU_{i6}^{Reactor}$	0.006									0.004	0.007	0.007	0.002	0.002	0.015	0.023	0.026	0.007		0.005	0.007	0.008	0.003
$HU_{i7}^{Reactor}$	0.004	0.001								0.004	0.007	0.007	0.002	0.002	0.014	0.023	0.025	0.007		0.005	0.007	0.008	0.003
$HU_{i8}^{Reactor}$																							
$HU_{i9}^{Reactor}$	2.976	0.522	0.470				0.001	0.159		0.005	0.011	0.012		0.291	0.294	0.304	0.285	0.308		0.003	0.006	0.008	0.002
$HU_{i10}^{Reactor}$	0.003	0.001							0.002	0.007	0.010	0.008	0.006	0.008	0.029	0.040	0.035	0.026	0.002	0.010	0.012	0.011	0.009
$HU_{i11}^{Reactor}$	0.031	0.004	0.006					0.001						0.003	0.003	0.004	0.003	0.003					
$HU_{i12}^{Reactor}$	0.307	7.631	2.482					0.027	0.008	0.043	0.124	0.084	0.021	0.032	0.004	0.014	0.012	0.001	0.012	0.064	0.148	0.112	0.034
HU_{u1}				1.001																			
HU_{u2}					1.000																		
HU_{u3}						1.000																	
$HU_{u14,i1}^{L}$	0.255		0.002					0.101	0.008	0.024	0.024	0.024	0.024	0.034	0.098	0.098	0.098	0.098	0.008	0.036	0.036	0.036	0.036
$HU_{u14,i2}^{L}$	0.003									0.033				0.001	0.136	0.003	0.002	0.001		0.029			
$HU_{u14,i3}^{L}$											0.033					0.132					0.029		
$HU_{u14,i4}^{L}$												0.033					0.133					0.028	
$HU_{u14,i5}^{L}$	0.013	0.001	0.002					0.029	0.008	0.008	0.008	0.008	0.025	0.033	0.033	0.033	0.033	0.103	0.009	0.009	0.009	0.009	0.037
$HU_{u14,i6}^{L}$	0.127							0.003															
$HU_{u14,i7}^{L}$	0.153							0.003															
$HU_{u14,i8}^{L}$																							
$HU_{u14,i9}^{L}$																							
$HU_{u14,i10}^{L}$																							
$HU_{u14,i11}^{L}$																							
$HU_{u14,i12}^{L}$		0.001																					
$HU_{u22,i1}^{L}$								0.790															
$HU_{u22,i2}^{L}$								0.004															
$HU_{u22,i3}^{L}$																							
$HU_{u22,i4}^{L}$																							
$HU_{u22,i5}^{L}$								0.128															
$HU_{u22,i6}^{L}$								0.039															
$HU_{u22,i7}^{L}$								0.028															
$HU_{u22,i8}^{L}$																							
$HU_{u22,i9}^{L}$								0.001															
$HU_{u22,i10}^{L}$																							
$HU_{u22,i11}^{L}$																							
$HU_{u22,i12}^{L}$																							
$T_{Settler}$	1.462	9.858	2.482					0.531	0.013	0.072	0.200	0.137	0.037	0.016	0.013	0.012	0.013	0.013	0.018	0.097	0.220	0.167	0.054

C.4.2.3 State Estimation – Flowchart of Algorithm for Initialization Route

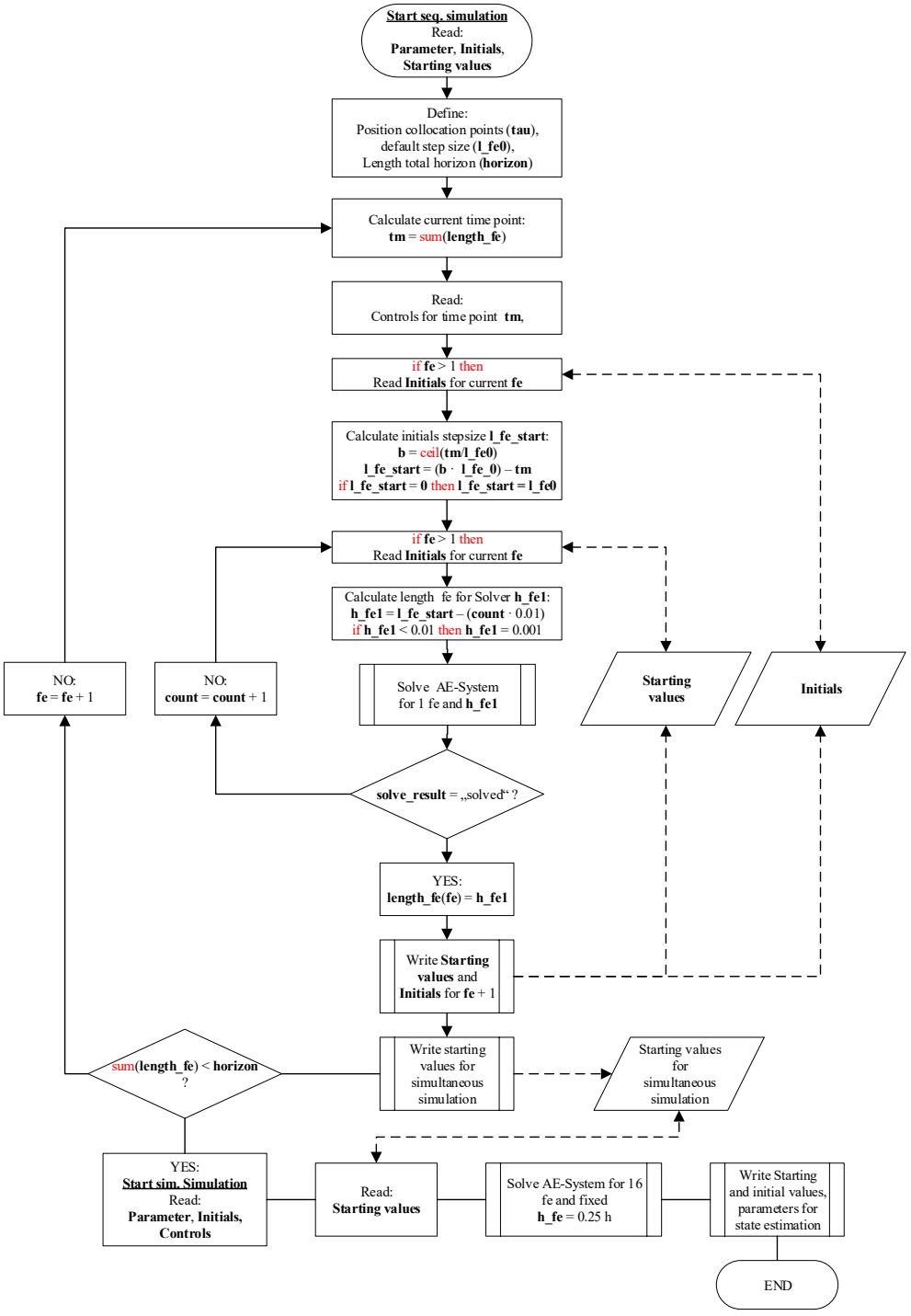

Fig. C.12: Flowchart of developed simulation framework for state estimation initialization, consisting of a sequential simulation with step size control and subsequent simultaneous simulation step.

C.4.3 Dynamic Optimization – Flowchart Algorithm

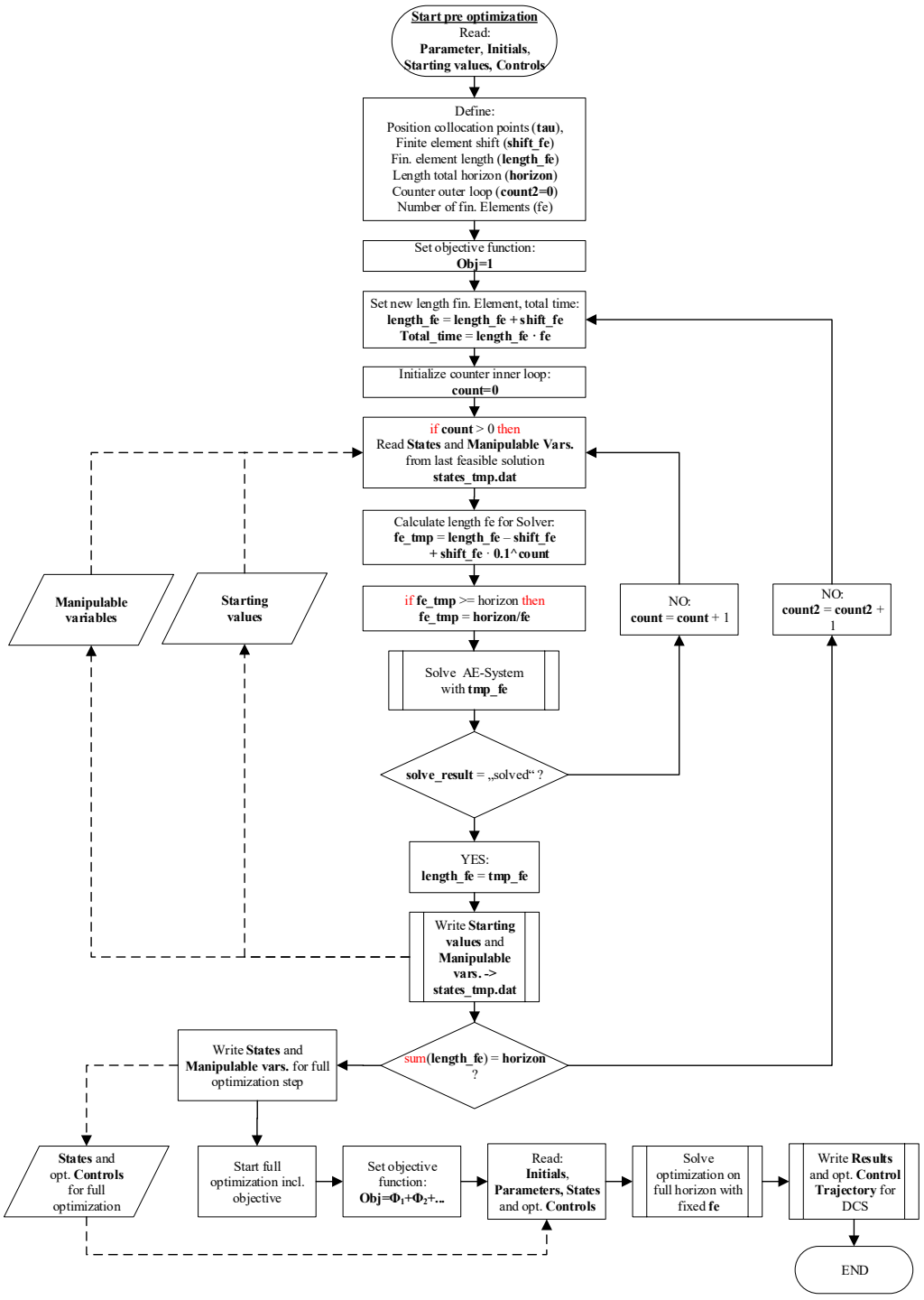

Fig. C.13: Flowchart of developed dynamic optimization framework, consisting of a pre-optimization for initialization excluding the objective function with finite element length step size control and subsequent full optimization step.

Appendix D
Supporting Information - Operation & Optimization Results

D.1 Calculations and Definitions

D.1.1 Calculation of Residence Times

To enable the comparison of mini-plant reaction performances with reference lab-scale experiments obtained from batch experiments, the definition of a suitable reaction residence time for the mini-plant is necessary. Given the fact of 3 internal recycles, the usually applied reactor residence time is not suitable for that. Hence, Fig. D.14 shows a reduced mini-plant scheme and according boundaries to define residence times for tanks and the whole system.

The required reaction residence time $\tau_{Reaction}$ is obtained using the following argumentation:

A volume element of alkene fed to the plant resides in the system for a certain residence time $\tau_{Process}$, which depends on the feedrate and the total oil phase volume of the plant. According to the applied recycle streams, this oil volume element encounters several recycle loops within its plant residence time, passing reactor and subsequent units. Assuming, that the reaction only takes place in the reactor, due to mixing and gas supply, the number of reactor passes $n_{Reactorpass}$ is relevant. If all tank residence times related to the oil phase are known, this number is given by the ratio of plant residence time and the sum of all unit residence times. $\tau_{Reaction}$ is then given by the multiplication of $n_{Reactorpass}$ with the reactor residence time.

$$n_{Reactorpass} = \frac{\tau_{Process}}{\tau_{Reactor} + \tau_{Settler} + \tau_{X04}} \tag{D.27}$$

$$\tau_{Reaction} = n_{Reactorpass} \cdot \tau_{Reactor} = \frac{\tau_{Process}}{\tau_{Reactor} + \tau_{Settler} + \tau_{X04}} \cdot \tau_{Reactor} \tag{D.28}$$

The respective single unit residence times are given in the following:

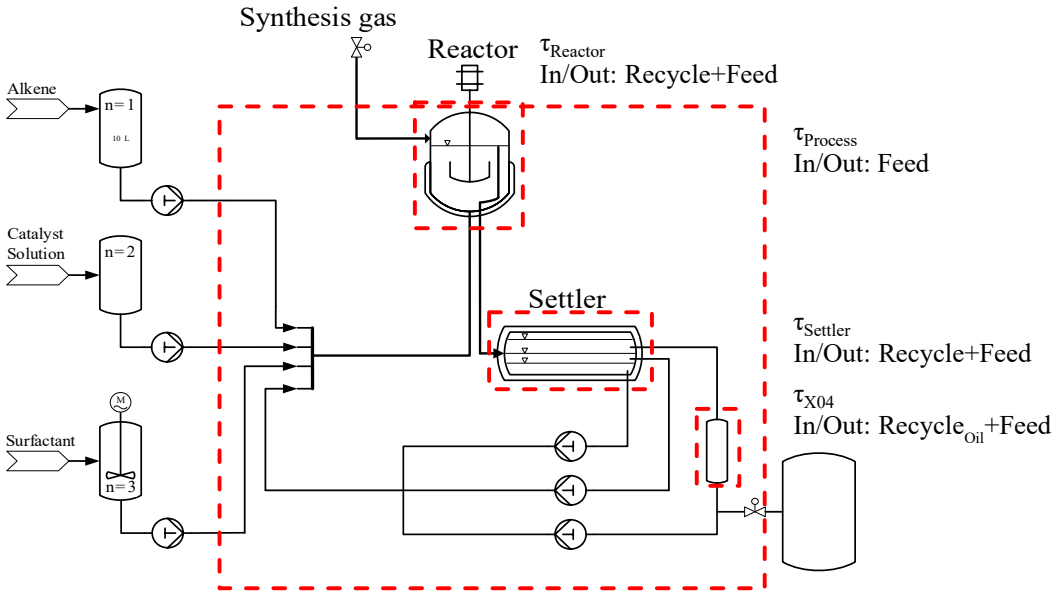

Fig. D.14: Residence time definitions for mini-plant.

$\tau_{Recktor}$ The residence time of the oil volume element is to be calculated. Since the oil mass fraction at inlet and outlet is assumed to be equal, it is given:

$$\tau_{Reactor} = \frac{V^{L}_{Reactor}}{\dot{F}_{Feed} + \dot{F}_{Recycle}} \tag{D.29}$$

$\tau_{Settler}$ Due to the phase distribution in the settler, each phase has to be evaluated separately according oil content and respective recycle stream. As a first guess however, the same assumption, as for the reactor can be made.:

$$\tau_{Settler} = \frac{\sum V^{Oil,Phase}_{Settler}}{\sum \dot{F}_{Feed} + \dot{F}_{Recycle}} \tag{D.30}$$

τ_{X04} The buffer tank X04 usually holds pure oil phase and thus the residence time is given by its level, diameter, and the oil phase recycle and feed:

$$\tau_{X04} = \frac{V^{Oil}_{X04} = f(V,L)}{\dot{F}_{Feed} + \dot{F}^{Oil}_{Recycle}} \tag{D.31}$$

$\tau_{Prozess}$ A single oil droplet will reside in the plant according to the total oil volume and feedrate:

$$\tau_{Process} = \frac{V^{total}_{Oil}}{\dot{F}_{Feed}} \tag{D.32}$$

D.1.2 Reaction Performance Indicators

To evaluate the reaction performance of batch and mini-plant experiments several definitions are given in the following. It is distinguished between batch and mini-plant experiments in continuous mode, since different definitions or assumptions have to be made. All definitions are based on molar concentration measures, while throughout this work molar fractions x are used. For the hydroformylation reaction educt is always referred to as 1-dodecene, whereby tridecanal is defined as target product for yield Y and the chemo-selectivity S.

- Reaction conversion X of 1-dodecene
  The conversion describes the consumption of a reactant over time and is a measure the reaction activity. Since for a steady state continuous plant operation no "starting point" can be defined, the conversion is defined by the total amount of already converted reactants and the total reactant amount:

$$\text{Batch}: \; X^{1-dodecene,B} = \frac{x^{1-dodecene}(t=0) - x^{1-dodecene}(t)}{x^{1-dodecene}(t=0)}, \tag{D.33}$$

$$\text{Plant}: \; X^{1-dodecene,P} = \frac{\sum x_i(t)_i^{Products}}{\sum x_i(t)_i^{Educts+Products}} \tag{D.34}$$

- Reaction yield tridecanal Y^{TDC}
  Amount of formed product i by the amount of available educt. Again the available educt mass is referred to as total reactant amount in case of the mini-plant:

$$\text{Batch}: \; Y^{TDC,B} = \frac{x^{TDC}(t) - x^{TDC}(t=0)}{x^{Educt}(t=0)}, \quad \text{Plant}: \; Y^{TDC,P} = \frac{x^{TDC}(t)}{\sum x_i(t)_i^{Educts+Products}} \tag{D.35}$$

- Chemo selectivity S
  The chemo-selectivity gives information on how much of the current conversion led to the production of the target product:

$$\text{Batch}: \; S^{TDC,B} = \frac{Y^{TDC,B}}{X^{1-dodecene,B}}, \quad \text{Plant}: \; S^{TDC,P} = \frac{Y^{TDC,P}}{X^{1-dodecene,P}} \tag{D.36}$$

- Regio selectivity or n/iso-selectivity $S^{n/iso}$
  In homogeneous catalysis regio-selectivity is often applied as an indicator of the catalyst

performance regarding the formation of desired linear or terminal product versus branched products. For the hydroformylation thus the formation of tridecanal and iso-tridecanal is compared:

$$\text{Batch}: \; S^{n/iso,B} = \frac{x^{TDC}(t)}{x^{TDC}(t) + x^{iso-TDC}(t)}, \quad \text{Plant}: \; S^{n/iso,P} = \frac{x^{TDC}(t)}{x^{TDC}(t) + x^{iso-TDC}(t)} \tag{D.37}$$

D.2 Computational Setups and Solver Settings

D.2.1 gPROMS Simulation and Optimization

All calculations are done in gPROMS® using the program's version 5.1.1 on an Intel Core i7-6700 4 core CPU with a maximum of 4 GHz with 16 GB RAM on a 64-Bit system. The following solution parameters are applied on the DAEs obtained from MOSAICmodeling:

Simulation

Code D.2: Solution parameters for simulations in gPROMS.

```
DASolver := "DASOLV" [
"AbsoluteTolerance" := 1E-006 ]
```

Optimization

Code D.3: Solution parameters for optimizations in gPROMS.

```
DASolver := "DASOLV" [
"AbsoluteTolerance" := 1E-006 ]
MINLPSolver := "NLPSQP" [
"ComplementarityTolerance" := 0,
"FeasibilityTolerance" := 0,
"InitialLineSearchStepLength" := 1,
"MaxFun" := 10000,
"MaximumLineSearchSteps" := 50,
"MaxLineSearchStepLength" := 1,
"NoImprovementTolerance" := 1e-012,
"OptimisationTolerance" := 0.0000005,
"OutputLevel" := 0,
"Scaling" := 1,
"TaylorTolerance" := 0 ]
```

D.2.2 AMPL State Estimation and Optimization

All calculations are done using AMPL® Version 20190223 on an Intel Core i7-4770 8 core CPU with a maximum of 3.9 GHz with 32 GB RAM on a 64-Bit Ubuntu machine. IPOPT ((Wächter, 2002)) and CONOPT[1] are used as NLP solvers, initially on default options. The following solution parameters are applied for simulation and optimization problems using the AEs model obtained from MOSAICmodeling:

Simulation Steps

Code D.4: Solution parameters for simulations in AMPL.

```
option solver ipopt;
option presolve_eps 1e-15;
option show_stats 1;
option ipopt_options "halt_on_ampl_error␣yes
linear_solver␣ma86
max_iter␣5000
expect_infeasible_problem␣yes
warm_start_init_point␣yes";
```

State Estimation Optimization Step

Code D.5: Solution parameters for state estimation optimization in AMPL.

```
option solver conopt;
option presolve_eps 1e-15;
option conopt_options "outlev␣3
workfactor␣5␣errlim␣5000
maxiter␣50000
rtnwmi=1e-7
rtnwma=1e-6";
```

Optimization Steps

Code D.6: Solution parameters for dynamic optimizations in AMPL.

```
option solver conopt;
option presolve_eps 1e-15;
option conopt_options "outlev␣3
workfactor␣5␣errlim␣5000
maxiter␣50000
rtnwmi=1e-7
rtnwma=1e-6";
```

[1] http://www.conopt.com/

D.3 Operation Results Mini-Plant

D.3.1 Standard Mini-Plant Operation - Plant Op 1

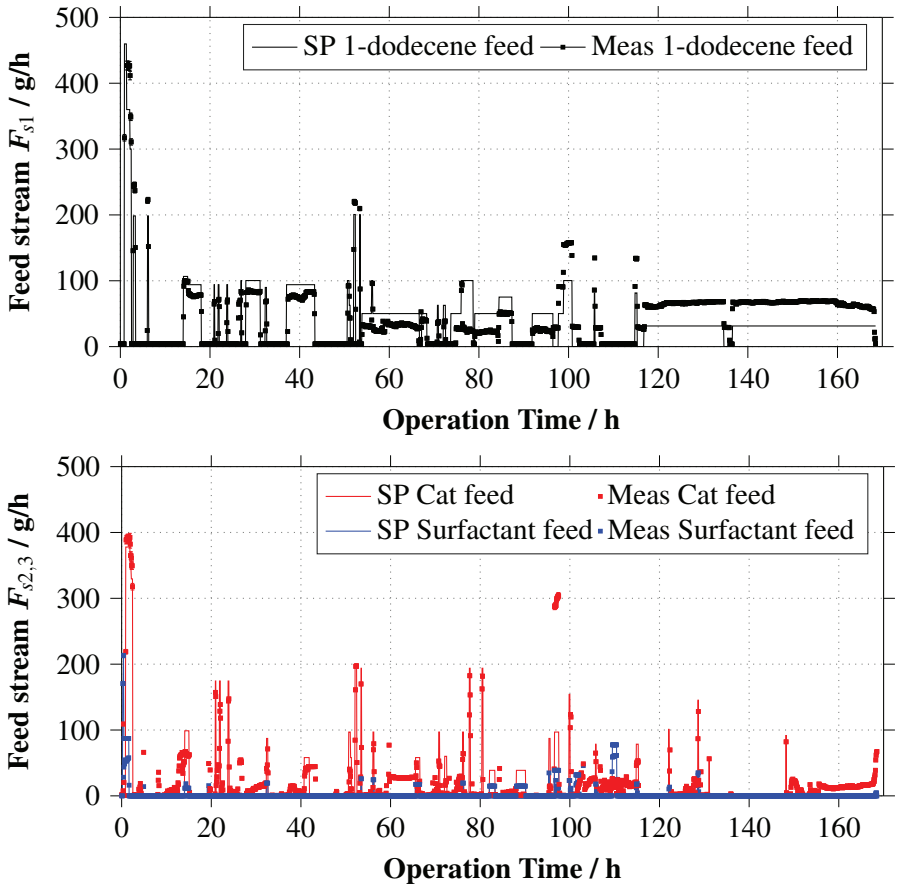

Fig. D.15: Feed rates of 1-dodecene, catalyst, and surfactant for conventional mini-plant operation.

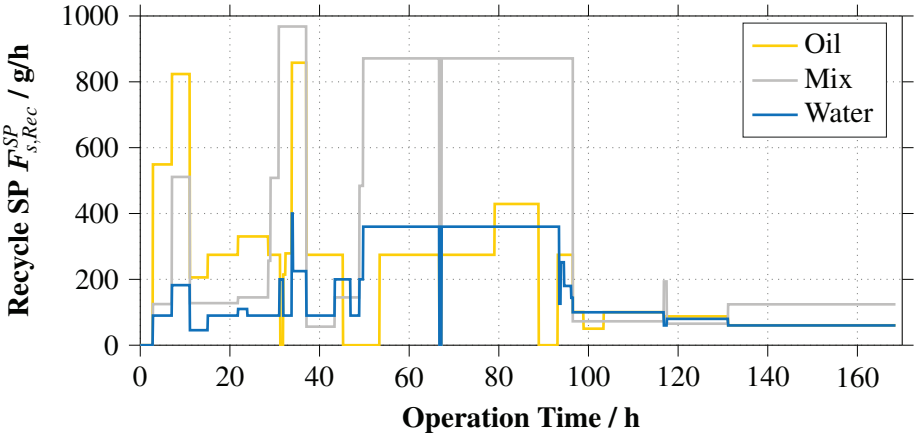

Fig. D.16: Operation Schedule conventional mini-plant campaign: recycle rates and total recycle.

D.3.2 Successful Mini-Plant Operation - Plant Op 2

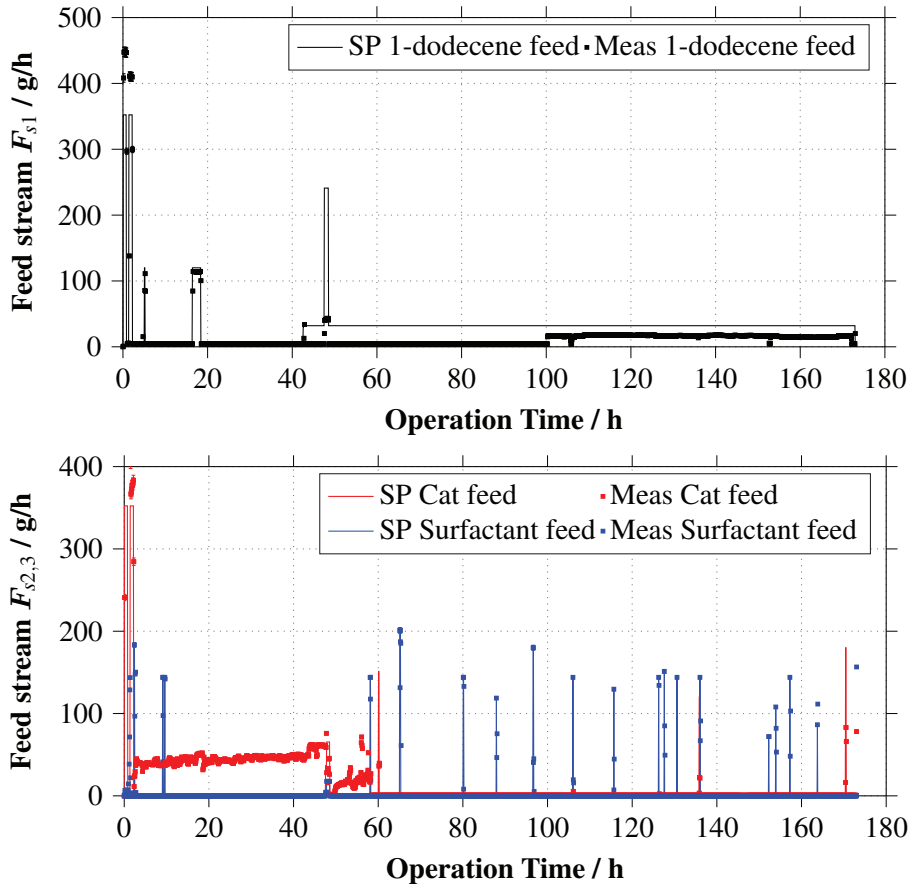

Fig. D.17: Applied feed rates of 1-dodecene, catalyst, and surfactant for Successful mini-plant operation.

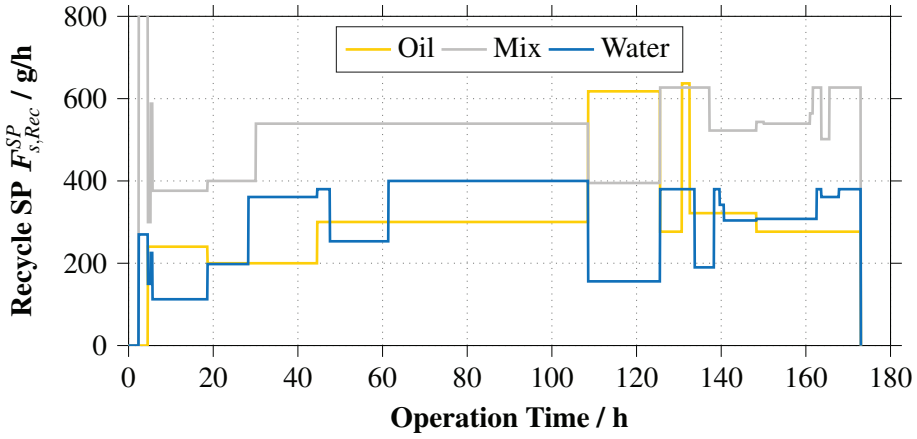

Fig. D.18: Operation Schedule Successful mini-plant campaign: recycle rates and total recycle.

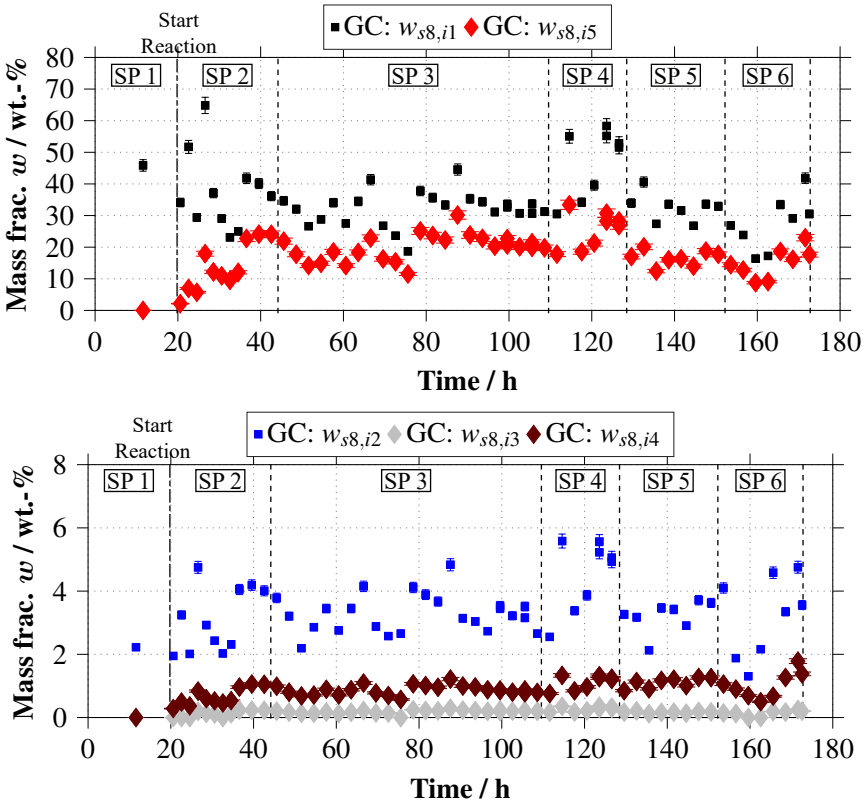

Fig. D.19: Operation results Successful mini-plant campaign: mass fractions in reactor $w_{s=8,i}$ for 1-dodecene ($i = 1$), iso-dodecene ($i = 2$), iso-tridecanal ($i = 3$), dodecane ($i = 4$), tridecanal ($i = 5$).

D.4 Optimization and State Estimation

D.4.1 Development of Start-Up Trajectories – Set Up

Tab. D.28: Control initials and bounds applied for start-up trajectory optimization.

Variable			Initial Guess	Lower Bound	Upper Bound
Alkene feed	$F^{SP}_{s=1}$	$\mathrm{g\,h^{-1}}$	30	30	30
Catalyst feed	$F^{SP}_{s=2}$	$\mathrm{g\,h^{-1}}$	0	0	5
Surfactant feed	$F^{SP}_{s=3}$	$\mathrm{g\,h^{-1}}$	0	0	5
Oil recycle	$F^{SP,Oil}_{s=13}$	$\mathrm{g\,h^{-1}}$	160	100	500
Mix recycle	$F^{SP,Mix}_{s=14}$	$\mathrm{g\,h^{-1}}$	330	200	400
Water recycle	$F^{SP,Water}_{s=16}$	$\mathrm{g\,h^{-1}}$	180	100	400
Reactor temperature	$T_{u=9}$	°C	368.15	358.15	368.15
Settler temperature	$T_{Settler}$	°C	350	344	354

D.4.2 Development of Start-Up Trajectories – Results

Tab. D.29: Results on controls for start-up trajectory optimization scenarios for: feed streams and settler temperature. Scenarios are marked as FR: full recycle, TDC: tridecanal prefill, and Con: continuous mode.

Time / h	$F^{SP}_{s=1}$ / g h^{-1}			$F^{SP}_{s=2}$ / g h^{-1}			$F^{SP}_{s=3}$ / g h^{-1}			$T_{u=9}$ / °C		
	FR	TDC	Con	FR	TDC	Con	FR	TDC	Con	FR	TDC	Con
1 – 2	2.49	29.58	29.58	2.67	0.00	0.00	0.40	0.00	0.00	368.15	368.15	368.15
2 – 3	1.92	29.58	29.58	2.06	0.00	0.00	0.31	0.00	0.00	366.09	366.09	368.15
3 – 4	0.00	29.58	29.58	0.00	0.05	0.58	0.00	0.03	0.19	368.15	366.22	368.15
4 – 5	0.00	29.58	29.58	0.00	0.05	0.58	0.00	0.03	0.16	368.15	368.15	368.15
5 – 6	0.00	29.58	29.58	0.00	0.05	0.55	0.00	0.03	0.18	368.15	368.15	368.15
6 – 7	0.00	29.58	29.58	0.00	0.05	0.55	0.00	0.03	0.23	368.15	368.15	368.15
7 – 8	0.00	29.58	29.58	0.00	0.05	0.55	0.00	0.03	0.07	368.15	368.15	368.15
8 – 9	0.00	29.58	29.58	0.00	0.05	0.59	0.00	0.03	0.05	368.15	368.15	368.15
9 – 10	0.00	29.58	29.58	0.00	0.05	0.45	0.00	0.03	1.50	368.15	368.15	368.15
10 – 11	0.00	29.58	29.58	0.00	0.05	0.48	0.00	0.03	0.95	368.15	368.15	368.15
11 – 12	0.00	29.58	29.58	0.00	0.05	0.54	0.00	0.03	0.53	368.15	368.15	368.15
12 – 13	0.00	29.58	29.58	0.00	0.05	0.57	0.00	0.03	0.52	368.15	368.15	368.15
13 – 14	0.00	29.58	29.58	0.00	0.05	0.53	0.00	0.03	0.49	368.15	368.15	368.15
14 – 15	0.00	29.58	29.58	0.00	0.05	1.15	0.00	0.03	0.45	368.15	368.15	368.15
15 – 16	29.58	29.58	29.58	0.19	0.05	1.16	0.02	0.03	0.45	368.15	368.15	368.15
16 – 17	29.58	29.58	29.58	0.19	0.05	1.16	0.02	0.03	0.45	368.15	368.15	368.15
17 – 18	29.58	29.58	29.58	0.19	0.05	1.16	0.02	0.03	0.45	368.15	368.15	368.15
18 – 19	29.58	29.58	29.58	0.19	0.05	1.17	0.02	0.03	0.45	368.15	368.15	368.15
19 – 20	29.58	29.58	29.58	0.19	0.05	1.17	0.02	0.03	0.45	368.15	368.15	368.15
20 – 21	29.58	29.58	29.58	0.19	0.05	1.17	0.02	0.03	0.45	368.15	368.15	368.15
21 – 22	29.58	29.58	29.58	0.19	0.05	1.17	0.02	0.03	0.45	368.15	368.15	368.15
22 – 23	29.58	29.58	29.58	0.19	0.05	1.18	0.02	0.03	0.45	368.15	368.15	368.15
23 – 24	29.58	29.58	29.58	0.18	0.05	1.17	0.02	0.03	0.45	368.15	368.15	368.15
24 – 25	29.58	29.58	29.58	0.16	0.05	0.43	0.02	0.03	0.02	368.15	368.15	368.15
25 – 26	29.58	29.58	29.58	0.14	0.05	0.43	0.02	0.03	0.02	368.15	368.15	368.15
26 – 27	29.58	29.58	29.58	0.14	0.05	0.43	0.02	0.03	0.02	368.15	368.15	368.15
27 – 28	29.58	29.58	29.58	0.14	0.05	0.43	0.02	0.03	0.02	368.15	368.15	368.15
28 – 29	29.58	29.58	29.58	0.14	0.05	0.43	0.02	0.03	0.02	368.15	368.15	368.15
29 – 30	29.58	29.58	29.58	0.14	0.05	0.43	0.02	0.03	0.02	368.15	368.15	368.15
30 – 31	29.58	29.58	29.58	0.14	0.05	0.43	0.02	0.03	0.02	368.15	368.15	368.15
31 – 32	29.58	29.58	29.58	0.14	0.05	0.43	0.02	0.03	0.02	368.15	368.15	368.15
32 – 33	29.58	29.58	29.58	0.14	0.05	0.43	0.02	0.03	0.02	368.15	368.15	368.15
33 – 34	29.58	29.58	29.58	0.14	0.05	0.43	0.02	0.03	0.02	368.15	368.15	368.15
34 – 35	29.58	29.58	29.58	0.14	0.05	0.43	0.02	0.03	0.02	368.15	368.15	368.15
35 – 36	29.58	29.58	29.58	0.14	0.05	0.43	0.02	0.03	0.02	368.15	368.15	368.15
36 – 37	29.58	29.58	29.58	0.14	0.05	0.44	0.02	0.03	0.02	368.15	368.15	368.15
37 – 38	29.58	29.58	29.58	0.14	0.05	0.44	0.02	0.03	0.02	368.15	368.15	368.15
38 – 39	29.58	29.58	29.58	0.14	0.05	0.44	0.02	0.03	0.02	368.15	368.15	368.15
39 – 40	29.58	29.58	29.58	0.14	0.05	0.44	0.02	0.03	0.02	368.15	368.15	368.15
40 – 41	29.58	29.58	29.58	0.14	0.05	0.44	0.02	0.03	0.02	368.15	368.15	368.15
41 – 42	29.58	29.58	29.58	0.14	0.05	0.45	0.02	0.03	0.02	368.15	368.15	368.15
42 – 43	29.58	29.58	29.58	0.14	0.05	0.45	0.02	0.03	0.02	368.15	368.15	368.15
43 – 44	29.58	29.58	29.58	0.14	0.05	0.45	0.02	0.03	0.02	368.15	368.15	368.15
44 – 45	29.58	29.58	29.58	0.14	0.05	0.46	0.02	0.03	0.02	368.15	368.15	368.15
45 – 46	29.58	29.58	29.58	0.14	0.05	0.46	0.02	0.03	0.02	368.15	368.15	368.15
46 – 47	29.58	29.58	29.58	0.14	0.05	0.46	0.02	0.03	0.02	368.15	368.15	368.15
47 – 48	29.58	29.58	29.58	0.14	0.05	0.47	0.02	0.03	0.02	368.15	368.15	368.15
48 – 49	29.58	29.58	29.58	0.14	0.05	0.47	0.02	0.03	0.02	368.15	368.15	368.15
49 – 50	29.58	29.58	29.58	0.14	0.05	0.48	0.02	0.03	0.02	368.15	368.15	368.15
50 – 51	29.58	29.58	29.58	0.15	0.05	0.48	0.02	0.03	0.02	368.15	368.15	368.15
51 – 52	29.58	29.58	29.58	0.15	0.05	0.48	0.02	0.03	0.02	368.15	368.15	368.15
52 – 53	29.58	29.58	29.58	0.15	0.05	0.49	0.02	0.03	0.02	368.15	368.15	368.15
53 – 54	29.58	29.58	29.58	0.15	0.05	0.49	0.02	0.03	0.02	368.15	368.15	368.15
54 – 55	29.58	29.58	29.58	0.15	0.05	0.11	0.02	0.03	0.02	368.15	368.15	368.15
55 – 56	29.58	29.58	29.58	0.15	0.05	0.11	0.02	0.03	0.02	368.15	368.15	368.15
56 – 57	29.58	29.58	29.58	0.15	0.05	0.11	0.02	0.03	0.02	368.15	368.15	368.15
57 – 58	29.58	29.58	29.58	0.15	0.05	0.11	0.02	0.03	0.02	368.15	368.15	368.15
58 – 59	29.58	29.58	29.58	0.15	0.05	0.11	0.02	0.03	0.02	368.15	368.15	368.15
59 – 60	29.58	29.58	29.58	0.15	0.05	0.11	0.02	0.03	0.02	368.15	368.15	368.15
60 – 61	29.58	29.58	29.58	0.15	0.05	0.12	0.02	0.03	0.02	368.15	368.15	368.15
61 – 62	29.58	29.58	29.58	0.15	0.05	0.12	0.02	0.03	0.02	368.15	368.15	368.15
62 – 63	29.58	29.58	29.58	0.15	0.05	0.12	0.02	0.03	0.02	368.15	368.15	368.15
63 – 64	29.58	29.58	29.58	0.15	0.05	0.12	0.02	0.03	0.02	368.15	368.15	368.15
64 – 65	29.58	29.58	29.58	0.14	0.05	0.12	0.02	0.03	0.02	368.15	368.15	368.15
65 – 66	29.58	29.58	29.58	0.12	0.05	0.13	0.02	0.03	0.02	368.15	368.15	368.15
66 – 67	29.58	29.58	29.58	0.02	0.05	0.13	0.03	0.03	0.02	368.15	368.15	368.15
67 – 68	29.58	29.58	29.58	0.02	0.05	0.13	0.03	0.03	0.02	368.15	368.15	368.15
68 – 69	29.58	29.58	29.58	0.02	0.05	0.13	0.03	0.03	0.02	368.15	368.15	368.15
69 – 70	29.58	29.58	29.58	0.02	0.05	0.15	0.03	0.03	0.02	368.15	368.15	368.15

Tab. D.30: Results on controls for start-up trajectory optimization scenarios for: recycle streams and settler temperature. Scenarios are marked as FR: full recycle, TDC: tridecanal prefill, and Con: continuous mode.

Time / h	$F_{s=13}^{SP,Oil}$ / g h^{-1}			$F_{s=14}^{SP,Mix}$ / g h^{-1}			$F_{s=16}^{SP,Water}$ / g h^{-1}			$T_{Settler}$ / °C		
	FR	TDC	Con	FR	TDC	Con	FR	TDC	Con	FR	TDC	Con
1 – 2	149.70	113.72	143.35	323.50	330.65	321.36	159.23	156.20	155.76	351.39	348.83	351.30
2 – 3	175.84	189.85	178.61	258.50	327.01	297.01	155.10	179.99	155.93	350.36	346.27	350.98
3 – 4	203.24	176.63	187.18	308.39	342.90	281.78	183.47	176.39	155.91	349.33	345.60	350.96
4 – 5	193.11	159.18	183.00	329.07	341.92	283.90	177.86	175.85	156.05	348.90	345.60	350.94
5 – 6	188.78	160.36	173.26	334.70	345.69	286.35	178.61	175.05	156.33	347.82	345.60	350.89
6 – 7	186.39	160.17	175.24	338.79	345.80	285.34	178.68	175.13	157.87	347.72	345.60	350.81
7 – 8	185.65	160.87	170.60	337.78	346.26	282.83	181.21	176.02	159.78	346.12	345.60	350.72
8 – 9	185.92	159.28	161.52	339.70	342.46	286.78	181.21	174.87	159.34	345.80	345.60	350.56
9 – 10	185.65	154.45	155.96	340.32	332.89	288.05	182.05	170.75	165.13	345.60	345.60	350.60
10 – 11	185.52	173.09	162.36	340.01	327.22	285.13	182.85	170.82	167.97	345.60	345.60	349.86
11 – 12	186.25	173.09	157.03	339.62	327.22	281.86	184.25	170.82	163.06	345.60	345.60	349.87
12 – 13	186.35	173.09	159.34	337.55	327.22	282.49	183.84	170.82	162.88	345.60	345.60	349.87
13 – 14	186.88	173.09	161.75	335.19	327.22	284.54	183.08	170.82	162.58	345.60	345.60	349.10
14 – 15	191.10	173.09	161.30	338.17	327.22	287.98	185.75	170.82	162.74	345.60	345.60	349.24
15 – 16	157.75	173.09	161.30	328.31	327.22	289.51	181.02	170.82	162.40	345.60	345.60	349.21
16 – 17	159.33	173.09	161.42	331.53	327.22	291.06	182.35	170.82	162.05	345.60	345.60	348.70
17 – 18	159.64	173.09	161.81	332.50	327.22	292.12	182.41	170.82	161.59	345.60	345.60	348.65
18 – 19	159.41	173.09	162.16	332.21	327.22	293.00	181.92	170.82	161.09	345.60	345.60	348.61
19 – 20	159.72	173.09	165.38	332.85	327.22	300.85	181.99	170.82	162.32	345.60	345.60	348.74
20 – 21	158.31	173.09	164.58	330.46	327.22	299.87	180.42	170.82	161.84	345.60	345.60	348.30
21 – 22	160.97	173.09	162.20	335.20	327.22	291.37	182.78	170.82	159.71	345.60	345.60	348.06
22 – 23	161.36	173.09	164.62	335.95	327.22	291.69	182.96	170.82	155.44	345.60	345.60	347.44
23 – 24	161.18	173.09	164.32	335.88	327.22	291.08	182.65	170.82	154.10	345.60	345.60	347.44
24 – 25	161.60	173.09	164.79	336.53	327.22	290.97	182.85	170.82	154.33	345.60	345.60	347.44
25 – 26	161.60	173.09	164.91	336.59	327.22	291.23	182.78	170.82	165.54	345.60	345.60	347.43
26 – 27	161.45	173.09	164.89	336.39	327.22	291.33	182.53	170.82	165.52	345.60	345.60	346.99
27 – 28	161.48	173.09	164.93	336.50	327.22	291.40	182.47	170.82	165.50	345.60	345.60	346.99
28 – 29	161.47	173.09	164.96	336.54	327.22	291.44	182.36	170.82	165.48	345.60	345.60	346.48
29 – 30	161.44	173.09	165.01	336.55	327.22	291.52	182.24	170.82	165.45	345.60	345.60	346.48
30 – 31	161.40	173.09	165.05	336.54	327.22	291.60	182.11	170.82	165.42	345.60	345.60	346.47
31 – 32	161.37	173.09	165.08	336.53	327.22	291.64	181.98	170.82	165.41	345.60	345.60	346.46
32 – 33	161.33	173.09	165.13	336.53	327.22	291.76	181.85	170.82	165.37	345.60	345.60	345.97
33 – 34	161.28	173.09	165.17	336.52	327.22	291.88	181.72	170.82	165.33	345.60	345.60	345.97
34 – 35	161.24	173.09	165.21	336.52	327.22	292.00	181.60	170.82	165.30	345.60	345.60	345.97
35 – 36	161.20	173.09	165.25	336.52	327.22	292.11	181.47	170.82	165.27	345.60	345.60	345.97
36 – 37	161.16	173.09	165.28	336.52	327.22	292.23	181.34	170.82	165.23	345.60	345.60	345.97
37 – 38	161.12	173.09	165.33	336.52	327.22	292.38	181.22	170.82	165.18	345.60	345.60	345.48
38 – 39	161.08	173.09	165.37	336.52	327.22	292.53	181.09	170.82	165.13	345.60	345.60	345.48
39 – 40	161.04	173.09	165.42	336.52	327.22	292.67	180.97	170.82	165.09	345.60	345.60	345.48
40 – 41	160.99	173.09	165.47	336.53	327.22	292.81	180.84	170.82	165.05	345.60	345.60	345.48
41 – 42	160.95	173.09	165.52	336.53	327.22	292.96	180.71	170.82	165.01	345.60	345.60	345.48
42 – 43	160.91	173.09	165.57	336.53	327.22	293.12	180.59	170.82	164.96	345.60	345.60	345.48
43 – 44	160.86	173.09	165.62	336.53	327.22	293.29	180.46	170.82	164.91	345.60	345.60	345.48
44 – 45	160.82	173.09	165.68	336.54	327.22	293.47	180.34	170.82	164.86	345.60	345.60	345.48
45 – 46	160.77	173.09	165.74	336.54	327.22	293.66	180.21	170.82	164.81	345.60	345.60	345.48
46 – 47	160.73	173.09	165.79	336.54	327.22	293.69	180.09	170.82	164.78	345.60	345.60	345.48
47 – 48	160.68	173.09	165.81	336.55	327.22	293.50	179.96	170.82	164.75	345.60	345.60	345.48
48 – 49	160.64	173.09	165.93	336.55	327.22	294.08	179.84	170.82	164.61	345.60	345.60	345.48
49 – 50	160.60	173.09	166.59	336.55	327.22	295.30	179.71	170.82	165.01	345.60	345.60	345.48
50 – 51	160.55	173.09	166.27	336.56	327.22	294.18	179.59	170.82	164.87	345.60	345.60	345.48
51 – 52	160.50	173.09	165.60	336.56	327.22	293.14	179.46	170.82	164.14	345.60	345.60	345.48
52 – 53	160.46	173.09	166.05	336.56	327.22	293.82	179.33	170.82	164.33	345.60	345.60	345.48
53 – 54	160.41	173.09	165.38	336.57	327.22	293.82	179.21	170.82	163.62	345.60	345.60	345.48
54 – 55	160.37	173.09	165.20	336.57	327.22	294.04	179.08	170.82	163.61	345.60	345.60	345.46
55 – 56	160.32	173.09	162.45	336.57	327.22	294.19	178.95	170.82	163.56	345.60	345.60	345.46
56 – 57	160.28	173.09	162.47	336.58	327.22	294.39	178.83	170.82	163.51	345.60	345.60	345.46
57 – 58	160.23	173.09	162.52	336.58	327.22	294.56	178.70	170.82	163.45	345.60	345.60	345.46
58 – 59	160.19	173.09	162.57	336.59	327.22	294.73	178.57	170.82	163.40	345.60	345.60	345.46
59 – 60	160.13	173.09	162.62	336.58	327.22	294.90	178.44	170.82	163.35	345.60	345.60	345.46
60 – 61	160.10	173.09	162.68	336.61	327.22	295.10	178.32	170.82	163.29	345.60	345.60	345.46
61 – 62	160.03	173.09	162.73	336.58	327.22	295.26	178.17	170.82	163.24	345.60	345.60	345.46
62 – 63	160.06	173.09	162.76	336.71	327.22	295.41	178.11	170.82	163.15	345.60	345.60	345.46
63 – 64	159.73	173.09	162.83	336.23	327.22	295.62	177.72	170.82	163.11	345.60	345.60	345.46
64 – 65	160.44	173.09	163.22	337.56	327.22	296.33	178.29	170.82	163.32	345.60	345.60	345.46
65 – 66	158.82	173.09	163.08	334.80	327.22	295.61	176.68	170.82	163.24	345.60	345.60	345.46
66 – 67	162.46	173.09	162.70	336.71	327.22	295.01	180.01	170.82	162.77	345.60	345.60	345.46
67 – 68	160.28	173.09	163.05	336.51	327.22	295.56	178.61	170.82	162.90	345.60	345.60	345.46
68 – 69	160.31	173.09	162.53	337.15	327.22	294.87	179.47	170.82	162.33	345.60	345.60	345.46
69 – 70	160.46	173.09	163.03	337.08	327.22	295.77	178.44	170.82	162.60	345.60	345.60	345.46

D.4.3 Result Trajectories D-RTO Case Study on Successful Mini-Plant Operation

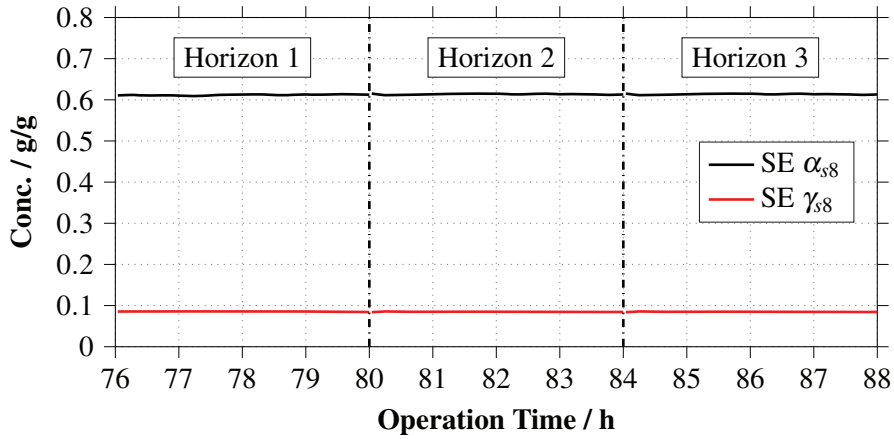

Fig. D.20: Results for the D-RTO case study on SP 3 of Plant Op 2: oil to water ratio α_{s8} and surfactant concentration γ_{s8} in the reactor are shown for three state estimation and optimization horizons.

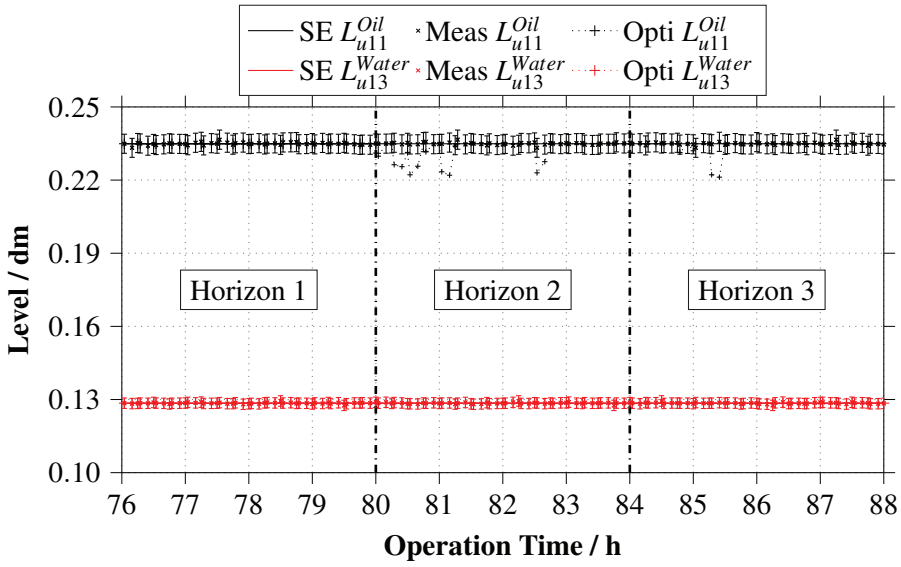

Fig. D.21: Results for the D-RTO case study on SP 3 of Plant Op 2: levels of settler excess phases. For three application horizons the trajectories from state estimation (SE) and optimization (Opti) are compared with measurement data (Meas).

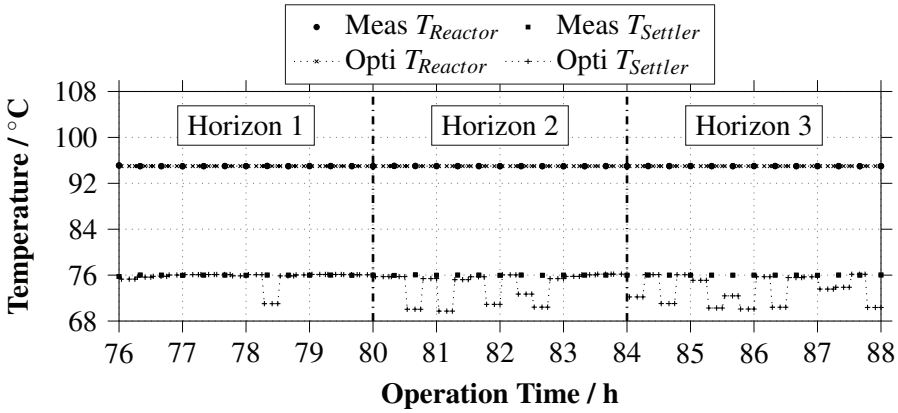

Fig. D.22: Results for the D-RTO case study on SP 3 of Plant Op 2: comparison of settler and reactor temperature trajectories from optimization (Opti) and actual plant measurements (Meas).